Towards the measurement of photon polarisation in the decay B$^+$ → K$^+$ π$^-$ π$^+$ γ

THÈSE N^O 6896 (2016)

PRÉSENTÉE LE 15 JANVIER 2016
À LA FACULTÉ DES SCIENCES DE BASE
LABORATOIRE DE PHYSIQUE DES HAUTES ÉNERGIES 2
PROGRAMME DOCTORAL EN PHYSIQUE

ÉCOLE POLYTECHNIQUE FÉDÉRALE DE LAUSANNE

POUR L'OBTENTION DU GRADE DE DOCTEUR ÈS SCIENCES

PAR

Giovanni VENEZIANO

acceptée sur proposition du jury:

Prof. F. Mila, président du jury
Prof. O. Schneider, Dr F. Blanc, directeurs de thèse
Dr E. Kou, rapporteuse
Prof. T. Gershon, rapporteur
Dr T. Schietinger, rapporteur

EPFL

ÉCOLE POLYTECHNIQUE
FÉDÉRALE DE LAUSANNE

Suisse
2016

On ne découvre pas de terre nouvelle sans consentir
à perdre de vue, d'abord et longtemps, tout rivage.
— André Paul Guillaume Gide

I am among those who think that science has a great
beauty. A scientist in his laboratory is not only a
technician: he is also a child placed before natural
phenomena which impress him like a fairy tale.
— Marie Curie

Abstract

This thesis presents a study of the flavour-changing neutral-current radiative $B^+ \to K^+\pi^-\pi^+\gamma$ decay performed using $3\,\mathrm{fb}^{-1}$ of data collected with the LHCb detector in proton-proton collisions at 7 and $8\,\mathrm{TeV}$ centre-of-mass energies. The study of radiative decays with three scalar hadrons in the final state gives access to the polarisation of the photon, one of the very few predictions of the Standard Model of particle physics that has not been precisely tested experimentally and that is sensitive to new physics effects in the $b \to s\gamma$ penguin loop. Nearly $14\,000$ signal events, containing all possible intermediate resonances with a $K^+\pi^-\pi^+$ final state in the $[1,2]\,\mathrm{GeV}/c^2$ mass interval, are reconstructed and selected in the data sample. The distribution of the angle of the photon direction with respect to the plane defined by the final-state hadrons in their rest frame is studied in intervals of $K^+\pi^-\pi^+$ mass and the asymmetry between the number of signal events with the photon emitted on each side of the plane is obtained. The first direct observation of the photon polarisation in the $b \to s\gamma$ transition is reported with a significance of $5.2\,\sigma$. The contributions of the resonances populating the studied $K^+\pi^-\pi^+$ mass interval are then disentangled by means of a three-dimensional amplitude analysis of the invariant squared masses of the $K^+\pi^-\pi^+$, $K^+\pi^-$ and $\pi^+\pi^-$ systems, integrating out the angular dimensions that describe the direction of the photon. The results of this analysis are the most precise ever obtained in this decay channel, allowing for an accurate description of the decay modes of the intermediate resonances and their interference patterns: the $K_1(1270)^+ \to K^+\rho(770)^0$ channel has been found to be the dominant kaon resonance decay mode, followed by $K_1(1270)^+ \to K^*(892)^0\pi^+$; the fraction of the $K_1(1270)^+$ decaying to $K^*(1430)^0\pi^+$ has been found to be much lower than the world average, analogously to already existing experimental and theoretical studies; a significant interference between the $K_1(1270)^+$ and $K_1(1400)^+$ kaon resonances decay modes is observed. Based on the results of these studies, the full five-dimensional amplitude analysis of the invariant masses and the angular variables is introduced, aiming at the first determination of a numerical value for the polarisation of the photon.

Keywords: experimental particle physics, flavour physics, radiative B decays, photon polarisation, amplitude analysis.

Résumé

Cette thèse présente une étude de la désintégration radiative à courant neutre avec changement de saveur $B^+ \to K^+\pi^-\pi^+\gamma$, réalisée en utilisant 3 fb^{-1} de données recueillies avec le détecteur LHCb dans les collisions proton-proton à des énergies dans le centre de masse de 7 et 8 TeV. L'étude des désintégrations radiatives en trois hadrons scalaires donne accès à la polarisation du photon, l'une des rares prédictions du modèle standard de la physique des particules qui n'a pas été testée expérimentalement de façon précise et qui est sensible à la nouvelle physique dans le diagramme en boucle de type pingouin $b \to s\gamma$. Près de 14 000 événements de signal, contenant toutes les résonances intermédiaires possibles avec l'état final $K^+\pi^-\pi^+$ dans l'intervalle de masse $[1,2]$ GeV/c^2, sont reconstruits et sélectionnés dans l'échantillon de données. La distribution de l'angle de la direction du photon par rapport au plan défini par les hadrons de l'état final dans le référentiel de leur centre de masse est étudiée dans différents intervalles de masse du système $K^+\pi^-\pi^+$ et l'asymétrie entre le nombre d'événements de signal avec le photon émis de chaque côté du plan est obtenue. La première observation directe de la polarisation du photon dans la transition $b \to s\gamma$ est présentée avec une signification statistique de $5.2\,\sigma$. Les contributions des résonances peuplant l'intervalle de masse du système $K^+\pi^-\pi^+$ étudié sont ensuite estimées par une analyse d'amplitude en trois dimensions des masses invariantes ($m^2_{K^+\pi^-\pi^+}$, $m^2_{K^+\pi^-}$ et $m^2_{\pi^+\pi^-}$), après intégration sur les dimensions angulaires qui décrivent la direction du photon. Les résultats de cette analyse sont les plus précis jamais obtenus dans ce canal de désintégration, permettant une description précise des modes de désintégration des résonances intermédiaires et leurs interférences : le canal $K_1(1270)^+ \to K^+\rho(770)^0$ se révèle être le mode de désintégration dominant, suivi par $K_1(1270)^+ \to K^*(892)^0\pi^+$; la fraction de $K_1(1270)^+$ qui se désintègre en $K^*(1430)^0\pi^+$ s'est avérée beaucoup plus petite que la moyenne mondiale, en accord avec les études expérimentales et théoriques récentes ; une interférence significative entre les résonances $K_1(1270)^+$ et $K_1(1400)^+$ est observée. Sur la base des résultats de ces études, l'analyse d'amplitude des masses invariantes et des variables angulaires en cinq dimensions est introduite, en vue de la première détermination d'une valeur numérique pour la polarisation du photon.

Mots clés: physique expérimentale des particules, physique des saveurs, désintégration radiative, polarisation du photon, analyse d'amplitude.

Riassunto

Questa tesi presenta uno studio del decadimento di corrente neutra con cambiamento di sapore $B^+ \to K^+\pi^-\pi^+\gamma$, realizzato utilizzando 3 fb^{-1} di dati raccolti con il rivelatore LHCb in collisioni protone-protone con energia del centro di massa di 7 e 8 TeV. Lo studio dei decadimenti con tre adroni scalari e un fotone nello stato finale dà accesso alla polarizzazione del fotone, una delle poche predizioni del Modello Standard della fisica delle particelle ancora non testate sperimentalmente con precisione, sensibile a effetti di fisica oltre il Modello Standard nel diagramma a loop $b \to s\gamma$. Nel campione di dati vengono ricostruiti e selezionati quasi $14\,000$ eventi, contenenti tutte le possibili risonanze intermedie con uno stato finale $K^+\pi^-\pi^+$ nell'intervallo di massa $[1, 2]$ GeV$/c^2$. La distribuzione angolare dei fotoni rispetto al piano definito dagli adroni nello stato finale nel loro sistema di riposo è studiata in intervalli di massa del sistema $K^+\pi^-\pi^+$ al fine di ottenere l'asimmetria tra il numero di eventi con il fotone emesso su ciascun lato di tale piano. La prima osservazione diretta della polarizzazione dei fotoni nella transizione $b \to s\gamma$ è ottenuta con una significativitá di $5,2\,\sigma$. I contributi delle risonanze che popolano l'intervallo di massa del sistema $K^+\pi^-\pi^+$ studiato vengono separati per mezzo di un'analisi delle ampiezze tridimensionale delle masse invarianti dei sistemi $K^+\pi^-\pi^+$, $K^+\pi^-$ e $\pi^+\pi^-$, integrando sugli angoli che descrivono la direzione del fotone. I risultati di questa analisi sono i più precisi ottenuti per questo decadimento, consentendo una descrizione accurata delle modalità di decadimento delle risonanze intermedie e dei loro schemi di interferenza: il decadimento $K_1(1270)^+ \to K^+\rho(770)^0$ risulta essere dominante, seguito da $K_1(1270)^+ \to K^*(892)^0\pi^+$; la frazione di $K_1(1270)^+$ che decade in $K^*(1430)^0\pi^+$ è molto ridotta rispetto alla media mondiale, analogamente a quanto osservato da altri studi sperimentali e teorici recenti; viene misurata un'interferenza significativa tra le risonanze $K_1(1270)^+$ e $K_1(1400)^+$. Sulla base dei risultati di questo studio, è introdotta l'analisi delle ampiezze in cinque dimensioni delle masse invarianti e delle variabili angolari, finalizzata alla prima determinazione numerica della polarizzazione del fotone.

Parole chiave: fisica sperimentale delle particelle, fisica del sapore, decadimenti radiativi, polarizzazione del fotone, analisi delle ampiezze.

Acknowledgements

People spending time with me know very well that what I do best is complaining. Even so, I only have words of praise for the years spent at EPFL. I would like to start by expressing my gratitude to my thesis supervisors Prof. Olivier Schneider and Dr Fred Blanc for always finding time to check on the progresses of my studies, and for all their helpful suggestions and comments. Working with people so motivated and passionate as you has been a great experience from both a personal and professional point of view.

A sincere thanks goes to all the professors, postdocs, fellow PhD students and LPHE staff members that I have had the honour to call *colleagues* during my years at EPFL and CERN, and in particular to Erika and Esther for being just awesome. I want to thank Prof. Aurelio Bay for always being available for any kind of advice and for giving me the chance of teaching some really cool topics. Thanks a lot also to Prof. Tatsuya Nakada for challenging me with the most clever questions whenever I showed my work to the group. A huge thank you to Karim for being an endless factory of great ideas and for being always ready to have fun with/of me. Thanks to Guido for baby-sitting me in the lab during a very painful first year of hardware studies. A special thanks goes, of course, to Albert: aside from having guided my first steps in the world of experimental particle physics and computing, he has been a great friend, always ready to help solving nasty bugs in the code as well as to join in for a burger and a beer after work.

I am personally indebted to the coffee machine, because *coffee does not ask silly questions, coffee understands* [cit.], YouTube and the Internet in general for providing a lot of amusement in desperate times of thesis writing, and Google for knowing just about everything.

Grazie mamma e papà for believing in this annoying kid that wanted to be an astronaut (or a millionaire depending on the day) and supporting him in any possible way. A special thanks to my brothers and to my friends, the new ones and the ones of a lifetime, for never making me feel alone despite being scattered across half the world. One last not less important thank you to my *moon and stars* Valentina for always being there.

December 2015   Giovanni

Contents

Context and outline

The Standard Model (SM) of particle physics has proven in the last decades to be very successful at describing nature at the most fundamental level. Despite being incomplete (it does not include gravitational forces and cannot explain neither the huge matter-antimatter asymmetry in the universe nor the neutrino masses) the model has brilliantly passed every test, and each new discovery has turned out to be a confirmation of one of its predictions. A few currently accessible *corners* remain unexplored with plenty of ongoing searches looking for any sign of physics beyond its predictions.

The polarisation of the photon, accessible through the study of radiative B decays, is one of the predictions of the model that have never been precisely tested. Rare $b \to s\gamma$ flavour-changing neutral-current transitions are expected to be sensitive to new physics effects that may arise from the exchange of heavy fermions in the electroweak penguin loop. These effects might result in the enhancement of the photon right-handed component, whereas the SM predicts it to be mostly left-handed.

This thesis presents a study of the $B^+ \to K^+\pi^-\pi^+\gamma$ decay, with $K^+\pi^-\pi^+$ mass in the $[1, 2]\,\mathrm{GeV}/c^2$ interval, performed on data collected with the LHCb detector at 7 and 8 TeV centre-of-mass energies. The three scalar hadrons in the final state can be used to build a parity-odd triple product with the photon momentum that can be used to access the photon helicity. In particular, the angular distribution of the photon can be directly related to the photon polarisation parameter λ_γ, expected to be $+1(-1)$ for B ($\overline{B}$) decays in the SM, up to small corrections. A simplified approach consists in determining the photon polarisation from the asymmetry between the number of signal events with the photon observed on each side of the $K^+\pi^-\pi^+$ plane, the *up-down* asymmetry, that is directly proportional to λ_γ. However, since the available theoretical predictions cannot account for the many kaon resonances that populate the studied $K^+\pi^-\pi^+$ mass interval, this measurement cannot be translated into a numerical value for the polarisation of the photon.

The road towards the experimental determination of λ_γ goes through the separation of the

1

modes that crowd the $K^+\pi^-\pi^+$ mass spectrum and the identification of their interference patterns. This can be achieved by means of a multidimensional amplitude analysis that characterises the final state $K^+\pi^-\pi^+\gamma$ system using all its degrees of freedom: three invariant masses ($m^2_{K^+\pi^-\pi^+}$, $m^2_{K^+\pi^-}$ and $m^2_{\pi^+\pi^-}$) and two angles (θ and χ) defining the direction of the photon with respect to the decay plane of the final state hadrons. An amplitude analysis relying solely on the three invariant masses can be exploited to identify the $m_{K^+\pi^-\pi^+}$ resonance content, laying the foundations for a subsequent full amplitude study that will allow for a direct measurement of the polarisation of the photon.

A theoretical introduction to the SM and to the photon polarisation is given in Chapter 1. The LHCb detector is presented in Chapter 2, highlighting the contribution of each subdetector to tracking, particle identification and trigger. In Chapter 3 a fit to the $B^+ \to K^+\pi^-\pi^+\gamma$ invariant mass is performed to separate signal and background events; the background-subtracted photon angle, $m_{K^+\pi^-\pi^+}$, $m_{K^+\pi^-}$ and $m_{\pi^+\pi^-}$ distributions are determined. In Chapter 4 the *up-down* asymmetry is exploited to claim the first observation of a nonzero photon polarisation in $b \to s\gamma$ transitions. This result has led to the publication of Ref. [1]. The three-dimensional amplitude analysis performed to identify the resonances peaking in the $K^+\pi^-\pi^+$ mass interval and their interference patterns is presented in Chapter 5. A conclusion is given in Chapter 6 together with an outlook on the extension of the amplitude analysis to the photon angular dimensions.

This thesis has been performed in the context of the LHCb experiment, one of the three main experiments aimed at the detection of new physics effects in proton-proton collisions placed along the 27 km LHC ring that runs across the border between Switzerland and France. The LHCb detector has successfully delivered 3 fb^{-1} of data during its Run 1, and is already collecting Run 2 data at 13 TeV centre-of-mass energy. A long shutdown is foreseen at the end of Run 2, during which the detector will be upgraded to efficiently perform at higher luminosities.

As a member of the LHCb collaboration, I have been leading the study presented in this thesis, being personally involved in every step of the analysis. I have also contributed to the detector R&D studies for the scintillating fibre tracker for the LHCb upgrade, characterising silicon photomultiplier detectors and testing their radiation hardness, and realising part of the software for testbeam data analysis. My contributions to these R&D studies are not covered in this document.

1
Theoretical introduction

Starting from the first pioneering experiments of Thomson [2], who discovered the electron (1897), Röntgen, whose studies on X-rays (1895) set the basis for the understanding of the wave-particle dual nature of the photon [3], and Rutherford, responsible for the identification of the nucleus (1908) [4], the study of the infinitesimal components of matter has involved many physicists, aiming at a fundamental description of particles and their interactions.

Following the first quantum description of the structure of the atom by Niels Bohr (1913) [5], who introduced the concept of energy *quanta* in Ernest Rutherford's planetary atom model, and the observation of protons (Rutherford 1908 [4]) and neutrons (Chadwick 1932 [6]) in the nucleus, a very close interplay between theoretical predictions and experimental searches has led to many discoveries that, over the years, have repeatedly expanded our understanding of the structure of matter. This is the case, for example, of neutrinos, experimentally discovered in the '50s [7], after having been theorized by Pauli twenty years earlier in order to justify the missing energy in β decays.

Three kinds of interactions amongst the discovered particles were identified:

- *electromagnetic interactions*, with an infinite range, mediated by the massless photon;

- low-energy *weak interactions*, responsible for the decays with neutrinos in the final state, such as the β decay, and described by Fermi's point interaction theory [8], without any mediators;

- *strong interactions*, accounting for the attraction and repulsion forces in the nucleus, whose mediator was theorized by Yukawa (1935) [9] to be massive (~ 100 MeV/c^2) in order for the interaction to be confined within the nucleus (short-range).

Around 1947 Tomonaga, Schwinger and Feynman independently found a solution to the divergences that were encountered in electromagnetic interactions calculations when combining Dirac equations for spin-1/2 particles and electromagnetic field equations, laying the foundations for a quantum theory of electrodynamics (QED) [10–15].

With the first experimental observation of pions (1947) [16, 17], Yukawa's theory found its strong-force carrier, giving an almost complete description of particles and their interactions at the energy levels accessible at the time. Some years earlier, the first antiparticles were discovered (positrons [18] and antiprotons [19]), giving a physical meaning to the negative energy solutions of the Dirac theory. The description of matter was not complete though: an additional particle discovered a couple of years earlier, the muon [20], could not fit in, being just a massive copy of the electron, and behaving like a fundamental particle. Soon after, with the development of more sophisticated experiments, it was possible to access higher energies, opening the way to the discovery of a multitude of strongly interacting particles (hadrons) that could not be included in any existing theory.

It was not until the '60s that Gell-Mann and Zweig independently proposed a way of describing all the discovered hadrons as a combination of elementary building blocks, called quarks, posing the bases for the development of quantum chromodynamics (QCD) [21–23]. It was then possible to interpret strong interactions at a more fundamental level: protons and neutrons in the nucleus are made of quarks, that interact exchanging massless mediators called gluons.

Concerning the study of weak interactions, Fermi's description was not well behaved at high energies. In 1968 Glashow, Salam and Weinberg proposed a theory that unified electromagnetic and weak interactions introducing very massive mediators (~ 80 GeV/c^2) in order to solve such difficulties at high energies, while still preserving Fermi's point interaction in the low-energy limit [24–26]. The theory also predicted the unexpected existence of electroweak neutral currents. With the observation of these currents at CERN in 1973 [27], and the subsequent discovery of the W and Z bosons in 1983 [28, 29], a very clear and detailed description of the particle universe was achieved.

1.1   The Standard Model of particle physics

It is common to refer to the model that describes strong, weak and electromagnetic interactions with a unified formalism as the Standard Model (SM) of particle physics (Fig. 1.1)[1].

In the SM particles are divided in two large families: fermions, half-integer spin particles that are the building blocks of matter, and bosons, with integer spin, responsible for the interactions amongst fermions. At a fundamental level, the SM fermions are six quarks and six leptons, organized in three generations. Twelve gauge bosons are foreseen in the SM: eight gluons, mediating the strong interaction that keeps the nucleus together, a photon, exchanged in electromagnetic transitions, and three vector bosons $W^{\pm}$ and Z^0, responsible for the weak interaction. To complete the picture, an additional spinless massive boson is requested, responsible for giving mass to all particles. This boson was theorized in 1964 by Brout, Englert, and Higgs, after whom it has been named [32–34]. It has been observed for the first time in 2012 by the CMS and ATLAS experiments at

---

[1]The calculations presented in this section follow the notations and developments of Refs. [30, 31].
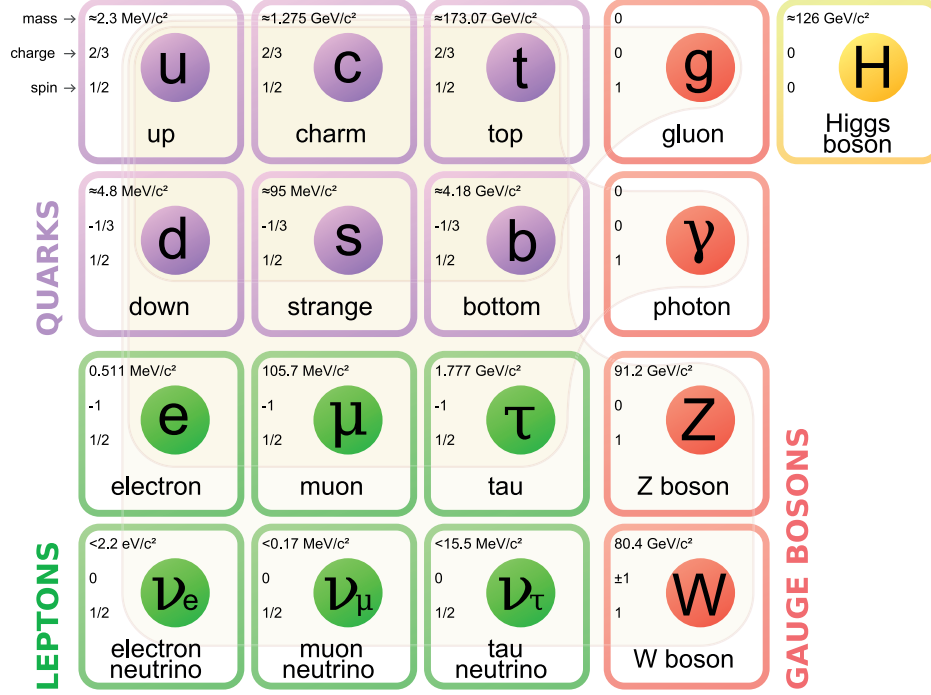
Figure 1.1   A schematic representation of the Standard Model of particle physics. Credits to https://en.wikipedia.org/wiki/Standard_Model .

CERN [35, 36] and represents the final validation of the model.

The SM represents our best understanding of the properties of all the particles and fields described above, and almost all its predictions have been experimentally validated. Nonetheless, it is far from being a *theory of everything*: in fact, it completely neglects gravitational forces, and it does not address the nature of dark matter and dark energy, which account for about 95% of the total energy of the universe, as found from the study of astrophysical and cosmological sources [37]. Without leaving the realm of particle physics, it is important to point out that the SM fails to explain the evident asymmetry between matter and antimatter observed in the universe, while non-SM physics effects have already been seen in the neutrino sector, with the observation of neutrino flavour oscillations [38, 39]. In fact, in order to oscillate, neutrinos are requested to have a mass which is not easily accounted for in the SM, where they are massless, left-handed particles.

1.1.1   Symmetries in the Standard Model

The SM describes strong and electroweak interactions by means of a lagrangian density $\mathcal{L}_{SM}$ in a local $\mathrm{SU}(3)_C \times \mathrm{SU}(2)_L \times \mathrm{U}(1)_Y$ gauge symmetry group, where $\mathrm{SU}(3)_C$ represents the colour symmetry of strong interactions, and $\mathrm{SU}(2)_L \times \mathrm{U}(1)_Y$ are the representations of the weak isospin and hypercharge symmetries of the electroweak interactions. The ultimate goal would be to write a lagrangian density describing all the physics of the universe in the most compact and elegant way possible, with the fewest free parameters.

In order to do so, the description of the SM lagrangian has to rely on the continuous symmetries of the laws of physics, which represent the mathematical expression of physical conservation laws, as stated by the well-known Noether theorem [40].

Groups

The mathematical approach to the study of symmetries relies on the concept of groups. A group is an algebraic collection of symmetries, where an operation $*$ is defined (*e.g.* the sum or the product of symmetries), and that satisfies certain properties (axioms):

- $A * B$ is an element of the group, for any elements A and B of the group;

- $A * (B * C) = (A * B) * C$ (associative property);

- the group contains an identity element $\hat{I}$ defined such that $\hat{I} * A = A$;

- each element of the group has an inverse such that $A * A^{-1} = \hat{I}$.

Each group is characterized by its generators, a set of elements of the group from which all the group elements can be obtained. The dimension[2] of a group is the number of its independent parameters.

If the symmetries are continuous, then the group is a *Lie group*. Let's consider for example a circle in a plane: rotating it by any angle around any axis will leave the circle unchanged. The collection of such continuous symmetries defines a Lie group, where the term continuous indicates that they are defined for any value of a continuous parameter, as, for example, the rotation angle.

Examples of relevant groups for particle physics are

- the unitary group $U(n)$, containing all $n \times n$ unitary matrices[3], with the matrix multiplication operation. For $n = 1$ the trivial circle group is obtained, consisting of all complex numbers with magnitude 1. This group has dimension one, and is *abelian*, because its symmetries commute;

- the special unitary group $SU(n)$, containing all the $n \times n$ unitary matrices with determinant 1, the group operation being matrix multiplication. These groups have dimension $n^2 - 1$, and are, in general, *non-abelian*, meaning that their symmetries do not commute. For $n = 2$ the matrices are traceless[4] and anti-hermitian[5] of the form

$$\begin{pmatrix} ia & -z^* \\ z & -ia \end{pmatrix} \qquad z \in \mathbb{C}, \, a \in \mathbb{R} \,. \tag{1.1}$$

---

[2]In general, this is not the dimension of the matrices that represent the group.
[3]A matrix U is unitary if $U^\dagger U = U U^\dagger = \hat{I}$.
[4]The trace $\mathrm{Tr}(A)$ of a matrix A is the sum of the elements along its diagonal.
[5]A matrix U is hermitian if $U^\dagger = U$, and anti-hermitian if $U^\dagger = -U$.

The Lie algebra generators of SU(2) are

$$\tau^1 = \begin{pmatrix} 0 & i \\ i & 0 \end{pmatrix}, \qquad \tau^2 = \begin{pmatrix} 0 & -1 \\ 1 & 0 \end{pmatrix}, \qquad \tau^3 = \begin{pmatrix} i & 0 \\ 0 & -i \end{pmatrix}. \qquad (1.2)$$

For $n = 3$, the group has eight traceless hermitian generators of the form $T_a = \frac{\lambda_a}{2}$

$$\lambda_1 = \begin{pmatrix} 0 & 1 & 0 \\ 1 & 0 & 0 \\ 0 & 0 & 0 \end{pmatrix} \qquad\qquad \lambda_2 = \begin{pmatrix} 0 & -i & 0 \\ i & 0 & 0 \\ 0 & 0 & 0 \end{pmatrix}$$

$$\lambda_3 = \begin{pmatrix} 1 & 0 & 0 \\ 0 & -1 & 0 \\ 0 & 0 & 0 \end{pmatrix} \qquad\qquad \lambda_4 = \begin{pmatrix} 0 & 0 & 1 \\ 0 & 0 & 0 \\ 1 & 0 & 0 \end{pmatrix}$$

$$\lambda_5 = \begin{pmatrix} 0 & 0 & -i \\ 0 & 0 & 0 \\ i & 0 & 0 \end{pmatrix} \qquad\qquad \lambda_6 = \begin{pmatrix} 0 & 0 & 0 \\ 0 & 0 & 1 \\ 0 & 1 & 0 \end{pmatrix}$$

$$\lambda_7 = \begin{pmatrix} 0 & 0 & 0 \\ 0 & 0 & -i \\ 0 & i & 0 \end{pmatrix} \qquad\qquad \lambda_8 = \frac{1}{\sqrt{3}} \begin{pmatrix} 1 & 0 & 0 \\ 0 & 1 & 0 \\ 0 & 0 & -2 \end{pmatrix} \qquad (1.3)$$

As will be shown in the following sections, the three generators of SU(2) and the eight generators of SU(3) are the mathematical representation of the mediator bosons of weak interactions and the gluons mediating strong interactions, respectively. The photon is the representation of the U(1) symmetry, whose generator is the identity.

Discrete symmetries

Three additional discrete symmetries play a relevant role in the SM: *parity P*, *charge conjugation C*, and *time reversal T*, corresponding to the invariance of physical laws when the sign of the spatial coordinates is flipped, when the particles are exchanged into their antiparticles, and when the direction of time is reversed, respectively. Strong and electromagnetic interactions respect all the discrete symmetries, while weak interactions violate each of them individually [41, 42]. For many years the CP symmetry was believed to be respected, until it was discovered to be violated in weak interactions (1964) [43]. CP violation is the only known source of matter-antimatter asymmetry in the SM.

The simultaneous application of the three discrete symmetries, the CPT symmetry, is conserved in the SM [44].

Gauge invariance in U(1)

A gauge theory is a quantum field theory whose lagrangian is invariant under a continuous (Lie) group of local transformations. The principle of local gauge invariance enforces the

theory to be invariant under transformations of the type

$$\psi(x) \rightarrow e^{i\xi^a(x)T^a}\psi(x)\,, \tag{1.4}$$

where $\psi(x)$ is a wavefunction that describes a generic field, T^a are the generators of the Lie group, and $\xi^a(x)$ are a set of arbitrary real functions. The invariance is local because ξ is different at each point of the space-time.

Let's introduce an example of how a gauge invariant field theory may be constructed, using a Dirac field describing massive fermions. It is straightforward to notice that a free Dirac lagrangian[6]

$$\mathcal{L}_\psi = \bar{\psi}(i\slashed{\partial} - m)\psi \tag{1.5}$$

is invariant under a global phase transformation of the form

$$\psi \rightarrow \psi' = e^{iq\xi}\psi\,, \tag{1.6}$$

where ξ is constant, q is a constant that weighs the strength of the transformation, and the dependency of the Dirac fields on the space-time coordinates is implied. The generator of simple phase transformations is the identity, suggesting that its symmetry group is U(1).

In the case of local transformations, $\xi \rightarrow \xi(x)$, the phase becomes a function of the space-time coordinates. Under the transformation, the mass term of the lagrangian does not change, while the kinetic term introduces complications because of the derivative

$$\mathcal{L}_\psi \rightarrow \mathcal{L}'_\psi = \bar{\psi}\gamma^\mu\left[i\partial_\mu - q\partial_\mu\xi(x)\right]\psi - m\bar{\psi}\psi\,. \tag{1.7}$$

The invariance of the lagrangian under local phase transformations can be restored with the introduction of a *covariant derivative* D_μ that transforms as

$$D_\mu\psi \rightarrow (D_\mu\psi)' = e^{iq\xi(x)}(D_\mu\psi) \tag{1.8}$$

in order to absorb the additional term in Eq. 1.7.

It is natural to build the covariant derivative so that

$$D_\mu\psi = (\partial_\mu + iqA_\mu(x))\psi \tag{1.9}$$

$$D_\mu\psi \rightarrow (D_\mu\psi)' = e^{iq\xi(x)}(\partial_\mu - i\partial_\mu\xi(x) + iqA'_\mu(x))\psi\,, \tag{1.10}$$

where $A_\mu(x)$ is a local quantity, with a transformation rule

$$A_\mu \rightarrow A'_\mu = A_\mu + \frac{1}{q}\partial_\mu\xi(x) \tag{1.11}$$

as follows from Eq. 1.8. Such quantity is a *gauge* field.

---

[6]The notation $\gamma_\mu\partial^\mu = \slashed{\partial}$ is used, γ_μ being the Dirac matrices.

The lagrangian is now symmetric with respect to local phase transformations

$$
\begin{aligned}
\mathcal{L}_\psi &= \bar{\psi}(i\slashed{D} - m)\psi \\
&= \bar{\psi}(i\slashed{\partial} - m)\psi - q\bar{\psi}\gamma^\mu\psi A_\mu \\
&= \bar{\psi}(i\slashed{\partial} - m)\psi - j^\mu A_\mu
\end{aligned}
\tag{1.12}
$$

at the cost of adding an interaction term for the fermions, in the form of a conserved current j_μ. The conservation of this current, $\partial_\mu j^\mu = 0$, is the effect of the U(1) symmetry of the lagrangian of Eq. 1.12, as stated by Noether's theorem.

The gauge field describes a boson that mediates the interaction of fermions. For the U(1) lagrangian to be complete, a kinetic term for the gauge field is needed. From A_μ the covariant and gauge invariant curvature tensor can be built

$$
F_{\mu\nu} = \partial_\mu A_\nu - \partial_\nu A_\mu \,,
\tag{1.13}
$$

where the dependency of A_μ on the space-time coordinates is implied.

Adding the term of Eq. 1.13 to the lagrangian gives

$$
\mathcal{L}_\psi = \bar{\psi}(i\slashed{\partial} - m)\psi - j_\mu A^\mu - \frac{1}{4}F_{\mu\nu}F^{\mu\nu}.
\tag{1.14}
$$

It is interesting to point out that the mass term for the gauge field $\frac{1}{2}m^2 A_\mu A^\mu$ cannot be featured in this lagrangian, because it would invalidate its gauge invariance. This suggests the existence of an additional mechanism to give mass to gauge bosons.

To summarise, a lagrangian that describes fermions interacting with a gauge field has been introduced by just imposing it to be invariant with respect to local phase transformations. In the specific case in which A_μ is the vector potential, it is straightforward to see that the theory described is electrodynamics, $F_{\mu\nu}$ being the strength of the electromagnetic field, q the electric charge, and j_μ the conserved electromagnetic current.

Gauge invariance in non-abelian groups

The arguments introduced above for simple local phase transformations still hold for more complex gauge transformations depending on more than one parameter. A number of independent gauge fields corresponding to the number of parameters is needed to describe the system: this leads to the existence of more mediator bosons than in the simple U(1) case.

Let's start by imposing the Dirac lagrangian in Eq. 1.5 to be invariant with respect to generic non-abelian local gauge transformations of the form

$$
\psi \to \psi' = e^{i\vec{T}\cdot\vec{\xi}(x)}\psi \,,
\tag{1.15}
$$

1.1. The Standard Model of particle physics

where the Dirac fields are represented by spinor multiplets $\psi = \begin{pmatrix} \psi_1 \\ ... \\ \psi_N \end{pmatrix}$, $\vec{\xi}(x)$ are arbitrary local functions, and the matrices $\vec{T}$ are the generators of the group, bound by the relation

$$[T^i, T^j] = i f_{ijk} T^k \,, \tag{1.16}$$

with f_{ijk} being the structure constants of the group.

To ease the notation, the local transformation $U(x)$ is defined:

$$U(x) = e^{i\vec{T} \cdot \vec{\xi}(x)} \,. \tag{1.17}$$

In order for the lagrangian to be invariant under the transformation 1.15, the covariant derivative has to be generalized to the form

$$D_\mu(x) = \partial_\mu + i\Gamma_\mu(x) \,, \tag{1.18}$$

where $\Gamma_\mu(x)$ is a generic object, corresponding to $qA_\mu(x)$ in the case of U(1), whose transformation law is

$$\Gamma_\mu(x) \to \Gamma_\mu(x)' = U(x)\Gamma_\mu(x)U^\dagger(x) + i(\partial_\mu U(x))U^\dagger(x) \,. \tag{1.19}$$

It is common to relate Γ_μ to the generators,

$$\Gamma_\mu = \Gamma_\mu^j T^j \,, \tag{1.20}$$

$$\Gamma_\mu' = [\Gamma_\mu^k + \xi^j \Gamma_\mu^i f_{jik} - (\partial_\mu \xi^k)]T^k \,, \tag{1.21}$$

where the dependence on the space-time coordinates is implicit.

The local gauge transformation invariant lagrangian will be made of two parts

$$\begin{aligned} \mathcal{L}_\psi &= \mathcal{L}_0 + \mathcal{L}_{\text{gauge}} \\ &= \bar{\psi}(i\slashed{D} - m)\psi + \mathcal{L}_{\text{gauge}} \,. \end{aligned} \tag{1.22}$$

The term $\mathcal{L}_0$ accounts for the description of the fermions and their interactions with the gauge fields, while $\mathcal{L}_{\text{gauge}}$ describes the gauge field. In the case of U(1), $\mathcal{L}_{\text{gauge}} = -\frac{1}{4}F_{\mu\nu}F^{\mu\nu}$.

The generalized Yang-Mills strength tensor $G_{\mu\nu}$ [45] can be obtained as

$$G_{\mu\nu} = \partial_\nu \Gamma_\mu - \partial_\mu \Gamma_\nu - ig[\Gamma_\nu, \Gamma_\mu] \,, \tag{1.23}$$

where g is the coupling constant, and the last term accounts for the non commutativity of the transformations. If the group is abelian, the Yang-Mills tensor becomes $F_{\mu\nu}$ (Eq. 1.13).

The Yang-Mills gauge invariant lagrangian can be built from this tensor, after noticing that $\text{Tr}(G_{\mu\nu}G^{\mu\nu})$ is invariant. After explicitly calculating the trace, the lagrangian can

be expressed as

$$\mathcal{L}_{\text{gauge}} = \frac{1}{4g^2}(G_{\mu\nu})^k (G^{\mu\nu})^k$$
$$= \frac{1}{4g^2}\left[\partial_\nu(\Gamma_\mu)^k - \partial_\mu(\Gamma_\nu)^k + g(\Gamma_\nu)^i(\Gamma_\mu)^j f_{ijk}\right]\left[\partial^\nu(\Gamma^\mu)^k - \partial^\mu(\Gamma^\nu)^k + g(\Gamma^\nu)^i(\Gamma^\mu)^j f_{ijk}\right],$$
$$(1.24)$$

where the Yang-Mills tensor has been related to the generators of the group using the relation

$$G_{\mu\nu} = (G_{\mu\nu})^j T^j. \tag{1.25}$$

In the case of abelian U(1) transformations, the coupling constant g is the charge, $\Gamma_\mu = qA_\mu$, and $G_{\mu\nu} = F_{\mu\nu}$, with all the terms $\Gamma_\mu\Gamma_\nu$ equal to zero. This corresponds to a theory with a massless boson of spin 1, the photon, mediating the electromagnetic interactions amongst fermions. For non-abelian groups, the lagrangian 1.24 describes a system of fermions interacting via N "photons", N being the dimension of the group. Since the terms in $\Gamma_\mu\Gamma_\nu$ are different from zero, in this case the mediator fields can interact with each other. SU(2) and SU(3) have respectively 3 and 8 interacting gauge bosons. Since the experiments show that these bosons can be massive, there must be an additional process that gives them mass. This process is known as the Brout-Englert-Higgs mechanism [32–34].

Symmetry breaking

Let's introduce a complex scalar field that describes interacting bosons, using a Klein-Gordon lagrangian with an interaction term

$$\mathcal{L}_\phi = \partial_\mu\phi\,\partial^\mu\phi^\dagger - \mu^2\phi^\dagger\phi - \lambda(\phi^\dagger\phi)^2. \tag{1.26}$$

It is easy to see that this lagrangian is invariant with respect to global phase transformations

$$\phi \to \phi' = e^{i\xi}\phi. \tag{1.27}$$

Noether's theorem predicts the current

$$j_\mu = i\left[(\partial_\mu\phi)\phi^\dagger - \phi(\partial_\mu\phi^\dagger)\right] \tag{1.28}$$

to be conserved, $\partial_\mu j^\mu = 0$.

The hamiltonian associated to the obtained lagrangian is

$$\mathcal{H}_\phi = \frac{\partial\mathcal{L}_\phi}{\partial\dot{\phi}}\,\dot{\phi} + \frac{\partial\mathcal{L}_\phi}{\partial\dot{\phi}^\dagger}\,\dot{\phi}^\dagger - \mathcal{L}_\phi$$
$$= \dot{\phi}^\dagger\dot{\phi} + (\vec{\nabla}\phi)(\vec{\nabla}\phi^\dagger) + \mu^2\phi^\dagger\phi + \lambda(\phi^\dagger\phi)^2, \tag{1.29}$$

where the dot indicates the derivative over time, and $\vec{\nabla}$ is the gradient operator. For

the energy to be larger than zero, λ has to be positive, because in the limit $\phi \to \infty$ the interaction term dominates, completely determining the sign of energy.

The lagrangian and the hamiltonian can be rewritten as

$$\mathcal{L}_\phi = (\partial_\mu \phi) (\partial^\mu \phi^\dagger) - V(\phi) \tag{1.30}$$

$$\mathcal{H}_\phi = \dot{\phi}\dot{\phi}^\dagger + V(\phi) \tag{1.31}$$

with

$$V(\phi) = \mu^2 \phi^\dagger \phi + \lambda(\phi^\dagger \phi)^2 \,, \tag{1.32}$$

so that $V(\phi)_{\min}$ corresponds to the fundamental energy state, often called the quantum vacuum state $|0\rangle$.

The potential minima satisfy the condition

$$\phi \left(\mu^2 + 2\lambda \phi^\dagger \phi \right) = 0 \,. \tag{1.33}$$

To better understand this result, the bosonic field ϕ can be expressed in its cartesian representation

$$\phi = \frac{\phi_1 + i\phi_2}{\sqrt{2}} \qquad \phi_1, \phi_2 \in \mathbb{R} \,, \tag{1.34}$$

so that the phase transformation can easily be interpreted as a rotation in the (ϕ_1, ϕ_2) plane (Fig. 1.2).
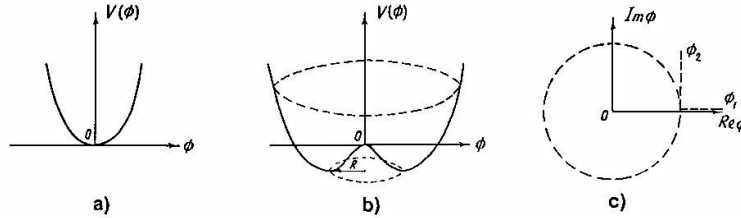
Figure 1.2   A representation of the potential $V(\phi)$ for $\mu^2 > 0$ (a) and $\mu^2 < 0$ (b). Credits to http://portal.kph.uni-mainz.de/lectures/emk/Astroteilchen02/ .

For $\mu^2 > 0$, Eq. 1.33 is satisfied only if $\phi = 0$. This is the case in which the global phase transformation is an exact symmetry of the system. In fact, any rotation in the (ϕ_1, ϕ_2) plane leaves the system in the same minimum, where the expectation value of the field is zero, $\langle 0|\phi|0\rangle = 0$.

For $\mu^2 < 0$, the potential has a local maximum at 0, and its minima are distributed along a circumference of radius $|\phi| = \sqrt{\frac{-\mu^2}{2\lambda}} \equiv \eta$. In this case, a phase transformation of the field changes the state of the system: the symmetry of the lagrangian is broken.

The expectation value of the field at the minimum has been found to be different from zero in case of spontaneous symmetry breaking, $\langle 0|\phi|0\rangle = \eta$.

The fluctuations of the system around its fundamental state can be described in terms of

the quantized oscillations of the field ϕ around its value at the minimum, different from zero only in case of a broken symmetry

$$\phi = \eta + \frac{\sigma_1 + i\sigma_2}{\sqrt{2}} \,, \tag{1.35}$$

where the fields σ_i represent the oscillations.

Developing the potential of Eq. 1.32 in a Taylor series, up to the second order, gives

$$V(\phi) = V_0 + \frac{1}{2} \sum_{i,j=1}^{2} \overline{\left(\frac{\partial^2 V}{\partial \phi_i \partial \phi_j}\right)} \sigma_i \sigma_j \,, \tag{1.36}$$

where V_0 is the potential at the minimum, and the horizontal line indicates that the derivatives are calculated at $\phi = \phi_{\min}$. By construction, the term in the first derivative is null when calculated at the minimum.

In analogy to the Klein-Gordon formulation of the lagrangian, the quadratic term is expected to be related to the masses of the system. Defining the squared masses

$$M_{ij}^2 = \overline{\left(\frac{\partial^2 V}{\partial \phi_i \partial \phi_j}\right)} \,, \tag{1.37}$$

the mass matrix for the system is found to be

$$M^2 = \begin{pmatrix} -2\mu^2 & 0 \\ 0 & 0 \end{pmatrix} . \tag{1.38}$$

The lagrangian can then be written as

$$\mathcal{L}_\phi = \frac{1}{2} \partial_\mu \sigma_1 \partial^\mu \sigma_1 + \mu^2 \sigma_1^2 + \frac{1}{2} \partial_\mu \sigma_2 \partial^\mu \sigma_2 \,. \tag{1.39}$$

The spontaneous breaking of the symmetry has caused the two degrees of freedom of the theory, associated to the real fields ϕ_1 and ϕ_2, to transfer to two particles of mass $\sqrt{-2\mu^2}$ and 0.

In case the symmetry is conserved, the curvature of the potential is always zero, and the mass terms for the field vanish.

This result, which predicted for the first time the existence of a scalar massless boson, was, though, not supported by the experiments, since no such particle was ever observed.

The theory developed by Goldstone [46] for global phase transformations can be extended to local transformations, analogously to what has been shown earlier for Yang-Mills gauge fields. For simplicity, gauge transformations in the abelian group U(1) are considered, where gauge invariance is achieved by introducing the covariant derivative D_μ, the gauge field A_μ, and the field strength tensor $F_{\mu\nu}$.

The gauge invariant lagrangian developed from the combination of Eq. 1.14 and Eq. 1.26

becomes, neglecting the fermion fields,

$$\mathcal{L}_{\text{gauge}} = (D_\mu \phi)(D^\mu \phi^\dagger) - \mu^2 \phi^\dagger \phi - \lambda(\phi^\dagger \phi)^2 - \frac{1}{4} F_{\mu\nu} F^{\mu\nu}. \tag{1.40}$$

For $\mu^2 > 0$, $\langle 0|\phi|0\rangle = 0$ and using Eq. 1.35 with $\eta = 0$ at second order the lagrangian reads

$$\mathcal{L}_{\text{gauge}} = \frac{1}{2} \partial_\mu \sigma_1 \partial^\mu \sigma_1 - \frac{1}{2} \mu^2 \sigma_1^2 + \frac{1}{2} \partial_\mu \sigma_2 \partial^\mu \sigma_2 - \frac{1}{2} \mu^2 \sigma_2^2 - \frac{1}{4} F_{\mu\nu} F^{\mu\nu}, \tag{1.41}$$

that describes two particles of mass μ and opposite charge, interacting by means of a mediator for which no mass term is foreseen in the lagrangian. The gauge symmetry of QED is respected, hence the photons mediating electromagnetic interactions have no mass.

When the symmetry is broken ($\mu^2 < 0$), η is different from zero, and from Eq. 1.35 follows

$$\phi \rightarrow \phi' = \eta + \frac{\sigma_1 + i[\sigma_2 + \sqrt{2}\eta \xi(x)]}{\sqrt{2}}, \tag{1.42}$$

where the approximation $e^{i\xi(x)} \sim (1 + i\xi(x))$ has been used. In contradiction with what is observed in the Goldstone case for global gauge transformations, σ_1 is left unchanged by the local transformation, while $\sigma_2 \rightarrow \sigma_2 + \sqrt{2}\eta \xi(x)$ and an opportune choice of the gauge condition can eliminate the latter field, formerly associated to the massless Goldstone boson. In the unitary gauge

$$\xi(x) = -\frac{\sigma_2}{\sqrt{2}\eta}, \tag{1.43}$$

Eq 1.35 simplifies to

$$\phi = \eta + \frac{\sigma_1}{\sqrt{2}} \qquad \phi \in \mathbb{R}. \tag{1.44}$$

Developing the potential at second order Taylor expansion, as done previously, the lagrangian becomes

$$\mathcal{L}_{\text{gauge}} = \frac{1}{2} \partial_\mu \sigma_1 \partial^\mu \sigma_1 - \frac{1}{2} M_H^2 \sigma_1^2 - \frac{1}{4} F_{\mu\nu} F^{\mu\nu} + \frac{1}{2} M_A^2 A_\mu A^\mu + \text{interaction terms}, \tag{1.45}$$

where

$$M_H^2 = -2\mu^2 = 4\lambda \eta^2 \tag{1.46}$$
$$M_A^2 = 2q^2 \eta^2. \tag{1.47}$$

Imposing local gauge invariance to the QED lagrangian, two new pieces of the SM puzzle are obtained

$$\mathcal{L}_A = -\frac{1}{4} F_{\mu\nu} F^{\mu\nu} + \frac{1}{2} M_A^2 A_\mu A^\mu, \tag{1.48}$$

which describes a massive gauge mediator of spin 1, and

$$\mathcal{L}_H = \frac{1}{2} \partial_\mu \sigma_1 \partial^\mu \sigma_1 - \frac{1}{2} M_H^2 \sigma_1^2, \tag{1.49}$$

describing a massive scalar neutral boson, the Higgs boson.

The one just described is the Higgs mechanism, which reunites Yang-Mills gauge theories with the Goldstone model, predicting the existence of a new field, and coincidentally a new boson, transferring the initial degrees of freedom of the system into mass terms for the interaction mediators when the symmetry is broken.

1.1.2 Electroweak interactions

At the beginning of the $1960s$, before Higgs introduced his symmetry breaking mechanism, Glashow [24] unveiled for the first time the electromagnetic and weak interactions as a single force, with the observed differences being related to the mass of their propagators.

Let's consider a leptonic doublet spinor and its associated Dirac lagrangian

$$\mathcal{L} = \bar{\psi} i \partial\!\!\!/ \psi - m \bar{\psi} \left(\frac{1 - \tau^3}{2} \right) \psi \,, \qquad \psi = \begin{pmatrix} \nu \\ e \end{pmatrix} \tag{1.50}$$

where the matrix τ^3, introduced in Eq.1.2, ensures that only the electron term is coupled to the mass. Neglecting the mass terms, the lagrangian is symmetric under

- the rotation of the spinor (*isospin* transformation)

$$\psi \to \psi' = e^{\frac{i}{2} \alpha^j \tau^j} \psi \tag{1.51}$$

- chiral transformations

$$\psi \to \psi' = e^{\frac{i}{2} \beta^j \tau^j \gamma^5} \psi \tag{1.52}$$

where $\gamma^5 = \begin{pmatrix} 0 & \mathbb{I}_2 \\ \mathbb{I}_2 & 0 \end{pmatrix}$ from a combination of Dirac matrices. Chirality is a property of Dirac spinors used to separate their left- and right-handed components

$$\psi = \psi_L + \psi_R = \frac{1}{2}(1 - \gamma^5)\psi + \frac{1}{2}(1 + \gamma^5)\psi \,. \tag{1.53}$$

The transformation $U = e^{\frac{i}{2}(\alpha^j \tau^j + \beta^j \tau^j \gamma^5)}$ describes an SU(2) algebra, separated for left- and right-handed components because of the chirality transformation. Adding the global phase transformation symmetry, the most general group for describing the properties of the spinor ψ is obtained

$$\text{SU(2)}_L \times \text{SU(2)}_R \times \text{U(1)}_L \times \text{U(1)}_R$$

with eight generators and eight associated conserved currents[7].

Glashow understood that it was possible to determine the electromagnetic current $j_\mu^{\text{em}} = -\bar{e}\gamma_\mu e$ and the weak current $j_\mu^{\text{weak}} = \bar{e}\gamma_\mu(1 - \gamma^5)\nu$ by combining the currents of SU(2)_L to

---

[7]If the electron mass term is added, the electromagnetic current is still conserved, while the other symmetries are broken.

an additional group $U(1)_Y$ describing the symmetry for weak hypercharge transformations, where $Y = 2(Q - I_3)$ with Q the electromagnetic charge and I_3 the third component of isospin. Given the expression for the $SU(2)_L$ currents

$$L_\mu^j = \psi_L \gamma_\mu \frac{\tau^j}{2} \psi \qquad j = 1, 2, 3 \tag{1.54}$$

it is easy to see that

$$2(L_\mu^1 - iL_\mu^2) = \bar{e}\gamma_\mu(1 - \gamma^5)\nu = j_\mu^{\text{weak}} \tag{1.55}$$

$$2(j_\mu^{\text{em}} - L_\mu^3) = -(\bar{e}_L\gamma_\mu e_L + \bar{\nu}_L\gamma_\mu\nu_L) - \bar{e}_R\gamma_\mu e_R = Y_\mu \,. \tag{1.56}$$

Since $SU(2)_L$ and $U(1)_Y$ commute, $SU(2)_L \times U(1)_Y$ is still a symmetry group for our system. It is, in fact, the minimal gauge group representation that can be used to describe the electroweak interactions in a unified formalism.

Studying the symmetry breaking mechanism in Glashow's minimal gauge group for local transformations, Weinberg and Salam [25, 26] developed a unified electroweak theory, which is now considered to be the main building block of the SM.

Let's consider the former leptonic doublet ψ in its chiral representation

$$l = \begin{pmatrix} \nu_L \\ e_L \end{pmatrix}_{Y=-1} \qquad r = (e_R)_{Y=-2}$$

where the right-handed neutrino ν_R is not considered because it does not play a role in electroweak interactions.

Four gauge fields can be introduced: $W_\mu^i (i = 1, 2, 3)$ corresponding to the three generators of the non-abelian group $SU(2)_L$, and B_μ that is the generator of $U(1)_Y$. Analogously to what has been introduced for the Yang-Mills tensor

$$(W_{\mu\nu})^i = \partial_\nu W_\mu^i - \partial_\mu W_\nu^i + ig\epsilon_{ijk}W_\mu^j W_\nu^k \,, \tag{1.57}$$

$$(B_{\mu\nu}) = \partial_\nu B_\mu - \partial_\mu B_\nu \,. \tag{1.58}$$

The lagrangian of the system is

$$\mathcal{L}_{\text{ew}} = \mathcal{L}_{\text{lept}} + \mathcal{L}_{\text{gauge}} \,, \tag{1.59}$$

where

$$\mathcal{L}_{\text{lept}} = \bar{l}\left[i\gamma^\mu(D_\mu)_L\right]l + \bar{r}\left[i\gamma^\mu(D_\mu)_R\right]r \,, \tag{1.60}$$

with

$$(D_\mu)_L = \partial_\mu - ig\frac{\tau^i}{2}W_\mu^i - i\frac{g'}{2}Y_l B_\mu \tag{1.61}$$

$$(D_\mu)_R = \partial_\mu - i\frac{g'}{2}Y_r B_\mu \,, \tag{1.62}$$

and

$$\mathcal{L}_{\text{gauge}} = -\frac{1}{4}(W_{\mu\nu})^i(W^{\mu\nu})^i - \frac{1}{4}B_{\mu\nu}B^{\mu\nu}\,. \tag{1.63}$$

The current description of the system presents two issues

- the lagrangian is invariant under local gauge transformations in $\text{SU}(2)_L \times \text{U}(1)_Y$ only in the limit of massless leptons;

- it predicts four massless boson mediators, not observed by experiments.

Both problems are solved introducing the Higgs mechanism for spontaneous symmetry breaking.

A scalar Higgs doublet with hypercharge $Y_H = 1$ is introduced, so that the hypercharge of the system is conserved:

$$\phi = \begin{pmatrix} \phi^+ \\ \phi^0 \end{pmatrix}_{Y=1}\,.$$

The covariant derivative for the Higgs scalar field, ensuring that the symmetry of the lagrangian holds under local gauge transformation, has the form

$$D_\mu\phi = \left(\partial_\mu - \frac{i}{2}g\vec{\tau}\cdot\vec{W}_\mu - \frac{i}{2}g'Y_H B_\mu\right)\phi\,. \tag{1.64}$$

The Higgs field introduces two lagrangian terms

$$\begin{aligned}
\mathcal{L}_H &= (D_\mu\phi)(D^\mu\phi)^\dagger - V(\phi^\dagger\phi) \\
&= (D_\mu\phi)(D^\mu\phi)^\dagger - \mu^2(\phi^\dagger\phi) - \lambda(\phi^\dagger\phi)^2
\end{aligned} \tag{1.65}$$

and

$$\mathcal{L}_{m_e} = -g_e(\bar{r}\,\phi^\dagger\,l + \bar{l}\,\phi\,r)\,, \tag{1.66}$$

the latter being the term from which the mass of the electron arises, with g_e the coupling constant.

One can already see how the Higgs field has allowed the introduction of a mass term for the leptons that respects the gauge invariance of the minimal symmetry group under study, with a convenient choice of its hypercharge.

As seen in the previous section, according to the sign of μ^2 in the Higgs potential, the symmetry of the lagrangian can be broken in the physical observed state. With an opportune transformation, the expectation value of the Higgs field on the vacuum state can be expressed as

$$\langle 0|\phi|0\rangle = \begin{pmatrix} 0 \\ \eta \end{pmatrix} \qquad \eta = \sqrt{\frac{-\mu^2}{2\lambda}}\,. \tag{1.67}$$

The symmetry breaking of the system should preserve the conservation of the electromagnetic current, because the electromagnetic interaction is mediated by a massless photon,

and the charge is conserved

$$SU(2)_L \times U(1)_Y \to U(1)_{\text{e.m}}$$

where $U(1)_{\text{e.m}}$ indicates the gauge symmetry of electromagnetism. The symmetry that has to be conserved is not one of the initial symmetries of the system. From the definition of the hypercharge, the quantity $Q = \frac{Y}{2} + I_3 = \begin{pmatrix} 1 & 0 \\ 0 & 0 \end{pmatrix}$ is such that the transformation $U(x) = e^{iQ\xi(x)}$ does not break the symmetry. The quantity Q is the conserved charge.

Let's study the case of broken symmetry ($\mu^2 < 0$), and, in particular, how the oscillations of the Higgs field around the vacuum state transfer the degrees of freedom of the initial system to massive mediator bosons. In the unitary gauge the Higgs field can be expressed as

$$\phi = \begin{pmatrix} 0 \\ \eta + \frac{\sigma}{\sqrt{2}} \end{pmatrix}_{Y=1}, \tag{1.68}$$

where σ is the scalar field that describes the oscillations.

The lagrangian of the system reads

$$\mathcal{L}_{\text{ew}} = \mathcal{L}_{\text{lept}} + \mathcal{L}_{\text{gauge}} + \mathcal{L}_H + \mathcal{L}_{\text{m}_e}. \tag{1.69}$$

The mass of the interaction mediators comes from the Higgs lagrangian

$$\begin{aligned} \mathcal{L}_H = & \frac{1}{2} \partial_\mu \sigma \partial^\mu \sigma - \frac{1}{2} \mu^2 \sigma^2 \\ & + \frac{1}{2} M_W^2 \left[(W_\mu)^1 (W^\mu)^1 + (W_\mu)^2 (W^\mu)^2 \right] \\ & + \frac{1}{4} \eta^2 \left((W_\mu)^3 \quad B_\mu \right) \begin{pmatrix} g^2 & -gg' \\ -gg' & (g')^2 \end{pmatrix} \begin{pmatrix} (W_\mu)^3 \\ B_\mu \end{pmatrix}, \end{aligned} \tag{1.70}$$

where the additional interaction terms are not considered for simplicity. The lagrangian contains the masses of the charged mediators $W^\pm$ associated to the fields $(W_\mu)^1$ and $(W_\mu)^2$

$$M_W^2 = \frac{1}{2} \eta^2 g^2 \tag{1.71}$$

as well as those of the neutral mediators

$$\mathcal{M}^2 = \frac{1}{2} \eta^2 \begin{pmatrix} g^2 & -gg' \\ -gg' & (g')^2 \end{pmatrix}. \tag{1.72}$$

The expression for $\mathcal{M}^2$ can be simplified introducing the electroweak mixing angle θ_{ew}, that rotates the lagrangian basis into the physical observable fields Z_μ, representing the neutral weak current field associated to the mediator boson Z^0, and A_μ, that represents

the electromagnetic field associated to the photon γ:

$$\begin{pmatrix} Z_\mu \\ A_\mu \end{pmatrix} = \begin{pmatrix} \cos\theta_{\text{ew}} & -\sin\theta_{\text{ew}} \\ \sin\theta_{\text{ew}} & \cos\theta_{\text{ew}} \end{pmatrix} \begin{pmatrix} (W_\mu)^3 \\ B_\mu \end{pmatrix} . \tag{1.73}$$

For the photon to be massless, the condition

$$g\sin\theta_{\text{ew}} = g'\cos\theta_{\text{ew}} = e \tag{1.74}$$

has to be respected, so that the eigenvalue associated to A_μ is null, where e is the electric charge.

The term describing how the electrons mass arises from the interaction with the Higgs field becomes

$$\mathcal{L}_{\text{m}_e} = -g_e\eta\,\bar{e}e - g_e\frac{\sigma}{\sqrt{2}}\,\bar{e}e\,, \tag{1.75}$$

where $-g_e\eta$ is the mass of the electron in analogy to the Dirac lagrangian mass term, and the second term represents the interaction between the electron field and the Higgs field.

Following Glashow, Weinberg and Salam, the application of the Higgs mechanism to a gauge invariant lagrangian in $\text{SU}(2)_L \times \text{U}(1)_Y$ has resulted into the unified gauge invariant description of electroweak interactions. The masses of fermions and mediator bosons have been obtained from their interaction with the Higgs field in case of symmetry breaking, preserving the gauge invariance of the theory. As an additional result, the theory predicted for the first time the existence of neutral weak currents, whose subsequent discovery represented the final validation of the model.

The masses of the quarks can also be obtained from the Higgs field, since, being fermions, they are also described by the Dirac lagrangian.

Let's introduce the first generation of quarks (up and down quarks) in their $\text{SU}(2)_L \times \text{U}(1)_Y$ representation

$$q = \begin{pmatrix} u_L \\ d_L \end{pmatrix}_{Y=1/3} \qquad \left(u_R\right)_{Y=4/3} \qquad \left(d_R\right)_{Y=-2/3}$$

In this case there is an additional right-handed singlet. Analogously to Eq. 1.66, it can be shown that the quark mass terms are

$$\mathcal{L}m_d = -g_d(\bar{q}\phi d_R + h.c.) = -g_d\eta(\bar{d}_L d_R + \bar{d}_R d_L) + \mathcal{L}_{\phi-d} \tag{1.76}$$

$$\mathcal{L}m_u = -g_u(\bar{u}_R\epsilon_{ij}\phi^i q^i + h.c.) = -g_u\eta(\bar{u}_L u_R + \bar{u}_R u_L) + \mathcal{L}_{\phi-u} \tag{1.77}$$

where $h.c.$ indicates the hermitian conjugate of the term it follows in the equation, and $\mathcal{L}_{\phi-q}$ indicates the Higgs-quark interaction term, and the masses of the quarks are

$$m_d = g_d\eta \tag{1.78}$$

$$m_u = g_u\eta\,. \tag{1.79}$$

1.1. The Standard Model of particle physics

Flavour physics

Extending the theory to the three experimentally observed generations of quarks and leptons is straightforward, but has some interesting implications. It is usual to refer to the different quarks and leptons as *flavours*. Flavour physics is the branch of particle physics dedicated to the study of flavour-changing processes.

In the lepton sector, the general mass lagrangian becomes

$$\mathcal{L}_{m_{\text{lept}}} = \bar{L}_L \phi G L_R + h.c. \tag{1.80}$$

where L is the spinor describing the left-handed component of a generation of quarks, and G is a 3×3 complex matrix of coupling constants. The matrix G is non-hermitian, and its diagonalisation requires two transformations:

- a unitary transformation T on the right-handed fields

$$L_R \to T L'_R \tag{1.81}$$

  that does not affect weak interactions, and where only the left-handed components contribute;

- a base transformation U for the left-handed components

$$L_L \to U L'_L \tag{1.82}$$

  that also leaves the weak lagrangian unchanged.

The lagrangian Eq. 1.80 becomes

$$\mathcal{L}_{m_{\text{lept}}} \to \bar{L}'_L \phi (U^\dagger G T) L'_R + h.c. . \tag{1.83}$$

Since every complex matrix G can be written as $(U \rho T^\dagger)$, with ρ diagonal, real matrix, with non-negative eigenvalues, with an opportune choice of the initial transformations $U^\dagger G T \to \rho$, the eigenvalues of ρ being the masses of the leptons

$$
\begin{aligned}
\mathcal{L}_{m_{\text{lept}}} &= \bar{L}'_L \mathcal{M}_{\text{lept}} L'_R + h.c. \\
&= m_e(\bar{e}_L e_R + \bar{e}_R e_L) + m_\mu(\bar{\mu}_L \mu_R + \bar{\mu}_R \mu_L) + m_\tau(\bar{\tau}_L \tau_R + \bar{\tau}_R \tau_L) .
\end{aligned} \tag{1.84}
$$

Analogously, the weak current

$$
\begin{aligned}
j_\mu^{\text{weak}} &= (\bar{L}\gamma_\mu \tau^+ L) + h.c. \qquad\qquad \tau^+ = \begin{pmatrix} 1 & 0 \\ 0 & 0 \end{pmatrix} \\
&= (\bar{\nu}_{e_L}\gamma_\mu e_L + \bar{\nu}_{\mu_L}\gamma_\mu \mu_L + \bar{\nu}_{\tau_L}\gamma_\mu \tau_L) + h.c. \tag{1.85}
\end{aligned}
$$

because of the transformation becomes

$$
\begin{aligned}
j_\mu^{\text{weak}} &\to (\bar{L}' \gamma_\mu \tau^+ L') + h.c. \\
&= (\bar{\nu}'_{e_L} \gamma_\mu e'_L + \bar{\nu}'_{\mu_L} \gamma_\mu \mu'_L + \bar{\nu}'_{\tau_L} \gamma_\mu \tau'_L) + h.c. \, .
\end{aligned}
\tag{1.86}
$$

It is evident that the weak leptonic currents are diagonal, that is, lepton flavour changing is forbidden. This happens because the transformations used to diagonalize the mass matrix commute with the minimal gauge group, and do not modify its algebra.

The situation is different in the quark sector. The mass lagrangian of the system is more complex and the former procedure fails to diagonalize the matrices

$$
\mathcal{L}_{m_{\text{quark}}} = \bar{Q}_L \phi G_d D_R + \bar{U}_R G_u \epsilon_{ij} \phi^i Q_L^j
\tag{1.87}
$$

where Q_L indicates the left-handed quark doublets and U_R, D_R the right-handed singlet of each generation.

An opportune basis in which one of the mass matrices is diagonal can always be found, but any transformation that diagonalizes one of them without affecting the other would not commute with $\text{SU}(2)_L \times \text{U}(1)_Y$. Hence, the corresponding mass lagrangian is

$$
\mathcal{L}_{m_{\text{quark}}} = \mathcal{M}_U \bar{U} U + \eta (\bar{D}_L G_d D_R) + h.c.
\tag{1.88}
$$

with U indicating the spinor containing the up-like quarks, u,c, and t (Fig. 1.1).

The weak current in the quark sector $j_\mu^{\text{weak}} = \bar{Q}_L \gamma_\mu \tau^+ Q_L$ becomes

$$
j_\mu^{\text{weak}} \to \bar{Q}_L \, \gamma_\mu \, \tau^+ \, V_{\text{CKM}} \, Q_L = \begin{pmatrix} \bar{u}_L & \bar{c}_L & \bar{t}_L \end{pmatrix} \gamma_\mu V_{\text{CKM}} \begin{pmatrix} d_L \\ s_L \\ b_L \end{pmatrix} .
\tag{1.89}
$$

The non-diagonal 3×3 unitary matrix V_{CKM} is known as the Cabibbo-Kobayashi-Maskawa (CKM) matrix [47]. Since the CKM matrix is not diagonal, quark mixing is allowed, and weak interactions do not conserve flavour in the quark sector. The CKM matrix can be written as

$$
V_{\text{CKM}} = \begin{pmatrix} V_{ud} & V_{us} & V_{ub} \\ V_{cd} & V_{cs} & V_{cb} \\ V_{td} & V_{ts} & V_{tb} \end{pmatrix} ,
\tag{1.90}
$$

where the V_{ij} are the complex elements of the matrix, related by the relation

$$
\sum_{k=1}^{3} V_{ki}^* V_{kj} = \delta_{ij} ,
\tag{1.91}
$$

following from the unitarity condition $V_{\text{CKM}} V_{\text{CKM}}^\dagger = 1$.

To better understand the nature of mixing, it is helpful to look at its first introduction. At the beginning of 1960 physicists were puzzled by the long standing issue of the universality of electroweak interactions. The first observations of weak processes evidenced how $s \to u$

transitions are about twenty times less likely to happen than $d \to u$ transitions, despite the coupling constant of the interaction being expected to be the same for any generation of quarks. Cabibbo [48] explained the discrepancy introducing the idea that the interaction and mass eigenstates of the fields representing the quarks were related by a rotation, so that

$$\begin{pmatrix} d' \\ s' \end{pmatrix} = \begin{pmatrix} \cos\theta_C & \sin\theta_C \\ -\sin\theta_C & \cos\theta_C \end{pmatrix} \begin{pmatrix} d \\ s \end{pmatrix}, \tag{1.92}$$

where θ_C is the Cabibbo angle. The different magnitudes of the transitions were due to the rotation

$$\frac{\Gamma(s \to uW)}{\Gamma(d \to uW)} = \left| \frac{g_{us}}{g_{ud}} \right|^2 = \left| \frac{\sin\theta_C}{\cos\theta_C} \right|^2 \simeq \frac{1}{20} \tag{1.93}$$

that recovers weak interactions universality for $\theta_C \simeq 12°$.

The extension of this concept to the three generations of quarks led Kobayashi and Maskawa to the formulation of the CKM matrix introduced above. The mixing matrix can be parametrised in many ways. A common choice is to introduce three real mixing angles θ_{ij} and an imaginary phase δ, responsible for CP violation, so that the matrix can be expressed as

$$V_{\text{CKM}} = \begin{pmatrix} c_{12}c_{13} & s_{12}c_{13} & s_{13}e^{-i\delta} \\ -s_{12}c_{23} - c_{12}s_{23}s_{13}e^{i\delta} & c_{12}c_{23} - s_{12}s_{23}s_{13}e^{i\delta} & s_{23}c_{13} \\ s_{12}s_{23} - c_{12}c_{23}s_{13}e^{i\delta} & -c_{12}s_{23} - s_{12}c_{23}s_{13}e^{i\delta} & c_{23}c_{13} \end{pmatrix}, \tag{1.94}$$

where $s_{ij} = \sin\theta_{ij}$ and $c_{ij} = \cos\theta_{ij}$.

The magnitude of the CKM matrix elements makes one quark transition more probable than another. This concept is made evident using the Wolfenstein parametrisation [49], that describes the parameters as an expansion of s_{12}, renamed to λ, with the following convention

$$s_{12} = \lambda = \frac{|V_{us}|}{\sqrt{|V_{ud}|^2 + |V_{us}|^2}} \tag{1.95}$$

$$s_{23} = A\lambda^2 = \lambda \left| \frac{V_{cb}}{V_{us}} \right| \tag{1.96}$$

$$s_{13}e^{i\delta} = V_{ub}^* = A\lambda^3(\rho + i\eta) = \frac{A\lambda^3(\bar{\rho} + i\bar{\eta})\sqrt{1 - A^2\lambda^4}}{\sqrt{1 - \lambda^2}[1 - A^2\lambda^4(\bar{\rho} + i\bar{\eta})]} \tag{1.97}$$

where $\bar{\rho} + i\bar{\eta} = -\frac{V_{ud}V_{ub}^*}{V_{cd}V_{cb}^*}$ does not depend on the phase convention.

The CKM matrix can then be written as

$$V_{\text{CKM}} = \begin{pmatrix} 1 - \lambda^2/2 & \lambda & A\lambda^3(\rho - i\eta) \\ -\lambda & 1 - \lambda^2/2 & A\lambda^2 \\ A\lambda^3(1 - \rho - i\eta) & -A\lambda^2 & 1 \end{pmatrix} + \mathcal{O}(\lambda^4). \tag{1.98}$$

Exploiting Eq. 1.91, the unitarity of the CKM matrix can be represented as triangles in the $(\bar{\rho}, \bar{\eta})$ plane, so that the angles of the triangle are directly related to the phase

differences of the V_{ij} elements. Amongst the possible triangles, a common choice is

$$V_{ud}V_{ub}^* + V_{cd}V_{cb}^* + V_{td}V_{tb}^* = 0 \,. \tag{1.99}$$

The corresponding unitary triangle is shown in Fig. 1.3, with the current best experimental knowledge represented as 68% confidence level bands [50].
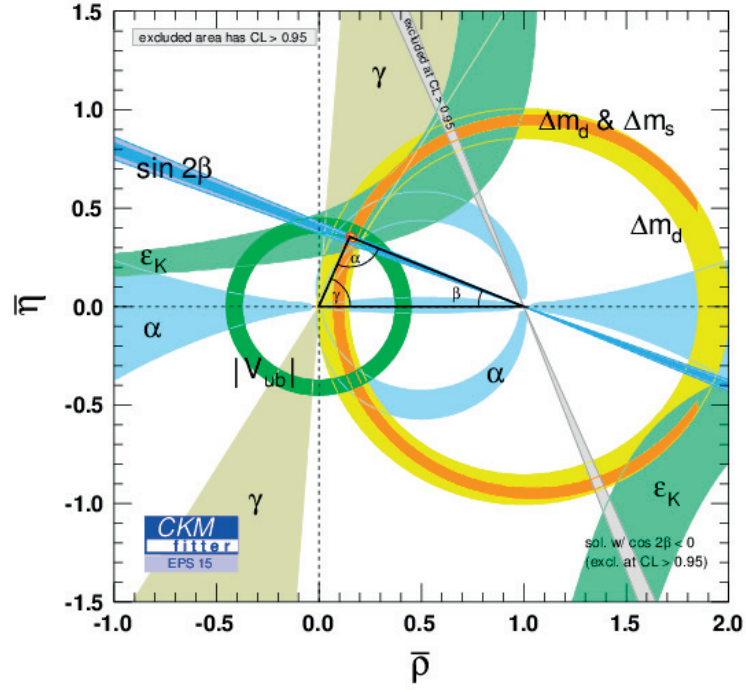
Figure 1.3   Unitary triangle representation of the CKM matrix [50].

GIM mechanism

The CKM matrix describes flavour-changing charged transitions, mediated by the massive charged gauge bosons $W^\pm$. As seen before, the SM provides additional neutral weak currents, mediated by the neutral boson Z^0, which should, in principle, also be responsible for flavour-changing interactions. From the experiments, though, the rate of flavour-changing neutral current (FCNC) decays is strongly suppressed

$$\Gamma(s \to dZ^0) \ll \Gamma(s \to uW^-) \,. \tag{1.100}$$

It can be shown that this is due to a cancellation mechanism for the neutral current terms in the weak lagrangian, proposed for the first time by Glashow, Iliopoulos and Maiani (GIM) [51]. The three physicists introduced for the first time the *charm* quark, so that at the Z^0 tree-level vertex only the $\bar{q}_i q_i$ flavour conserving contributions would

survive (*e.g.* $\bar{u}u$), while the flavour-changing contributions from the first quark generation would be cancelled by the ones from the second generation due to the unitarity of the CKM matrix. As a result, FCNC are allowed in the SM only at loop level, explaining the observed suppression.

1.1.3 Strong interactions

Strong interactions amongst quarks are described in the SM by a non-abelian quantum field theory known as quantum chromodynamics (QCD) [21–23]. Murray Gell-Mann hypothesized the existence of an additional quantum number characterizing quarks, the *colour* charge, with three possible states

$$\begin{pmatrix} 1 \\ 0 \\ 0 \end{pmatrix}, \begin{pmatrix} 0 \\ 1 \\ 0 \end{pmatrix}, \text{ and } \begin{pmatrix} 0 \\ 0 \\ 1 \end{pmatrix},$$

describing a $\mathrm{SU}(3)_C$ algebra. The group has eight generators corresponding to as many physical massless mediators, the gluons, described by a Yang-Mills gauge lagrangian.

Unlike the photons in QED, gluons transport the colour, hence they can interact not only with quarks, but also amongst themselves. This causes an effect called *confinement*, consisting in the impossibility of observing an isolated colour-charged particle. Quarks and gluons inside a proton can be depicted as a system of particles bound by strings: because of the strong interaction potential, the tension of the strings increases with the distance between the particles. Trying to isolate a particle would result in the strings breaking and releasing their energy in the form of a shower of particles, through a process called hadronisation.

Quarks and gluons can then be observed as *jets* of particles, but their detection as isolated objects is forbidden. Systems of a quark and an antiquark, $q\bar{q}$ mesons, and of three quarks, qqq baryons, are colour-neutral, and so they are not confined. Tetra- ($q\bar{q}q\bar{q}$) and penta- ($qqqq\bar{q}$) quarks can also be observed.

For the study of QCD processes the experiments need to have access to very large energies, corresponding to very small distances between quarks in a hadron (deep inelastic scattering experiments), so that the quarks can be studied as quasi-free objects. This property of the QCD potential is called asymptotic freedom [52, 53].

1.1.4 Parametrising new physics in the Standard Model

In order to study non-SM new physics (NP) interactions, effective field theories have to be introduced, gauge-invariant quantum field theories with an energy scale Λ interpreted as the NP scale [54]. Such theories have to return the SM in the limit $\Lambda \to \infty$,

$$\mathcal{L} = \mathcal{L}_{\mathrm{SM}} + \frac{1}{\Lambda^2} \sum_i C_i \mathcal{O}_i \,, \tag{1.101}$$

where C_i are the dimensionless Wilson coefficients, and $\mathcal{O}_i$ are operators built from SM fields.

This formulation has the advantage that it can be used to describe the effect of NP interactions mediated by particles of mass $\sim \Lambda$ at current energy scales; the new interaction can then be described from the behaviour of the system at lower energies[8].

1.2 Photon polarisation in the Standard Model

Rare $b \to s\gamma$ FCNC transitions (Fig. 1.4) are expected to be very sensitive to NP effects. These transitions are, in the SM, allowed only at loop level because of the GIM mechanism, and NP may be observed in the exchange of heavy particles in the electroweak penguin loop.

In the SM, the recoil s quark that couples to a W boson is left-handed, causing the photon emitted in $b \to s\gamma$ decays to be left-handed. This implies a maximal parity violation up to small corrections of the order m_s/m_b. Various measurements of the inclusive $b \to s\gamma$ rate have shown good agreement with the SM predictions, strongly constraining possible NP effects (see Ref. [55] for a detailed review of this topic). Several theories beyond the SM, though, suggest that there is still the possibility of a non-SM photon polarisation. In some scenarios [56] the photon may acquire a significant right-handed component, because of a heavy fermion being exchanged in the electroweak penguin loop. This effect is due to a chirality flip along the heavy fermion line in the electroweak loop. Relevant examples are the minimal supersymmetric model (MSSM), where left-right squark mixing causes a chirality flip along the gluino line in the loop [57], and the $\mathrm{SU}(2)_L \times \mathrm{SU}(2)_R \times \mathrm{U}(1)_Y$ left-right symmetric model [58–64] where a chirality flip along the top quark line in the loop involves $W_L - W_R$ mixing. In addition, in grand unification models, right-handed neutrinos (and the consequent right-handed quark coupling) are expected to enhance the right-handed photon component [65].

Effective field theory description of $b \to s\gamma$

Following Ref. [65], the study of NP effects in the $b \to s\gamma$ sector can be carried out introducing the effective hamiltonian

$$\mathcal{H}_{\text{eff}} = -\frac{G_F}{\sqrt{2}} V_{tb} V_{ts}^* \left[\sum_{i=1}^{6} C_i(\mu)\mathcal{O}_i(\mu) + \sum_{i=7}^{10} \left(C_i(\mu)\mathcal{O}_i(\mu) + C_i'(\mu)\mathcal{O}_i'(\mu) \right) \right] . \quad (1.102)$$

The $C_i^{(\prime)}$ Wilson coefficients account for the short distance physics effects, the operators $\mathcal{O}_{1-6}$ are the local four-quarks operators, $\mathcal{O}_7^{(\prime)}$ is the operator describing electromagnetic penguins, $\mathcal{O}_8^{(\prime)}$ is the chromomagnetic penguin operator, and $\mathcal{O}_{9,10}^{(\prime)}$ are the semileptonic

---

[8]This is analogous to what has been done for weak interactions in the former century: Fermi's theory can be considered as an effective theory of weak interactions with $\Lambda^2 \sim M_W^2$; a solid understanding of the simplified theory led to the prediction of the behaviour of electroweak interactions at larger masses.
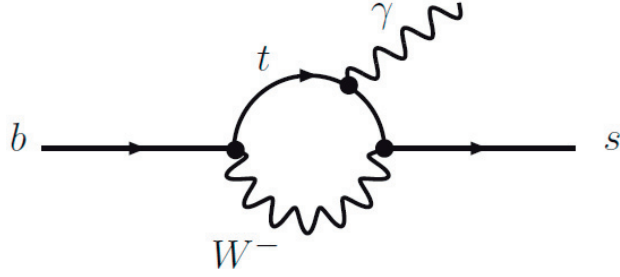
Figure 1.4   Feynman diagram for the $b \to s\gamma$ transition.

operators. Primed (non-primed) coefficients and operators indicate right- (left-) handed currents. The scale of renormalization μ is commonly the mass of the b quark.

The electromagnetic penguin operators $\mathcal{O}_7$ and $\mathcal{O}_7'$ are very relevant in $b \to s\gamma$ transitions, since they describe the SM-favoured left-handed photon, and the SM-suppressed right-handed photon respectively

$$\mathcal{O}_7 \propto \bar{s}_{\alpha_L} \sigma^{\mu\nu} b_{\alpha_R} F_{\mu\nu} \tag{1.103}$$

$$\mathcal{O}_7' \propto \bar{s}_{\alpha_R} \sigma^{\mu\nu} b_{\alpha_L} F_{\mu\nu} \tag{1.104}$$

where α is a colour index, $\sigma^{\mu\nu} = \frac{i}{2}[\gamma^\mu, \gamma^\nu]$, and $F_{\mu\nu}$ is the electromagnetic field strength tensor.

In general, it is common to refer to the effective Wilson coefficients $C_7^{(\prime)\,\mathrm{eff}}$, which absorb the effects of mixing between $\mathcal{O}_7$ and $\mathcal{O}_{1-6}$ operators, due to short distance effects. Under these assumptions, the leading order amplitude for $b \to s\gamma$ transitions can be written as

$$\langle f|\mathcal{H}_{\mathrm{eff}}|i\rangle = -4\frac{G_F}{\sqrt{2}}V_{tb}V_{ts}^* \left[C_7^{\mathrm{eff}}(m_b)\langle f|\mathcal{O}_7(m_b)|i\rangle + C_7'^{\,\mathrm{eff}}(m_b)\langle f|\mathcal{O}_7'(m_b)|i\rangle \right] \tag{1.105}$$

with f and i the final and initial states.

In the SM, $C_{9,10}' = 0$ and

$$\frac{|C_7'|}{|C_7|} \simeq \frac{|C_8'|}{|C_8|} \simeq \frac{m_s}{m_b} \simeq 0.02\,. \tag{1.106}$$

It is common to represent the Wilson coefficients in the $(\delta C_i, \delta C_i')$ plane, where δ indicates the difference with the SM expectation. The most precise results for C_7', obtained combining the latest experimental observations, are shown in Fig. 1.5.

In the past years, the precision on C_7' has increased substantially, with a central value becoming more and more compatible with the SM expectations[9].

---

[9]The semileptonic operators attract a lot of interest, because of a significant discrepancy observed by the LHCb collaboration in the distribution of the angular observables of the $B^0 \to K^{*0}\mu^+\mu^-$ decay [67,68], which might be explained in terms of NP.
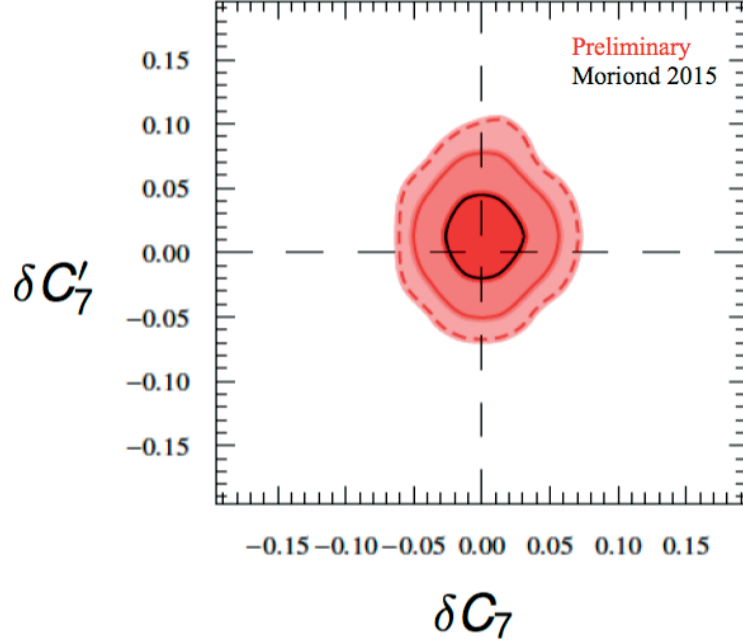
Figure 1.5   Combination of the experimental data for the Wilson coefficient C_7' after the results presented in Moriond 2015. Credits to Ref. [66].

Determination of the photon polarisation

Introducing the weak amplitudes involving left- and right-handed photons as c_L and c_R, and the corresponding strong decay amplitudes as $\mathcal{M}_L$ and $\mathcal{M}_R$, the decay width for a radiative B meson decay can in general be written as

$$\Gamma(\overline{B} \to \bar{X}_s \gamma) \propto |c_L|^2 |\mathcal{M}_L|^2 + |c_R|^2 |\mathcal{M}_R|^2 \,, \tag{1.107}$$

where the left- and right-handed components do not interfere because the helicity of the photon is, in principle, a measurable quantity.

In the SM the photon from radiative $\overline{B}$ (B) decays is predominantly left (right) handed, *i.e.* $|c_L|^2 \gg |c_R|^2$ ($|c_L|^2 \ll |c_R|^2$). Defining the *photon polarisation* λ_γ as

$$\lambda_\gamma \equiv \frac{|c_R|^2 - |c_L|^2}{|c_R|^2 + |c_L|^2} \,, \tag{1.108}$$

the SM implies $\lambda_\gamma \simeq -1$ $(+1)$ for radiative $\overline{B}$ (B) decays up to $\mathcal{O}(m_s^2/m_b^2)$ corrections.

The weak amplitudes $c_{L,R}$ are the product of hadronic form factors and the radiative Wilson coefficients in the effective weak Hamiltonian. The left- and right-handed configurations are sensitive to the same form factors, so that for a $\overline{B}$ decay [69, 70]

$$\frac{|c_R|}{|c_L|} = \frac{|C_7'|}{|C_7|} \tag{1.109}$$

and the photon polarisation parameter λ_γ can be translated directly into information about underlying new physics effects in terms of Wilson coefficients

$$\lambda_\gamma = \frac{|C_7'|^2 - |C_7|^2}{|C_7'|^2 + |C_7|^2}. \tag{1.110}$$

The analogous result for B decays is obtained exchanging C_7 and C_7' in Eqs. 1.109 and 1.110.

Various complementary approaches have been proposed for the determination of λ_γ in radiative decays:

- Radiative decays with three charged hadrons in the final state allow direct access to the photon polarisation parameter λ_γ. This method is the main topic of this thesis, and will be discussed in detail from the next section on.

- An indirect method for the determination of the polarisation of the photon consists in studying the time-dependent decay rate of $B_{(s)} \to f^{CP}\gamma$ decays, f^{CP} being a particle (or system of particles) in a CP eigenstate. Following Ref. [71], the decay rate can be expressed as

$$\Gamma\left(B_{(s)}(\overline{B}_{(s)}) \to f^{CP}\gamma\right)(t) \propto \tag{1.111}$$
$$e^{-\Gamma_{(s)}t}\left[\cosh\left(\frac{\Delta\Gamma_{(s)}}{2}t\right) - H\sinh\left(\frac{\Delta\Gamma_{(s)}}{2}t\right) \pm C\cos\left(\Delta m_{(s)}t\right) \mp S\sin\left(\Delta m_{(s)}t\right)\right],$$

where the coefficients C, S and H are the direct CP asymmetry, the CP asymmetry associated with $B_{(s)} - \overline{B}_{(s)}$ mixing, and a parameter related to the polarisation of the photon:

$$
\begin{aligned}
C &= \frac{(|c_L|^2 + |c_R|^2) - (|\bar{c}_R|^2 + |\bar{c}_L|^2)}{|c_L|^2 + |\bar{c}_L|^2 + |c_R|^2 + |\bar{c}_R|^2}, \\
S &= \frac{2\,\mathcal{I}m[(\bar{c}_L c_L^* + \bar{c}_R c_R^*)]}{|c_L|^2 + |\bar{c}_L|^2 + |c_R|^2 + |\bar{c}_R|^2}, \\
H &= \frac{2\,\mathcal{R}e[(\bar{c}_L c_L^* + \bar{c}_R c_R^*)]}{|c_L|^2 + |\bar{c}_L|^2 + |c_R|^2 + |\bar{c}_R|^2}.
\end{aligned}
\tag{1.112}
$$

$\Delta\Gamma_{(s)}$ and $\Delta m_{(s)}$ are the decay width and mass differences between the $B_{(s)}$ CP eigenstates.

In case $B_{(s)}$ and $\overline{B}_{(s)}$ decays cannot be distinguished (untagged analyses), the overall decay rate $\Gamma(t)$ is studied as

$$\Gamma(t) = \Gamma\left(B_{(s)} \to f^{CP}\gamma\right)(t) + \Gamma\left(\overline{B}_{(s)} \to f^{CP}\gamma\right)(t)$$
$$\simeq e^{-\Gamma_{(s)}t}\left[\cosh\left(\frac{\Delta\Gamma_{(s)}}{2}t\right) - H\sinh\left(\frac{\Delta\Gamma_{(s)}}{2}t\right)\right], \tag{1.113}$$

that relies on the precise knowledge of the $\Delta\Gamma_{(s)}$ parameter and provides access to the polarisation of the photon.

When the decay can be tagged, it is possible to study the time-dependent asymmetry

$$\mathcal{A}^{CP}(t) = \frac{\Gamma(\overline{B}_{(s)} \to f^{CP}\gamma)(t) - \Gamma(B_{(s)} \to f^{CP}\gamma)(t)}{\Gamma(\overline{B}_{(s)} \to f^{CP}\gamma)(t) + \Gamma(B_{(s)} \to f^{CP}\gamma)(t)} \tag{1.114}$$

aiming at the determination of the mixing CP asymmetry S, expected to be zero in the SM, up to small corrections since the left- and right-handed amplitudes $c_{\rm L}$ and $c_{\rm R}$ do not interfere [65]. Neglecting direct CP violation and the decay width difference between the B mesons one has [65, 72]

$$\mathcal{A}^{CP}(t) \simeq S \sin(\Delta m_{(s)} t). \tag{1.115}$$

Introducing the CP violating phase $\phi_{\rm mix}$ corresponding in the SM to $2\beta \simeq 43°$ and $-2\beta_s \simeq -2°$ for B^0 and B_s^0 respectively, S can be related to the Wilson coefficients by the relation

$$S \simeq -\frac{2\mathcal{I}m[e^{-i\phi_{\rm mix}}C_7'C_7]}{|C_7'|^2 + |C_7|^2}, \tag{1.116}$$

that has to be compared to the SM prediction for $b \to s\gamma$ transitions

$$S^{\rm SM} \simeq -2\frac{m_s}{m_b}\sin\phi_{\rm mix}. \tag{1.117}$$

- An alternative approach consists in studying NP effects in the angular distributions of the four bodies in the final state of $B^0 \to K^{*0}l^+l^-$ decays. Following the notation of Ref. [73], the differential decay rate is

$$\frac{\mathrm{d}\Gamma(\overline{B}^0 \to \overline{K}^{*0}\ell^+\ell^-)}{dq^2\,d\cos\theta_\ell\,d\cos\theta_K\,d\phi} = \frac{9}{32\pi}\Big\{I_1^s(q^2)\sin^2\theta_K + I_1^c(q^2)\cos^2\theta_K$$
$$+ [I_2^s(q^2)\sin^2\theta_K + I_2^c(q^2)\cos^2\theta_K]\cos 2\theta_\ell + I_3(q^2)\sin^2\theta_K\sin^2\theta_\ell\cos 2\phi$$
$$+ I_4(q^2)\sin 2\theta_K\sin 2\theta_\ell\cos\phi + I_5(q^2)\sin 2\theta_K\sin\theta_\ell\cos\phi$$
$$+ [I_6^s(q^2)\sin^2\theta_K + I_6^c(q^2)\cos^2\theta_K]\cos\theta_\ell + I_7(q^2)\sin 2\theta_K\sin\theta_\ell\sin\phi$$
$$+ I_8(q^2)\sin 2\theta_K\sin 2\theta_\ell\sin\phi + I_9(q^2)\sin^2\theta_K\sin^2\theta_\ell\sin 2\phi\Big\}, \tag{1.118}$$

where the functions $I_i(q^2)$ can be expressed in terms of two transverse amplitudes, $A_{\perp,\parallel}(q^2)$, a longitudinal one, $A_0(q^2)$, related to the spin of the K^{*0}, and an additional time-like amplitude, $A_t(q^2)$, describing the decay of the virtual gauge boson to the

lepton pair, as

$$I_2^s(q^2) = \frac{\beta_\ell^2}{4} \left[|A_\perp^{\ell_L}|^2 + |A_\perp^{\ell_R}|^2 + |A_\parallel^{\ell_L}|^2 + |A_\parallel^{\ell_R}|^2 \right] ,$$

$$I_3(q^2) = \frac{\beta_\ell^2}{2} \left[|A_\perp^{\ell_L}|^2 + |A_\perp^{\ell_R}|^2 - |A_\parallel^{\ell_L}|^2 - |A_\parallel^{\ell_R}|^2 \right] ,$$

$$I_6^s(q^2) = 2\beta_\ell \mathcal{R}e \left[A_\parallel^{\ell_L} A_\perp^{\ell_L *} - A_\parallel^{\ell_R} A_\perp^{\ell_R *} \right] ,$$

$$I_9(q^2) = \beta_\ell^2 \mathcal{I}m \left[A_\perp^{\ell_L} A_\parallel^{\ell_L *} + A_\perp^{\ell_R} A_\parallel^{\ell_R *} \right] . \tag{1.119}$$

The transverse asymmetries, which can be obtained combining Eqs. 1.119, are expected to have small theoretical uncertainties, and can be related to the Wilson coefficients in the limit $q^2 \to 0$ [74, 75]

$$\mathcal{A}_T^{(2)}(q^2) = \frac{I_3(q^2)}{2I_2^s(q^2)} \to \frac{2\mathcal{R}e[C_7 C_7'^*]}{|C_7|^2 + |C_7'|^2} , \tag{1.120}$$

$$\mathcal{A}_T^{(\mathrm{im})}(q^2) = \frac{I_9(q^2)}{2I_2^s(q^2)} \to \frac{2\mathcal{I}m[C_7 C_7'^*]}{|C_7|^2 + |C_7'|^2} , \tag{1.121}$$

$$\mathcal{A}_T^{(\mathrm{re})}(q^2) = \frac{\beta_\ell}{4} \frac{I_6^s(q^2)}{I_2^s(q^2)} \to 0 . \tag{1.122}$$

- As an alternative to the method proposed above, $b \to s\gamma$ transitions can be studied in the case real photons convert to $e^+ e^-$ pairs.

- The study of photon polarisation in b-baryon decays is also very promising [76–78]. The idea is to exploit the angular distributions of the photon and the proton in the final state of the $\Lambda_b \to \Lambda_X(\to ph)\gamma$ decay, where h is a kaon or a pion. The spin S of the Λ_X baryon determines the helicity states accessible by the decay. For $S = \frac{1}{2}$, introducing the angles θ_γ and θ_p, respectively defined as the angle between the direction of the photon and of the spin of the Λ_b in the rest frame of the Λ_b, and the angle between the Λ_X momentum and the direction of the proton in the Λ_X rest frame, the rate of the decay can be written as

$$\frac{d\Gamma}{d\cos\theta_\gamma} \propto 1 - \lambda_\gamma P_{\Lambda_b} \cos\theta_\gamma \tag{1.123}$$

$$\frac{d\Gamma}{d\cos\theta_p} \propto 1 - \lambda_\gamma \alpha_{p,\frac{1}{2}} \cos\theta_p . \tag{1.124}$$

The proton asymmetry parameter $\alpha_{p,\frac{1}{2}}$ is known experimentally with good precision ($\sim 2\%$) for the $\Lambda(1115)$, while it has to be zero for heavier Λ baryons because of parity conservation. A nonzero polarisation of the Λ_b, P_{Λ_b}, recently measured by the LHCb experiment [79], gives access to the polarisation of the photon.

The peculiarity of this method is that it provides a double handle on λ_γ, which can be related to the angular distributions of the photon and of the proton independently.
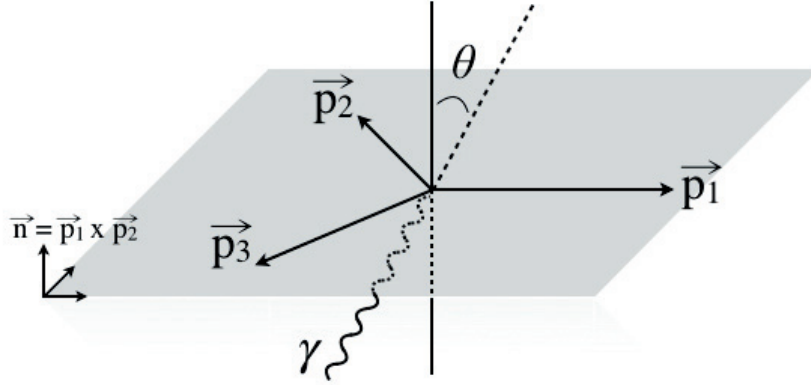
Figure 1.6   Sketch of a $B \to K_{\mathrm{res}}\gamma \to P_1 P_2 P_3 \gamma$ decay in the rest frame of the intermediate kaon resonance (K_{res}). The direction of the photon is defined by the angle θ between the direction opposite to the photon momentum and the normal to the decay plane of the $P_1 P_2 P_3$ hadronic system defined by $\vec{p}_1 \times \vec{p}_2$.

- It as also been proposed [80] to probe photon helicity in radiative B decays using the interference between charmonium resonant states.

1.2.1   Photon polarisation in radiative decays with three charged hadrons in the final state

Let's consider radiative decays of the type $B \to K_{\mathrm{res}}\gamma \to P_1 P_2 P_3 \gamma$, where K_{res} is a kaon resonance, P_1, P_2, P_3 are three pseudo-scalar mesons with four-momenta p_1, p_2 and p_3, and γ is a photon with four-momentum p_γ (Fig. 1.6). In these decays, the angular distribution of the photon can be used for the determination of its polarisation. A parity-odd (pseudoscalar) triple product $\vec{p}_\gamma \cdot (\vec{p}_i \times \vec{p}_j)$, whose sign changes according to the photon chirality, can be defined in the rest frame of the three hadrons. This is not possible with two hadrons in the final state, because the decay is symmetric along the helicity axis, offering no way of distinguishing left- and right-handed photons (Fig. 1.7).

Figure 1.7   Sketch of the $B \to K_{\mathrm{res}}\gamma$ decay in the B meson rest frame, in the case of a two-body (left) and three-body (right) decay of K_{res}.
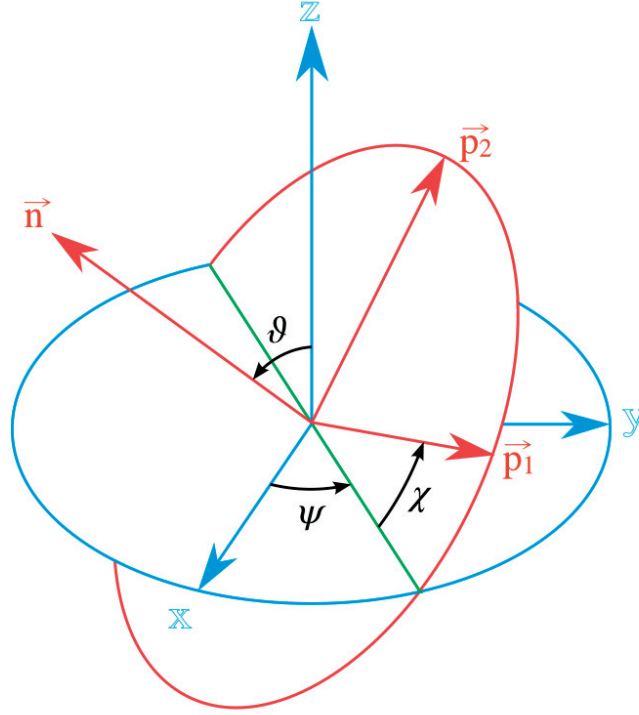
Figure 1.8   Representation of the Euler angles that describe the orientation of the $K^+\pi^-\pi^+$ system (red plane) with respect to the helicity vector z, defined to be along the photon momentum direction and opposite to it. Adaptation of the Figure from https://en.wikipedia.org/wiki/Euler_angles.

Choosing the helicity vector $\hat{e}_z$ to be opposite to the photon momentum direction $(\hat{e}_z = -\vec{p}_\gamma / |\vec{p}_\gamma|)$, and the normal vector $\hat{n}$ to the kaon resonance decay plane to be defined as

$$\hat{n} \equiv \frac{\vec{p}_1 \times \vec{p}_2}{|\vec{p}_1 \times \vec{p}_2|} \,, \tag{1.125}$$

the orientation of the $K^+\pi^-\pi^+$ system with respect to the helicity vector is uniquely identified by three Euler angles: the polar angle θ, the azimuthal angle χ, and the angle ψ that parametrises the rotations around the helicity vector (Fig. 1.8). In particular the angle θ is defined as

$$\cos\theta \equiv \hat{e}_z \cdot \hat{n} = -\frac{\vec{p}_\gamma}{|\vec{p}_\gamma|} \cdot \hat{n} \,. \tag{1.126}$$

The momenta of the final state hadrons do not depend on the angle ψ, meaning that a rotation of the system around $\hat{e}_z$ leaves them unchanged.

Following the notation and calculations of Refs. [69, 70], integrating over the azimuthal

angle χ, the $B \to K_{\mathrm{res}}\gamma \to P_1 P_2 P_3 \gamma$ decay rate can be written as

$$\frac{\mathrm{d}\Gamma(B \to K_{\mathrm{res}}\gamma \to P_1 P_2 P_3 \gamma)}{\mathrm{d}s\,\mathrm{d}s_{13}\,\mathrm{d}s_{23}\,\mathrm{d}\cos\theta} \propto$$

$$\sum_{\mathrm{pol=L,R}} \Gamma(B \to K_{\mathrm{res,pol}}\gamma_{\mathrm{pol}}) \times \frac{\mathrm{d}\Gamma(K_{\mathrm{res,pol}} \to P_1 P_2 P_3)}{\mathrm{d}s\,\mathrm{d}s_{13}\,\mathrm{d}s_{23}\,\mathrm{d}\cos\theta} \times \frac{1}{(s - m_{K_{\mathrm{res}}}^2)^2 + m_{K_{\mathrm{res}}}^2 \Gamma_{K_{\mathrm{res}}}^2},$$

$$(1.127)$$

where $s_{ij} = (p_i + p_j)^2$ and $s = (p_1 + p_2 + p_3)^2$.

The strong decay width of the K_{res} resonance in Eq. 1.127, can be described with an helicity amplitude $\mathcal{H}_\mu$,

$$\mathcal{M}(K_{\mathrm{res,pol}} \to P_1 P_2 P_3) = \xi_{\mathrm{pol}}^\mu \mathcal{H}_\mu \,, \qquad (1.128)$$

with the circular polarisation vectors ξ_{pol}^μ (pol = L, R) defined as

$$\xi_{\mathrm{L}}^\mu = \frac{1}{\sqrt{2}}\,(0, 1, -i, 0)\,, \quad \xi_{\mathrm{R}}^\mu = \frac{1}{\sqrt{2}}\,(0, 1, i, 0)\,. \qquad (1.129)$$

Then, in the K_{res} rest frame,

$$\frac{\mathrm{d}\Gamma(K_{\mathrm{res,pol}} \to P_1 P_2 P_3)}{\mathrm{d}s\,\mathrm{d}s_{13}\,\mathrm{d}s_{23}\,\mathrm{d}\cos\theta} \propto |\mathcal{M}(K_{\mathrm{res,pol}} \to P_1 P_2 P_3)|^2 \propto \left|\xi_{\mathrm{pol}}^\mu \mathcal{H}_\mu\right|^2\,. \qquad (1.130)$$

The actual value of this quantity will change according to the property of the K_{res} state.

1.2.2 Photon polarisation in $B^+ \to K^+ \pi^- \pi^+ \gamma$

Gronau *et al.* [69, 70] propose to study $B^+ \to K^+ \pi^- \pi^+ \gamma$ decays, with intermediate kaon resonances decaying to a $K^+ \pi^- \pi^+$ final state with masses in the $[1, 2]$ GeV/c^2 interval, adopting the identification $P_1 = \pi^-$, $P_2 = \pi^+$ and $P_3 = K^+$.[10] In this mass interval, they consider only K_{res} states with quantum numbers $J^P = 1^+$, 2^+ and 1^-. The amplitude in Eq. 1.127 for left and right-polarised photons in the rest frame of the $K^+ \pi^- \pi^+$ system is developed as

$$\mathcal{A}_{R,L}(B \to K\pi\pi\gamma_{R,L}) = A(\vec{\xi}_\pm \cdot \vec{\mathcal{J}}) \pm B\left((\vec{\xi}_\pm \cdot \hat{n})(\vec{\xi}_0 \cdot \vec{\mathcal{K}}) + (\vec{\xi}_\pm \cdot \vec{\mathcal{K}})(\vec{\xi}_0 \cdot \hat{n})\right) \pm C(\vec{\xi}_\pm \cdot \hat{n})\,,$$

$$(1.131)$$

where the $+(-)$ sign refers to the right (left) polarisation, the coefficients A, B and C contain the information about the strong amplitude of $K_{\mathrm{res}} \to K^+ \pi^- \pi^+$ for kaon resonances with spin-parity $J^P = 1^+$, 2^+ and 1^-, respectively, and the vectors $\vec{\mathcal{J}}$ and $\vec{\mathcal{K}}$ contain all the dependencies on the Dalitz variables s_{13} and s_{23}. The polarisation vectors $\vec{\xi}_i$ are defined in terms of the helicity vector $\hat{e}_z$ and two arbitrary vectors $\hat{e}_x$ and $\hat{e}_y$ in the plane perpendicular to $\hat{e}_z$ as

$$\vec{\xi}_\pm = \mp\frac{1}{\sqrt{2}}(\hat{e}_x \pm i\hat{e}_y)\,, \quad \vec{\xi}_0 = \hat{e}_z\,. \qquad (1.132)$$

---

[10]Charge conjugates are implied throughout this thesis, unless explicitly stated.

1.2. Photon polarisation in the Standard Model

Following the developments of Refs. [69, 70], the $\cos\theta$ dependence is introduced, and the decay distribution of $B^+ \to K^+\pi^-\pi^+\gamma$ becomes sensitive to the photon polarisation parameter λ_γ, that contains the weak amplitude information (Eq. 1.108):

$$\frac{\mathrm{d}\Gamma(B^+ \to K^+\pi^-\pi^+\gamma)}{\mathrm{d}s\,\mathrm{d}s_{13}\,\mathrm{d}s_{23}\,\mathrm{d}\cos\theta} =$$

$$|A|^2 \left\{ \frac{1}{4}|\vec{\mathcal{J}}|^2(1+\cos^2\theta) + \frac{1}{2}\lambda_\gamma\,\mathcal{I}m\left[\hat{n}\cdot(\vec{\mathcal{J}}\times\vec{\mathcal{J}}^*)\right]\cos\theta \right\} +$$

$$+ |B|^2 \left\{ \frac{1}{4}|\vec{\mathcal{K}}|^2(\cos^2\theta + \cos^2 2\theta) + \frac{1}{2}\lambda_\gamma\,\mathcal{I}m\left[\hat{n}\cdot(\vec{\mathcal{K}}\times\vec{\mathcal{K}}^*)\right]\cos\theta\cos 2\theta \right\} + |C|^2\frac{1}{2}\sin^2\theta +$$

$$+ \left\{ \frac{1}{2}(3\cos^2\theta - 1)\mathcal{I}m\left[AB^*\,\hat{n}\cdot(\vec{\mathcal{J}}\times\vec{\mathcal{K}}^*)\right] + \lambda_\gamma\,\mathcal{R}e\left[AB^*\,(\vec{\mathcal{J}}\cdot\vec{\mathcal{K}}^*)\right]\cos^3\theta \right\}. \quad (1.133)$$

The interference between the amplitudes for the $J^P = 1^+$ and 2^+ resonances gives rise to the expression in the last line of Eq. 1.133; the interferences between 1^- resonance and the other spin-parity states vanish. The terms in $|A|^2$, $|B|^2$ and the interference contribution introduce an asymmetry between left and right-handed amplitudes that can be used to determine λ_γ by counting the number of photons on each side of the $K^+\pi^-\pi^+$ decay plane (Sec. 1.2.3).

The definition of the photon angle plays a key role in the determination of λ_γ. The $\cos\theta$ variable changes sign under the exchange of s_{13} and s_{23}, hence it is replaced with the new angular variable, $\cos\tilde{\theta} \equiv \mathrm{sign}(s_{12} - s_{23})\cos\theta$, as done in Ref. [70]. The angle $\tilde{\theta}$ is then the angle between $-\vec{p}_\gamma$ and the normal to the decay plane defined by $\vec{p}_{\mathrm{slow}} \times \vec{p}_{\mathrm{fast}}$, where $\vec{p}_{\mathrm{slow}}$ and $\vec{p}_{\mathrm{fast}}$ correspond to the momenta of the slowest and fastest pions in the final state hadrons rest frame, respectively.

In the case of $B^0 \to K^+\pi^-\pi^0\gamma$ and $B^+ \to K^0\pi^+\pi^0\gamma$ decays, using the angle θ would cancel the effect of the asymmetry, because of the symmetric structure of the s_{13}, s_{23} Dalitz plot. In fact $\vec{\mathcal{J}}$ and $\vec{\mathcal{K}}$ are such that under the exchange $s_{13} \leftrightarrow s_{23}$ the former changes sign and the latter stays unchanged, causing the cancellation of the terms in $|A^2|$ and $|B^2|$ in Eq. 1.133.

This is not true in the case under study, where both conventions lead to non-zero, and generally different, results. Hence, the results obtained using both angle definitions will be presented in this thesis. Moreover, the differences between the values obtained in the two scenarios is expected to give information about the structure of the Dalitz plot. The two cases will be referred to hereinafter as the *sign-flip* ($\cos\tilde{\theta}$) and *no-flip* ($\cos\theta$) scenarios.

It is evident from Eq. 1.133 that neglecting the interferences between resonances with different spin-parity, photon polarisation can be experimentally accessed only in case the helicity amplitudes contain more than one term with non-vanishing relative phase, *i.e.*, interference is needed to measure λ_γ. In fact, in such case the terms proportional to λ_γ are different from zero only when $\vec{\mathcal{J}}$ and $\vec{\mathcal{K}}$ contain complex values ($\vec{\mathcal{J}}, \vec{\mathcal{K}} \in \mathbb{C}$).

Gronau *et al.* distinguish three different interference patterns for the $B^+ \to K^+\pi^-\pi^+\gamma$ system:

- Interference between two intermediate $K^*\pi$ states with different charges, related by isospin symmetry, *e.g.* $K_1(1270)^0 \to K^{*0}\pi^0$ and $K_1(1270)^0 \to K^{*+}\pi^-$; in our case of study, the decay of $B^\pm$ into charged hadrons, this interference is not possible.

- Interferences between intermediate resonances amplitudes, *e.g.* $K_1(1270)^+ \to K^{*0}\pi^+$ and $K_1(1270)^+ \to \rho^0 K^+$.

- Interferences between S and D wave amplitudes in the decay, *e.g.* in the decay $K_1(1270)^+ \to K^{*0}\pi^+$ the angular momentum states $L = 0$ and $L = 2$ are both allowed.

Another source of interference expected to play a significant role is the interference between kaon resonances with the same spin-parity, *e.g.* $K_1(1270)^+$ and $K_1(1400)^+$, both with 1^+ spin-parity and close enough in mass to interfere. This kind of interference has not been considered in any theoretical study of $B^+ \to K^+\pi^-\pi^+\gamma$ decays, because of the limited experimental knowledge of the $K^+\pi^-\pi^+$ spectrum in the past years: at the time of the writing of the Gronau *et al.* articles, the $K_1(1400)$ was believed to be the dominant 1^+ resonance in the $K^+\pi^-\pi^+$ mass window considered, so $K_1(1270)$ was not considered; it has now been established at the B-factories that the $K_1(1270)\gamma$ state has the largest branching fraction [81], with only an upper limit available for the $K_1(1400)\gamma$ branching fraction.

In case the latter interference term turns out to be not negligible, the currently available theory will not help in the determination of the photon polarisation from the experimental observations. A more general description that extends the theory of Gronau *et al.* to account for this interference pattern is needed.

1.2.3 Up-down asymmetry

A simplified approach to the study of the photon polarisation consists in exploiting the angular distribution of the photon, integrating Eq. 1.133 over the Dalitz variables. Developing Eq. 1.133 in terms of the angular dependence, the $B^+ \to K^+\pi^-\pi^+\gamma$ differential branching fraction can be written as

$$\frac{\mathrm{d}\Gamma(B \to K_{\mathrm{res}}\gamma \to P_1 P_2 P_3 \gamma)}{\mathrm{d}s\,\mathrm{d}s_{13}\,\mathrm{d}s_{23}\,\mathrm{d}\cos\tilde{\theta}} \propto \sum_{i=0,2,4} a_i(s, s_{13}, s_{23}) \cos^i\tilde{\theta}$$
$$+ \lambda_\gamma \sum_{j=1,3} a_j(s, s_{13}, s_{23}) \cos^j\tilde{\theta}, \qquad (1.134)$$

showing that only terms in odd powers of $\cos\tilde{\theta}$ are sensitive to the photon polarisation. The sums in Eq. 1.134 extend to the fourth order and the a_k parameters depend on the resonances and their interference patterns.

Integrating over the Dalitz variables [69, 70] Gronau *et al.* introduce the *up-down* asym-

metry $\mathcal{A}_{\rm ud}$, defined as

$$\mathcal{A}_{\rm ud} \equiv \frac{\int_0^1 {\rm d}\cos\tilde\theta \frac{{\rm d}\Gamma}{{\rm d}\cos\tilde\theta} - \int_{-1}^0 {\rm d}\cos\tilde\theta \frac{{\rm d}\Gamma}{{\rm d}\cos\tilde\theta}}{\int_{-1}^1 {\rm d}\cos\tilde\theta \frac{{\rm d}\Gamma}{{\rm d}\cos\tilde\theta}} \, . \tag{1.135}$$

The terms in even powers of $\cos\tilde\theta$ integrate out, so that the resulting asymmetry is directly proportional to λ_γ. As an example, for 1^+ resonances, the asymmetry is found to be

$$\mathcal{A}_{\rm ud}^{1^+} = \frac{3}{4}\lambda_\gamma \frac{\int {\rm d}s\, {\rm d}s_{13}\, {\rm d}s_{23}\, {\rm Im}\left[\hat{n} \cdot (\vec{\mathcal{J}} \times \vec{\mathcal{J}}^*)\right]}{\int {\rm d}s\, {\rm d}s_{13}\, {\rm d}s_{23} |\mathcal{J}|^2} \, , \tag{1.136}$$

proportional to λ_γ as expected. If $\vec{\mathcal{J}}$ is known, it allows the determination of the photon polarisation. In case of no interference, $\vec{\mathcal{J}}$ is real and the asymmetry vanishes.

In the more realistic case of multiple resonance contents, the asymmetry is still proportional to the photon polarisation, but the determination of the proportionality constant is more complicated. Reference [70] introduces a detailed study of the case of $K_1(1400)$, $K_2^*(1430)$ and $K^*(1410)$, adequately illustrating the nature of the problem. Gronau *et al.* calculate a $\sim 10\%$ up-down asymmetry for the charged $K_1(1400)^+\gamma$ decay, with some dilution coming from the other two resonances. A realistic calculation of the expected up-down asymmetry has not been performed so far.

In the case of $B^+ \to K^+\pi^-\pi^+\gamma$, one has to take into account that the multitude of resonances peaking in the $K^+\pi^-\pi^+$ region of interest cannot be easily distinguished due to their overlap. Each of these resonances has its own distribution in the $K^+\pi^-$ and $\pi^+\pi^-$ dimensions, and thus can contribute differently to the inclusive up-down asymmetry. Moreover, the interference between overlapping resonances can enhance or dilute the asymmetry.

As a first, largely simplified, approach to the problem, four intervals of $K^+\pi^-\pi^+$ mass are considered. In Ref. [70], a recommendation is made to use the $[1400, 1600]$ MeV/c^2 range for up-down asymmetry studies. This region includes the $K_1(1400)$, $K_2^*(1430)$ and $K^*(1410)$ resonances, with strong, small and null up-down asymmetries, respectively; it also avoids the upper tail of the $K_1(1270)$, which would interfere with the $K_1(1400)$. As said earlier, since the publication of Gronau's paper, the understanding of the $K^+\pi^-\pi^+$ has evolved considerably, and $K_1(1270)$ has been shown to be the prominent resonance in the mass range of interest. For this reason, the $[1100, 1300]$ MeV/c^2 range will also be studied. The $[1300, 1400]$ MeV/c^2 mass bin is studied since it contains the overlap region between the two K_1 resonances. The results are also obtained for the high mass $K^+\pi^-\pi^+$ region, $[1600, 1900]$ MeV/c^2, which mainly includes 2^- resonances not considered in the development of Eq. 1.133.

Binning the $K^+\pi^-\pi^+$ spectrum is very helpful for getting a first understanding of the system and the up-down asymmetry. It is still, though, a significant simplification that prevents the extraction of λ_γ from the observations, but can reveal the presence of photon polarisation.

1.3 Study of the $K^+\pi^-\pi^+$ system

As previously stated, the study of the photon polarisation in $B^+ \to K^+\pi^-\pi^+\gamma$ decays is not easy because of the multitude of kaon resonances populating the $[1,2]$ GeV/c^2 $K^+\pi^-\pi^+$ mass interval. To proceed a step further from what is proposed in Sec. 1.2.3, the kaon resonances need to be separated fitting the single modes peaking in the $K^+\pi^-\pi^+$ mass spectrum, so that all the interference contributions that allow access to the photon polarisation parameter λ_γ can be highlighted.

1.3.1 Experimental status

The Belle [82] and BaBar [83,84] experiments have studied the $B^+ \to K^+\pi^-\pi^+\gamma$ decay as a control sample for the study of the time-dependent CP asymmetry in $B^0 \to K^0_S\rho\gamma$ decays. The $K^+\pi^-\pi^+$ mass distributions obtained are shown in Fig. 1.9. In both existing experimental efforts from the B-factories, the resonant structure of the $K^+\pi^-\pi^+$ spectrum has been studied without exploiting completely the final state system, leading to incomplete descriptions of the resonance content: in the Belle analysis a $2D$ fit is performed on the $m_{K^+\pi^-}$ and $m_{\pi^+\pi^-}$ dimensions, while the BaBar study consists in a simple fit of the $m_{K^+\pi^-\pi^+}$ distribution.

The LHCb dataset, being significantly larger than the Belle and BaBar ones (about $14\,000$ signal events against $\sim 1\,500$ and $\sim 2\,500$ respectively), allows the $m^2_{K^+\pi^-\pi^+}$ data distribution to be complemented by the $m^2_{K^+\pi^-}$ and $m^2_{\pi^+\pi^-}$ information, so that the complete information can be seen as a collection of $(m^2_{K^+\pi^-}, m^2_{\pi^+\pi^-})$ Dalitz plots for all values of the $K^+\pi^-\pi^+$ mass.

This full *amplitude analysis* of the $K^+\pi^-\pi^+$, $K^+\pi^-$, $\pi^+\pi^-$ Dalitz plot is expected to provide the separation power needed for the identification of the single resonances contributions, allowing for a better understanding of the interference patterns that give access to the photon polarisation parameter λ_γ. A measurement of such a quantity could eventually help in constraining the effects of physics beyond the SM in the $b \to s\gamma$ sector.
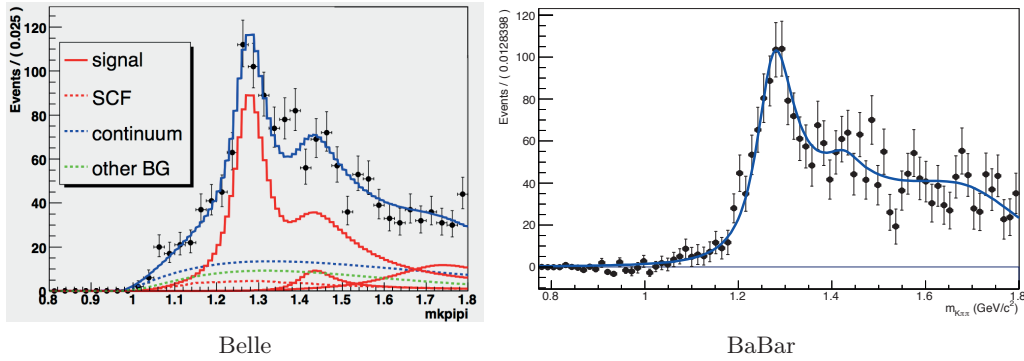

Belle   BaBar

Figure 1.9 $K^+\pi^-\pi^+$ mass distributions obtained by the Belle and BaBar experiments. Credits to Refs. [85] and [83].

1.3. Study of the $K^+\pi^-\pi^+$ system

Some theoretical and technical aspects to be faced for the Dalitz study are presented in Sec. 1.3.2.

Further considerations on 1^+ resonances

In the chosen $K^+\pi^-\pi^+$ mass range 1^+ resonances are expected to play a relevant role, the $K_1(1270)$ being the dominant state with a small contribution from the $K_1(1400)$, as observed by the Belle collaboration [81]. As pointed out in Ref. [86], the $K_1(1270)$ and $K_1(1400)$ are the two mass eigenstates of the interaction states K_{1A} and K_{1B}

$$\begin{pmatrix} |K_1(1270)\rangle \\ |K_1(1400)\rangle \end{pmatrix} = \begin{pmatrix} \sin\theta_K & \cos\theta_K \\ \cos\theta_K & -\sin\theta_K \end{pmatrix} \begin{pmatrix} |K_{1A}\rangle \\ |K_{1B}\rangle \end{pmatrix}, \tag{1.137}$$

with the mixing angle θ_K predicted to be $33°$ or $57°$ [87] in agreement with the results reported by the CLEO collaboration [88].

Concerning the expected branching fractions for the 1^+ states, the PDG [89] reports in its averages the values obtained by the ACCMOR collaboration [90]: it has been questioned [86, 91] whether those results have been properly interpreted. Most of the discussion arises in the study of the $K^+\pi^-$ spectrum, where Ref. [92] observes a much reduced rate of $K_1(1270)^+ \to K_0^*(1430)^0\pi^+$, with respect to what is claimed in the PDG, in the study of both $B^+ \to J/\psi K^+\pi^-\pi^+$ and $B^+ \to \psi' K^+\pi^-\pi^+$ decays. It has been suggested [93] that the scalar component observed by the ACCMOR collaboration in the $K^+\pi^-$ mass spectrum might be the $K^*(800)^0$, also known as κ. Moreover, in all the studies of the $K^+\pi^-\pi^+$ spectrum performed so far, the D wave component of the $K_1(1270)^+ \to K^{*0}\pi^+$ decay has never been considered: the interference between the S and D wave amplitudes for this decay, introduced in Sec. 1.2.2, might be large and then very helpful in the study of the polarisation of the photon.

On another issue, Ref. [91] points out that the proximity of the $K_1(1270)$ resonance to the production threshold of the $K^+\rho(770)^0$ channel causes the definition of the kaon resonance width to be ambiguous. Therefore, the possibility that the width from Ref. [89] is not correct has to be considered.

1.3.2   Dalitz plot and meson spectroscopy

The decay rate for a particle of mass M and four-momentum p decaying to a final state with n particles with four-momenta $p_i = (E_i, \vec{p}_i)$ can be expressed as

$$\mathrm{d}\Gamma = \frac{1}{2M}|\mathcal{M}|^2 \, \mathrm{d}\phi^n \tag{1.138}$$

where $\mathcal{M}$ is the decay amplitude and the n-body phase-space $\mathrm{d}\phi^n$ is given by

$$\mathrm{d}\phi^n = (2\pi)^4 \delta^4\left(p - \sum_{i=1}^n p_i\right) \prod_{i=1}^n \frac{\mathrm{d}^3\vec{p}_i}{16\pi^3 E_i} \tag{1.139}$$

where four-momentum conservation is enforced by the Dirac delta function $\delta^4(p_{\text{initial}} - p_{\text{final}})$.

The phase-space element of Eq. 1.139 provides $3n$ degrees of freedom to the system, that, because of four-momenta conservation, reduce to $3n - 4$ independent degrees of freedom, corresponding to the relative orientation of the n momenta $\vec{p}_i$ and to the Euler angles that describe the orientation of the reference frame with respect to the initial state.

Integrating Eq. 1.138 over the Dirac delta function the phase-space term can be expressed as a function of $3n - 4$ independent kinematic variables x_i

$$\mathrm{d}\phi^n = \phi^n(x_1, ..., x_{3n-4}) \prod_{i=1}^{3n-4} \mathrm{d}x_i \,. \tag{1.140}$$

The kinematic variables are chosen so that the phase-space term $\phi^n(x_1, ..., x_{3n-4})$ is constant within the kinematically allowed region. As a result, the decay rate of Eq. 1.138 becomes

$$\mathrm{d}\Gamma \propto |\mathcal{M}|^2 \prod_{i=1}^{3n-4} \mathrm{d}x_i \,, \tag{1.141}$$

highlighting how, using this formalism, any non-uniformity observed in the distribution of the kinematic variables x_i can be directly related to the structure of the amplitude $\mathcal{M}$. A common choice for the kinematic variables are the final state squared invariant masses $m_{ij}^2 = (p_i + p_j)^2$.

In case the initial and final state particles are spinless, the system is invariant under any rotation and three additional degrees of freedom can be removed choosing a reference frame, leaving $3n - 7$ independent degrees of freedom.

This technique was first used by R. H. Dalitz in 1953 for the study of the decay of a particle into a three-body final state [94, 95].

Three-body decays

For a generic three-body decay $P \rightarrow abc$ of a pseudoscalar with mass M in three pseudoscalar particles, the system has only 2 degrees of freedom and, following Ref. [96], Eq. 1.138 can be written as

$$\mathrm{d}\Gamma = \frac{1}{(2\pi)^3} \frac{1}{32M^3} \left| \mathcal{M}(m_{ab}^2, m_{bc}^2) \right|^2 \mathrm{d}m_{ab}^2 \, \mathrm{d}m_{bc}^2 \,. \tag{1.142}$$

The squared invariant masses of the abc system are related by the linear relation

$$m_{ab}^2 + m_{ac}^2 + m_{bc}^2 = M^2 + m_a^2 + m_b^2 + m_c^2 \,. \tag{1.143}$$

Introducing the energies of b and c in the ab rest frame as

$$E_b^* = \frac{m_{ab}^2 - (m_a^2 - m_b^2)}{2m_{ab}},$$
$$E_c^* = \frac{M^2 - (m_{ab}^2 + m_c^2)}{2m_{ab}},$$

(1.144)

and the corresponding momenta

$$p_b^* = \sqrt{E_b^{*2} - m_b^2},$$
$$p_c^* = \sqrt{E_c^{*2} - m_c^2},$$

(1.145)

the range of the invariant mass m_{bc}^2 can be written as a function of the other kinematic variable m_{ab}^2.

$$\left(m_{bc}^2\right)_{\min} = (E_b^* + E_c^*)^2 - (p_b^* + p_c^*)^2,$$
$$\left(m_{bc}^2\right)_{\max} = (E_b^* + E_c^*)^2 - (p_b^* - p_c^*)^2.$$

(1.146)
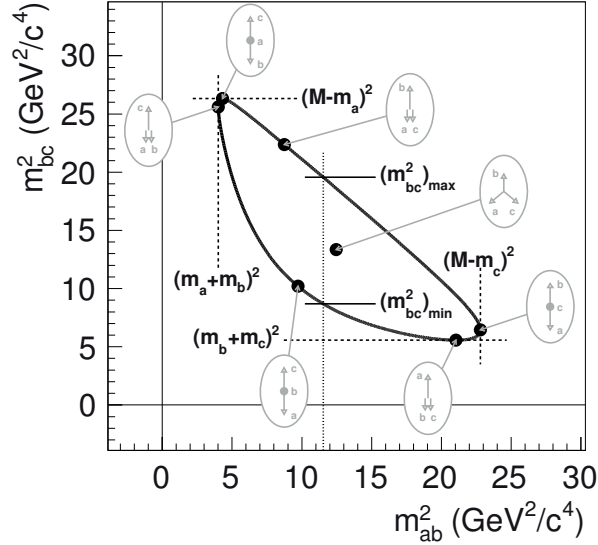
Figure 1.10   Kinematic boundaries of the three-body decay phase-space. Credits to Ref. [96].

The resulting drop-shaped (m_{ab}^2, m_{bc}^2) region (Fig. 1.10) represents the kinematically allowed phase-space for the three-body decay described by Eq. 1.142. The (m_{ab}^2, m_{bc}^2) scatter plot of the events in this region is referred to as Dalitz plot.

The three-body decay can take place through many intermediate resonant states R_k, so that

$$|\mathcal{M}|^2 = \left| \sum_k f_k \mathcal{A}_k \right|^2,$$

(1.147)

where f_k are complex coefficients accounting for the relative magnitude and phase of the amplitudes. For example, using Eq. 1.142 to describe a decay of the type $P \to aR_k(\to bc)$ results in a vertical band at $m_{bc}^2 = m_{R_k}^2$ in the Dalitz plot. In case $\mathcal{M}$ is a constant, the Dalitz plot is uniformly populated.

The amplitudes $\mathcal{A}_k$ are commonly parametrised using the isobar formalism [97,98], which describes the amplitude for the decay going through the resonance R_k as

$$\mathcal{A}_k = F_P \times F_{R_k} \times T_{R_k} \times W_{R_k} \, , \tag{1.148}$$

where F_P and F_{R_k} are the form factors describing the transition for the parent particle and the resonance, and T_{R_k} and W_{R_k} are the dynamical and angular part of the resonance propagator, respectively.

The Dalitz plot of $B^+ \to K^+\pi^-\pi^+\gamma$ decays

In order to simplify the description of the system, the four-body $K^+\pi^-\pi^+\gamma$ final state is described using a two-body approximation as a kaon resonance (K_{res}) plus a photon, allowing the study of the $K^+\pi^-\pi^+$ system *per se*[11].

The three-body $K_{\mathrm{res}} \to K^+\pi^-\pi^+$ decay features important differences with respect to the example of the previous section:

- The initial state is a resonance, hence its mass varies for each event.

- Since the mother resonance K_{res} has spin different from zero, only one degree of freedom associated to the Euler angles can be removed choosing a reference direction in space.

For the sake of simplicity, for this initial stage of the study the rotational degrees of freedom are not considered. This corresponds to analysing the resonant structure of the $K^+\pi^-\pi^+$ system after integrating over the angles θ, χ and ψ introduced in Sec. 1.2.1, so that the decay amplitude depends only on $m_{K^+\pi^-\pi^+}^2$, $m_{K^+\pi^-}^2$ and $m_{\pi^+\pi^-}^2$. A detailed description of the decay amplitudes is presented in Chapter 5.

In a future extension of this work, the angular dimensions can be added, aiming at a direct fit of the photon angle, providing direct access to the photon polarisation parameter λ_γ (Chapter 6).

---

[11]The procedure applied is similar to the one described in the $B^+ \to J/\psi K^+\pi^-\pi^+$ analysis with Belle data [99].

2

The LHCb experiment

The Large Hadron Collider (LHC) at CERN, designed to collide protons at 14 TeV, is the largest and most powerful particle accelerator ever built. Starting from 2010, the accelerator has been smoothly running at 7 and 8 TeV centre-of-mass energy until the beginning of 2013 (Run I), when it has undergone a long shutdown before the 13 TeV restart in 2015 (Run II).

The LHC 27 km ring, running across the border between Switzerland and France, hosts a number of experiments, of which three main ones aim at the observation of new physics phenomena in proton-proton (pp) collisions: ATLAS, CMS and LHCb.

The main goal of the LHCb experiment is to search for new physics phenomena in flavour physics by testing the SM through high precision measurements of rare decays and CP violation. Such searches are usually referred to as indirect searches, to mark the difference with the direct searches performed by ATLAS and CMS.

At the high luminosity of the LHC, a very large number of b hadrons is produced in the pp interactions. The LHCb detector is designed to trigger, reconstruct, and identify as many as possible of these events in this very challenging experimental environment. In order to accomplish this task, the detector must be equipped with

- a tracking system with very high momentum resolution;

- subdetectors devoted to the identification of charged and neutral particles;

- an efficient and flexible trigger system.

Additionally, a powerful data acquisition system, capable of online processing, is necessary to optimize the data taking.

During Run I of the LHC, the LHCb detector has efficiently collected ~ 3 fb^{-1} of data, at an average luminosity of 4×10^{32} cm^{-2}s^{-1}, above the design value. In order to run at higher luminosities with an improved trigger efficiency and data acquisition rate, the LHCb detector will be upgraded in $2019 - 2020$.
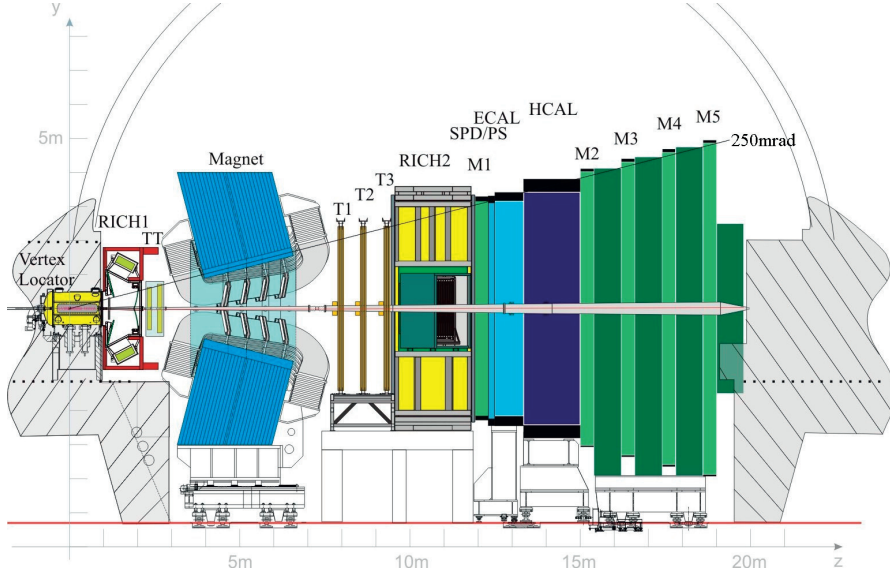
2.1 The LHCb detector

Figure 2.1 Lateral view of the LHCb detector.

The LHCb detector (Fig. 2.1) is a single-arm spectrometer designed for the study of particles containing b or c quarks [100, 101].

It covers the pseudorapidity range $2 < \eta < 5$, corresponding to a narrow polar angle of $10 - 300$ mrad in the horizontal bending plane, and $10 - 250$ mrad in the vertical plane. Its forward design exploits the characteristic distribution of b and $\bar{b}$ hadrons produced by a $b\bar{b}$ pair in a pp collider environment. In fact, the momentum distributions of the constituents of the protons are such that the $b\bar{b}$ pair gets a strong boost along the beam direction z, implying that most of the $b\bar{b}$ pairs are produced at small angles with respect to the beam axis, in the forward or backward direction (Fig. 2.2). The detector coordinate system is completed by the horizontal x axis and the vertical y axis.

The LHCb detector systems are described in the following sections, organized according to the main purpose of the subdetectors. The detector description is based on Ref. [100], which is also the source of the figures presented in the text, while the performances are taken from Ref. [101].

2.1.1 Tracking

The tracking system (Fig. 2.3) has been designed for a very precise reconstruction of charged particles traversing the detector, in order to allow the necessary momentum and vertex resolution needed for the study of c and b hadrons. These particles are reconstructed as tracks made of many hits, before and after a dipole magnet that bends them to allow the determination of the ratio between their charge and momentum. Upstream of the magnet, hits are produced first in the Vertex Locator (VELO), situated around the pp
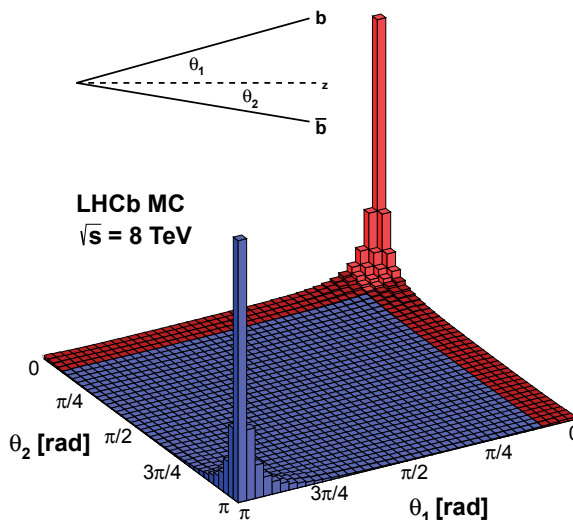
44

Figure 2.2   Polar angle distribution of b and $\bar{b}$ hadrons produced in a pp collider environment. The distribution shown is simulated using the PYTHIA event generator.

interaction point and responsible for the reconstruction of collision and decay vertices, and then in the Tracker Turicensis (TT). Both subdetectors are based on a silicon technology. Downstream of the magnet, three tracking stations T1–T3 are responsible for the precise determination of the trajectory. Each station is made of an Inner Tracker (IT) situated in the high occupancy region close to the beam axis, and an Outer Tracker (OT), in the lower occupancy region. While the IT is made of silicon strips, the OT is a straw-tube gaseous detector, better suited to cover large areas.

The track reconstruction algorithm starts by searching for hits in the VELO compatible with a straight line. To fully reconstruct the track trajectory, this information is then first combined with hits in the T stations and then in the TT. A full track fit is then performed using a Kalman filter, that accounts for the effects of multiple scattering and energy loss $\mathrm{d}E/\mathrm{d}x$. Track quality is ensured monitoring the χ^2 of such fit.

Tracks traversing the full tracking system (long tracks) are usually preferred for physics analyses because of their better momentum resolution. For the study of long-lived particles, though, it is necessary to use downstream tracks (TT + T stations only), because the decay vertex is not reconstructed in the VELO. This is, for example, the case of K^0_S and Λ decays. Upstream tracks (VELO + TT only), corresponding to low momentum tracks bent outside the acceptance by the magnet, are usually not used because of their poor momentum resolution.

For Run I, the tracking system has provided an excellent combined momentum resolution, with an uncertainty $\delta p/p$ of $\sim 0.4\%$ for tracks of $5\,\mathrm{GeV}/c$ and $\sim 0.6\%$ at $100\,\mathrm{GeV}/c$.
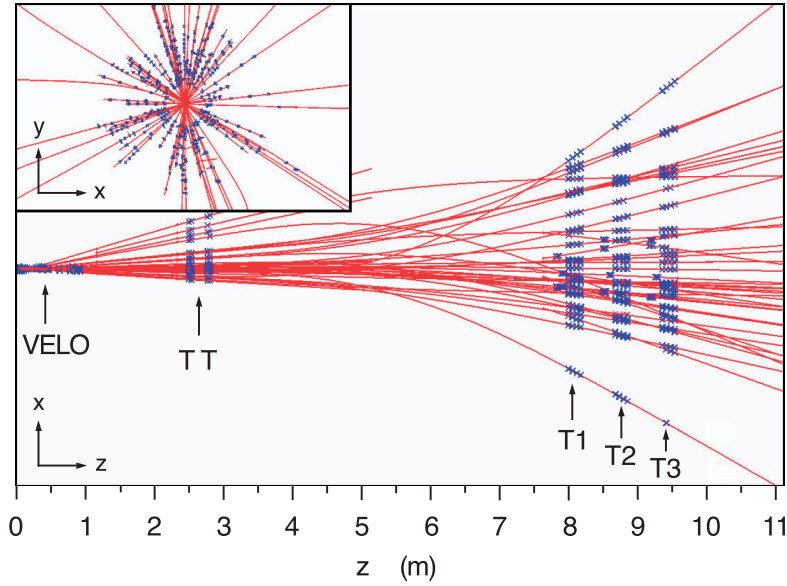
Figure 2.3   Overview of the LHCb tracking system.

Vertex Locator

The VELO subdetector has been designed in order to allow the best possible separation of the b hadron vertex, named *secondary* vertex (SV), from the pp interaction vertex, or *primary* vertex (PV). Since the b hadrons produced at the PV travel typical distances of a centimetre before decaying at the SV and because of the spread of the PV positions, the VELO has been designed to be sensitive in the region $|z| < 10.6$ cm around the nominal interaction point. The information from the backward region ($z < 0$) is also used for the PV reconstruction.

The VELO (Fig. 2.4) is made of a series of silicon stations perpendicular to the beam direction, providing radial (r) and azimuthal (ϕ) cylindrical coordinates for the track hits. In order to be as close as possible to the interaction point, the stations are placed inside a vacuum vessel, and split in two halves mounted on movable supports. The VELO is opened when the beam is not stable, to avoid damage during the LHC injection and dumping phases, and closed during data taking. Each station is made of two half-moon-shaped 300 μm thick silicon sensors, a ϕ and an r sensor, with a small hole in the centre to let the beam through (Fig. 2.5). The two halves are staggered in z, allowing an overlap of the sensors used for the detector alignment. The 2D (r, ϕ) information together with the z coordinate of the station provide a 3D localization of the track hit, with a hit resolution of $5 - 25$ μm, depending on the track angle and on the thickness of the silicon strip at the hit position (finer in the central region and coarser toward the outer part). The PV offline reconstruction resolution is 40 μm in the (x, y) plane.

Since most of the background comes from the PV, the precise determination of the SV has a very important role in the trigger stage. Hence, four additional r sensors are placed in the backward region to form the so-called *pile up* stations, used for the hardware trigger.

46
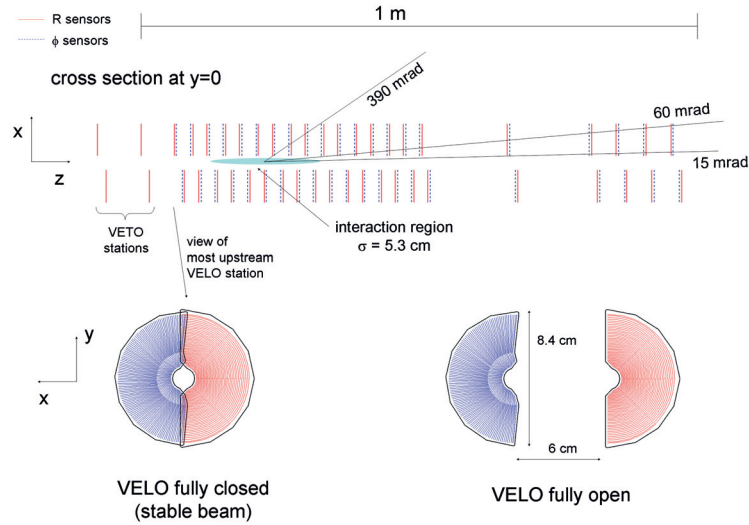
Figure 2.4 Overview of the VELO subdetector structure showing the spacing of the modules along the z axis (top). A sketch of the closed and open VELO positions is also shown (bottom).

Dipole magnet

A very important role in the tracking system is played by the dipole magnet. Particles are distinguished according to their charge q and momentum p exploiting the relation

$$\rho = \frac{qB}{p} \tag{2.1}$$

where ρ is the track curvature and B the magnetic field intensity, mapped with a relative precision of 4×10^{-4}.

The dipole magnet consists of two identical conical-shaped coils of 27 ton each, held by a 1450-ton steel frame. Its integrated magnetic field value of $4\,\mathrm{Tm}$ has been chosen in order to accommodate the needs of the nearby subdetectors.

In order to cancel left-right detection asymmetries of the tracking that would affect the CP asymmetry measurements, the polarity of the magnet is inverted regularly during data taking. The magnet and the profile of the magnetic field along the z axis are shown in Fig. 2.6.
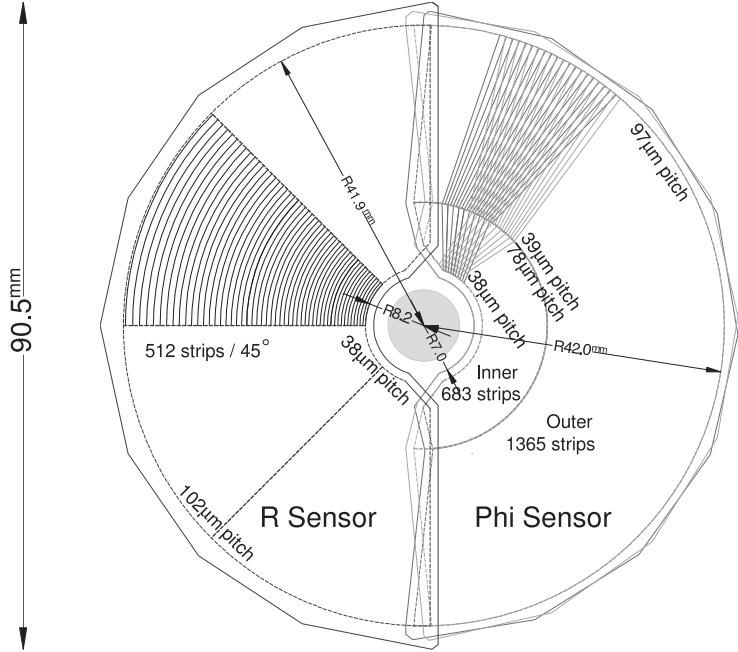
Figure 2.5   Schematic representation of the (r, ϕ) geometry of a VELO station during data collection.
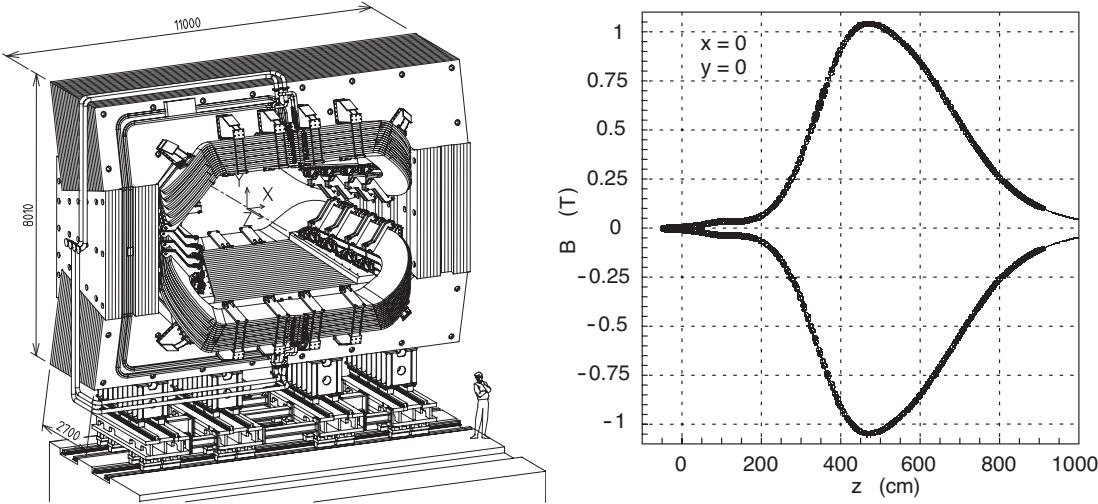
Figure 2.6   The LHCb magnet and the magnetic field profile along the z axis for both polarities.

Silicon Tracker

The Silicon Tracker (ST) is responsible for the detection of the hits of charged particles as they travel across the detector, after the VELO. Track hits are determined before and after the magnet by two silicon subdetectors, the TT and the IT respectively, both made of silicon microstrips sensors with a pitch of about $200\,\mu$m, allowing a spatial resolution of $\sim 50\,\mu$m. The silicon technology is chosen because of its very good resolution, signal-to-noise ratio and radiation tolerance, indispensable in the region close to the beam pipe because of the very high hit occupancy (5×10^{-2} per cm^2 in the TT and 1.5×10^{-2} per cm^2 in the IT for minimum bias events). Both TT and IT are requested to have a fast shaping time ($\sim 25\,$ns) to avoid the superposition of events from consecutive bunch crossings. The detectors are placed in light-tight insulated boxes, where the temperature is kept below $5°C$.

The TT (Fig. 2.7) is made of four $150 \times 130\,$cm^2 layers, organized in two stations separated by $27\,$cm along the beam axis, and covering a total active area of $8.4\,$m^2. In each station, the two layers are slightly tilted with respect to each other ($\pm 5°$ stereo angle) in order to allow a 2D hit position measurement.
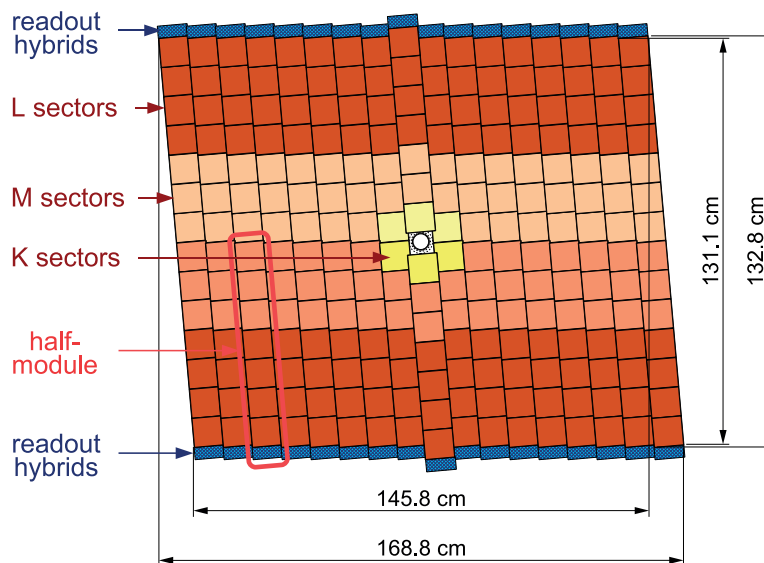
Figure 2.7   Layout of the stereo layer of a TT station.

The IT (Fig. 2.8) consists of four detector boxes arranged around the beam pipe to form a cross shape. The structure has three replica, that together with the OT form the T1–T3 tracking stations. Despite covering only 2% of the IT + OT area, the IT detects $\sim 20\%$ of the tracks because of the larger track density close to the beam. The detector boxes contain four detection layers, each of them made of seven detector modules. In order to minimize the material budget without compromising the tracking performance, a different design has been chosen for the detector modules according to their location: a single $320\,\mu$m-thick silicon sensor is placed in the top and bottom boxes, while two $410\,\mu$m-thick
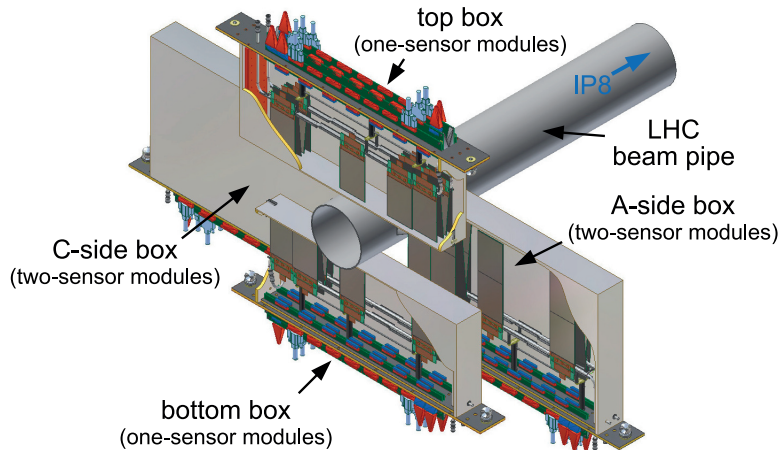
Figure 2.8 Structure of one of the IT stations.

sensors are placed in the side boxes. Each silicon sensor additionally contains a readout hybrid. With its mechanical supports, cooling pipes, readout hybrids and cables, the IT is responsible for most of the inactive material in the LHCb acceptance.

Outer tracker

The OT (Fig. 2.9) is a gaseous straw-tube detector that detects track hits by measuring the drift time of the ions freed when a charged particle goes through the tube. Its ~ 55000 tubes of $4.9\,\mathrm{mm}$ diameter are divided in three $6 \times 5\,\mathrm{m}^2$ panels surrounding the IT stations. The straw-tubes are filled with a mixture of Ar (70%) and CO_2 (30%), carefully chosen to provide a drift time below $50\,\mathrm{ns}$, a spatial resolution of $200\,\mu\mathrm{m}$, and resistance against aging. Each OT station consists of 72 modules, each made of two layers glued together to improve gas tightness. The tubes present a double-layer structure: an inner layer acts as cathode collecting the positive ions, while an outer layer provides shielding and fast signal transmission.

The OT spatial resolution is worse than the ST one. Anyway, straw tubes being much cheaper and easier to handle than silicon, they represent the best choice for covering large detector areas. Moreover, a higher resolution would not be needed because of the lower occupancy in the region occupied by the OT.
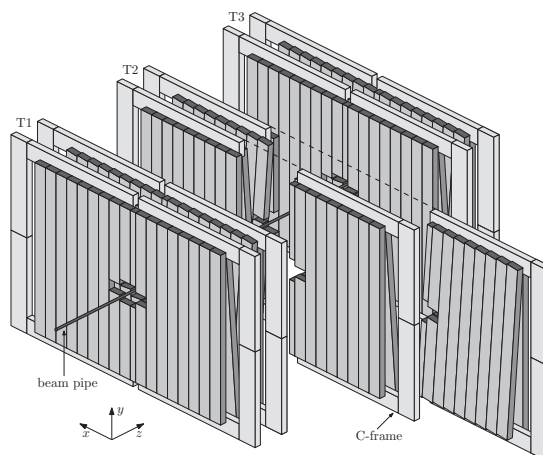
Figure 2.9   Arrangement of the OT subdetector modules.

2.1.2   Particle identification

Flavour physics relies on the ability of distinguishing the particles in the final state of a decay. The excellent particle identification (PID) performance of the LHCb experiment is guaranteed by two ring-imaging Cherenkov detectors (RICH), which identify charged hadrons, a calorimeter system consisting of a pad/preshower calorimeter (SPD/ PS), an electromagnetic (ECAL) and a hadron calorimeter (HCAL) for the identification of high momentum e, γ and π^0, and five muon chambers (M1–M5). The calorimeters also provide energy measurements, while the input from the muon chambers is crucial for the trigger.

Ring Imaging Cherenkov detectors

The main goal of the RICH detectors is to identify kaons, pions and protons. In addition, they complement the information from the ECAL and the muon chambers for the identification of charged leptons.

The RICH system is made of two subdetectors (Fig. 2.10), placed before and after the magnet, to detect particles in different angle and momentum ranges. They use the Cherenkov light produced by a charged particle travelling in a medium at a speed larger than the speed of light in that medium, to relate the light emission angle θ_c to its velocity v

$$\frac{v}{c} = \frac{1}{n \cos \theta_c} \tag{2.2}$$

where c is the speed of light in vacuum and n is the refraction index of the medium. A system of spherical and flat mirrors brings the Cherenkov light on a plane of photodetectors located outside of the acceptance, to reduce the material budget. The shape of the light ring, combined with the information from the tracking system, allows the determination of the particle mass.

The RICH1 subdetector, placed between the VELO and the TT, covers the low momentum
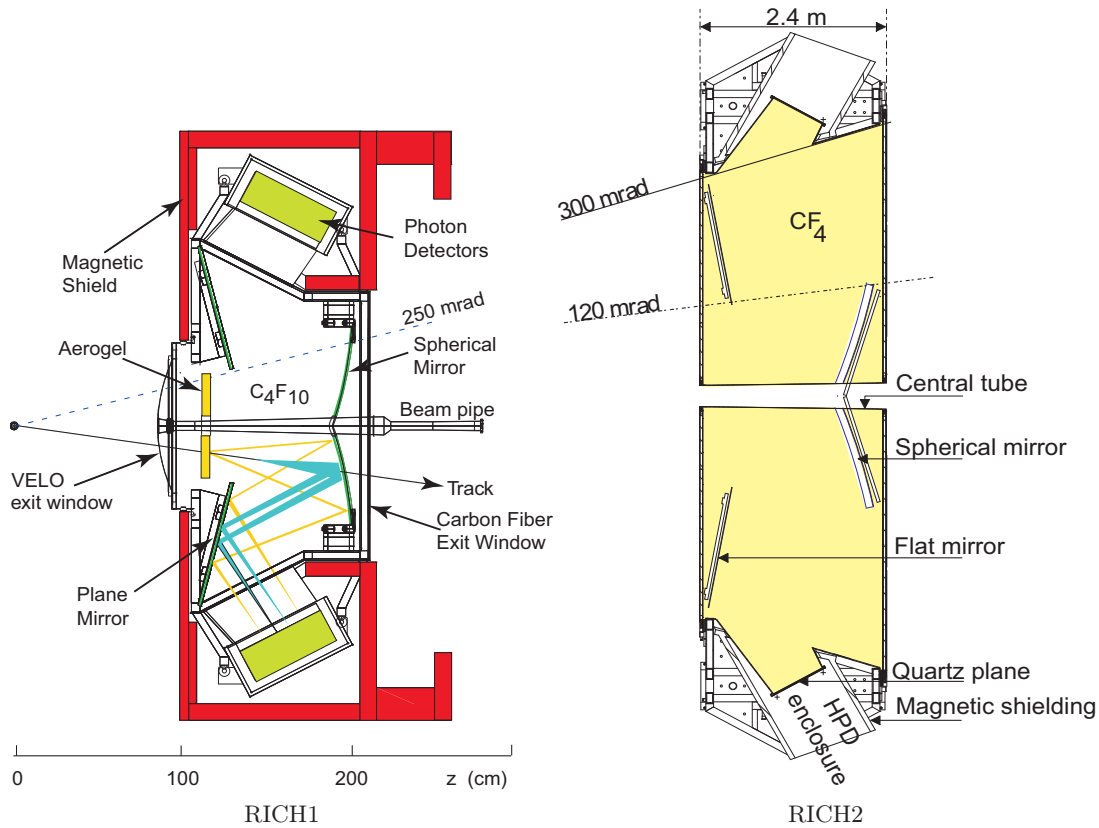
Figure 2.10 Layout of the RICH1 and RICH2 subdetectors.

range $(1 - 60\,\text{GeV}/c)$ and uses silicon aerogel tiles and C_4F_{10} gas as radiator media. The RICH2 subdetector is placed downstream of the magnet, between the T1–T3 trackers and the calorimeters, and covers the high momentum range $(> 15\,\text{GeV}/c)$ using CF_4 gas. The difference in density of the gases increases the discrimination power of the system, as shown in Fig. 2.11.

Averaging over particle momenta in the range $2 - 100\,\text{GeV}/c$, the RICH system provides a kaon detection efficiency of $\sim 95\%\,(85\%)$ at the cost of a $\sim 10\%\,(3\%)$ pion misidentification rate.
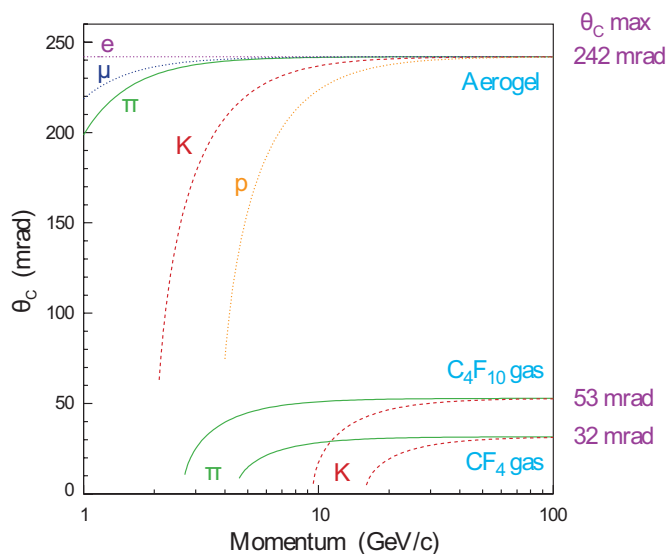
Figure 2.11   Cherenkov angle versus particle momentum for different media.

Calorimeter

The calorimeter system uses the data collected by the ECAL and the HCAL subdetectors, to measure the energy of the final state particles. Its information is needed for the identification of electrons, photons and π^0, and as input to the trigger.

The calorimeter technology exploits a sequence of heavy absorbers and scintillating tiles. The scintillation light produced by the charged particles of a shower is then transmitted to photomultipliers by wavelength-shifting fibres. The inner acceptance of the system, which starts at $\theta_{x,y} > 25$ mrad, is limited by the high radiation level in the beam pipe region, while the outer dimensions match projectively those of the tracking system ($\theta_x < 300$ mrad, $\theta_y < 250$ mrad).

Particles hitting the calorimeter deposit their energy in clusters of different shape. Charged and neutral particles are discriminated according to the existence of tracks pointing to the calorimeter in correspondence to the showers. For neutral particles, the shape of the cluster is used to distinguish between photons and π^0, while for charged particles specific algorithms are used to distinguish electrons from hadrons.

The ECAL (Fig. 2.12) is optimized for the detection of particles with transverse energy lower than 10 GeV: at larger energies the calorimeter response saturates. Its design energy resolution results in a B mass resolution of ~ 65 MeV/c^2 for $B \to K^* \gamma$ decays with high-E_T photons. This is achieved with a structure width of 25 radiation lengths, deep enough to fully contain the high-E_T photon showers, and three different surface segmentations, because of the varying occupancies in the different portions of the calorimeter.

The HCAL is a 500 ton, 5.6 radiation length structure located $13 - 15$ m from the interaction point. Its reduced depth does not allow a full reconstruction of the hadronic showers in the detector, affecting the overall energy resolution. The main characteristic of the HCAL is that its scintillating tiles are parallel to the beam axis (Fig. 2.13).
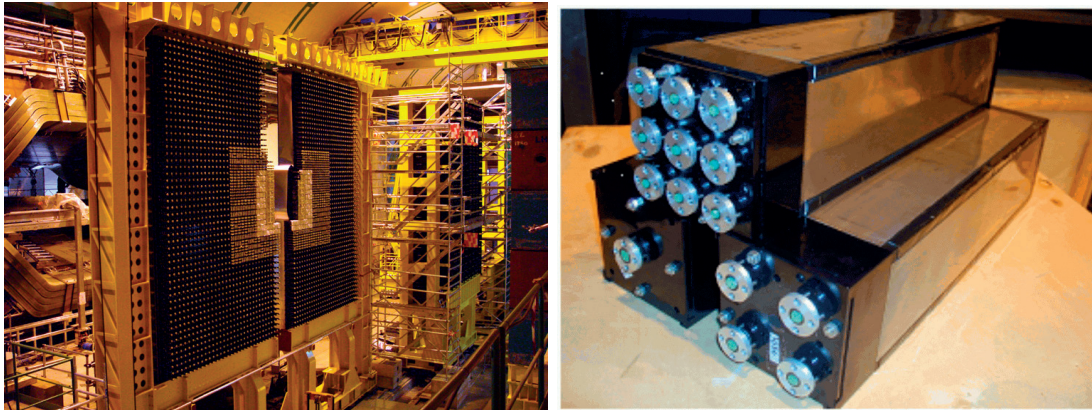
Figure 2.12   The ECAL subdetector during its assembly (left), and its three types of modules (right).
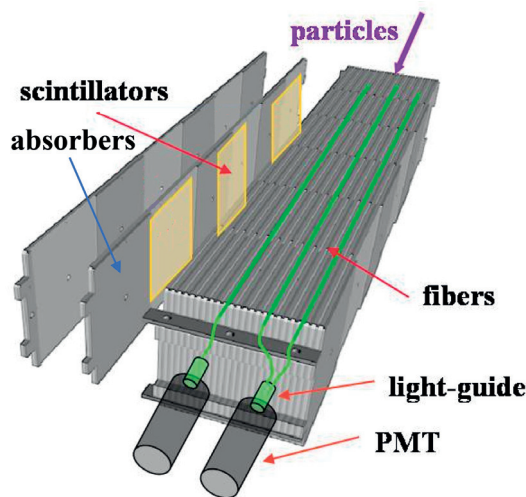
Figure 2.13   Schematic representation of the HCAL internal cell structure, with the scintillating tiles parallel to the beam axis.

Additionally, its cells are larger than the ECAL ones, and its surface is segmented in two different sections instead of three.

In order to reject background pions, a pre-shower (PS) detector is added in front of the ECAL, providing longitudinal segmentation for the detection of the electromagnetic showers. A scintillating detector (SPD) placed in front of the PS selects charged particles, identifying most of the high-E_{T} π^0 background. The full SPD/PS system has a depth of 2.5 radiation lengths, and shows the same segmentation as the ECAL.

The overall calorimeter system provides a photon detection efficiency of 95% while rejecting 45% of the merged π^0 background, consisting of π^0 decaying in two photons that form a single calorimeter cluster. Analogously, a $\sim 92\%$ identification efficiency for the electrons in $B^\pm \to K^\pm J/\psi (\to e^+e^-)$ decays is achieved at the cost of a $\sim 4.5\%$ misidentification rate.

Muon chambers

Being present in the final state of many rare decays of interest in the realm of flavour physics (*e.g.* $B_s^0 \to \mu^+ \mu^-$ and $B^0 \to K^{*0} \mu^+ \mu^-$), a performant muon identification system is fundamental for the LHCb experiment. The muon identification information is used in the trigger, as well as in the tracking reconstruction algorithms.

Muons are very penetrating particles, having a long lifetime and a low interaction probability, hence they traverse the full detector and they are identified in a system of five stations M1–M5 perpendicular to the beam located at the far end of the detector, just before (M1) and after (M2–M5) the calorimeters (Fig. 2.14).

The muon chambers are gaseous detectors, made of multi-wire proportional chambers (MWPC) containing a mixture of Ar (40%), CO_2 (55%) and CF_4 (5%), best suited to provide a fast time resolution (5 ns). The innermost part of M1 is made of three gas electron multipliers (GEM) chambers, with better radiation tolerance. The chambers are segmented, providing (x, y) information for the muon tracks hits used in the tracking. The stations M2–M5 are made of four active layers, separated by 80 cm thick iron plates acting as absorbers, so that only muons with momentum larger than 6 GeV/c are expected to reach the last station, while the M1 station has only two active layers.

The total efficiency for muon detection is larger than 95%.
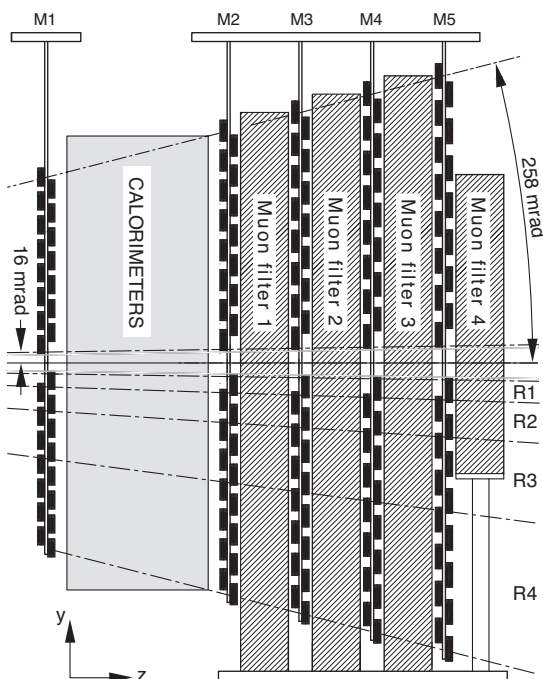
Figure 2.14   Schematic representation of the muon chambers.

55
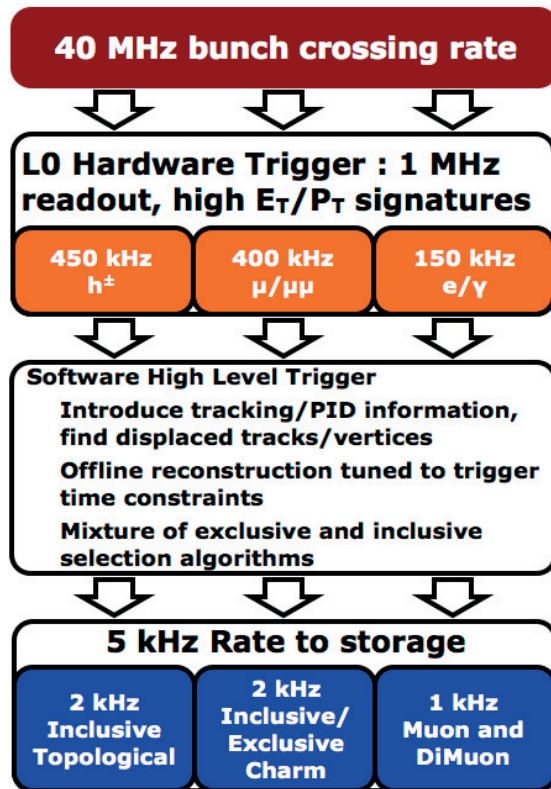
Figure 2.15   Schematic view of the LHCb trigger system in 2012.

2.1.3   Trigger

The trigger system [102, 103] consists of two levels, a hardware-based Level 0 (L0) and a software-based High Level Trigger (HLT), as shown in Fig. 2.15. The system design aims at reducing the event rate to a value below $5\,\mathrm{kHz}$, which allows storing and further processing of the data. The trigger selections have been stable during Run I data taking, with small modifications introduced to account for the changes in the running conditions between 2011 and 2012.

Level 0

The completely hardware-based L0 trigger uses the calorimeter and muon system information to reduce the rate to $1\,\mathrm{MHz}$, the largest rate at which the full detector can be readout. The calorimeter information is used to compute the transverse energy E_T associated with particle clusters, and build L0Hadron, L0Photon and L0Electron candidates. L0Hadron candidates correspond to clusters with high E_T in the HCAL, while L0Photon and L0Electron candidates are built from high-E_T ECAL clusters with one or two hits in the PS subdetector, the latter requiring an additional hit in the SPD subdetector. Events with too high SPD multiplicity are removed, because they would significantly slow down the following software stages. The muon system provides

the two muon tracks with the highest p_T in each quadrant from which `L0Muon` and `L0Dimuon` candidates are formed.

Given the detector design, the L0 trigger stage is not very efficient[1] for hadronic b decays $(40\% - 60\%)$, since only the calorimeter information is used. The efficiency is significantly higher for muonic final states ($\sim 90\%$).

High Level Trigger

Events passing L0 are forwarded to the online farm, where the software-based HLT further reduces the rate before the events are stored. The HLT is split in two levels: a HLT1 stage that provides fast partial event reconstruction, and a HLT2 stage where the complete reconstruction is made.

The inclusive single track HLT1 trigger, which represents the largest contribution (58 kHz) to the HLT1 bandwidth, efficiently selects high momentum track candidates that cannot be associated with any of the primary vertices in the event. Additional inclusive lines combine the L0 information from calorimeter clusters and muon chambers hits with tracking information to select electrons and photons (7 kHz), and muons (14 kHz), respectively. The remaining bandwidth is split between high-E_T jets, displaced vertices, diprotons, calibration, and technical lines. The HLT1 processes a L0 selected event in ~ 15 ms, with an average efficiency of $\sim 90\%$, before passing it to the HLT2 stage, where the reconstruction is refined.

Around 80 kHz of events reach the HLT2 stage, where time-expensive operations can be performed. As an example, the VELO vertex-finding algorithms used during the previous trigger stages are run again in the HLT2, including tracks with softer requirements. A large fraction of the HLT2 output rate (2 kHz) corresponds to events selected by *topological* lines, designed to retain b hadron decays also when not all the tracks in the decay are reconstructed. These inclusive n-body topological lines select any event with at least n tracks forming a displaced vertex, tracks and vertex being requested to satisfy certain quality requirements. Several HTL2 lines are dedicated to the detection of decays with one or more muons in the final state, corresponding to 1 kHz of bandwidth: single muons are selected only if they have a very large transverse momentum ($p_T > 10$ GeV/c), while softer requirements are enforced on dimuon candidates ($p_T > 2$ GeV/c). The charm trigger also accounts for a large HLT2 output rate. The very strong requirements applied to reduce the output rate of charm decays to 2 kHz significantly affect the channel-by-channel efficiency. The remaining HLT2 bandwidth is reserved for lower-rate exclusive lines designed to enhance the efficiency of channels that are not efficiently selected by the inclusive triggers.

Trigger performance

During Run I, the trigger has shown a very good performance with a total output rate of 5 kHz, despite running conditions much more challenging than what had been initially

---

[1]In this section, trigger efficiencies are normalized to the number of events in the corresponding offline-selected sample.

Table 2.1   Efficiencies of selected channels, normalized to the corresponding offline-selected samples, for 2012 trigger conditions [101].

Channel	L0	HLT1	HLT2
$B^+ \to J/\psi\,K^+,\ J/\psi \to \mu^+\mu^-$	89%	92%	87%
$B^0 \to K^+\pi^-$	53%	97%	80%
$B^0 \to D^+\pi^-,\ D^+ \to K^-\pi^+\pi^+$	59%	98%	77%
$D^+ \to K^-\pi^+\pi^+$	44%	89%	91%
$D^{*+} \to D^0\pi^+,\ D^0 \to K^-\pi^+\pi^-\pi^+$	49%	93%	30%

foreseen: the design luminosity of $2 \times 10^{32}\,\mathrm{cm}^{-2}\mathrm{s}^{-1}$, with an expected interaction rate of $10\,\mathrm{MHz}$ and mostly dominated by single interactions, was raised to $\sim 4 \times 10^{32}\,\mathrm{cm}^{-2}\mathrm{s}^{-1}$ causing the rate to increase and multiple interactions to dominate.

The Run I trigger efficiencies of a few selected channels are shown in Table 2.1.

2.2   Upgrade plans

In $2019-2020$, the LHC will go through a long shutdown during which the LHCb detector will be upgraded in order to allow an efficient collection of events at higher luminosity ($\mathcal{L} = 2 \times 10^{33}\,\mathrm{cm}^{-2}\mathrm{s}^{-1}$), with a full detector readout at $40\,\mathrm{MHz}$.

In the upgrade conditions, the current detector would not be efficient because of the higher occupancy, interaction rate and event multiplicity: the current trigger design cannot withstand such a rate, and the current subdetectors cannot cope with the higher occupancy that would cause a premature aging and a very inefficient data collection.

In order to face these problems, the LHCb detector will go through a series of deep modifications, like the rebuilding of the front-end electronics, the complete rethinking of the trigger (which will be fully software-based), and a change of technology for the tracking stations. Various consolidations of the existing subdetectors are also foreseen.

- The VELO detector resolution will be improved introducing $55 \times 55\,\mathrm{\mu m}^2$ silicon pixels. Its acceptance will also be extended, and the material budget will be reduced using thinner materials. A new radiation-hard readout chip will be introduced, designed to withstand up to $50\,\mathrm{fb}^{-1}$ of integrated luminosity.

- The upstream tracker will be moved closer to the beam pipe to improve its small-angle acceptance. Thinner silicon strip sensors will provide better hit resolution. The material budget will also be reduced.

- The current downstream tracker (T1–T3 stations) will be replaced with a scintillating fibre tracker covering the full acceptance, read out with silicon photomultipliers (SiPM).

- The RICH structure will remain unchanged, except for some modifications to the

RICH1 optical layout aimed at reducing hit occupancy. The aerogel radiator in the RICH1 will be removed.

- The SPD/ PS system will be removed, since simulations show that removing it will help rejecting more background with the same signal efficiency.

- The muon chamber M1 will be removed, and shielding will be installed around the beam pipe to reduce the occupancy in the other stations.

A detailed description of the foreseen detector upgrade can be found in Refs. [104–108].

3

Study of the $B^+ \to K^+\pi^-\pi^+\gamma$ signal

The $B^+ \to K^+\pi^-\pi^+\gamma$ decay has been studied in two stages, first using data collected in 2012, and then adding the 2011 sample. Different analysis strategies have been used according to the available statistics. In this Chapter, the analysis performed on the full LHCb Run I data sample is described in detail: after introducing the event selection strategy and discussing the description of signal and backgrounds, the unbinned extended maximum likelihood fit to the $K^+\pi^-\pi^+\gamma$ mass distribution performed to identify the signal is presented. Some relevant aspects that were studied only for the 2012 sample, such as the *CP* asymmetry, are reported in Appendix A.

3.1   Data samples

The full LHCb Run I data sample corresponds to an integrated luminosity of about 3 fb^{-1} of proton-proton collisions at $\sqrt{s} = 7$ and 8 TeV recorded with the LHCb detector during 2011 and 2012. With a measured inclusive $B^+ \to K^+\pi^-\pi^+\gamma$ branching fraction of $(2.8 \pm 0.2) \times 10^{-5}$ [89, 109, 110], taking into account acceptance, reconstruction and selection efficiencies, approximately 14 000 $B^+ \to K^+\pi^-\pi^+\gamma$ signal events are expected in a $K^+\pi^-\pi^+$ mass range of $[1, 2]$ GeV/c^2.

Monte Carlo (MC) simulated data generated with 2011 and 2012 conditions in the PYTHIA [111] simulation environment, have been used to study signal and background. All simulated events are truth-matched, meaning that the MC distributions obtained from signal events do not include any unwanted background (*e.g.* combinatorial). For signal studies, due to the lack of an inclusive MC simulation sample, simulations of the dominant $B^+ \to K_1(1270)^+\gamma$, $B^+ \to K_1(1400)^+\gamma$ and $B^+ \to K_2^*(1430)^+\gamma$ decays have been performed. Table 3.1 summarizes basic information on the MC simulation samples used for the studies described in this Chapter.

Table 3.1 Monte Carlo samples used for signal (upper section) and background (lower section) studies.

	MC production	Number of events
$B^+ \to K_1(1270)^+\gamma$	MC12	3.080×10^6
$B^+ \to K_1(1400)^+\gamma$	MC12	1.035×10^6
$B^+ \to K_2^*(1430)^+\gamma$	MC12	1.030×10^6
$B^+ \to \overline{D}^0(\to K^+\pi^-\pi^0)\pi^+$	MC11	0.110×10^6
$B^+ \to \overline{D}^{*0}(\to \overline{D}^0(\to K^+\pi^-)\gamma)\pi^+$	MC11	0.503×10^6
$B^0 \to K^{*0}\gamma$	MC11	7.551×10^6
$B^+ \to K^{*0}\pi^+\gamma$	MC11	2.013×10^6
$B^+ \to K^{*+}(\to K^+\pi^0)\pi^+\pi^-$	MC11	1.042×10^6
$B^0 \to K_1(1270)^0\gamma$	MC12	0.205×10^6
$B^+ \to K_1(1270)^+\eta$	MC12	0.358×10^6
$B^+ \to a_1^+(\to \pi^+\pi^-\pi^+)\gamma$	MC12	0.088×10^6

3.2 Event selection

Kaon resonances, decaying to three charged tracks, and high energy photons are used to build signal $B^+ \to K_{\mathrm{res}}^+\gamma \to K^+\pi^-\pi^+\gamma$ candidates. At first, three charged tracks with a total electric charge of $+1$ are combined to form the kaon resonance vertex. This resonance is then combined with a high-E_T photon to build a B^+ candidate.

Selected events are mainly triggered by the `Photon` and `Electron` L0 lines (accounting for $\sim 95\%$ of the sample), the `TrackAllL0` and `TrackPhoton` HLT1 lines (fired by $\sim 99\%$ of the events), and the radiative [112] (only in 2012) and regular topological [113] HLT2 lines. In this study, however, no trigger lines are explicitly required in order to maximise the sensitivity; it has been checked that the differences between using all triggered events and using only candidates firing specific HLT2 lines are well below the size of the statistical error.

The following sections show the selection stages applied to collected (triggered) events to obtain the final sample.

3.2.1 Event pre-selection (stripping)

Collected data are, at first, subject to a coarse selection, aimed at reducing the disk space and computational power for the following steps. The `Radiative` stripping stream, processed with the Stripping S20r1 and S20r0p1 configurations for 2011 and 2012 data respectively, is used. More precisely, the selected candidates pass the `B2K1Gamma_B2VG` line selection requirements, which reconstruct $B^+ \to K_{\mathrm{res}}^+\gamma \to K^+\pi^-\pi^+\gamma$ decays with very soft PID cuts.

The main selection requirements applied at stripping level are listed in Table 3.2 and are

Table 3.2 `B2K1Gamma_B2VG` stripping line selection requirements for the charged tracks (first and second sections), the kaon resonance (third section), the photon (fourth section) and the B^+ candidate (last section).

Variable	Requirement	Unit
Track p_T	> 350	MeV/c
Track p	> 2000	MeV/c
Track χ^2	< 3	
Track IP χ^2	> 16	
Track ghost probability	< 0.4	
π DLL$_{K-\pi}$	< 20	
K DLL$_{K-\pi}$	> -10	
Resonance tracks DOCA	< 0.5	mm
Resonance tracks $\sum p_T$	> 1500	MeV/c
Resonance vertex χ^2	< 20	
Resonance IP χ^2	> 64	
Resonance mass window	$[800, 3500]$	MeV/c^2
Photon E_T	> 2500	MeV
Photon CL	> 0.25	
Photon and tracks $\sum p_T$	> 5000	MeV/c
B^+ vertex χ^2	< 9	
B^+ IP χ^2	< 9	
B^+ DIRA	> 0.9998	
B^+ mass window	$[4000, 7000]$	MeV/c^2

described below.

- Minimum momentum p and transverse momentum p_T requirements are used to reject low momentum combinatorial background.

- The impact parameter (IP) χ^2 establishes the compatibility of a particle with the PV; this cut is used to ensure that the B meson comes from the PV and the other particles do not.

- Vertex quality criteria ensure that the χ^2 of the decay vertex fit is small.

- Track ghost probability requirements remove tracks wrongly reconstructed from random hits in the tracking subdetectors.

- PID requirements use the RICH information to discriminate between two different particles hypotheses (*e.g.* kaons and pions) using the difference of the logarithm of their likelihoods (DLL).

- A maximum value is set for the distance of closest approach (DOCA) between the directions defined by the momenta of the tracks.

- Photons are requested to be *hard*, applying a minimum transverse energy E_T requirement.

- The photon confidence level (CL) uses the calorimeter information to assign a certain probability for the photon to be correctly reconstructed. It is calculated as

$$CL = \frac{\tanh(\gamma\, DLL_{\gamma-e}) + 1}{2}\,, \tag{3.1}$$

  where $\gamma\, DLL_{\gamma-e}$ is the difference of the logarithm of the likelihoods for the photon and electron hypotheses provided by the calorimeter [114].

- The cosine of the angle between the reconstructed momentum of the B candidate and the direction defined by the vector from the PV to the decay vertex of the B (DIRA) is constrained to separate signal from partially reconstructed backgrounds. A signal event is characterized by a DIRA very close to one, the two directions being parallel because the B comes from the PV. For partially reconstructed events, instead, the angle is different from zero since the non reconstructed daughters cause the reconstructed momentum not to be parallel to the direction of flight.

3.2.2 Offline event selection

In order to obtain the final analysis sample, stripped data are subject to a further selection step, removing most of the combinatorial background. This offline selection consists of a cut-based set of criteria, followed by a multivariate (MVA) selection.

Cut-based selection

In the cut-based offline selection, a further photon calibration—with more precise calibration constants—is applied and several of the stripping cuts are tightened. Specially significant is the increase of the photon E_T cut, which is introduced in order to avoid border effects due to the calorimeter energy post-calibration, in analogy to the L0 photon threshold.

Several new requirements are introduced:

- A vertex isolation is used to remove partially reconstructed B decays in which one charged particle has not been reconstructed. Each track in the event is combined with the resonance vertex and the χ^2 of the new vertex is computed. A cut is then applied on the difference between the original χ^2 and the minimum χ^2 of all vertex+track combinations.

- A γ/π^0 separation criterion is applied by means of a multivariate tool which takes into account the different geometry of the electromagnetic showers in the ECAL and PS detectors: most of the time, a π^0 with $p_T > 4\,\text{GeV}/c$ decays in two photons that form a single calorimeter cluster, faking a photon signal; the algorithm distinguishes

Table 3.3 $B^+ \to K^+\pi^-\pi^+\gamma$ offline selection cuts, applied on top of the Stripping requirements detailed in Table 3.2. Track cuts are listed in the first and second sections, followed by cuts on the $K^+\pi^-\pi^+$ system, the photon and the B^+ candidate; the last two sections are the mass cuts to remove $\overline{D}^0$ and ρ^+ backgrounds and the fiducial cut.

Variable	Requirement	Unit
Max track p_T	> 1200	MeV/c
Min track p_T	> 500	MeV/c
$K\,\mathrm{Prob}(K) \times (1 - K\,\mathrm{Prob}(\pi))$	> 0.2	
$\pi^+\,\mathrm{Prob}(\pi^+) \times (1 - \pi^+\,\mathrm{Prob}(K))$	> 0.2	
$\pi^-\,\mathrm{Prob}(\pi^-) \times (1 - \pi^-\,\mathrm{Prob}(K))$	> 0.2	
$K^+\pi^-\pi^+$ vertex isolation $\Delta\chi^2$	> 2	
$m_{K^+\pi^-\pi^+}$ mass window	$[1100, 1900]$	MeV/c^2
Photon E_T	> 3000	MeV
Photon CL	> 0.25 and $\neq 0.5$	
Photon/π^0 separation	> 0.6	
$B\ p_\mathrm{T}$	> 2500	MeV/c
$K^+\pi^-\pi^0$ mass	> 2000	MeV/c^2
$\pi^+\pi^0$ mass	> 1100	MeV/c^2
Fiducial cut on $|p_x|$	$\leq 0.317(p_z - 2400)$	MeV/c

γ from π^0 because clusters coming from the latter are expected to be more elliptical than spherical, their energy being concentrated in two different focal points.

- The photon CL is asked to be different from 0.5, because, as seen from Eq. 3.1, CL $= 0.5$ when $\mathrm{DLL}_{\gamma-e} = 0$, a condition met every time the calorimeter PID variable fails to be evaluated. Candidates with this CL value are thus removed.

- The $K^+\pi^-\pi^+$ mass spectrum is reduced to the range $1100 < m_{K\pi\pi} < 1900$ MeV/c^2 due to the lack of signal outside this region (Fig. 3.1). Future analyses will profit from softer stripping cuts on the momenta that are expected to increase the statistics at low $K^+\pi^-\pi^+$ masses.

- Additional PID requirements are introduced, combining the RICH and tracking information to determine the probability for a charged track to be a π or a K.

- The magnetic field breaks the left-right symmetry of the detector because it bends positive and negative particles in opposite directions, providing them a horizontal momentum kick of ~ 1.25 GeV/c [115]. This effect causes tracks with low momentum moving in certain directions to leave the detector acceptance for a given magnet polarity, leading to a charge-dependent acceptance of the detector. Regions with 100% charge asymmetry appear at the lower edge of the momentum distributions. This effect has been studied carefully for the $D^0 \to h^+h^-$ decay [115], where, using
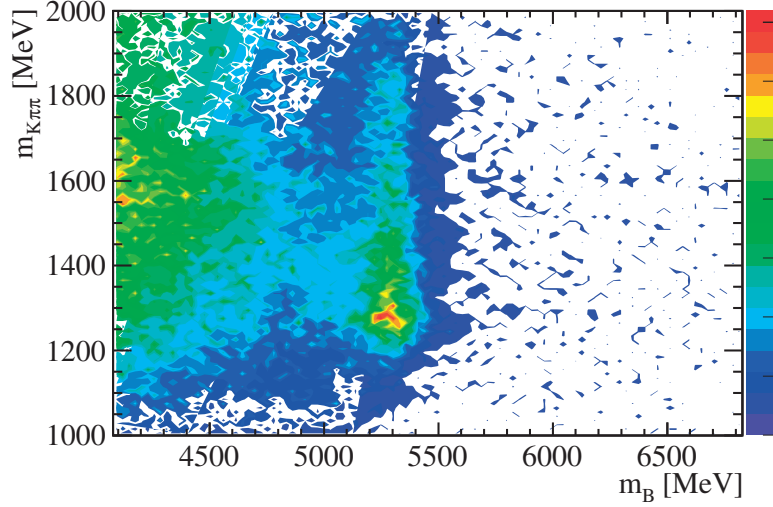
Figure 3.1 B-mass-constrained $m_{K^+\pi^-\pi^+}$ as a function of the mass of the $K^+\pi^-\pi^+\gamma$ system for 2012 data. It can be seen that removing the candidates outside the $1100 < m_{K^+\pi^-\pi^+} < 1900$ MeV/c^2 mass range improves the signal over background ratio.

a model of the magnetic field, a fiducial cut was defined as

$$|p_x| \leq \alpha(p_z - p_0),\qquad(3.2)$$

where p_x and p_z are the momenta along the x and z axis of the detector system, $\alpha = 0.317$ and $p_0 = 2400$ MeV/c. This fiducial cut, the effects of which are shown in Fig. 3.2, has been applied only when the B^+ and B^- candidates are fitted separately (App. A and B).

- Because of its large branching fraction, the $B^+ \to \overline{D}^0\rho^+$ decay constitutes a potentially dangerous partially reconstructed background when $\rho^+ \to \pi^+\pi^0$ and $\overline{D}^0 \to K^+\rho^-(\to \pi^-\pi^0)$, with a π^0 meson misidentified as a γ. The vertex isolation criterion does not help removing this background because the missing particle is neutral, hence, additional mass cuts are introduced (Table 3.3):

  1. In case the π^0 from the $\overline{D}^0$ is lost and the π^0 from the ρ^+ is misidentified as a γ, the $\pi^+\gamma$ mass with the γ reconstructed as a π^0 will peak at the ρ mass (Fig. 3.3). Requiring the $\pi^+\pi^0$ mass to be above the ρ mass is very effective in rejecting this background, without affecting the signal, as seen in simulated data (Fig. 3.3).

  2. When the π^0 from the ρ^+ is lost and the π^0 from the $\overline{D}^0$ is misidentified as a γ, the $K^+\pi^-\gamma$ mass spectrum with γ reconstructed as a π^0 is expected to peak at the $\overline{D}^0$ mass (Fig. 3.4). In Fig. 3.5 some ρ^- can be observed in the $\pi^-\pi^0$ mass spectrum: requiring the $K^+\pi^-\pi^0$ mass to be above the D^0 mass removes this background; also this requirement does not affect the signal (Fig. 3.4).

Magnet up

Magnet down
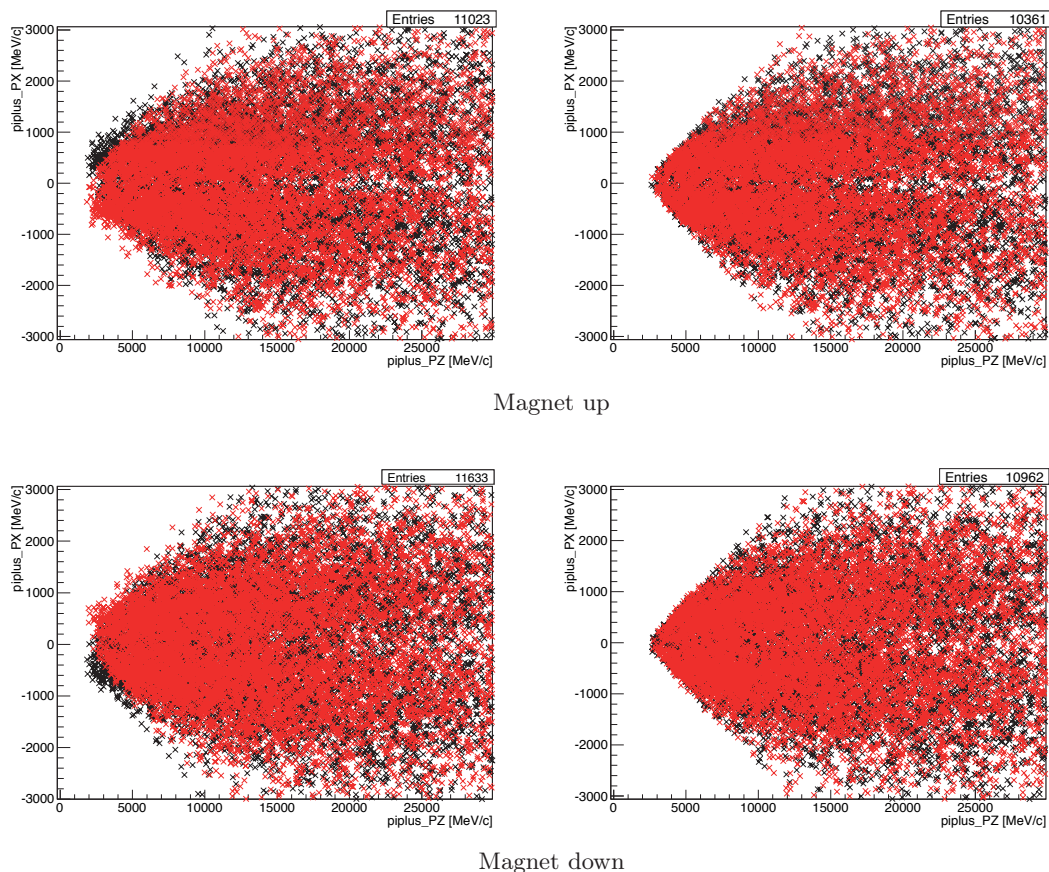
Figure 3.2 p_x versus p_z for the π^+ track of $B^+ \to K^+\pi^-\pi^+\gamma$ candidates (black) and for the π^- track of $B^- \to K^-\pi^+\pi^-\gamma$ candidates (red) before (left) and after (right) the fiducial cut for up (top) and down (bottom) magnet configurations in the full 2012 dataset. The artificial asymmetry between the number of B^+ and B^- decays is evident at low p_z.
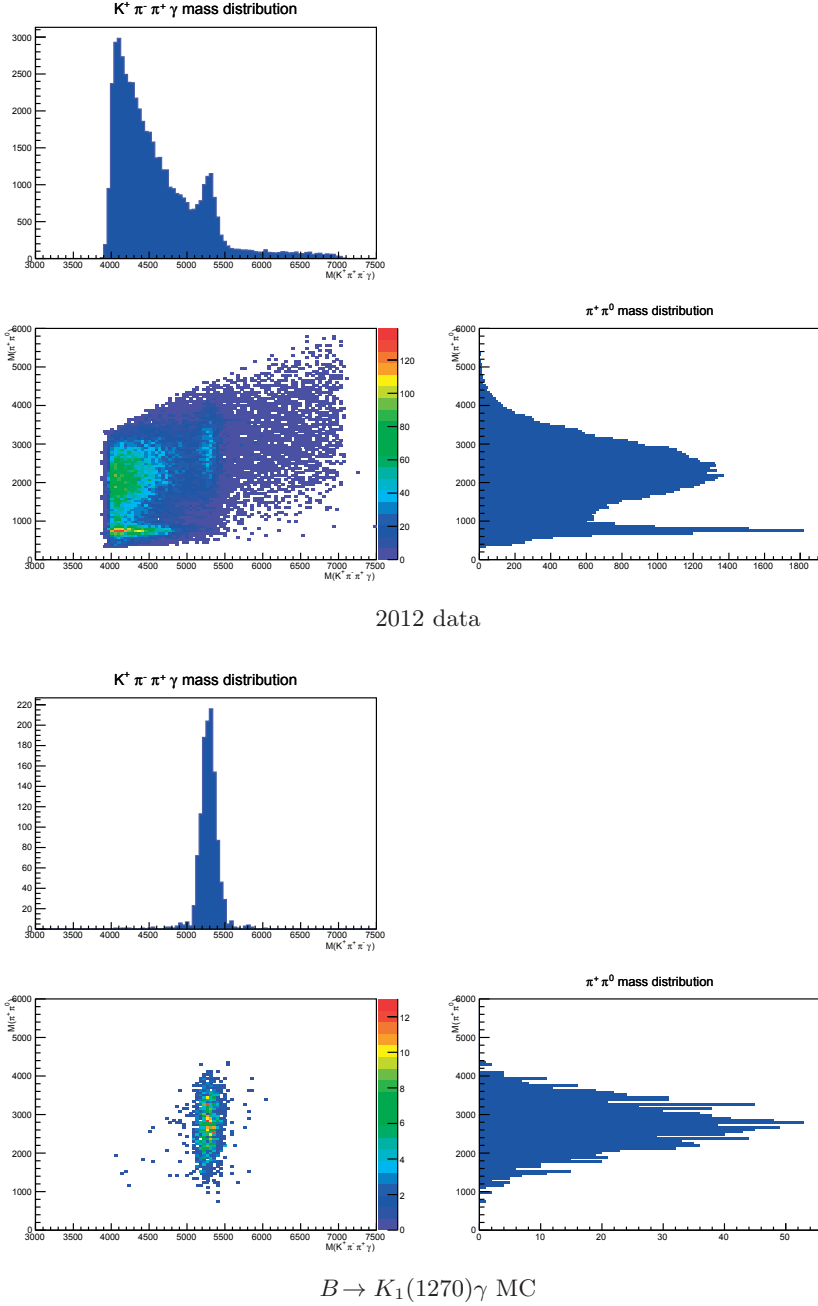
67

Figure 3.3 $\pi^+\gamma$ (with γ reconstructed as π^0) vs $K^+\pi^-\pi^+\gamma$ mass distribution for data (top) and signal MC (bottom). In the data, a peak corresponding to the ρ^+ can be observed in the $\pi^+\pi^0$ distribution. Credits to Ref. [116].
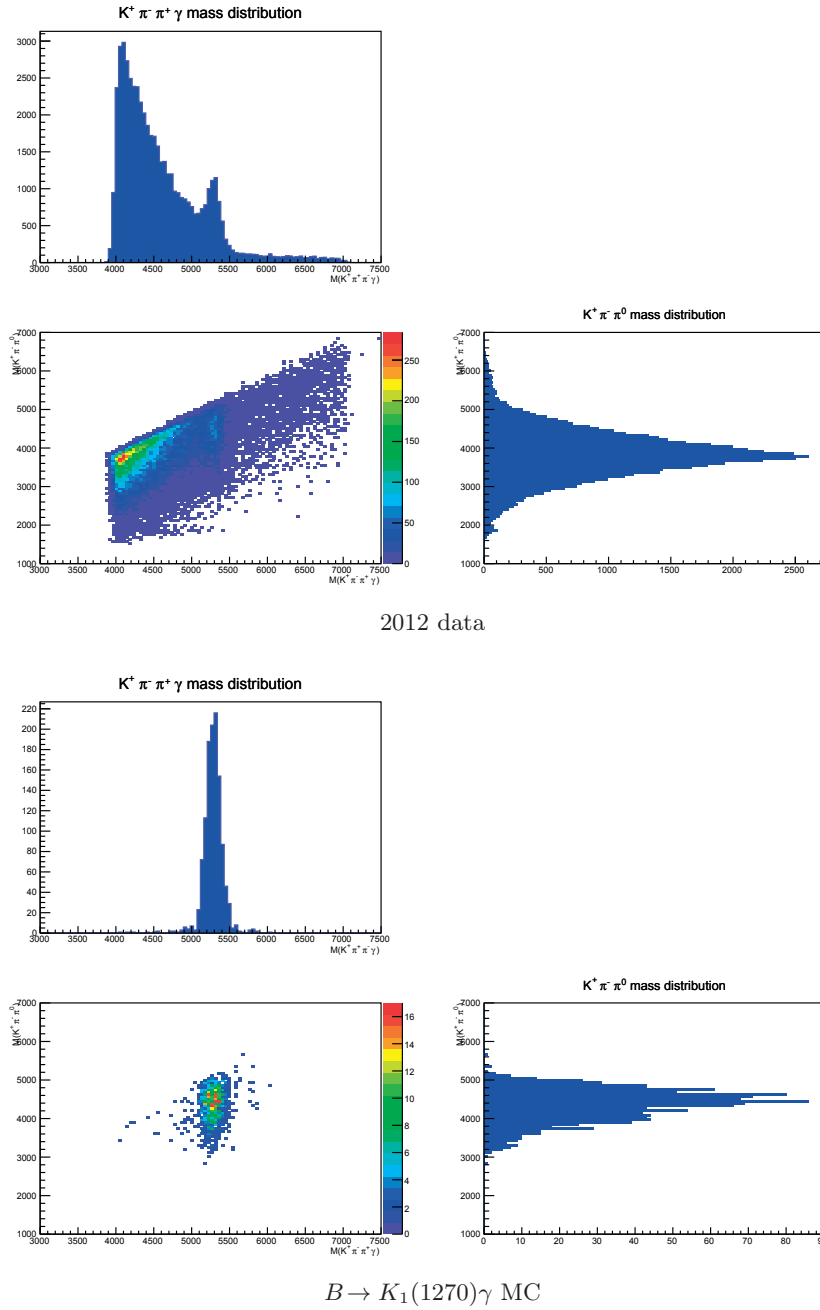
68

2012 data

$B \to K_1(1270)\gamma$ MC

Figure 3.4 $K^+\pi^-\gamma$ (with γ reconstructed as π^0) vs $K^+\pi^-\pi^+\gamma$ mass distribution for data (top) and signal MC (bottom). In the data, a small peak corresponding to the $\overline{D}^0$ can be observed in the $K^+\pi^-\pi^0$ distribution. Credits to Ref. [116].
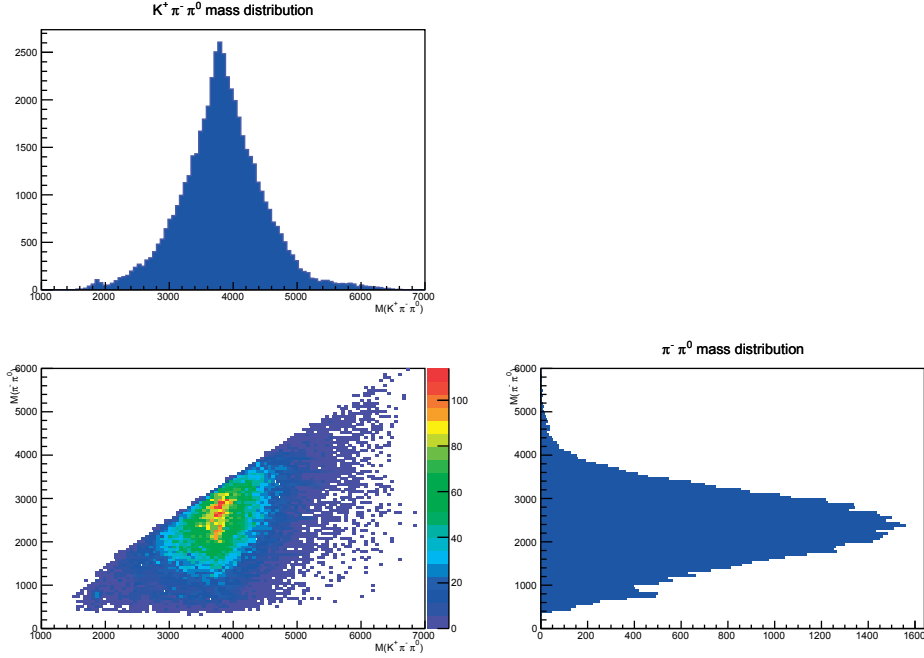
Figure 3.5 $\pi^-\gamma$ vs $K^+\pi^-\gamma$ mass distribution, with γ reconstructed as π^0, for 2012 data, showing the correlation of the $\bar{D}^0$ peak from Fig. 3.4 with the small peak at the ρ^- mass in the $\pi^-\pi^0$ plot. Credits to Ref. [116].

A summary of the offline pre-selection, applied after the stripping selection, is given in Table 3.3.

Multivariate selection

After the cut-based selection, a MVA selection is implemented to further separate signal and background events. With its high discriminating power, speed, and robustness to overtraining, a boosted decision tree (BDT) [117,118] represents the best choice for our needs. The BDT is trained, optimised and applied following the scheme of Fig. 3.6:

1. The pre-selected 3 fb^{-1} data sample and the signal MC sample are randomly divided in two equal-sized subsamples $A0$ and $A1$: data sidebands ($|m_B - 5279.0| > 200$ MeV/c^2) are used for describing the background and a mixture of different $B^+ \to K^+_{\mathrm{res}}\gamma$ MC decays are used for the signal;

2. 2/3 of each subsample ($B0$) are used for training and testing the BDT;

3. the remaining third ($B1$) is used to select the BDT response cut that maximises the signal significance;

4. the BDT weights obtained on the sample $A0$ are then applied to the other sample $A1$ and vice versa. This avoids possible sources of bias without removing any data.
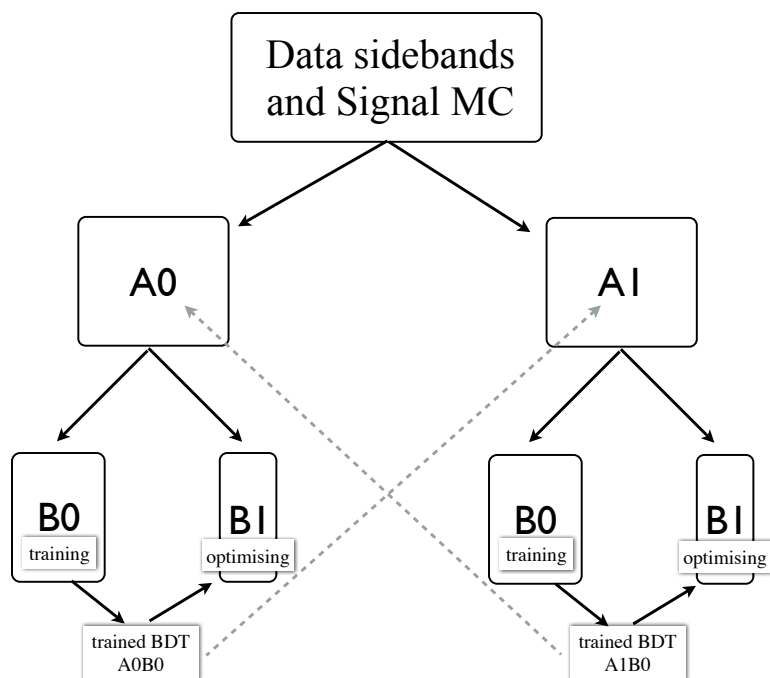
Figure 3.6   Scheme used to train and optimise the BDT. The sidebands of the pre-selected
data sample and the signal MC sample are divided in two subsamples $A0$ and $A1$;
$2/3$ of each subsample ($B0$) are used for training and testing, and the remaining
$1/3$ ($B1$) is used for selecting the BDT response cut that optimises the signal
significance. The BDT response cut found from the initial sample $A0$ is applied
to the sample $A1$, and vice versa.

The variables included in the BDT are the IP χ^2 of the tracks and of the B^+ candidate,
the B^+ DIRA, the B^+ flight distance χ^2 and the resonance vertex χ^2, whose distributions
for data and MC are shown in Fig. 3.7. These variables show the best discrimination
power between signal and background (Fig. 3.8). Other variables, even if showing a good
discrimination power like the γ/π^0 separation variable, are not used for the training,
because they are not well described in the MC and could lead to an incorrect training.

For all the BDT training variables except the resonance vertex χ^2, the logarithm of the
variable has been used instead of the variable itself.

Figure 3.9 shows the BDT response, with the separation between signal and background.
From the signal significance optimisation, the optimal cut for the BDT response is found
to be > -0.19 and > -0.18 for the two subsamples respectively.
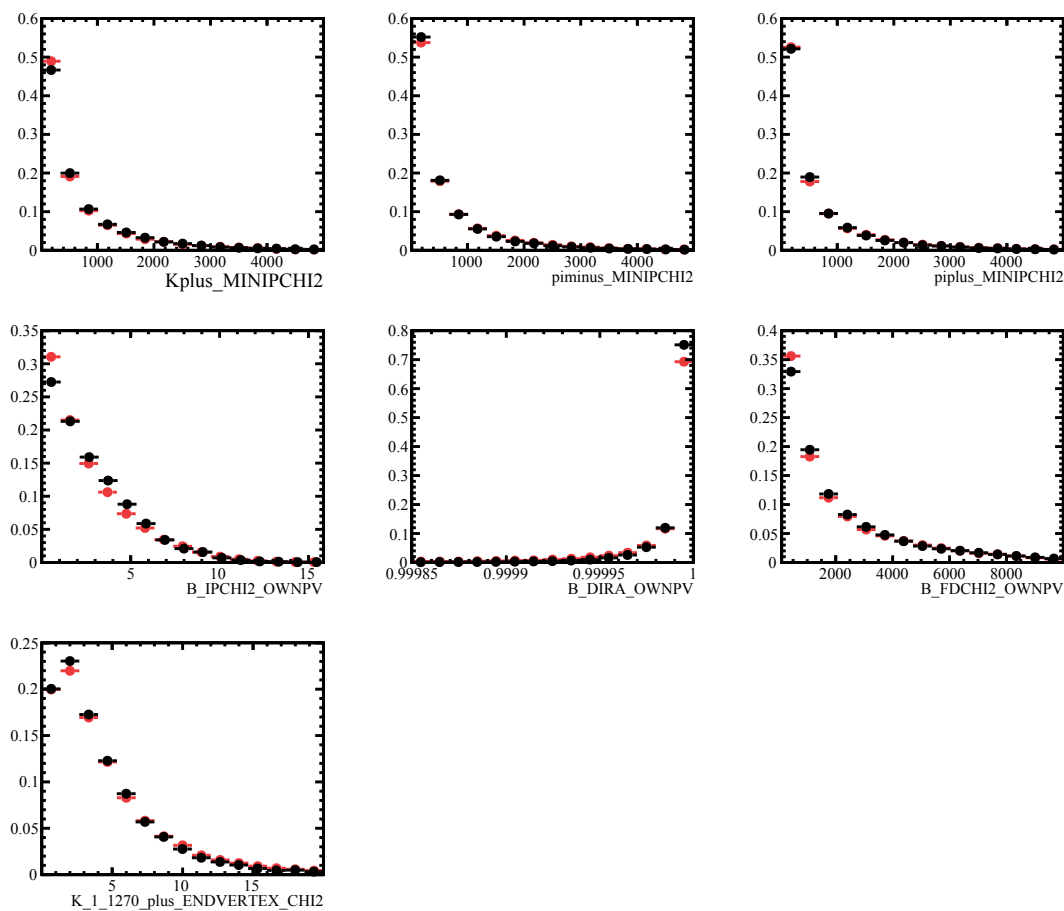
Figure 3.7 Normalised distributions of the BDT training variables (the tracks and B^+ IP χ^2, the B^+ DIRA, the B^+ flight distance χ^2 and the resonance vertex χ^2) for data (black) and signal MC (red).
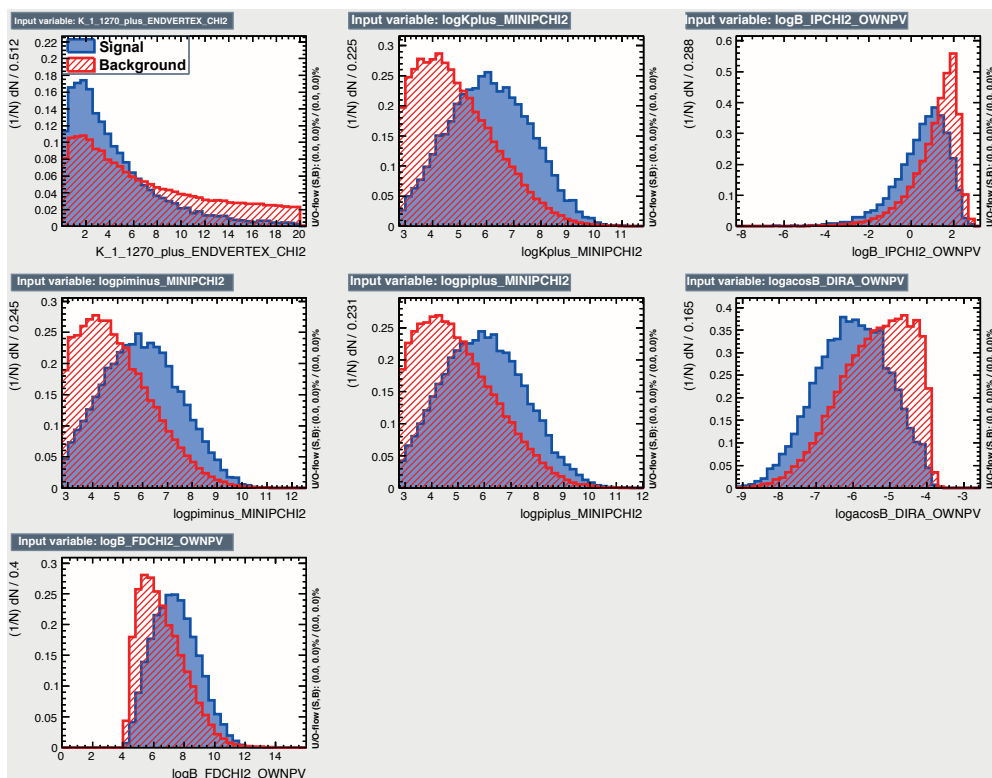
Figure 3.8   Signal (blue) and background (red) distributions of the BDT training variables (the resonance vertex χ^2, the tracks and B^+ IP χ^2, the B^+ DIRA, and the B^+ flight distance χ^2). For most of the variables, the logarithm of their value has been used instead of the values themselves, making the difference between signal and background more evident.
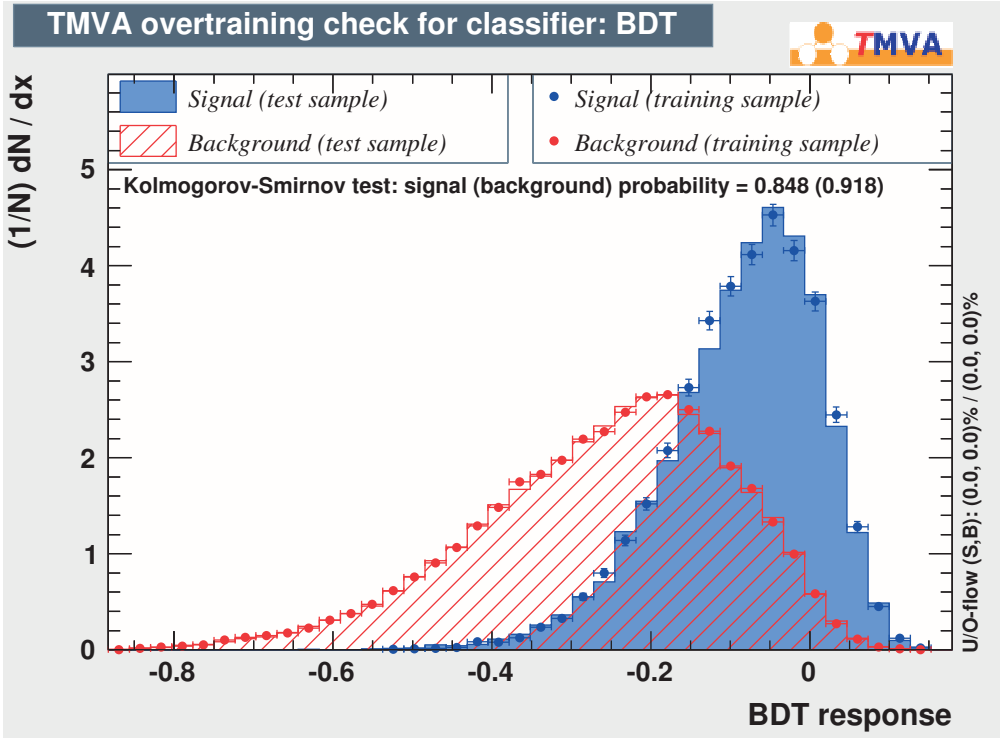
Figure 3.9   Distributions of the BDT output for signal (blue) and background (red) for one of the two subsamples. The training and test samples are overlaid. From the signal significance optimisation, the optimal cuts on the BDT output are found to be > -0.19 and -0.18 for the two subsamples.

3.2.3 Selection efficiency as a function of $\cos\tilde{\theta}$

The overall acceptance effect due to reconstruction and selection is determined from simulation in order to assess whether an artificial asymmetry is introduced in the distribution of the photon angle $\tilde{\theta}$. Figure 3.10 shows the efficiency for the B candidates in bins of $\cos\tilde{\theta}$ for the $K_1(1270)^+\gamma$ MC sample normalised to unity. The acceptance effect induced by the selection is accounted for in the fits described in the following sections. Using the $K_1(1400)^+\gamma$ and $K_2^*(1430)^+\gamma$ MC samples for the determination of the acceptance yields compatible results.

It has been checked that the discrepancies observed between data and MC in Fig. 3.7 lead to negligible effects on the acceptance.
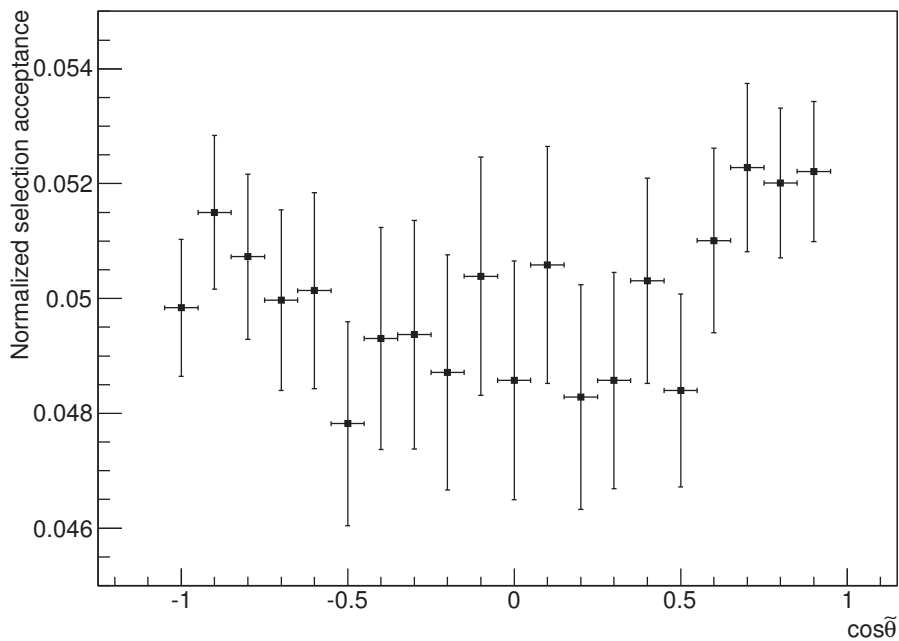
Figure 3.10   Normalised selection acceptance for the B candidates as determined from the $K_1(1270)^+\gamma$ simulated sample in bins of $\cos\tilde{\theta}$.

3.3 Signal study

The shape of the $K^+\pi^-\pi^+\gamma$ mass distribution for the signal is studied using the $B^+ \to K_{res}^+\gamma$ MC samples introduced in Sec. 3.1. After applying the selection described in Sec. 3.2, the resulting B^+ mass distribution is fitted using a double-tail Crystal Ball function with tails below and above the B mass,

$$CB(m;\mu,\sigma,\alpha_L,n_L,\alpha_R,n_R) = N \begin{cases} A_L\left(B_L - \frac{m-\mu}{\sigma}\right)^{-n_L}, & \text{for } \frac{m-\mu}{\sigma} \leq -\alpha_L \\ \exp\left(-\frac{(m-\mu)^2}{2\sigma^2}\right), & \text{for } -\alpha_L < \frac{m-\mu}{\sigma} < \alpha_R \\ A_R\left(B_R + \frac{m-\mu}{\sigma}\right)^{-n_R}, & \text{for } \frac{m-\mu}{\sigma} \geq \alpha_R \end{cases}$$

(3.3)

where μ and σ are the signal mean and resolution, α_L, α_R, n_L and n_R must be positive, N is a normalisation factor and

$$A_i = \left(\frac{n_i}{\alpha_i}\right)^{n_i} \exp\left(-\frac{\alpha_i^2}{2}\right),$$

(3.4)

$$B_i = \frac{n_i}{\alpha_i} - \alpha_i.$$

(3.5)

The results for $K_{res}^+ = K_1(1270)^+$, $K_1(1400)^+$ and $K_2^*(1430)^+$ are shown in Table 3.4 and Figs. 3.11–3.12. The shape parameters are reasonably consistent. Since the $K_1(1270)$ resonance is expected to be the leading contribution to the $K^+\pi^-\pi^+$ mass spectrum, it has been decided to use the parameters obtained from the $B^+ \to K_1(1270)^+\gamma \to K^+\pi^-\pi^+\gamma$ MC fit for describing the signal in the data.

Table 3.4 Fitted parameters of the double-tail Crystal Ball function describing the mass distribution of $B^+ \to K_{res}^+\gamma \to K^+\pi^-\pi^+\gamma$ MC decays.

Parameter	$K_1(1270)^+$	$K_1(1400)^+$	$K_2^*(1430)^+$	Unit
μ	5280.0 ± 0.7	5281.3 ± 1.4	5278.8 ± 1.5	MeV/c^2
σ	85.4 ± 0.7	86.5 ± 1.3	83.9 ± 1.4	MeV/c^2
α_L	2.21 ± 0.05	2.39 ± 0.10	2.35 ± 0.10	
α_R	1.58 ± 0.05	1.59 ± 0.11	1.39 ± 0.10	
n_L	1.41 ± 0.13	1.04 ± 0.19	1.16 ± 0.21	
n_R	7.6 ± 1.1	6.1 ± 1.5	13.0 ± 5.6	
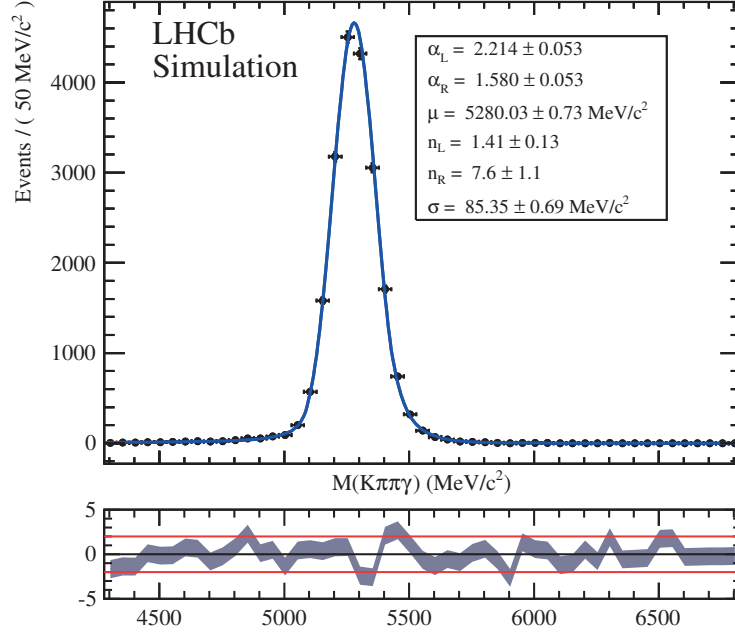
Figure 3.11   Mass distribution of $B^+ \to K_1(1270)^+\gamma \to K^+\pi^-\pi^+\gamma$ MC decays. The result of the fit to a double-tail Crystal Ball function is superimposed.
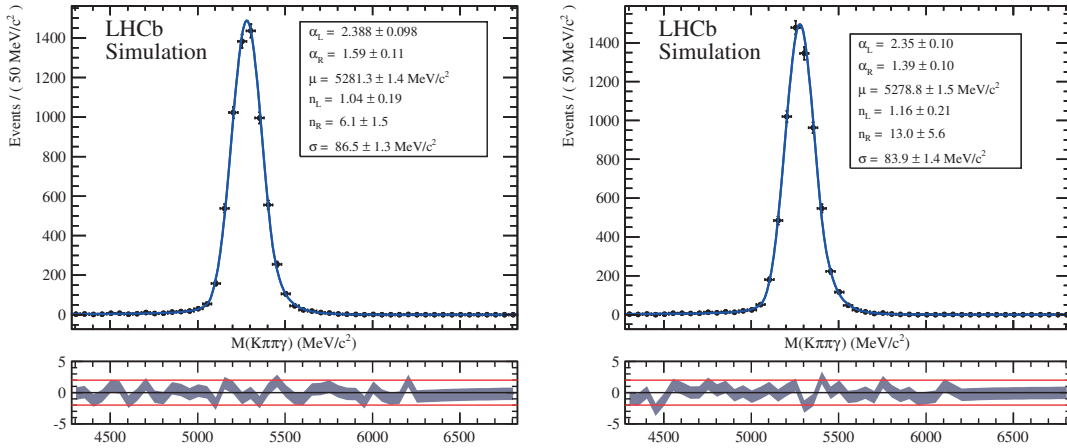
Figure 3.12   Mass distribution of $B^+ \to K_1(1400)^+\gamma \to K^+\pi^-\pi^+\gamma$ (left) and $B^+ \to K_2^*(1430)^+\gamma \to K^+\pi^-\pi^+\gamma$ (right) MC decays. The results of the fit of a double-tail Crystal Ball function are superimposed.

3.3.1 Double misidentification of same-sign K and π

Due to the relatively soft particle identification cuts applied on pions and kaons (Table 3.3), some signal events might have been selected with a double misidentification of the same-sign K and π, *i.e.*, the true K^+ (K^-) is identified as a π^+ (π^-) and, at the same time, the true π^+ (π^-) is misidentified as a K^+ (K^-). This misidentification may cause a wrong calculation of $\cos\tilde{\theta}$, since, as discussed in Sec. 1.2.2, the direction of the $K^+\pi^-\pi^+$ plane is defined by the momenta of the two pions. Moreover, it is also possible that both candidates—the one with and the one without double misidentification—are selected, leading to at least two candidates in the event.

The probability of double misidentification has been evaluated using the `PIDCalib` package [119] and found to be 1%. In the 2012 dataset, with a signal of about 8000 events, it is therefore expected to have ~ 80 of these events. The software determines also the probability of having multiple candidates in the event due to double misidentification, found to be half of the double misidentification probability. This is consistent with what is observed in data, where 44 events with multiple candidates are found in a ± 200 MeV/c^2 mass window around the B mass. In order to decrease the impact of these events, it is chosen to remove all events with multiple candidates, a total of 690 in the full mass region, the mass distribution of which is shown in Fig. 3.13.
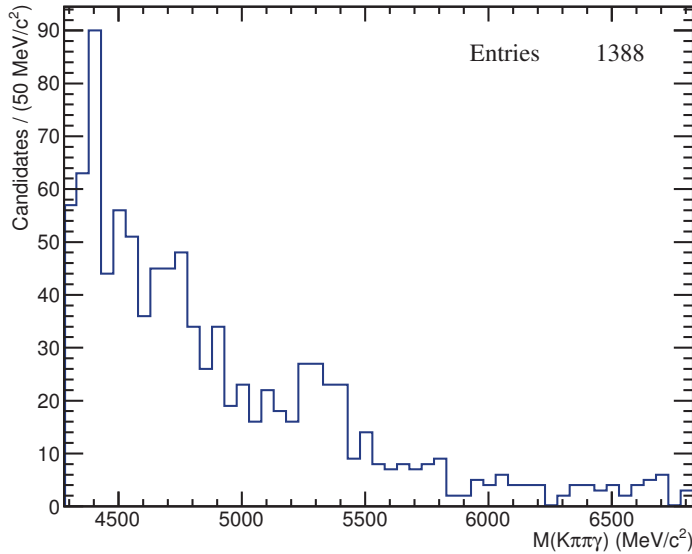
Figure 3.13   Mass distribution of selected $K^+\pi^-\pi^+\gamma$ combinations in the 2012 data sample corresponding to events with multiple candidates.

3.4 Background studies

In this section the possible background contributions to the B mass spectrum of $B^+ \to K^+\pi^-\pi^+\gamma$ candidates are presented: the combinatorial and partially reconstructed backgrounds (Secs. 3.4.1 and 3.4.2), the contamination from $B^+ \to K^+\pi^-\pi^+\eta$ (Sec. 3.4.3) and $B^0 \to K_1^0\gamma$ (Sec. 3.4.4), peaking backgrounds with or without π^0/γ misidentification (Sec. 3.4.5) and the crossfeed from the decay $B^+ \to \pi^+\pi^-\pi^+\gamma$ (Sec. 3.4.6), occurring when a pion is misidentified as a kaon. Other backgrounds not mentioned here, such as $B^+ \to \omega K^+$ and $B^+ \to \eta' K^+$ do not appear in the $\pi^+\pi^-\pi^0$ and $\pi^+\pi^-\gamma$ mass distributions respectively, ω and η' being outside the available phase space.

The contamination C_{bkg} from $B^0 \to K_1^0\gamma$, peaking backgrounds, $B^+ \to K^+\pi^-\pi^+\eta$ and crossfeed from $B^+ \to \pi^+\pi^-\pi^+\gamma$, summarized in Table. 3.5, is obtained from simulation studies, and is calculated as

$$C_{\text{bkg}} = \frac{N_{\text{bkg}}}{N_{\text{sig}}} = \frac{\mathcal{L} \cdot \sigma_{b\bar{b}} \cdot 2 \cdot f_{\text{bkg}} \cdot \mathcal{B}_{\text{bkg}} \cdot \varepsilon_{\text{bkg}}}{\mathcal{L} \cdot \sigma_{b\bar{b}} \cdot 2 \cdot f_{\text{sig}} \cdot \mathcal{B}_{\text{sig}} \cdot \varepsilon_{\text{sig}}} = \frac{f_{\text{bkg}} \cdot \mathcal{B}_{\text{bkg}} \cdot \varepsilon_{\text{bkg}}}{f_{\text{sig}} \cdot \mathcal{B}_{\text{sig}} \cdot \varepsilon_{\text{sig}}} , \qquad (3.6)$$

where $\mathcal{L}$ is the luminosity, $\sigma_{b\bar{b}}$ is the $b\bar{b}$ cross section, f is the fragmentation fraction and ε is the total efficiency. The branching fractions $\mathcal{B}$ for signal and backgrounds are taken from HFAG [120] and PDG [89], or estimated when not available. The number of events N is defined over the full mass range.

3.4.1 Combinatorial background

In the absence of high-mass peaking backgrounds, a good indication of the shape of the $K\pi\pi\gamma$ combinatorial background is given by the $K\pi\pi\gamma$ high-mass region, away from the B mass signal peak. Thus, in order to facilitate the fitting of the combinatorial background, a signal mass window with a long high-mass tail, up to 6829 MeV/c^2, is used.

The combinatorial background is modelled with a simple exponential function $e^{\frac{m}{\tau}}$, whose

Table 3.5 Contamination from $B^+ \to K^+\pi^-\pi^+\eta$, $B^0 \to K_1^0\gamma$, peaking backgrounds and the crossfeed from $B^+ \to \pi^+\pi^-\pi^+\gamma$ backgrounds to $B^+ \to K^+\pi^-\pi^+\gamma$. All upper limits are set at 90% CL.

Decay	$\mathcal{B}_{\text{bkg}}$	ϵ_{bkg}	C_{bkg}
$B^+ \to K^+\pi^-\pi^+\eta$	$\sim 4.1 \times 10^{-6}$ †	$\sim 1.6 \times 10^{-3}$	1×10^{-2}
$B^0 \to K_1^0\gamma \to K^+\pi^-\pi^0\gamma$	$\sim 2.8 \times 10^{-5}$ †	$< 6 \times 10^{-6}$	8×10^{-4}
$B^+ \to \bar{D}^0(\to K^+\pi^-\pi^0)\pi^+$	$(6.7 \pm 0.3) \times 10^{-4}$	$< 4 \times 10^{-6}$	$< 4 \times 10^{-2}$
$B^+ \to \bar{D}^{*0}(\to \bar{D}^0(\to K^+\pi^-)\gamma)\pi^+$	$(4.3 \pm 1.1) \times 10^{-5}$	$< 6 \times 10^{-7}$	$< 4 \times 10^{-4}$
$B^+ \to K^{*+}(\to K^+\pi^0)\pi^+\pi^-$	$(2.5 \pm 0.3) \times 10^{-5}$	$< 7 \times 10^{-7}$	$< 3 \times 10^{-4}$
$B^+ \to \pi^+\pi^-\pi^+\gamma$	$\sim 1.1 \times 10^{-6}$ †	$\sim 2 \times 10^{-5}$	6×10^{-4}

†estimated
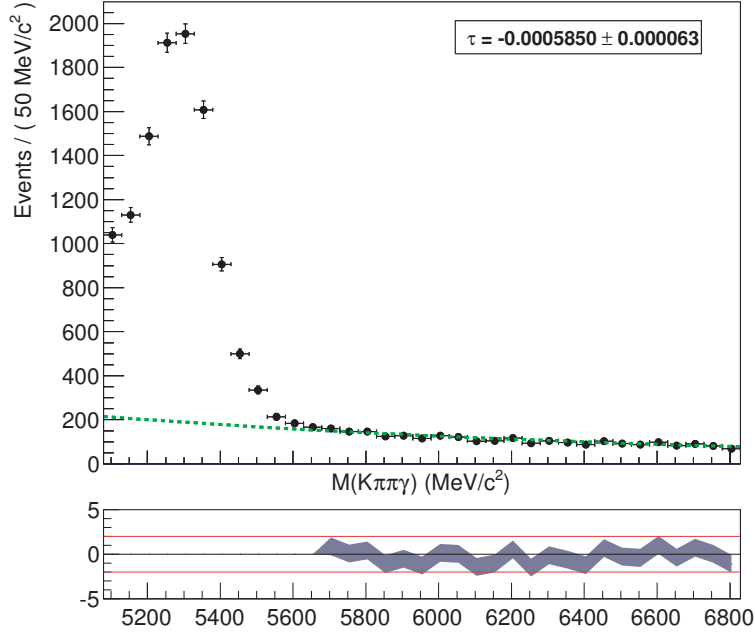
Figure 3.14 Mass distribution of the $B^+ \to K^+\pi^-\pi^+\gamma$ candidates selected in 2 fb^{-1} of data. The superimposed fit has been performed in the mass interval $5700 < m_B < 6829$ MeV/c^2, assumed to contain only combinatorial background.

decay constant τ is determined from a fit to the 2012 data sample for $m_B > 5700$ MeV/c^2 (Fig. 3.14) as

$$\tau = (-0.52 \pm 0.08) \text{ GeV}^{-1}c^2\,. \tag{3.7}$$

3.4.2 Partially reconstructed b-hadron background

The low-mass side of the mass region of interest is dominated by partially reconstructed events, *i.e.* events with the same final state as the signal, but with one or more particles not reconstructed. These types of backgrounds have a mass distribution with an endpoint given by the mass of the missing particle, and are usually described by a generalized Argus function

$$A(m; c, m_0, p) = \frac{2^{-p}c^{2(p+1)}}{\Gamma(p+1) - \Gamma(p+1, \frac{1}{2}c^2)} \cdot \frac{m^2}{m_0^2} \left(1 - \frac{m^2}{m_0^2}\right)^p \exp\left\{-\frac{1}{2}c^2\left(1 - \frac{m^2}{m_0^2}\right)\right\} \tag{3.8}$$

for $0 \leq m \leq m_0$, where c, m_0 and p are the curvature, endpoint and power, respectively. $\Gamma(\dots)$ is the gamma function and $\Gamma(\dots, \dots)$ is the upper incomplete gamma function. For $m > m_0$ the function returns zero.

In radiative decays, the resolution of the photon affects significantly the shape of the partially reconstructed background. Therefore, in our background model the generalized Argus PDF is convolved with a Gaussian PDF centered at zero and with the same

resolution of the signal PDF, $G(m; 0, \sigma)$, accounting for this effect.

In addition, the wide B^+ mass window may induce the appearance of two partially reconstructed background regimes: those where only one pion is missing, and those with at least two pions missing. While the first case represents a very well defined background, the latter corresponds basically to all possible backgrounds with two or more pions missing, one or more kaon missing, $K \to \pi$ misidentification, or combinations thereof. The general partially reconstructed background and the missing pion background are thus treated separately, and will be referred to hereinafter as *partially reconstructed background* and *missing pion background*, respectively.

The partially reconstructed background has been studied in previous radiative decays analyses [121]. It will be modelled with a generalized Argus function with its endpoint fixed at $m_B - 2m_{\pi^0}$ and the other parameters left free. The missing pion background is discussed in detail in the next section.

Missing pion background

In order to study the missing pion background, and because of the lack of a sizeable $B^{0(+)} \to K^+\pi^-\pi^+\pi^{-(0)}\gamma$ MC sample, the $B^0 \to K^{*0}\gamma$ decay is used as a signal proxy and the study is performed on $B^+ \to K^{*0}\pi^+\gamma$ reconstructed as $B^0 \to K^{*0}\gamma$. While the kinematics of the used decays slightly differ from those of the true $B^{0(+)} \to K^+\pi^-\pi^+\pi^{-(0)}\gamma$ background, it has been checked that the change in the mass shape mainly affects the tail of the Argus function, which does not significantly influence the determination of the parameters of interest.

The distribution of offline-selected $B^0 \to K^{*0}\gamma$ candidates reconstructed in a MC sample of $B^+ \to K^{*0}\pi^+\gamma$ decays is fitted with an Argus PDF convolved with a Gaussian PDF, accounting for the photon resolution. The μ and σ parameters obtained from fitting the $B^0 \to K^{*0}\gamma$ MC sample (Fig. 3.15) are used to fix the endpoint of the Argus PDF ($m_0^{\text{mis}-\pi} = \mu - m_{\pi^0}$) and the mass resolution, respectively. The resulting fit for the missing pion background is shown in Fig. 3.16 and the fitted values of the floated parameters are listed in Table 3.6.

Table 3.6   Fitted parameters of the Argus function (convolved with a Gaussian resolution) describing the mass distribution of $B^0 \to K^{*0}\gamma$ candidates reconstructed in a MC sample of $B^+ \to K^{*0}\pi^+\gamma$ decays. The μ and σ parameters obtained from fitting the $B^0 \to K^{*0}\gamma$ MC sample are used to fix the endpoint of the Argus function and the mass resolution.

Parameter	Value	Unit
$c^{\mathrm{mis}-\pi}$	-4.2 ± 0.3	
$p^{\mathrm{mis}-\pi}$	0.058 ± 0.032	
$m_0^{\mathrm{mis}-\pi}$	$\mu - m_{\pi^0}$ (fixed)	MeV/c^2
$\mu_{K^*\gamma}$	5278 (fixed)	MeV/c^2
$\sigma_{K^*\gamma}$	97.0 (fixed)	MeV/c^2
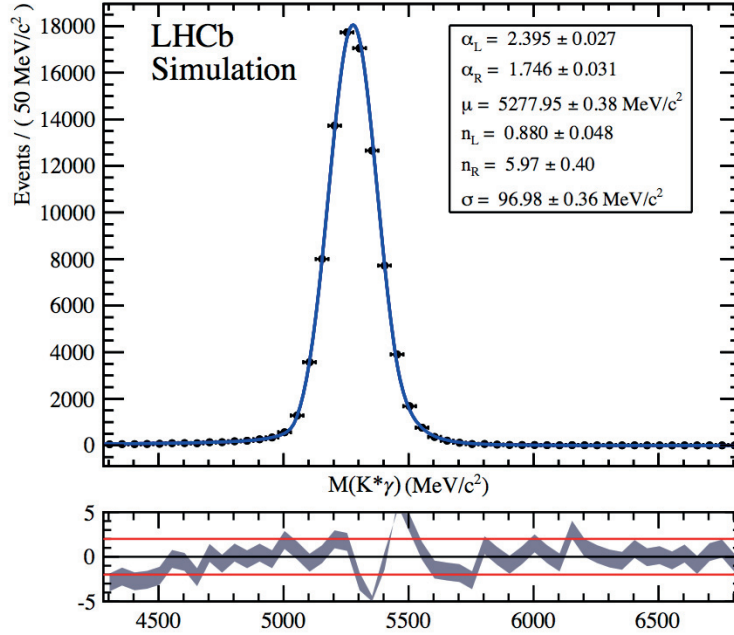
Figure 3.15   Mass distribution of $B^0 \to K^{*0}\gamma$ MC decays. The result of the fit of a double-tail Crystal Ball function is superimposed.
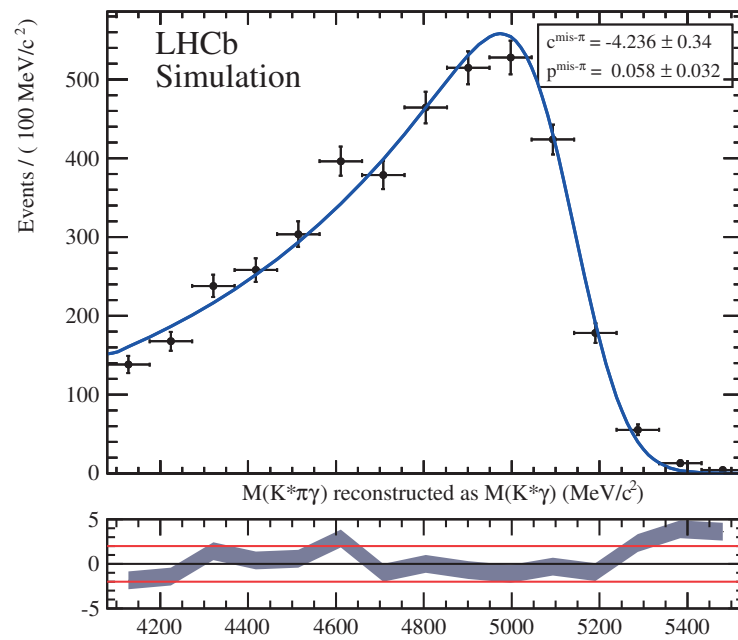
Figure 3.16   Mass distribution of $B^0 \to K^{*0}\gamma$ candidates selected in a MC sample of $B^+ \to K^{*0}\pi^+\gamma$ decays. The result of the fit to an Argus PDF convolved with a Gaussian PDF is superimposed.

3.4.3 Contamination from $B^+ \to K^+\pi^-\pi^+\eta(\to \gamma\gamma)$

The $B^+ \to K^+\pi^-\pi^+\eta$ decay, with $\eta \to \gamma\gamma$, can be misidentified as signal in case one of the photons from the η is not reconstructed. The detected photon is expected to be soft, with an energy below the photon E_T requirement (Table 3.3), which is then expected to remove most of these events.

The contamination from this partially reconstructed background has been checked using simulated data, since it is expected to peak very close to the signal mass peak. When applying the $B^+ \to K^+\pi^-\pi^+\gamma$ selection to the $B^+ \to K^+\pi^-\pi^+\eta$ MC sample, 567 events survive with a selection efficiency of $\sim 1.6 \times 10^{-3}$. The fit of their mass distribution with a double-tail Crystal Ball function is shown in Fig. 3.17.
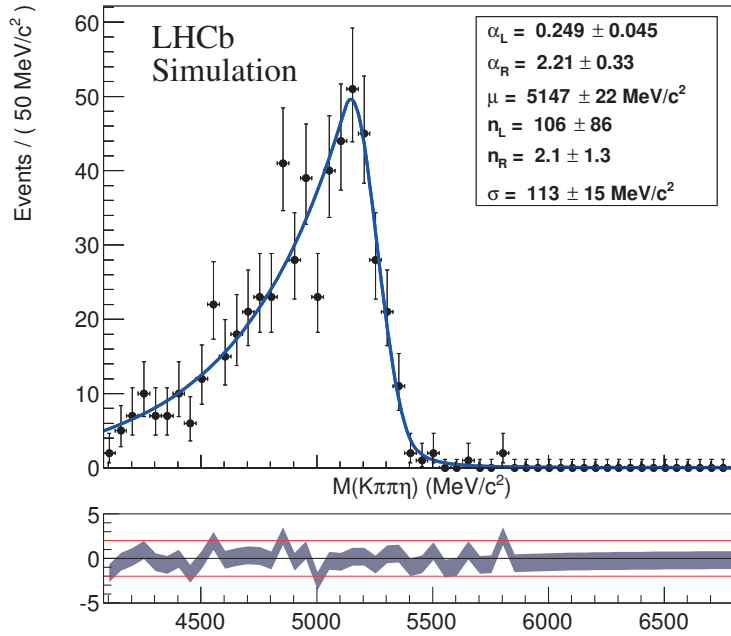
Figure 3.17 Mass distribution of $B^+ \to K^+\pi^-\pi^+\gamma$ candidates selected in $B^+ \to K^+\pi^-\pi^+\eta$ MC events. The curve shows the fit of a double-tail Crystal Ball function. The very long left tail is due to the energy that has been missed because one of the photons coming from the η has not been reconstructed.

The calculation of the $B^+ \to K^+\pi^-\pi^+\eta$ contamination to the $B^+ \to K^+\pi^-\pi^+\gamma$ signal is based on a branching fraction estimated to be $\sim 0.15 \times \mathcal{B}(B^+ \to K^+\pi^-\pi^+\gamma)$ from the analogy with the decays $B^0 \to K^{*0}\eta$ and $B^0 \to K^{*0}\gamma$, and considering that η decays to two photons 40% of the time. This branching fraction, combined with the ratio of efficiencies for signal and background, gives a contamination in the full mass range of $\sim 1.0\%$, of which only $\sim 0.6\%$ is under the mass peak (within $\pm 200\,\mathrm{MeV}/c^2$ of the B mass). As a result, the contamination from $B^+ \to K^+\pi^-\pi^+\eta(\to \gamma\gamma)$ is neglected. As a check, this background has been included in the final mass fit and found to be consistent with zero.

3.4.4 Contamination from $B^0 \to K_1^0\gamma$

Contamination from $B^0 \to K_1^0\gamma \to K^+\pi^-\pi^0\gamma$, where the π^0 is not detected and a charged π is randomly associated with the candidate, has also been studied using a $B^0 \to K^+\pi^-\pi^0\gamma$ MC sample reconstructed as $B^+ \to K^+\pi^-\pi^+\gamma$.

The shape resulting from applying only the stripping requirements, fitted with a Gaussian function, is shown in Fig. 3.18. When the full offline selection is applied, only two events survive in this neutral channel.
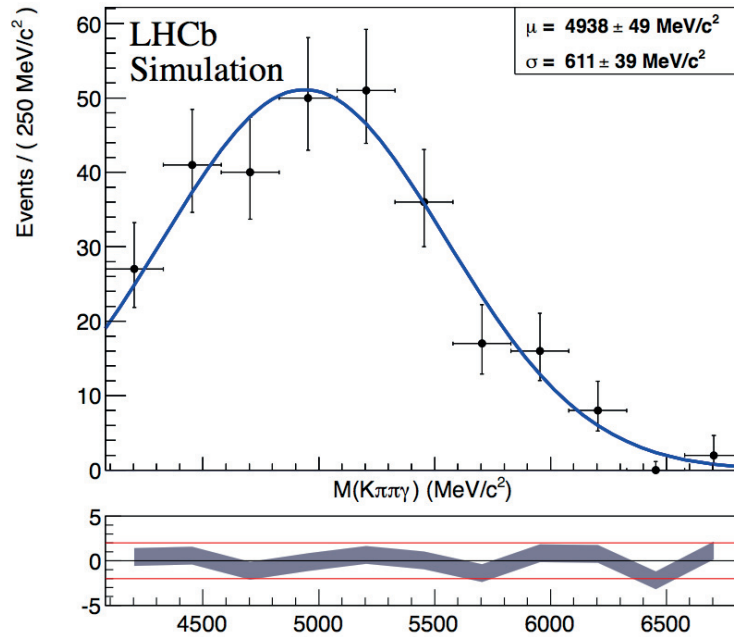
Figure 3.18   Mass distribution of $B^+ \to K^+\pi^-\pi^+\gamma$ candidates selected in $B^0 \to K_1^0\gamma \to$ $K^+\pi^-\pi^0\gamma$ MC events. Only the stripping requirements are applied. The result of the fit to a simple Gaussian function is superimposed.

An upper limit for the contamination is obtained from Eq. 3.6. The branching fraction of the $B^0 \to K_1^0\gamma \to K^+\pi^-\pi^0\gamma$ channel, which has not been measured so far, is chosen to be the same as for the charged channel. Setting an upper limit (at 90% CL) for the efficiency at 6×10^{-6} assuming a Poisson distribution [89], the contamination from $B^0 \to K_1^0\gamma$ to $B^+ \to K^+\pi^-\pi^+\gamma$ is expected to be smaller than 0.8%, and is therefore deemed negligible (Table 3.5).

3.4.5 Peaking backgrounds

The following peaking backgrounds—in which the final state is the same as the signal except for a possible π^0/γ misidentification—are taken into account:

- $B^+ \to \overline{D}^0(\to K^+\pi^-\pi^0)\pi^+$

- $B^+ \to \overline{D}^{*0}(\to \overline{D}^0(\to K^+\pi^-)\gamma)\pi^+$

- $B^+ \to K^{*+}(\to K^+\pi^0)\pi^+\pi^-$

The first background, which is very similar to the decay $B^+ \to \overline{D}^0\rho^+$ mentioned in Sec. 3.2.2, has a large branching fraction; however, the mass cuts used to remove $\overline{D}^0$ are also effective to reject it. The other backgrounds are suppressed by the hard photon cut. Nonetheless their contributions have been evaluated.

The procedure is analogous in the three cases: a MC sample of each of the backgrounds has been reconstructed as $B^+ \to K^+\pi^-\pi^+\gamma$, selection requirements have been applied and the selection efficiency has been calculated. In all cases, the number of surviving events is very small and therefore upper limits at 90% CL have been set.

Finally, the contamination from these channels is evaluated and included in Table. 3.5. It can be seen that the limit on the contamination coming from $B^+ \to \overline{D}^0(\to K^+\pi^-\pi^0)\pi^+$ is not very stringent. However, the specific cuts applied to remove its contribution provide the needed rejection power. In conclusion, peaking backgrounds have been found to be negligible, and will not be included in the full fit model.

3.4.6 Crossfeed from $B^+ \to \pi^+\pi^-\pi^+\gamma$

The crossfeed from the misidentification of the yet unobserved decay $B^+ \to \pi^+\pi^-\pi^+\gamma$ is taken into account following the same procedure as in the case of $B^0 \to K_1^0\gamma$. The $B \to a_1\gamma \to \pi\pi\pi\gamma$ simulated sample, reconstructed and selected as $B^+ \to K^+\pi^-\pi^+\gamma$, is described by a double-tail Crystal Ball function (Fig. 3.19).

In order to find the level of contamination, Eq. 3.6 requires the branching ratio for the decay $B^+ \to \pi^+\pi^-\pi^+\gamma$ with respect to the signal channel $B^+ \to K^+\pi^-\pi^+\gamma$ to be estimated. It is easy to see that, being a $b \to d\gamma$ transition, this background channel is strongly suppressed:

$$\frac{\mathcal{B}(B^+ \to \pi^+\pi^-\pi^+\gamma)}{\mathcal{B}(B^+ \to K^+\pi^-\pi^+\gamma)} \propto \left(\frac{V_{td}}{V_{ts}}\right)^2 = \lambda^2 \sim 0.04\,. \tag{3.9}$$

After applying the offline selection, only 22 events are left from the initial MC sample and the contamination is found to be at per mille level, $\sim 6 \times 10^{-4}$. Therefore, the contribution from this background will not be included in the fit.
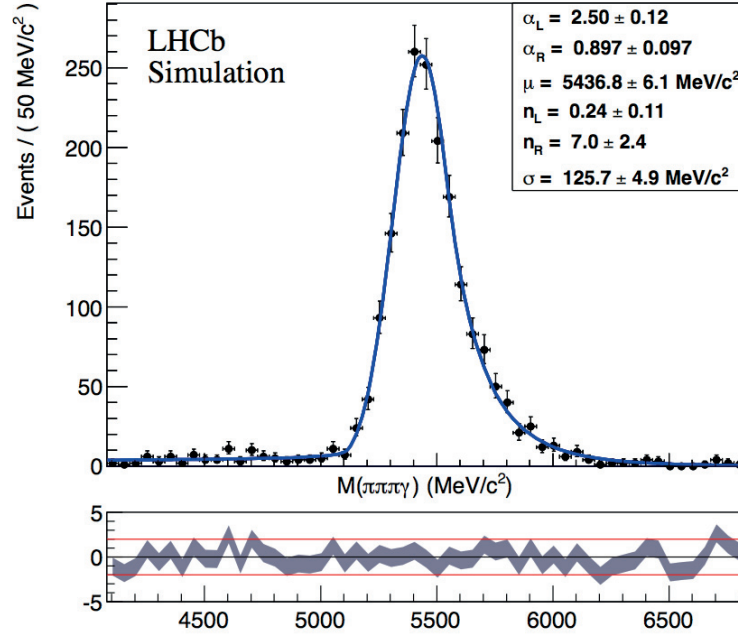
Figure 3.19 Mass distribution of $B^+ \to K^+\pi^-\pi^+\gamma$ candidates selected in a MC sample of $B^+ \to \pi^+\pi^-\pi^+\gamma$ events. The results of a fit to a double-tail Crystal Ball function is superimposed.

3.5 Mass fit to the full dataset

The fit function for the $K^+\pi^-\pi^+\gamma$ mass distribution is built taking into account the signal and background simulation studies detailed in the previous sections.

The signal is modelled with a double-tail Crystal Ball function with α_i and n_i tail parameters fixed from $B^+ \to K_1(1270)^+\gamma$ MC simulation (Table 3.4):

$$S(m; \mu, \sigma) = CB(m; \mu, \sigma, \alpha_L = 2.21, n_L = 1.41, \alpha_R = 1.58, n_R = 7.60). \qquad (3.10)$$

Three components have been included in the background model, as discussed in Sec. 3.4:

- the combinatorial background, modelled with an exponential function,

$$\mathrm{Comb}(m; \tau) = \exp(m/\tau); \qquad (3.11)$$

- the missing pion background, modelled with an Argus PDF convolved with a Gaussian resolution, with shape parameters fixed from simulation,

$$\mathrm{MissPi}(m; \mu, \sigma) = A(m; \mu - m_{\pi^0}, c = -4.2, p = 0.058) \otimes G(0, \sigma); \qquad (3.12)$$

- the partially reconstructed background, modelled with an Argus PDF convolved with a Gaussian resolution, with its endpoint fixed to the difference between the

signal peak position and $2m_{\pi^0}$,

$$\text{Partial}(m; \mu, \sigma, c, p) = A(m; \mu - 2m_{\pi^0}, c, p) \otimes G(0, \sigma) \,. \tag{3.13}$$

In this case both the curvature and power parameters are left free, since the overall shape is the superposition of different types of partially reconstructed events, *e.g.* missing kaon, three missing pions, π misidentification, *etc.* .

These three components are added together to form a total background PDF that reads

$$
\begin{aligned}
B(m; \mu, \sigma, \tau, c_{\text{partial}}, p_{\text{partial}}, f_{\text{partial}}, f_{\text{miss-}\pi}) = \\
(1 - f_{\text{miss-}\pi} - f_{\text{partial}}) \, \text{Comb}(m; \tau) + \\
f_{\text{miss-}\pi} \, \text{MissPi}(m; \mu, \sigma) + \\
f_{\text{partial}} \, \text{Partial}(m; \mu, \sigma, c_{\text{partial}}, p_{\text{partial}}) \,, \tag{3.14}
\end{aligned}
$$

so that the full fit function becomes

$$
\begin{aligned}
M(m; N_{\text{signal}}, N_{\text{bkg}}, \mu, \sigma, \tau, c_{\text{partial}}, p_{\text{partial}}, f_{\text{partial}}, f_{\text{miss-}\pi}) = \\
N_{\text{signal}} S(m; \mu, \sigma) + \\
N_{\text{bkg}} B(m; \mu, \sigma, \tau, c_{\text{partial}}, p_{\text{partial}}, f_{\text{partial}}, f_{\text{miss-}\pi}) \,. \\
\tag{3.15}
\end{aligned}
$$

Separate fits on the full $K^+\pi^-\pi^+\gamma$ mass range of the 2011 and 2012 datasets yield significantly different values for the signal mass resolution σ, as shown in Fig. 3.20 and Table 3.7. This is mainly due to the differences between the calorimeter calibrations and the trigger configurations at 7 and 8 TeV centre-of-mass energies. For example, the tightening of the E_{T} requirements in the `Photon` and `Electron` L0 lines—from $E_{\text{T}} > 2500 \, \text{MeV}/c$ in 2011 to $E_{\text{T}} > 2720 \, \text{MeV}/c$ in 2012—is particularly relevant for radiative decays.

Because of this effect, the datasets cannot be merged, and thus the mass fit is performed simultaneously on the 2011 and the 2012 datasets, with two functions (that together form the total $M(m)$ function) sharing all the shape parameters except σ and the background fractions in order to allow for differences in background levels due to the different trigger and data taking conditions.
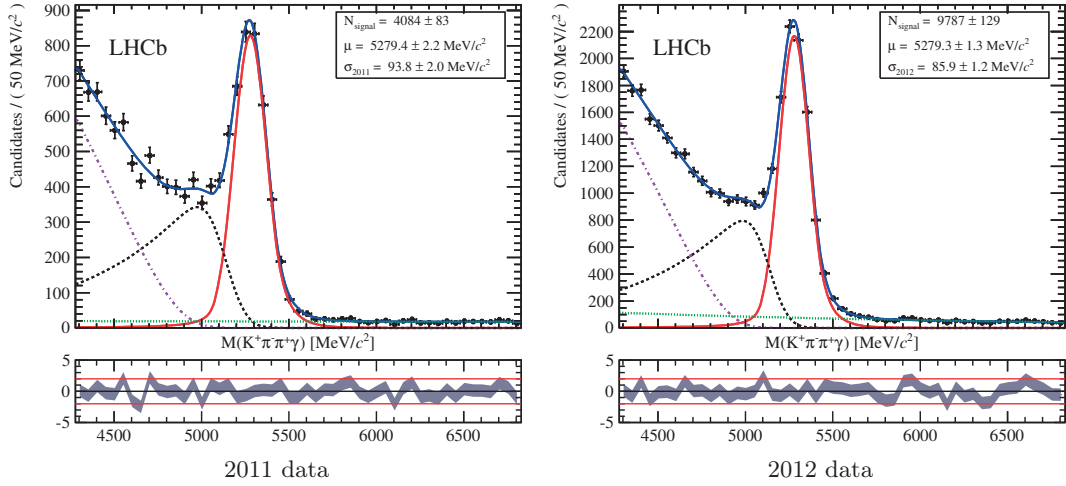
Figure 3.20   Mass distribution of the $B^+ \to K^+\pi^-\pi^+\gamma$ candidates in the 2011 (left) and 2012 (right) datasets. The superimposed fits include the following components: signal shown in red (solid), combinatorial background in green (dashed), missing pion background in black (dashed) and partially reconstructed background in purple (dashed). The mass resolution is significantly different in the two datasets.

Table 3.7   Fitted parameters obtained separately in the 2011 and 2012 datasets. The signal mass resolution σ differs significantly between the two samples.

Parameter	2011	2012	Units
N_{signal}	4084 ± 83	9787 ± 129	
N_{bkg}	9006 ± 108	23547 ± 175	
μ	5279.4 ± 2.2	5279.3 ± 1.3	MeV/c^2
σ	93.8 ± 2.0	85.9 ± 1.2	MeV/c^2
τ	-0.047 ± 0.144	-0.40 ± 0.08	GeV$^{-1}c^2$
c_{partial}	-2.1 ± 3.5	-1.7 ± 1.8	
p_{partial}	2.0 ± 0.7	1.8 ± 0.3	
f_{partial}	0.41 ± 0.02	0.43 ± 0.01	
$f_{\text{miss-}\pi}$	0.48 ± 0.02	0.42 ± 0.01	

89

3.5.1 Fit results

The results of the simultaneous unbinned extended maximum likelihood fit to the full dataset are shown in Table 3.8 and Fig. 3.21. A total of 13876 ± 153 $B^+ \to K^+\pi^-\pi^+\gamma$ events is observed, the largest sample recorded for this inclusive decay channel. The values obtained for the other parameters are in reasonable agreement with those found in the separate fits.
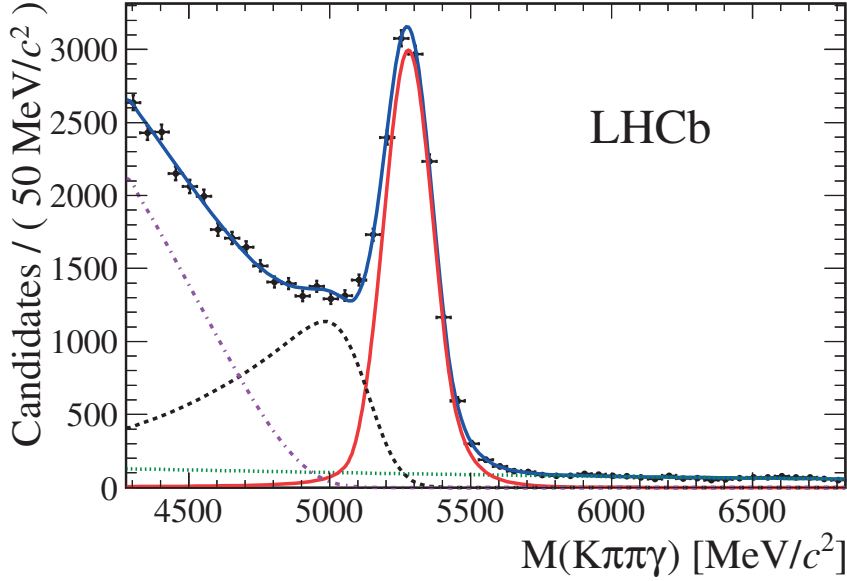
Figure 3.21   Mass distribution of the $B^+ \to K^+\pi^-\pi^+\gamma$ candidates in the full 3 fb^{-1} dataset, with the fit results superimposed. Colour code as in Fig. 3.20.

3.5.2 Determination of background-subtracted distributions

In order to achieve a better understanding of the $K^+\pi^-\pi^+$ mass spectrum present in our signal, the *sPlot* technique [122] is used to obtain the distribution of the B^+ mass-constrained $K^+\pi^-\pi^+$ mass for the $B^+ \to K^+\pi^-\pi^+\gamma$ signal (Fig. 3.22). This technique uses a set of discriminating variables to assign each event in the data sample a weight used to unfold the different contributions (*e.g.* signal and backgrounds) to the distribution of another variable (*e.g.* the mass of the $K^+\pi^-\pi^+$ system). The latter variable is required not to be correlated with the discriminating variables.

As introduced in Sec. 1.2.3, many kaon resonances, with different spin and parity values, are expected to appear in the considered mass interval. In Fig. 3.22, no evident peak other than the dominant $K_1(1270)^+$ can clearly be recognised. Since most of the resonances in the $K^+\pi^-\pi^+$ mass interval of interest are very wide and not well known, it is not straightforward to isolate single resonance contributions. The study of the $K^+\pi^-\pi^+$ mass spectrum can be simplified dividing it in four mass intervals

Table 3.8   Results of the simultaneous mass fit to the full 3 fb^{-1} dataset.

Parameter	Value	Unit
N_{signal}	13876 ± 153	
$N_{\mathrm{signal}}^{2012}$	9831 ± 125	
N_{bkg}^{2011}	9045 ± 104	
N_{bkg}^{2012}	23503 ± 171	
μ	5279.3 ± 1.1	MeV/c^2
σ_{2011}	92.9 ± 1.9	MeV/c^2
σ_{2012}	86.3 ± 1.2	MeV/c^2
τ	-0.31 ± 0.07	GeV$^{-1}c^2$
c_{partial}	-1.6 ± 1.4	
p_{partial}	1.8 ± 0.3	
$f_{2011}^{\mathrm{partial}}$	0.41 ± 0.01	
$f_{2012}^{\mathrm{partial}}$	0.43 ± 0.01	
$f_{2011}^{\mathrm{miss}\text{-}\pi}$	0.46 ± 0.01	
$f_{2012}^{\mathrm{miss}\text{-}\pi}$	0.43 ± 0.01	

- $[1100, 1300]\,\mathrm{MeV}/c^2$, where the leading contribution comes from the $K_1(1270)^+$ resonance;

- $[1300, 1400]\,\mathrm{MeV}/c^2$, where the $K_1(1270)^+$ and $K_1(1400)^+$ interfere;

- $[1400, 1600]\,\mathrm{MeV}/c^2$, where the $K_1(1400)^+$ and $K_2^*(1430)^+$ dominate;

- $[1600, 1900]\,\mathrm{MeV}/c^2$, where 2^- resonances are expected to give a large contribution.

A more complex approach where the resonances contributions are effectively separated by means of a multidimensional Dalitz analysis is presented in Chapter 5.

The $K^+\pi^-$ and $\pi^+\pi^-$ background-subtracted mass distributions (Figs. 3.23 and 3.24) are also extracted from data making use of the *sPlot* technique. The background-subtracted $(m_{K^+\pi^-}^2, m_{\pi^+\pi^-}^2)$ Dalitz plots in the four $K^+\pi^-\pi^+$ mass intervals of interest are shown in Fig. 3.25. The $\rho(770)^0$ and $K^*(892)^0$ peaks are evident in all distributions, while the contributions from higher mass states, such as the $K_2^*(1430)^0$ in $m_{K^+\pi^-}^2$ and the $f_2(1270)^0$ in $m_{\pi^+\pi^-}^2$, are visible only in the high $K^+\pi^-\pi^+$ mass interval. The background-subtracted distribution of $\cos\tilde{\theta}$ (Fig. 3.26) has also been determined from the full data sample.
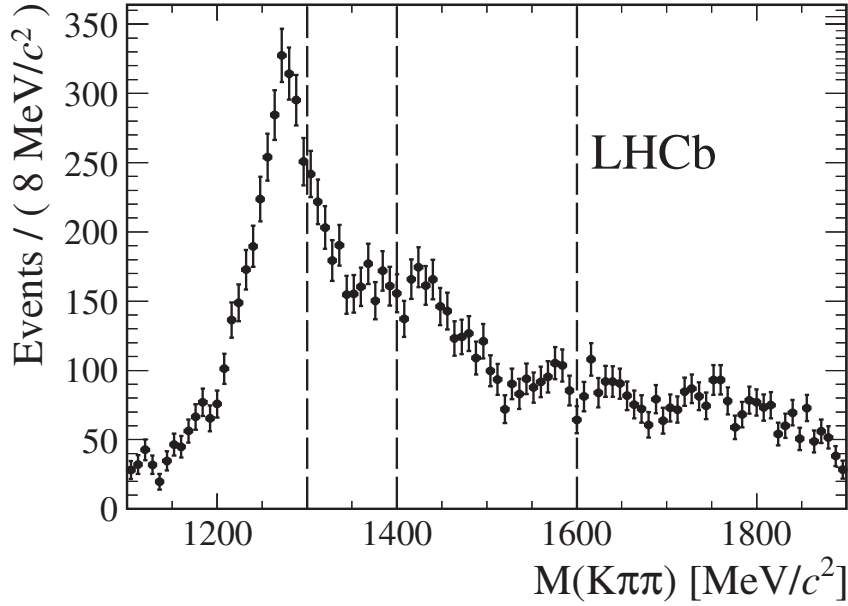
Figure 3.22   *B*-mass-constrained, background-subtracted $m_{K\pi\pi}$ distribution, obtained using the *sPlot* technique for $B^+ \to K^+\pi^-\pi^+\gamma$ decays in the full 3 fb^{-1} dataset. The four $K^+\pi^-\pi^+$ intervals of interest are delimited by dashed lines.
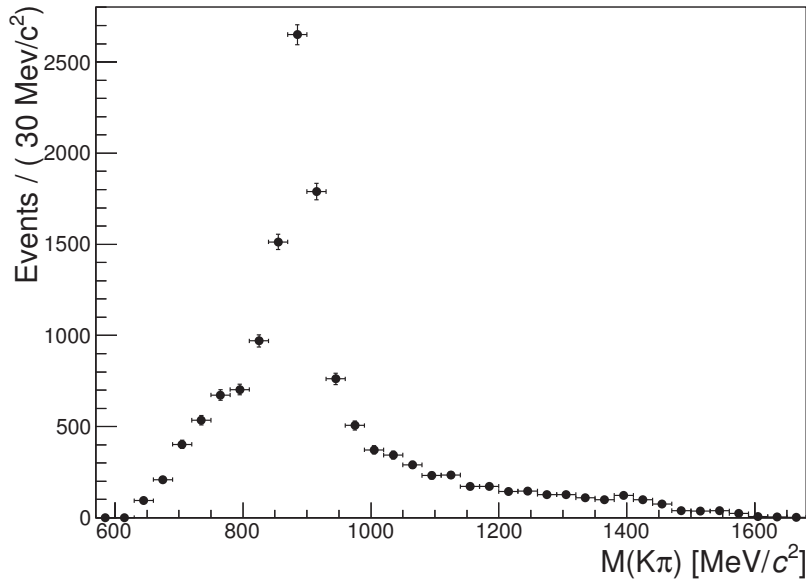
Figure 3.23   Background-subtracted $m_{K\pi}$ distribution, obtained using the *sPlot* technique for $B^+ \to K^+\pi^-\pi^+\gamma$ decays in the full 3 fb^{-1} dataset. The prominent peak corresponds to the $K^*(892)^0$ resonance.
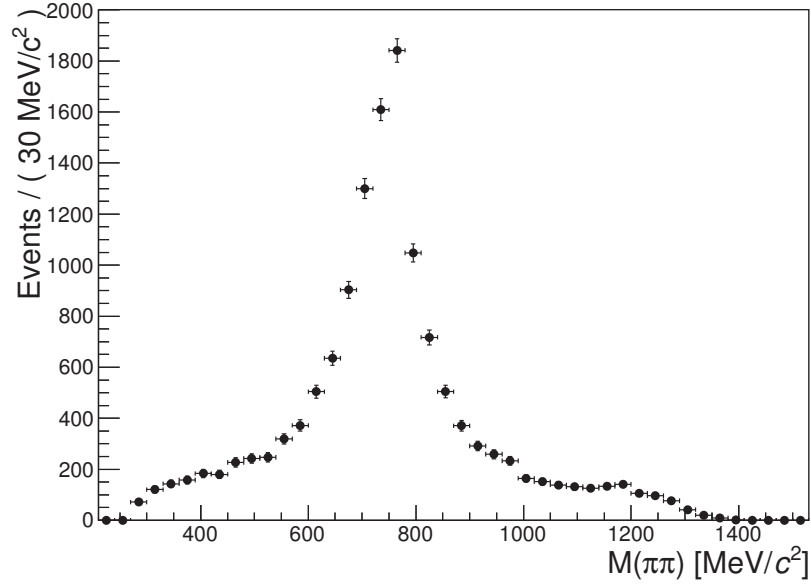
Figure 3.24 Background-subtracted $m_{\pi\pi}$ distribution, obtained using the *sPlot* technique for $B^+ \to K^+\pi^-\pi^+\gamma$ decays in the full 3 fb^{-1} dataset. The prominent peak corresponds to the $\rho(770)^0$ resonance.
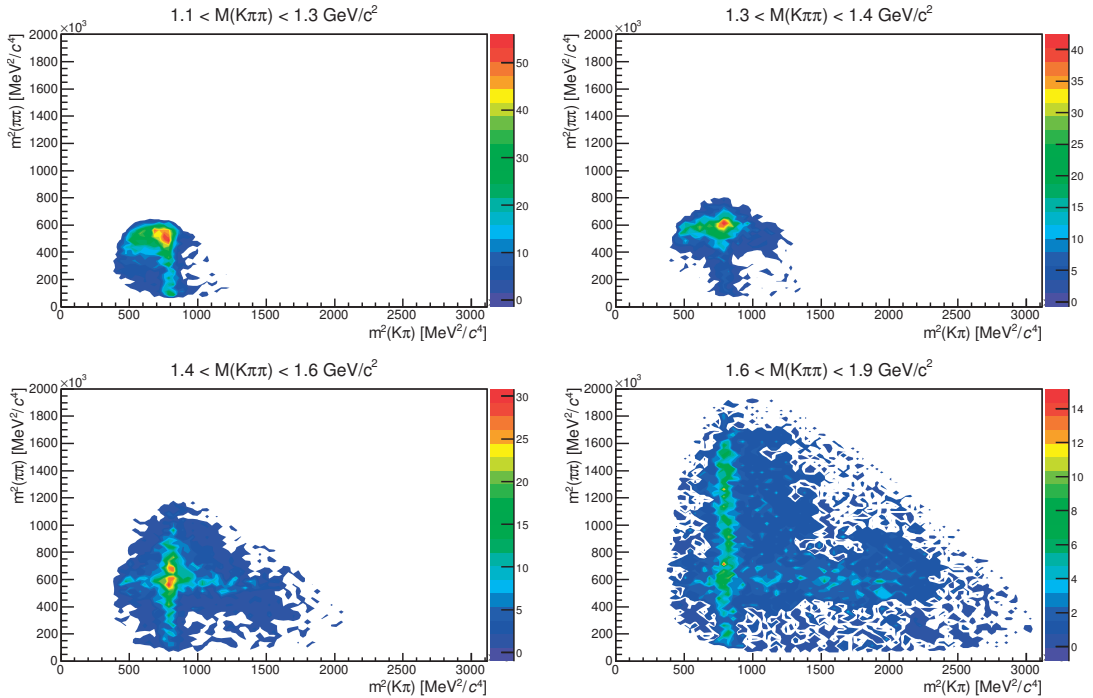
Figure 3.25 Background-subtracted Dalitz plots in the four $K^+\pi^-\pi^+$ mass intervals of interest, obtained using the *sPlot* technique for $B^+ \to K^+\pi^-\pi^+\gamma$ decays in the full 3 fb^{-1} dataset. The boundaries depend on the available phase space.
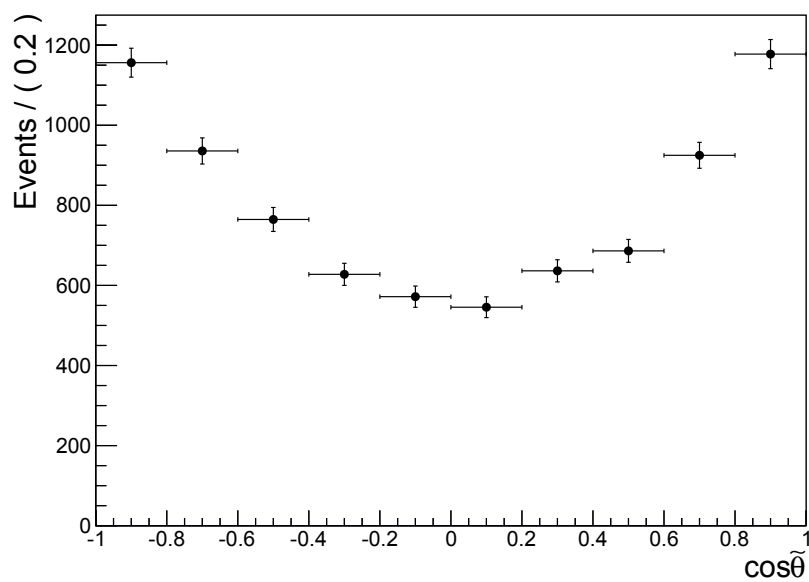
Figure 3.26   Background-subtracted $\cos\tilde\theta$ distribution, obtained using the *sPlot* technique for $B^+ \to K^+\pi^-\pi^+\gamma$ decays in the full 3 fb^{-1} dataset.

<div style="text-align: right;">

4

</div>

Observation of photon polarisation in $B^+ \to K^+\pi^-\pi^+\gamma$ decays

Starting from the results of the previous section, the angular distribution of the photon is analysed in the four $K^+\pi^-\pi^+$ mass intervals defined in Sec. 3.5.2. The up-down asymmetry obtained from the angular fit is measured to be significantly different from zero.

In each mass interval, a simultaneous fit to the B-candidate mass spectra in several bins of the photon direction angle is performed in order to determine the background-subtracted angular distribution. Since the sign of the photon polarisation changes with the charge of the B candidate, the sign-weighted angular variable $\cos\hat{\theta}$ is introduced as

$$\cos\hat{\theta} \equiv \mathrm{charge}(B^\pm)\cos\tilde{\theta}\,. \tag{4.1}$$

The same argument applies to the no-flip scenario replacing $\tilde{\theta}$ with θ in Eq. 4.1 [1]. The angles θ and $\tilde{\theta}$ have been defined in Secs. 1.2.1 and 1.2.2, respectively.

The PDF for the mass fit on the full dataset presented in Sec. 3.5 (Eq. 3.15) is used for each $\cos\hat{\theta}$ bin, and a full simultaneous PDF is built. All the shape parameters are shared between the bins, while the signal and background yields are free to vary. The chosen granularity for the study is 20 bins.

The resulting background-subtracted $\cos\hat{\theta}$ distribution, is then corrected bin-by-bin for the effect of the selection efficiency not being flat in $\cos\hat{\theta}$, as shown in Sec. 3.2.3. Finally, the efficiency-corrected yield in each bin is divided by the bin-width and the resulting distribution is fitted with a fourth-order polynomial function normalised to 1

$$f(\cos\hat{\theta}; c_0 = 0.5, c_1, c_2, c_3, c_4) = \sum_{i=0}^{4} c_i L^i(\cos\hat{\theta})\,, \tag{4.2}$$

---

[1] In this Chapter, $\cos\hat{\theta}$ will be used to refer both to the flip and no-flip scenarios in order to simplify the notation.

<div style="text-align: center;">

95

</div>

where $L^i(x)$ is the Legendre polynomial of order i and c_i are the fitted coefficients.

Given the fitting function in Eq. 4.2, the up-down asymmetry of Eq. 1.135 can be expressed in terms of the Legendre coefficients as

$$\mathcal{A}_{\mathrm{ud}} = \frac{\sum_{i=0}^{4} \left(\int_0^1 c_i \, L^i(\cos\hat{\theta}) \, \mathrm{dcos}\,\hat{\theta} - \int_{-1}^0 c_i \, L^i(\cos\hat{\theta}) \, \mathrm{dcos}\,\hat{\theta} \right)}{\sum_{i=0}^{4} \int_{-1}^1 c_i \, L^i(\cos\hat{\theta}) \, \mathrm{dcos}\,\hat{\theta}} \ . \tag{4.3}$$

Using the orthogonality of the Legendre polynomials, it is easy to see that only the odd terms contribute to the numerator, while in the denominator the only nonzero contribution is the one coming from L^0:

$$\mathcal{A}_{\mathrm{ud}} = \frac{c_1 - c_3/4}{2c_0} = c_1 - \frac{c_3}{4} \ . \tag{4.4}$$

4.1 Angular fit systematics

The systematic uncertainties affecting the study of the angular distribution are presented in this section. Once evaluated, they are added in quadrature to the statistical errors for each bin of $\cos\hat{\theta}$ and accounted for in the final fit.

MC-related and fit model systematics

In order to assess the systematic uncertainty associated with some parameters being fixed from MC simulations in the fit model (MC-related systematics), 2000 mass fits are performed on the data varying these PDF shape parameters. For each fit, a new set of fixed parameters, each generated gaussianly around their central value and taking into account the correlation matrix obtained from MC, is used for the fit. The endpoint of the Argus function used for the partially reconstructed background is treated along with the fit model systematics, while for the missing pion background it is not varied, since it has been fixed from physics principles. A summary of the parameters fixed from MC, for which this source of systematic uncertainty has been evaluated is shown in Table 4.1.

Table 4.1   Mean value and width of the Gaussian PDF used for the generation of the parameters fixed from MC in the data fits.

Parameter	μ	σ
α_L	2.214	0.053
n_L	1.41	0.13
α_R	1.580	0.053
n_R	7.6	1.1
$p_{\mathrm{miss}\text{-}\pi}$	0.058	0.032
$c_{\mathrm{miss}\text{-}\pi}$	-4.24	0.34
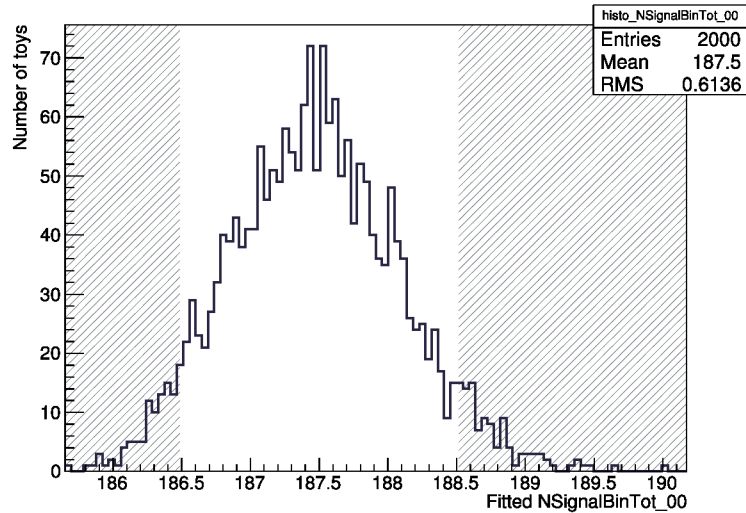
Figure 4.1   Distribution of the signal yield in the first $\cos\hat{\theta}$ bin, as obtained for the evaluation of the MC-related systematics. The non-shaded area contains 90 % of the probability.

The signal yields obtained from these fits for each bin distribute around the nominal fit values. As an example, Fig. 4.1 shows the distribution of the signal yield in the first $\cos\hat{\theta}$ bin. The systematic uncertainties are computed from these distributions using the central interval criterion at 90 % confidence level (CL).

The uncertainty related to the shapes chosen for describing signal and backgrounds (fit model systematics) has also been evaluated.

- For the signal shape, two main sources of systematic uncertainty (added in quadrature) are considered: a single left-tail Crystal Ball function is used instead of the double-tail Crystal Ball PDF, and the shape parameters of the signal PDF are replaced with those obtained from the $K_1(1400)^+$ and $K_2^*(1430)^+$ (Sec. 3.3);

- the Gaussian PDF used to describe the effect of mass resolution in the Argus PDF is replaced by a signal-like double-tail Crystal Ball function;

- the exponential PDF used in the fit model to describe the combinatorial background is replaced with a linear PDF;

- the endpoint of the Argus PDF for the partially reconstructed background is left free in the fit.

Other possible shapes have been tried, e.g. leaving the endpoint of the missing pion Argus free, but the resulting fits did not describe the data properly, the fits themselves became unstable, or the obtained results were perfectly compatible with the nominal fit, and so they have been discarded.
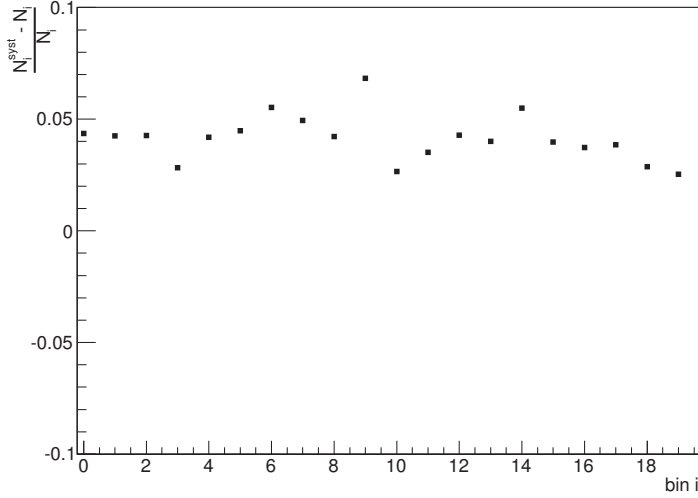
Figure 4.2   Relative difference between the signal yields obtained from the fit for calculating the systematical uncertainties and from the nominal fit in bins of $\cos\hat{\theta}$. A strong correlation between bins is observed. This figure refers to the fit model systematical uncertainty due to the change of the signal shape for $1100 < m_{K\pi\pi} < 1300$ MeV/c^2, but the same conclusion holds for each of the systematic uncertainties in every $K^+\pi^-\pi^+$ mass interval.

Such fit model systematics are determined for each bin of $\cos\hat{\theta}$, and the variations of the signal shape are found to dominate this uncertainty.

The MC and fit model related systematics are found to be of the order of 1 and $5-10$ events in each bin of $\cos\hat{\theta}$, respectively, the statistical error being of the order of $10-20$ events. Comparing the signal yields in bins of $\cos\hat{\theta}$ obtained in the systematics fit and in the nominal fit, the MC and fit model systematic errors are found to be strongly correlated between bins (Fig. 4.2), as expected since the mass fit is performed simultaneously, with all the shape parameters shared amongst the bins. As a result, a 100% correlation for the systematical uncertainties between bins is assumed.

Bin migration due to angular resolution

An additional source of uncertainty comes from the possibility that the events in one $\cos\hat{\theta}$ bin migrate to the neighbour bin because of detector resolution effects. This effect depends on the bin width and might largely affect the fit to the angular distribution.

In describing the resolution shape the possibility of a dependence in $\cos\hat{\theta}$ needs to be considered: the resolution obtained from truth MC (Fig. 4.3) is fitted with a triple Gaussian (with $\mu = 0$) in five bins of $|\cos\hat{\theta}|$ and the results are shown in Fig. 4.4. A strong dependency on the photon angle is observed, with values of $\cos\hat{\theta}$ closer to zero having a worse resolution. The resolution as a function of $\cos\hat{\theta}$ is fitted with a linear function and is used to calculate a per-event resolution for the bin migration studies.
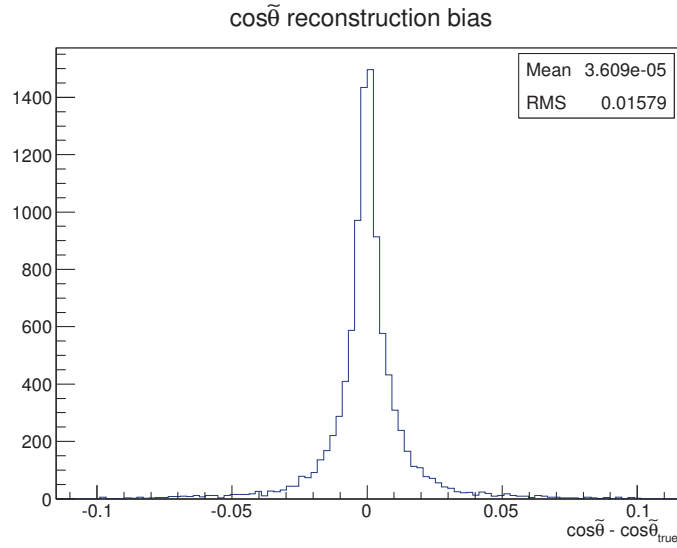
Figure 4.3 Difference between the reconstructed $\cos\hat{\theta}$ and its true value from MC.

For the evaluation of this systematic uncertainty 10000 $\cos\hat{\theta}$ distributions are generated according to the $\cos\hat{\theta}$ shape obtained by fitting the function described in Eq. 4.2 to the data in each interval of $K^+\pi^-\pi^+$ mass. Then each of the generated events is smeared according to its per-event resolution function. The smeared and non-smeared datasets are binned, and the bin-by-bin differences in yield are used to build the covariance matrix describing bin migration given the shape extracted from the data. As expected, the correlation is found to be high for neighbouring bins, decreasing for more distant bins. To give an idea of the size of the bin migration effect, the widths of the yield difference distributions are shown in Fig. 4.5 for each of the $K^+\pi^-\pi^+$ mass intervals of interest. The effect of bin migration on the signal yield is found to be $3-7$ events in each bin of $\cos\hat{\theta}$. The bias on the yield that arises from the asymmetry in the bin migration effect between the left and right neighbour bins is found to be below 1 event in all cases, and is thus negligible.

Acceptance systematics

The imperfect knowledge of the acceptance function (Fig. 3.10) is also a source of systematic uncertainty. For the angular fit, the statistical errors from the MC-determined acceptance are directly added to the covariance matrix, assuming no correlation.
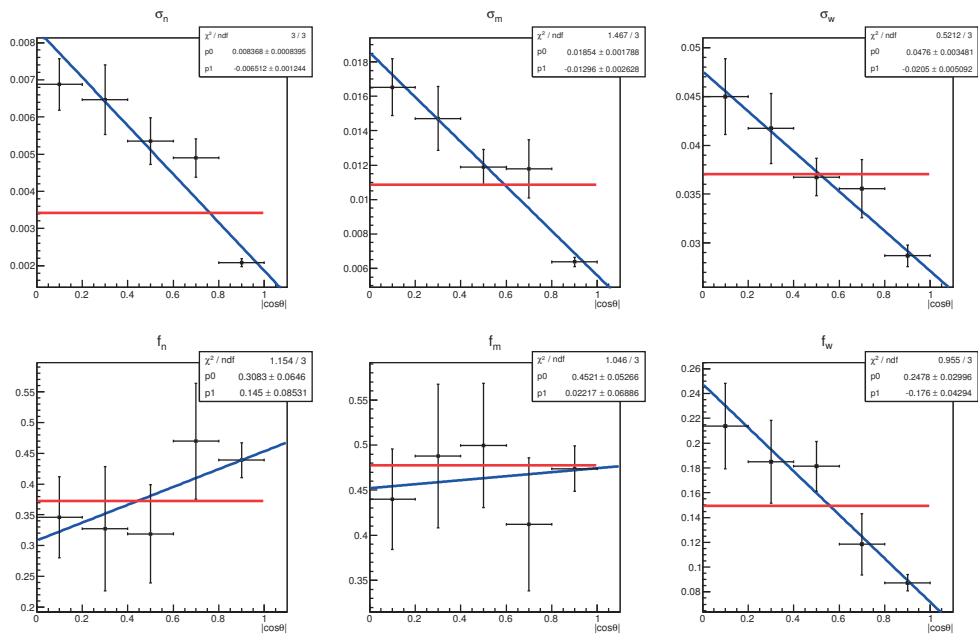
Figure 4.4 Widths (top) and fractions (bottom) of the narrow (left), medium (middle) and wide (right) Gaussians used to describe the $\cos\hat{\theta}$ resolution, as a function of $|\cos\hat{\theta}|$. Linear fits are overlaid in blue, while the average values (considering only one bin) are shown in red.

$1100 < m_{K\pi\pi} < 1300$ MeV/c^2

$1300 < m_{K\pi\pi} < 1400$ MeV/c^2

$1400 < m_{K\pi\pi} < 1600$ MeV/c^2

$1600 < m_{K\pi\pi} < 1900$ MeV/c^2
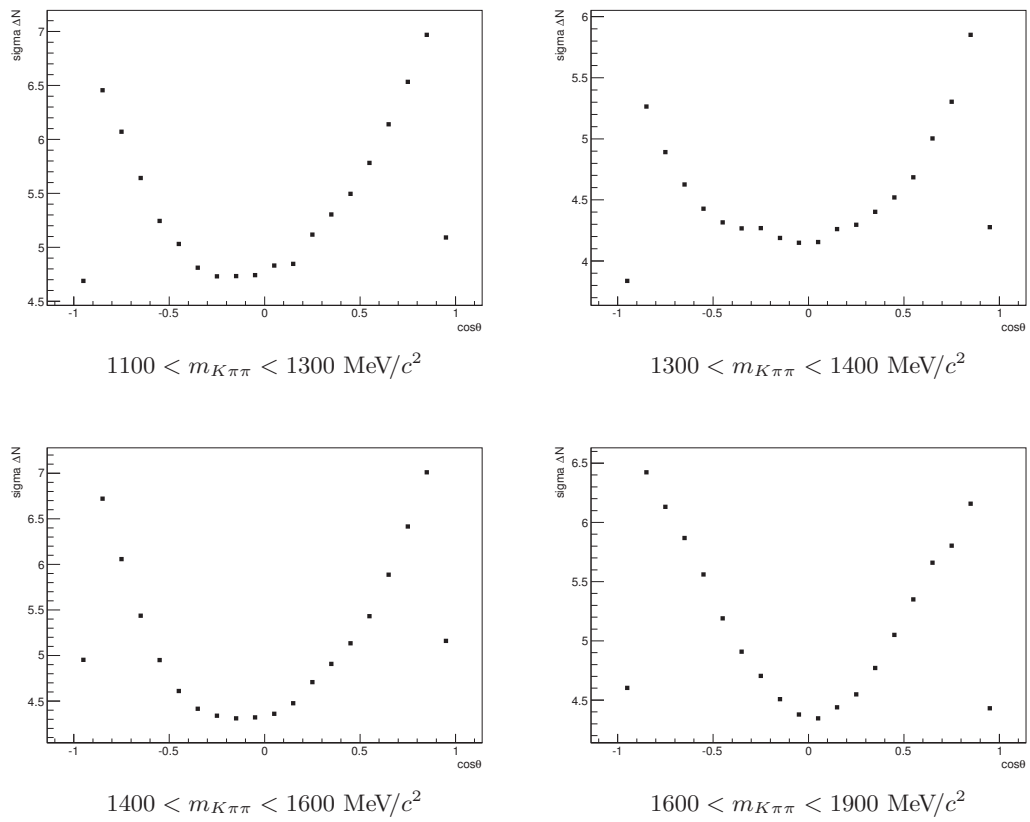
Figure 4.5   Width of the yield difference in bins of $\cos\hat{\theta}$ when comparing the yield in toy MC experiments with or without smearing in $\cos\hat{\theta}$. The first and last bins are subject to boundary effects.

4.2 Angular fit results

A χ^2 fit of the normalised binned angular distribution, built with the signal yields obtained from the simultaneous fits to the data in bins of $\cos\hat{\theta}$, is performed taking into account the full covariance matrix of the bin contents and all the systematic uncertainties.

In order to underline the effect of the photon polarisation on the $\cos\hat{\theta}$ distribution, an analogous fit using an even-only PDF ($c_1 = c_3 = 0$), hence forbidding the terms that carry the λ_γ dependence, is performed for comparison. The results of the two fits are shown in Fig. 4.6 for each $K^+\pi^-\pi^+$ mass interval of interest. The shape of the $\cos\hat{\theta}$ distribution depends on the resonances present in the interval and on their interference pattern. It is interesting to note how the shape of the distribution in the last bin is clearly different from the others.

The fit results are summarized in Tables 4.2 and 4.3, and the corresponding covariance matrices can be found in Tables 4.4 and 4.5.
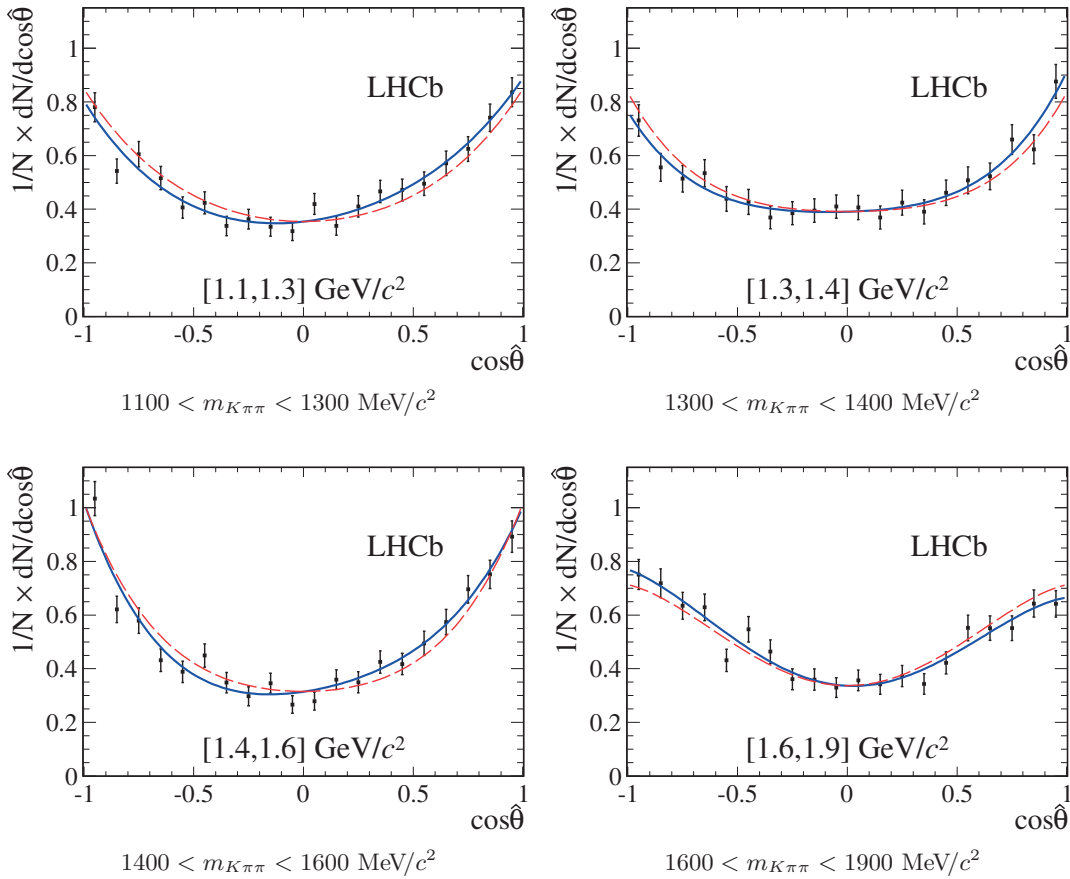
Figure 4.6 Normalised $\cos\hat{\theta}$ distribution for background-subtracted and efficiency-corrected $B^+ \to K^+\pi^-\pi^+\gamma$ events in four intervals of $K^+\pi^-\pi^+$ mass, in the sign-flip scenario. The blue (red) curve is the result of a fit allowing all (only even) Legendre components up to the fourth power.

Table 4.2   Legendre coefficients obtained from fits to the normalised background-subtracted and efficiency-corrected $\cos\hat{\theta}$ distribution in the four $K^+\pi^-\pi^+$ mass intervals of interest in the sign-flip scenario ($\cos\tilde{\theta}$). The quoted uncertainties contain statistical and systematic contributions. The $K^+\pi^-\pi^+$ mass ranges are indicated in GeV/c^2 and all the c parameters and the asymmetries are expressed in units of 10^{-2}.

	$[1.1, 1.3]$	$[1.3, 1.4]$	$[1.4, 1.6]$	$[1.6, 1.9]$
c_1	6.3 ± 1.7	5.4 ± 2.0	4.3 ± 1.9	-4.6 ± 1.8
c_2	31.6 ± 2.2	27.0 ± 2.6	43.1 ± 2.3	28.0 ± 2.3
c_3	-2.1 ± 2.6	2.0 ± 3.1	-5.2 ± 2.8	-0.6 ± 2.7
c_4	3.0 ± 3.0	6.8 ± 3.6	8.1 ± 3.1	-6.2 ± 3.2
$\mathcal{A}_{\mathrm{ud}}$	6.9 ± 1.7	4.9 ± 2.0	5.6 ± 1.8	-4.5 ± 1.9

Table 4.3   Legendre coefficients obtained from fits to the normalised background-subtracted and efficiency-corrected $\cos\hat{\theta}$ distribution in the four $K^+\pi^-\pi^+$ mass intervals of interest in the no-flip scenario ($\cos\theta$). The quoted uncertainties contain statistical and systematic contributions. The $K^+\pi^-\pi^+$ mass ranges are indicated in GeV/c^2 and all the c parameters and the asymmetries are expressed in units of 10^{-2}.

	$[1.1, 1.3]$	$[1.3, 1.4]$	$[1.4, 1.6]$	$[1.6, 1.9]$
c_1	-0.9 ± 1.7	7.4 ± 2.0	5.3 ± 1.9	-3.4 ± 1.8
c_2	31.6 ± 2.2	27.4 ± 2.6	43.6 ± 2.3	27.8 ± 2.3
c_3	0.8 ± 2.6	0.8 ± 3.1	-4.4 ± 2.8	2.3 ± 2.7
c_4	3.4 ± 3.0	7.0 ± 3.6	8.0 ± 3.1	-6.6 ± 3.2
$\mathcal{A}_{\mathrm{ud}}$	-1.1 ± 1.7	7.2 ± 2.0	6.4 ± 1.8	-3.9 ± 1.9

Table 4.4 Covariance matrices (in units of 10^{-3}) obtained from the fit to the background-subtracted $\cos\hat{\theta}$ distribution in the sign-flip scenario for the four $K^+\pi^-\pi^+$ mass intervals on the full 3 fb^{-1} dataset using all the Legendre components.

$[1.1, 1.3]$ GeV/c^2

$$\begin{pmatrix} 0.31 & & & \\ 0.01 & 0.47 & & \\ 0.09 & 0.03 & 0.68 & \\ -0.01 & 0.16 & 0.02 & 0.92 \end{pmatrix}$$

$[1.3, 1.4]$ GeV/c^2

$$\begin{pmatrix} 0.41 & & & \\ 0.02 & 0.66 & & \\ 0.12 & 0.04 & 0.93 & \\ 0.00 & 0.20 & 0.04 & 1.27 \end{pmatrix}$$

$[1.4, 1.6]$ GeV/c^2

$$\begin{pmatrix} 0.35 & & & \\ -0.01 & 0.52 & & \\ 0.14 & 0.00 & 0.76 & \\ -0.03 & 0.23 & -0.01 & 0.99 \end{pmatrix}$$

$[1.6, 1.9]$ GeV/c^2

$$\begin{pmatrix} 0.34 & & & \\ -0.02 & 0.51 & & \\ 0.08 & -0.04 & 0.75 & \\ -0.02 & 0.15 & -0.04 & 1.01 \end{pmatrix}$$

Table 4.5 Covariance matrices (in units of 10^{-3}) obtained from the fit to the background-subtracted $\cos\hat{\theta}$ distribution in the no sign-flip scenario for the four $K^+\pi^-\pi^+$ mass intervals on the full 3 fb^{-1} dataset using all the Legendre components.

$[1.1, 1.3]$ GeV/c^2

$$\begin{pmatrix} 0.30 & & & \\ 0.00 & 0.47 & & \\ 0.09 & 0.02 & 0.68 & \\ 0.02 & 0.16 & 0.02 & 0.92 \end{pmatrix}$$

$[1.3, 1.4]$ GeV/c^2

$$\begin{pmatrix} 0.41 & & & \\ 0.03 & 0.66 & & \\ 0.12 & 0.07 & 0.93 & \\ 0.01 & 0.20 & 0.10 & 1.27 \end{pmatrix}$$

$[1.4, 1.6]$ GeV/c^2

$$\begin{pmatrix} 0.35 & & & \\ 0.01 & 0.53 & & \\ 0.14 & 0.05 & 0.76 & \\ 0.00 & 0.24 & 0.03 & 0.99 \end{pmatrix}$$

$[1.6, 1.9]$ GeV/c^2

$$\begin{pmatrix} 0.34 & & & \\ 0.00 & 0.51 & & \\ 0.08 & 0.00 & 0.75 & \\ 0.02 & 0.15 & -0.01 & 1.01 \end{pmatrix}$$

4.3   Up-down asymmetry results

The up-down asymmetry values obtained from the angular fit are summarized in Fig. 4.7 and in Table 4.6, where the errors include the statistical and systematic uncertainties. The observed sign-change in the last bin can be due to the effect of the 2^- resonances populating that region, which have not been considered in theory works (Sec. 1.2.2).

The combined significance of the observed asymmetries is determined from a χ^2 test with null-hypothesis $\mathcal{A}_{\mathrm{ud}} = 0$ in each $K^+\pi^-\pi^+$ mass interval. The corresponding χ^2 distribution has four degrees of freedom and the observed asymmetries correspond to a p-value of 1.7×10^{-7}. This translates into a $5.2\,\sigma$ significance for the up-down asymmetry to be different from zero in the sign-flip scenario. A $4.6\,\sigma$ effect is found using $\cos\theta$ for describing the direction of the photon (no sign-flip). This result represents the first observation of a parity-violating nonzero photon polarisation in $b \to s\gamma$ transitions.

An alternative approach (and consistency check) to the determination of the significance of the odd components of the $\cos\theta$ distribution—the ones that carry all the photon polarisation information—is computed by making use of the difference in χ^2 $(\Delta\chi^2)$ of the fits to the angular distribution performed using all the Legendre polynomials up to order four or using the even components only. The significance of the odd+even with respect to the even-only hypothesis is computed assuming that $\Delta\chi^2$ is generated by the loss of two degrees of freedom (corresponding to c_1 and c_3); the values obtained are shown in Table 4.7. Assuming that these values are fully independent, and then the sum of their squares behaves as a χ^2 distribution with four degrees of freedom, the observed values correspond to a p-value equal to 3.2×10^{-6}, translating into a $4.7\,\sigma$ significance in the sign-flip scenario. A $4.0\,\sigma$ significance is found in the no-flip scenario.

Table 4.6   Up-down asymmetry values obtained from the angular fit in each bin of $K^+\pi^-\pi^+$ mass for both the sign-flipping and no flipping scenarios. The errors contain statistical and systematical uncertainties.

$m_{K^+\pi^-\pi^+}$ [MeV/c^2]	flip ($\cos\tilde{\theta}$)	no flip ($\cos\theta$)
[1100, 1300]	$+0.069 \pm 0.017$	-0.011 ± 0.017
[1300, 1400]	$+0.049 \pm 0.020$	$+0.072 \pm 0.020$
[1400, 1600]	$+0.056 \pm 0.018$	$+0.064 \pm 0.018$
[1600, 1900]	-0.045 ± 0.019	-0.039 ± 0.019
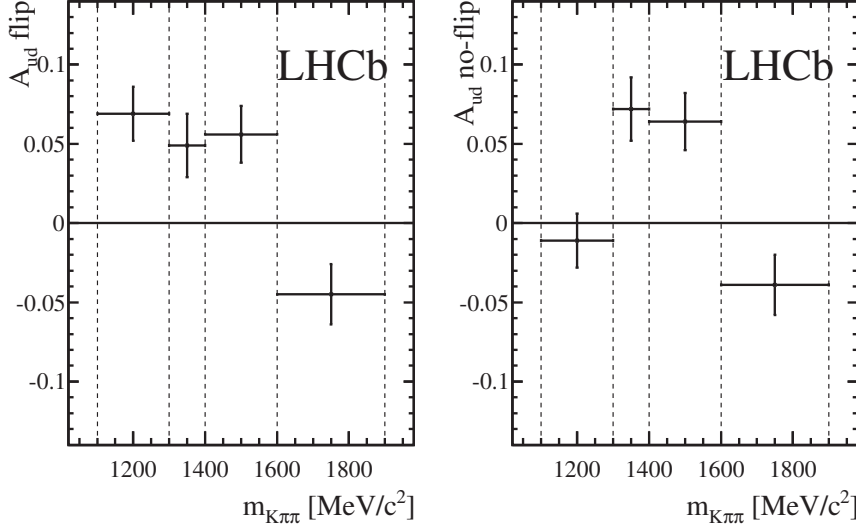
Figure 4.7 Values obtained for $\mathcal{A}_{ud}$ from the angular fit in each interval of $K^+\pi^-\pi^+$ mass for the sign-flip (left) and no-flip (right) scenarios.

Table 4.7 Significance of $\mathcal{A}_{ud}$ with respect to zero, in units of σ, for each interval of $K^+\pi^-\pi^+$ mass for the sign-flip and no-flip scenarios, as obtained from the angular fit described in Sec.4. The significance of the odd Legendre polynomial terms, carrying the photon polarisation information, has been determined from the difference in χ^2 between the fits to the distribution of the signal yield in bins of $\cos\hat\theta$ performed considering all the Legendre polynomial terms up to the order four and the even contributions only.

$m_{K^+\pi^-\pi^+}$ [MeV/c^2]	flip ($\cos\tilde\theta$)	no flip ($\cos\theta$)
[1100, 1300]	3.5	0.26
[1300, 1400]	2.2	3.2
[1400, 1600]	3.0	3.3
[1600, 1900]	2.0	1.6

106

<div align="right">

5

</div>

Amplitude analysis of the $K^+\pi^-\pi^+$ system

The resonant structure of the $K^+\pi^-\pi^+$ final state in the $B^+ \to K^+\pi^-\pi^+\gamma$ decay can be described by means of an amplitude analysis, as introduced in Sec. 1.3.2. A multidimensional unbinned maximum likelihood fit is performed on the background-subtracted $m^2_{K^+\pi^-\pi^+}$, $m^2_{K^+\pi^-}$ and $m^2_{\pi^+\pi^-}$ distributions in order to separate the resonances peaking in the $[1.1, 1.9]\,\mathrm{GeV}/c^2$ $K^+\pi^-\pi^+$ mass interval, and to highlight the interferences that give access to photon polarisation. The photon angular variables are not considered here, as discussed in Sec. 1.3.2.

5.1   Dataset preparation

The three-dimensional background-subtracted distribution in $m^2_{K^+\pi^-\pi^+}$, $m^2_{K^+\pi^-}$ and $m^2_{\pi^+\pi^-}$ is obtained from the B^+ mass fit using the *sPlot* technique, analogously to what is shown in Chapter 3. As first illustrated in a search for $B^0_s \to \phi\phi\gamma$ [123], the B meson mass resolution σ_B depends on the mass of the hadronic system in the final state; this is shown in Fig. 5.1 with simulated samples of different radiative decays (*e.g.* $B^0 \to K^{*0}\gamma$, $B^+ \to K_1(1270)^+\gamma$, *etc.*). To take this effect into account, the background subtracted distribution has been obtained independently in the four $K^+\pi^-\pi^+$ mass intervals introduced earlier. This expedient is useful in reducing the σ_B dependency effect in the fit without adding an explicit dependence of the resolution on $m_{K^+\pi^-\pi^+}$ that would invalidate the *sPlot* procedure, which requires the background-subtracted observables to be independent from the variables used to discriminate signal and background, as σ_B.

The distributions obtained for the three invariant masses are shown in Fig. 5.2.

Figure 5.1 B mass resolution as a function of the mass of the hadronic system in the final state, as obtained in Ref. [123] for various simulated radiative decays.
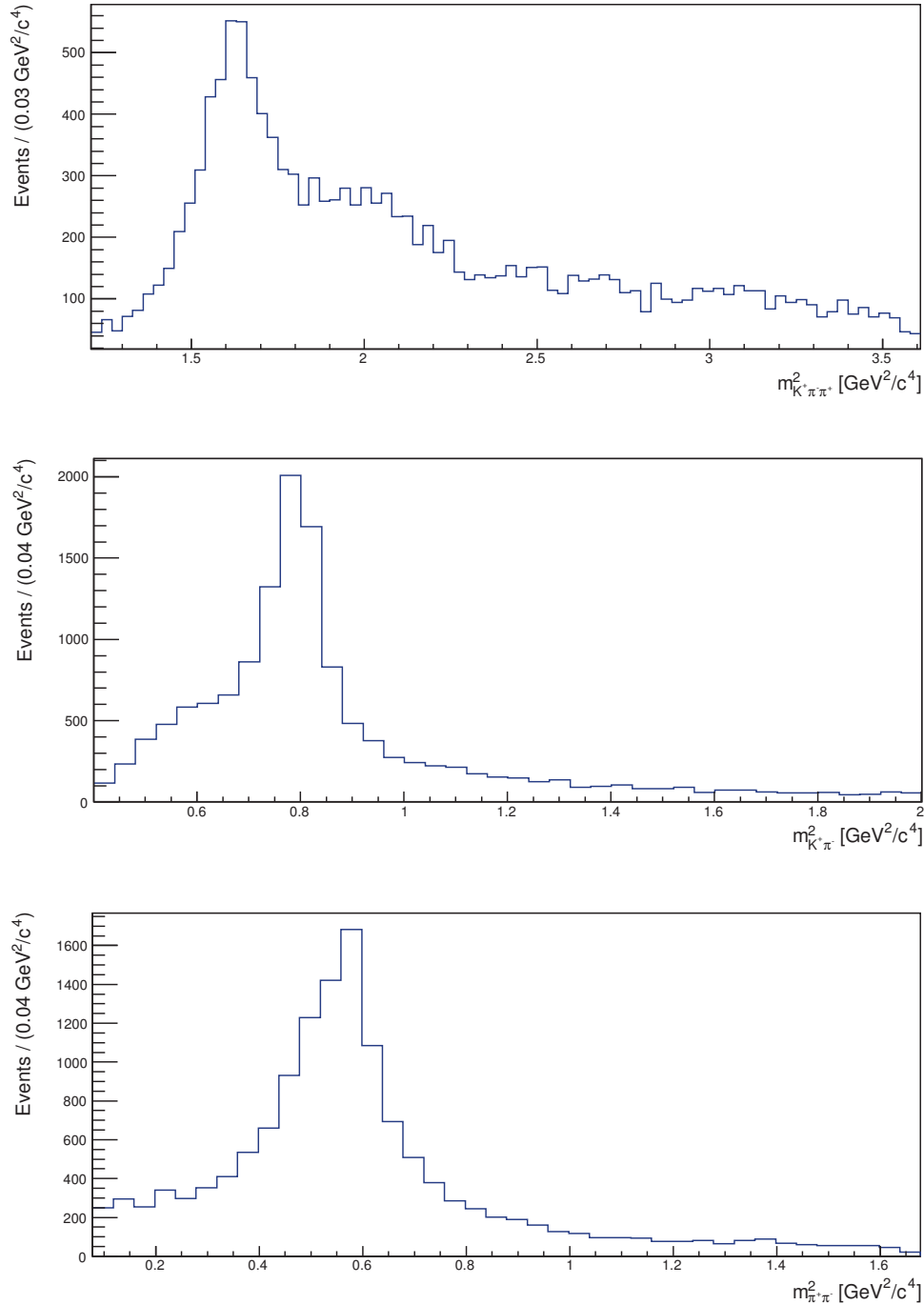
Figure 5.2   Background-subtracted invariant mass squared distribution, in GeV^2/c^4, for $m^2_{K^+\pi^-\pi^+}$, $m^2_{K^+\pi^-}$ and $m^2_{\pi^+\pi^-}$ as obtained using the *sPlot* technique. The *sPlot* weights are obtained from the B-candidate mass fit, as described in Sec. 3.5.2.

5.2 Amplitude analysis formalism

The three-dimensional $(m^2_{K^+\pi^-\pi^+}, m^2_{K^+\pi^-}, m^2_{\pi^+\pi^-})$ distribution is described using a normalised PDF implemented as

$$PDF(\vec{m}) = \frac{\xi(\vec{m}) \times \eta(\vec{m}) \times \text{Signal}(\vec{m})}{\int d\vec{m}\, \xi(\vec{m}) \times \eta(\vec{m}) \times \text{Signal}(\vec{m})}, \tag{5.1}$$

where $\vec{m}$ indicates the three invariant masses of the hadronic system, ξ is the efficiency over the Dalitz plot, η is the $B^+ \to K^+\pi^-\pi^+\gamma$ phase space, and $\text{Signal}(\vec{m})$ is the signal function.

5.2.1 Signal function

As a first approximation and in analogy to Refs. [82, 99], the signal is described as the sum of amplitudes $\mathcal{A}^J_k$ corresponding to various $B^+ \to K^+_{\text{res}}\gamma \to K^+\pi^-\pi^+\gamma$ decay modes k, where only amplitudes with the same K_{res} spin-parity J are allowed to interfere since the $\cos\theta$ variable is integrated out[1]. The resulting signal function has the form

$$\text{Signal}(\vec{m}) = \sum_J \left| \sum_k f_k\, \mathcal{A}^J_k \right|^2 + |f_{\text{nr}}\, \mathcal{A}_{\text{nr}}|^2, \tag{5.2}$$

where f_k is a complex coefficient accounting for the magnitude and phase of the decay k with respect to the other decays in the model. The term in $\mathcal{A}_{\text{nr}}$ represents a non resonant amplitude, assumed to be uniform over the phase space and not interfering with the other amplitudes.

For a decay k of the mother resonance R_1 with spin-parity J_1 into an abc final state through an intermediate daughter resonance R_2 with spin-parity J_2, introducing the notation $R_1 \to aR_2(\to bc)$, the amplitude can be expressed as

$$\mathcal{A}^{J_1}_{R_1 \to aR_2}(\vec{m}) = \tag{5.3}$$
$$\alpha_{J_1, J_2}(\vec{m}) \times F_{J_1}(p) \times \frac{\Gamma_{R_1}/2}{M_{R_1} - m_{abc} - i\,\Gamma_{R_1}/2} \times \frac{m_{bc}\Gamma_{R_2}(m_{bc})}{M^2_{R_2} - m^2_{bc} - i\,m_{bc}\Gamma_{R_2}(m_{bc})}.$$

The α_{J_1, J_2} coefficients, obtained in the Rarita-Schwinger covariant tensor formalism [124], account for the spin-parity of the resonances; they are listed in Table 5.1 for the different spin-parity combinations of interest. Following Ref. [89], the variables $\cos\psi$ and z introduced in Table 5.1 can be written as

$$\cos\psi = \frac{m_{bc}}{4pqm_{abc}} \left[m^2_{ac} - m^2_{ab} + \frac{(m^2_{abc} - m^2_a)(m^2_b - m^2_c)}{m^2_{bc}} \right], \tag{5.4}$$

$$z = p/m_{abc}, \tag{5.5}$$

---

[1]This implies that the contribution from the last line of Eq. 1.133 vanishes in the configuration under study.

Table 5.1 Spin factor α_{J_1,J_2} for the signal PDF, as calculated in Ref. [124] using the Rarita-Schwinger covariant tensor formalism.

J_1	J_2	α_{J_1,J_2}
anything	0^+ 0^-	1
0^+ 0^-	1^+ 1^-	$\sqrt{(1+z^2)\cos^2\psi}$
1^+ 1^-	1^- 1^+	$\sqrt{1+z^2\cos^2\psi}$
1^+ 1^- 2^+ 2^-	1^+ 1^- 1^- 1^+	$\sqrt{1-\cos^2\psi}$
2^+ 2^-	1^+ 1^-	$\sqrt{3+(1+4z^2)\cos^2\psi}$
2^+ 2^-	2^+ 2^-	$\sqrt{1+z^2/9+(z^2/3-1)\cos^2\psi-z^2(\cos^2\psi-1/3)^2}$
2^+ 2^-	2^- 2^+	$\sqrt{1+z^2(1/3+\cos^2\psi)+z^4(\cos^2\psi-1/3)^2}$

where ψ is the angle between the momenta of the particles a and b in the bc rest frame. The breakup momentum p is calculated as the momentum of a (or bc) in the abc rest frame as

$$p^2 = \frac{[m_{abc}^2-(m_a+m_{bc})^2][m_{abc}^2-(m_a-m_{bc})^2]}{4m_{abc}^2} \tag{5.6}$$

and the momentum q of b (or c) in the bc rest frame is found to be

$$q^2 = \frac{[m_{bc}^2-(m_b+m_c)^2][m_{bc}^2-(m_b-m_c)^2]}{4m_{bc}^2}. \tag{5.7}$$

The invariant masses of the abc system satisfy the relation

$$m_{ab}^2 + m_{ac}^2 + m_{bc}^2 = m_{abc}^2 + m_a^2 + m_b^2 + m_c^2, \tag{5.8}$$

analogous to Eq. 1.143, but with the mass of the abc system changing for every event.

The decays of R_1 and R_2 in Eq. 5.3 are described [82, 99] by a non-relativistic and a relativistic Breit-Wigner PDF, respectively, M_{R_i} and Γ_{R_i} being the nominal mass and width of R_i [89]. In the case of the relativistic Breit-Wigner PDF, the R_2 resonance width

$\Gamma_{R_2}(m_{bc})$ depends on the mass as

$$\Gamma_{R_2}(m_{bc}) = \Gamma_{R_2} \left(\frac{q}{q_0}\right)^{2J_2+1} \left(\frac{M_{R_2}}{m_{bc}}\right) F_{J_2}^2(q)\,, \tag{5.9}$$

where q_0 is the momentum q of Eq. 5.7 calculated at the m_{bc} pole, that is M_{R_2}. The Blatt-Weisskopf barrier factor $F_{J_2}(q)$ ensures that the width is well defined far from the decay kinematic threshold by quenching the distribution when the decay products are too slow to generate a sufficient angular momentum to conserve the spin of the resonance. It is defined from Ref. [89] as

$$
\begin{aligned}
F_J(q) &= 1 & J &= 0\,, \\
F_J(q) &= \sqrt{\frac{1 + R^2 q_0^2}{1 + R^2 q^2}} & J &= 1\,, \\
F_J(q) &= \sqrt{\frac{9 + 3R^2 q_0^2 + R^4 q_0^4}{9 + 3R^2 q^2 + R^4 q^4}} & J &= 2\,,
\end{aligned}
\tag{5.10}
$$

where R is the meson radial parameter set to $3\,(\,\mathrm{GeV}/c)^{-1}$.

Analogously, the Blatt-Weisskopf barrier factor $F_{J_1}(p)$ for the decay of the mother resonance R_1 is included in the amplitude, as a correction to the coefficient α_{J_1,J_2}, initially estimated in case R_1 has no width.

5.2.2 Phase space

The phase space term $\eta(\vec{m})$ is implemented as a lookup table in three-dimensional bins of $\vec{m}$ of size $0.03\,\mathrm{GeV}^2/c^4$, obtained from a sample of 1.5×10^8 $B^+ \to K^+\pi^-\pi^+\gamma$ phase space events generated using a decay-specific EvtGen [125] configuration: the generated B^+ are required to decay to $K_{\mathrm{res}}^+\gamma$, with the kaon resonance decaying to a uniform (phase space only) $K^+\pi^-\pi^+$ final state. Figure 5.3 shows the three resulting one-dimensional projections of the phase space distribution.
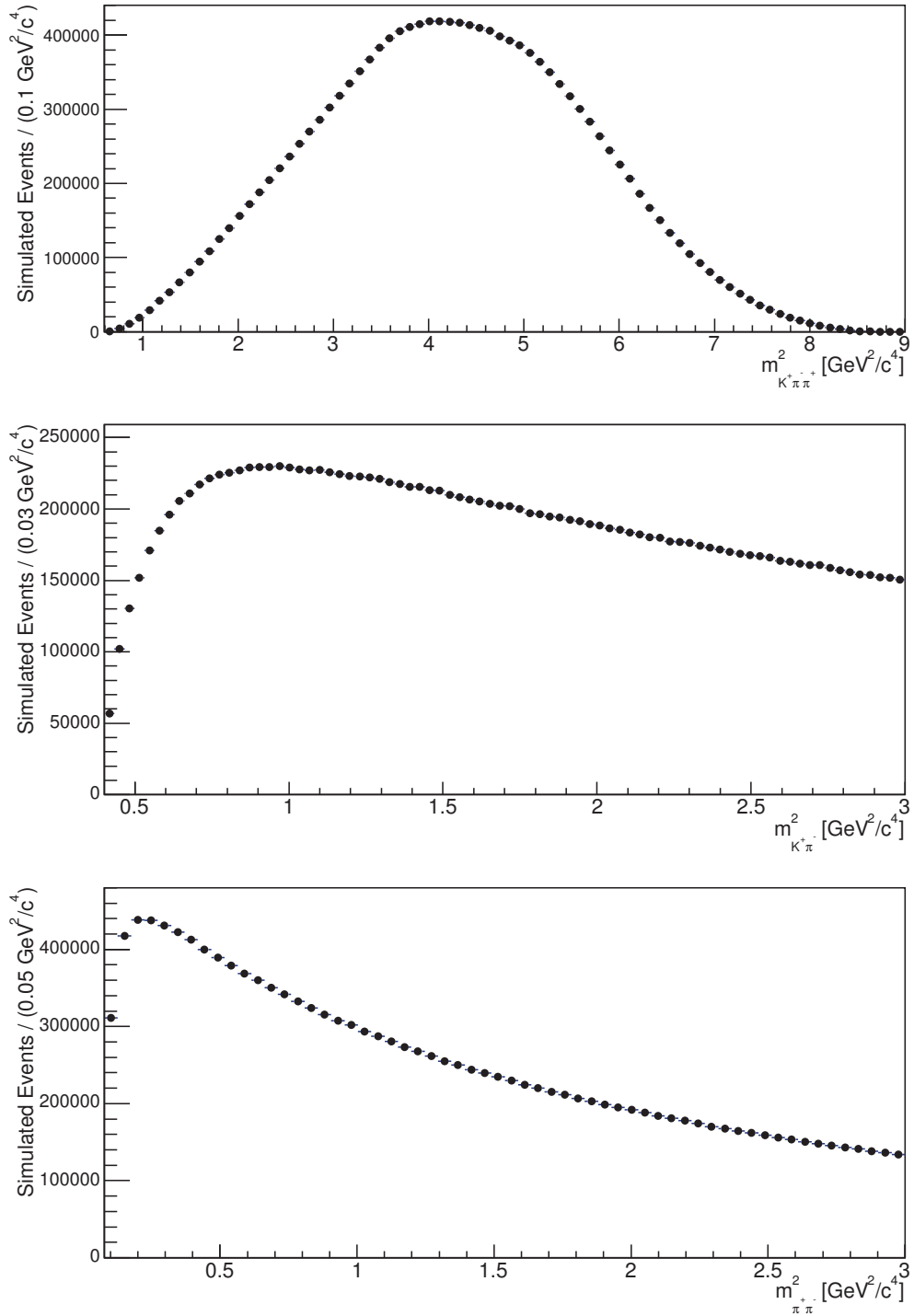
Figure 5.3 $B^+ \to K^+\pi^-\pi^+\gamma$ phase space distributions of $m^2_{K^+\pi^-\pi^+}$ (top), $m^2_{K^+\pi^-}$ (middle) and $m^2_{\pi^+\pi^-}$ (bottom) generated using the EVTGEN package.

5.2.3 Efficiency

The shape of the selection efficiency $\xi(\vec{m})$ over the Dalitz plot is evaluated with MC simulated samples generated using the EVTGEN configuration introduced in Sec. 5.2.2, with a stronger constraint on the allowed mass interval for the $K^+\pi^-\pi^+$ system ($m_{K^+\pi^-\pi^+} \in [1, 2]$ GeV/c^2).

In general, multidimensional efficiency studies require large statistics in order to achieve a high granularity. In the case under study, given the large amount of CPU resources and time needed for the production of the samples, it has not been possible to generate more than 1×10^6 MC simulated events (the generated sample). An additional set of 5×10^5 MC events, the selected sample, is generated by means of a *filtered* production, with Stripping cuts (Sec. 3.2.1) and cut-based offline selection criteria (Sec. 3.2.2) applied at generator level. The MVA selection (Sec. 3.2.2) is applied afterwards.

The two distributions obtained are binned in three-dimensional bins of $\vec{m}$ of size $0.09\,\text{GeV}^2/c^4$ and the selection efficiency is determined as the ratio of selected to generated events in each bin. The chosen binning is coarser that the one used for the phase space because of the lower statistics available. The Dalitz plot of the efficiency distribution in the four studied $K^+\pi^-\pi^+$ mass intervals is shown in Fig. 5.4.

Given the low statistics available, the efficiency map has some empty bins, that would end up giving an inaccurate description of the data in the fit. In order to account for this effect, the efficiency distribution is fitted to a three-dimensional function

$$\xi(x, y, z) = (p_0 + p_1\,x + p_2\,x^2) \times (p_3 + p_4\,y + p_5\,y^2) \times (p_6 + p_7\,z + p_8\,z^2)\,, \qquad (5.11)$$

where $x = m^2_{K^+\pi^-}$, $y = m^2_{K^+\pi^+}{}^2$ and $z = m^2_{\pi^+\pi^-}$, so that the efficiency can be described with a continuous $3D$ surface. The resulting fit parameters are listed in Table 5.2.

Table 5.2   Fit parameters obtained from the three-dimensional fit of the selection efficiency.

Parameter	Value	Unit
p_0	0.997 ± 0.010	
p_1	-0.769 ± 0.025	$(\,\text{GeV}^2/c^4)^{-1}$
p_2	0.447 ± 0.011	$(\,\text{GeV}^2/c^4)^{-2}$
p_3	0.994 ± 0.011	
p_4	-0.692 ± 0.029	$(\,\text{GeV}^2/c^4)^{-1}$
p_5	0.414 ± 0.013	$(\,\text{GeV}^2/c^4)^{-2}$
p_6	0.884 ± 0.030	
p_7	-0.395 ± 0.040	$(\,\text{GeV}^2/c^4)^{-1}$
p_8	0.625 ± 0.039	$(\,\text{GeV}^2/c^4)^{-2}$

---

[2]From Eq. 5.8 follows that $y = m^2_{K^+\pi^+} = m^2_{K^+\pi^-\pi^+} - m^2_{K^+\pi^-} - m^2_{\pi^+\pi^-} + m^2_K + 2m^2_\pi$.

$m_{K^+\pi^-\pi^+} \in [1.1, 1.3]\,\text{GeV}/c^2$

$m_{K^+\pi^-\pi^+} \in [1.3, 1.4]\,\text{GeV}/c^2$

$m_{K^+\pi^-\pi^+} \in [1.4, 1.6]\,\text{GeV}/c^2$

$m_{K^+\pi^-\pi^+} \in [1.6, 1.9]\,\text{GeV}/c^2$
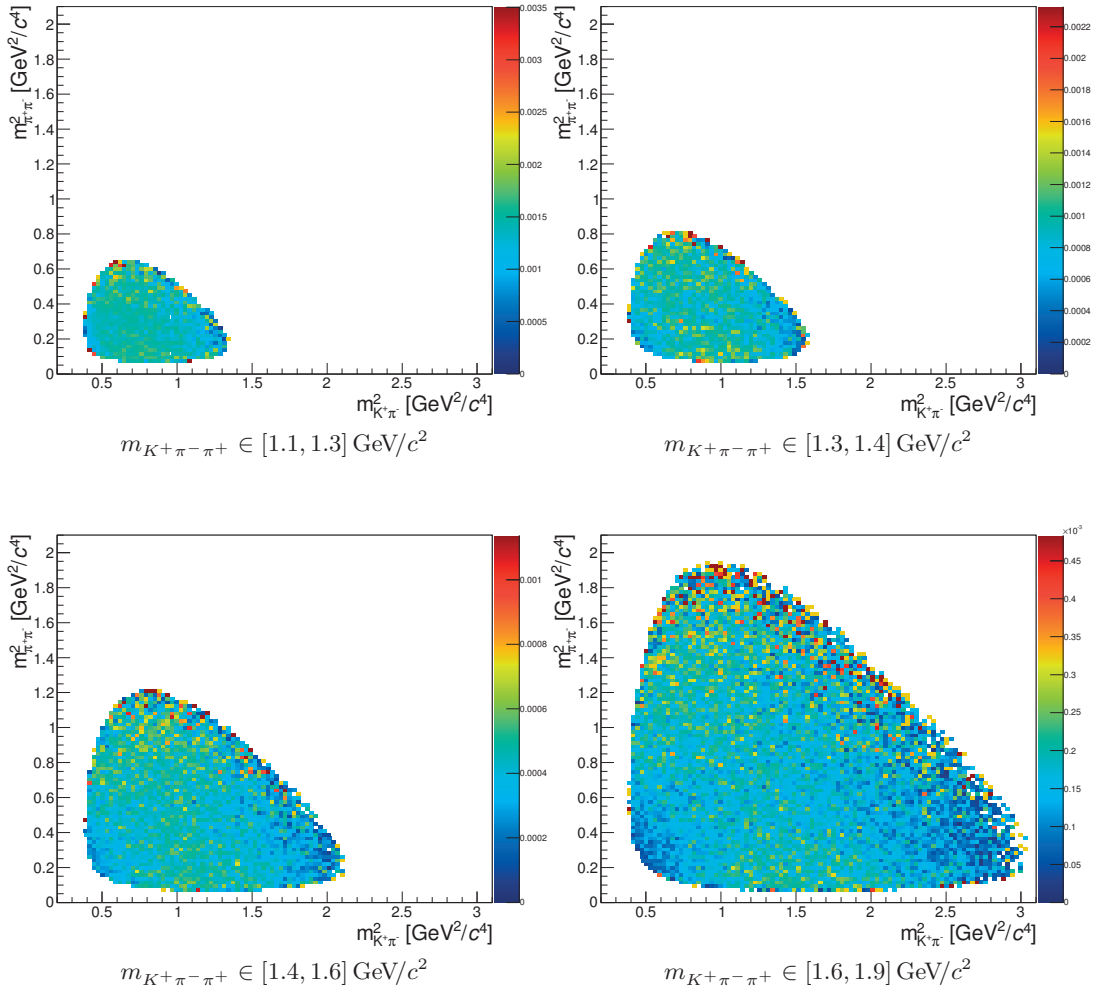
Figure 5.4   Dalitz plots of the $B^+ \to K^+\pi^-\pi^+\gamma$ selection efficiency from simulation in four $K^+\pi^-\pi^+$ mass intervals.

5.2.4 Fitting technique

An unbinned maximum likelihood fit is performed using the CFIT package [126], a framework designed for handling standalone MINUIT [127] fits of Dalitz plots. Originally developed for the Dalitz analysis of the $D^0 \rightarrow K_\mathrm{S}^0 \pi^+ \pi^-$ decay, the framework has been extended for this study to handle different masses, widths and spin-parities of the mother resonances decaying to the $K^+\pi^-\pi^+$ final state. The modular structure of the code has shown to be very practical for this task.

In order to account for the *sPlot* weights w used to describe the dataset, the logarithm of the likelihood to be maximised has the form

$$\ln \mathcal{L} = \alpha \sum_{i=1}^{N_\mathrm{sig}+N_\mathrm{bkg}} w_i \ln PDF(\vec{m}_i) \,, \tag{5.12}$$

where the sum is performed over all (signal and background) events, and with the scaling factor α accounting for the *sPlot* weights in the error estimation[3] defined as

$$\alpha = \frac{\sum_{i=1}^{N_\mathrm{sig}+N_\mathrm{bkg}} w_i}{\sum_{i=1}^{N_\mathrm{sig}+N_\mathrm{bkg}} w_i^2} \,. \tag{5.13}$$

PDF normalisation

The rectangle method approximation is used to perform numerically the integrals required for normalising Eq. 5.1. The integration step size is chosen to be $0.04 \, \mathrm{GeV}^2/c^4$ in $m_{K^+\pi^\mp}^2$ and $m_{\pi^+\pi^-}^2$, for a total of 70 bins in each dimension with the lower limits of integration set at $(m_K + m_\pi)^2$ and $4m_\pi^2$, respectively. For the fit to be sensitive to the narrow $\omega(782)^0$ state, the binning is refined in the mass interval $m_{\pi^+\pi^-}^2 \in [0.57, 0.65] \, \mathrm{GeV}^2/c^4$ where the step size becomes $0.002 \, \mathrm{GeV}^2/c^4$. This granularity represents a good compromise between performance and timing.

It has been checked on simulated pseudo-experiments that a coarser binning in $m_{\pi^+\pi^-}^2$ leads to a biased estimation of the fit parameters related to the $\omega(782)^0$ contributions.

Validation of the PDF

In order to validate the fitter for various decays, the PDF implemented in CFIT is projected on the corresponding EVTGEN-generated samples. For this test, the efficiency is assumed to be uniform, and the event weights in the likelihood (Eq. 5.12) are set to unity for all events. As an example, the projections to the EVTGEN distributions for the 1^+ resonances $K_1(1270)^+$ and $K_1(1400)^+$ decaying to $K^*(892)^0\pi^+$ and $K^+\rho(770)^0$ are shown in Figs. 5.5 and 5.6 respectively. Figures 5.7 and 5.8 show the analogous distributions for the $K_2^*(1430)^+$ and $K^*(1680)^+$ resonances, with spin-parity 2^+ and 1^-

---

[3]This approach is identical to the one used for the study of $B_s^0 \rightarrow J/\psi K^+ K^-$ at LHCb [128].

respectively. A reasonable overall agreement is observed, the main discrepancies being due to minor differences between the description of the decays in the two frameworks.

$$K_1(1270)^+ \to K^*(892)^0\pi^+ \qquad\qquad K_1(1270)^+ \to K^+\rho(770)^0$$
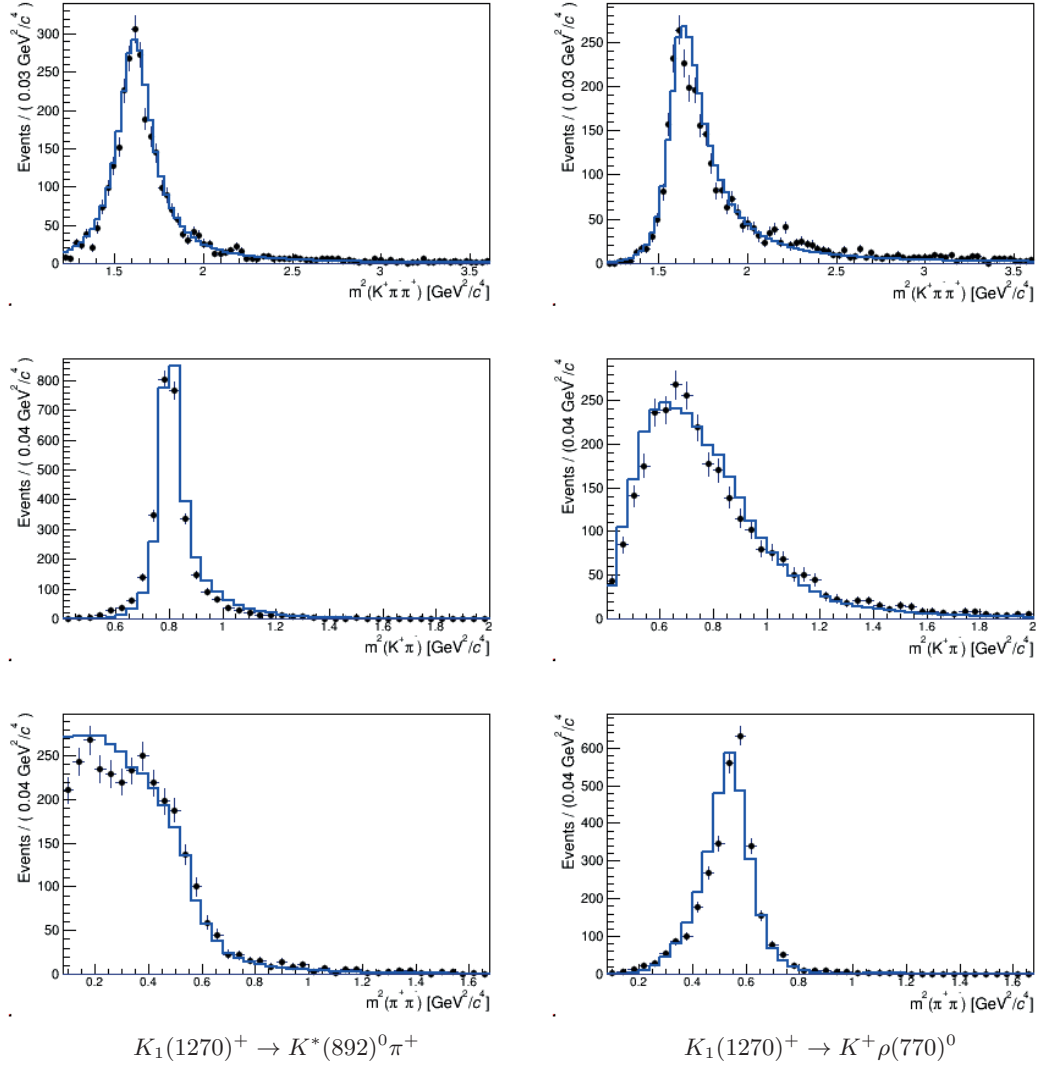
Figure 5.5   Projection of the cFIT PDF (blue curve) on the distribution (data points) for the $K_1(1270)^+ \to K^*(892)^0\pi^+$ (left) and $K_1(1270)^+ \to K^+\rho(770)^0$ (right) decay modes generated with EVTGEN.
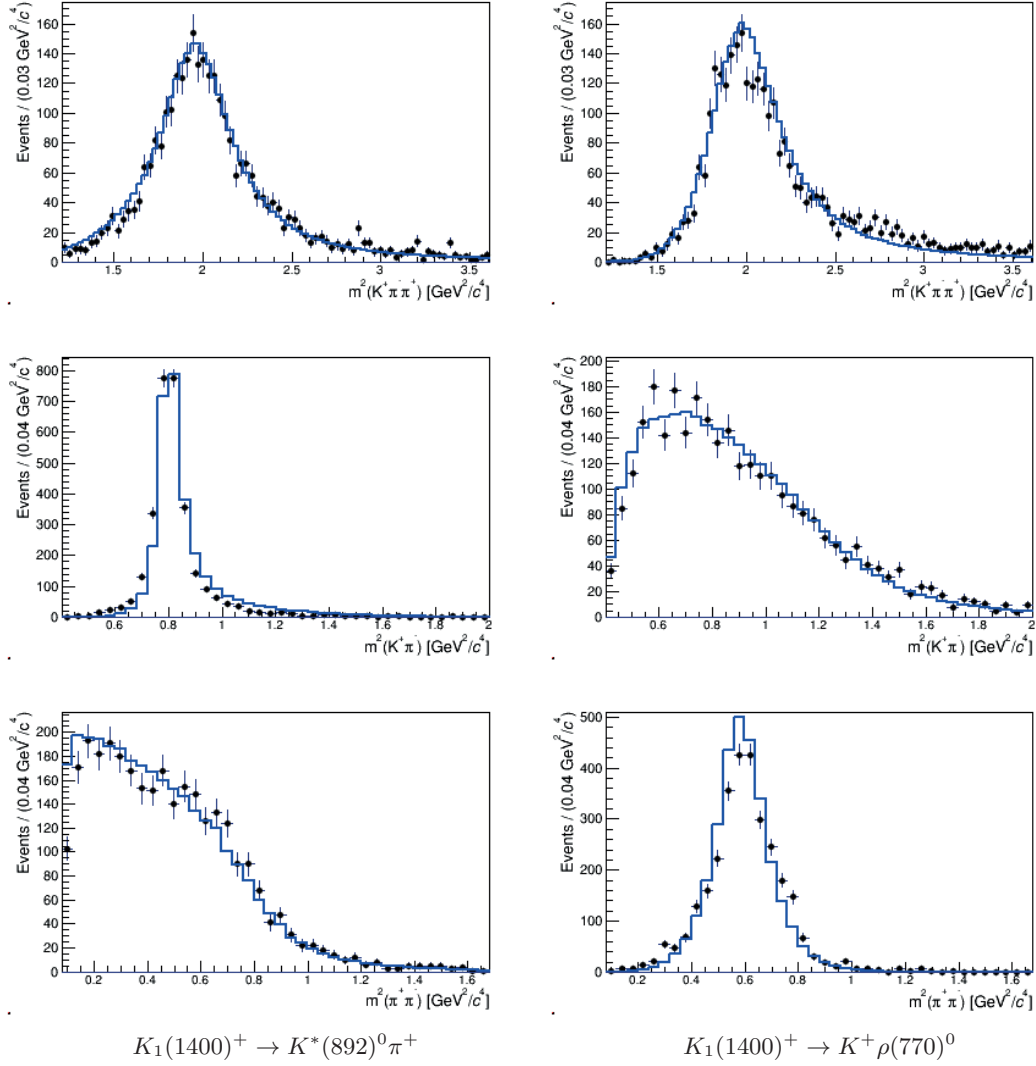
Figure 5.6   Projection of the cFIT PDF (blue curve) on the distribution (data points) for the $K_1(1400)^+ \to K^*(892)^0\pi^+$ (left) and $K_1(1400)^+ \to K^+\rho(770)^0$ (right) decay modes generated with EVTGEN.

$K_2^*(1430)^+ \to K^*(892)^0\pi^+$ $\qquad\qquad$ $K_2^*(1430)^+ \to K^+\rho(770)^0$
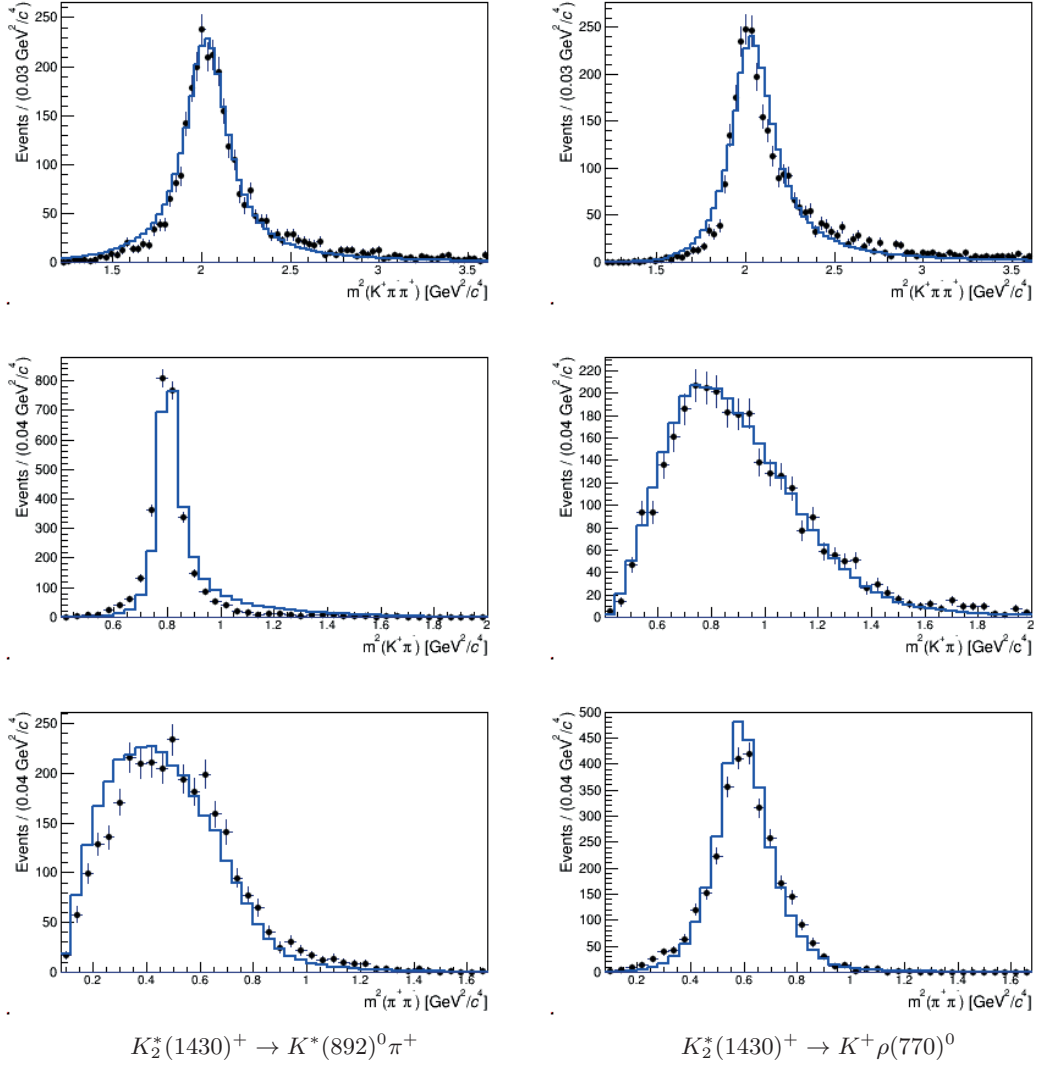
Figure 5.7   Projection of the cFit PDF (blue curve) on the distribution (data points) for the $K_2^*(1430)^+ \to K^*(892)^0\pi^+$ (left) and $K_2^*(1430)^+ \to K^+\rho(770)^0$ (right) decay modes generated with EvtGen.

$$K^*(1680)^+ \to K^*(892)^0\pi^+ \qquad\qquad K^*(1680)^+ \to K^+\rho(770)^0$$
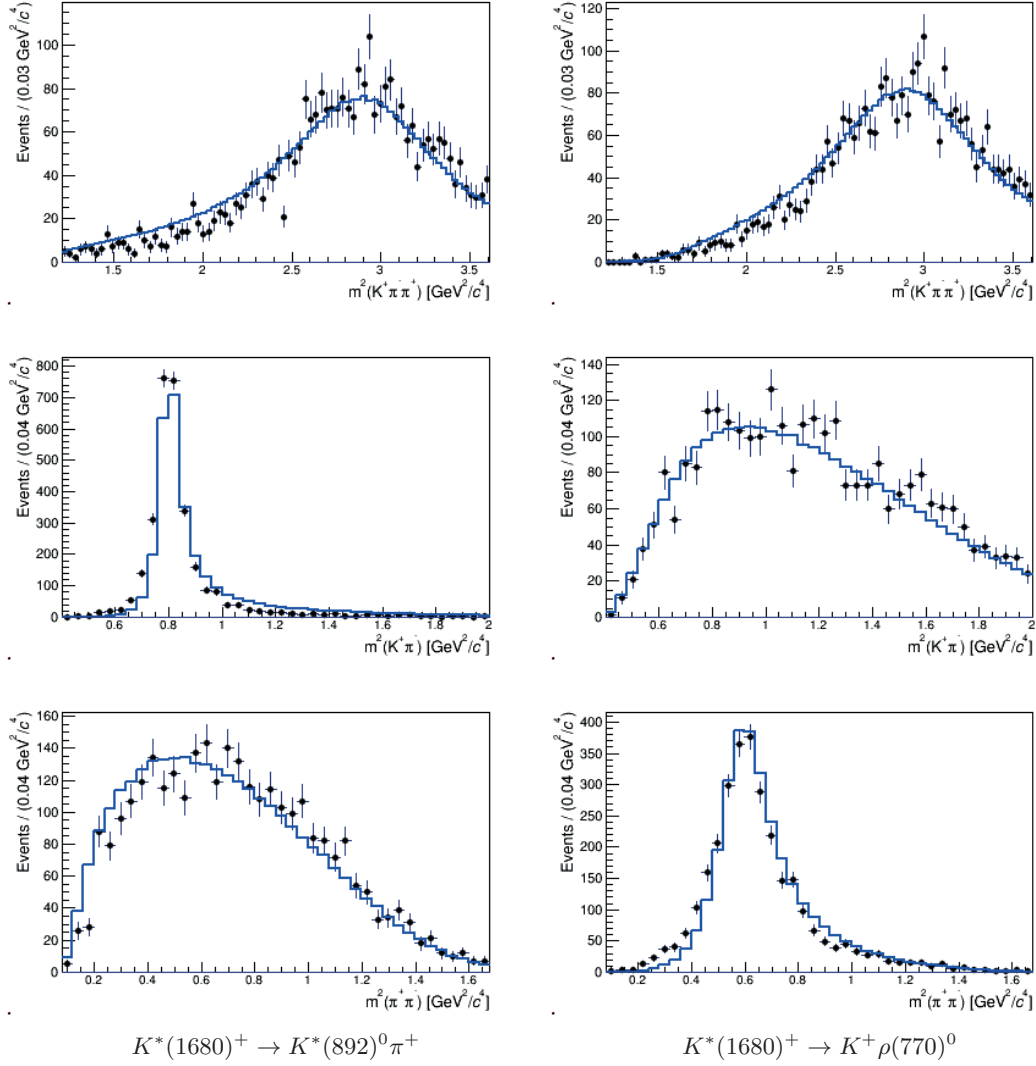
Figure 5.8   Projection of the CFIT PDF (blue curve) on the distribution (data points) for the $K^*(1680)^+ \to K^*(892)^0\pi^+$ (left) and $K^*(1680)^+ \to K^+\rho(770)^0$ (right) decay modes generated with EVTGEN.

5.3 Baseline fit model

The baseline model used for the description of the $K^+\pi^-\pi^+$ mass spectrum in data is detailed in Table 5.3. The decay modes featured in the model have been selected looking

Table 5.3   Baseline fit model.

J_1	Submode	J_2
1^+	$K_1(1270)^+ \to K^*(892)^0\pi^+$	1^-
	$K_1(1270)^+ \to K^+\rho(770)^0$	1^-
	$K_1(1270)^+ \to K^+\omega(782)^0$	1^-
	$K_1(1270)^+ \to K^*(1430)^0\pi^+$	0^+
	$K_1(1400)^+ \to K^*(892)^0\pi^+$	1^-
1^-	$K^*(1410)^+ \to K^*(892)^0\pi^+$	1^-
	$K^*(1680)^+ \to K^+\rho(770)^0$	1^-
	$K^*(1680)^+ \to K^*(892)^0\pi^+$	1^-
2^+	$K_2^*(1430)^+ \to K^*(892)^0\pi^+$	1^-
	$K_2^*(1430)^+ \to K^+\rho(770)^0$	1^-
	$K_2^*(1430)^+ \to K^+\omega(782)^0$	1^-
2^-	$K_2(1600)^+ \to K^*(892)^0\pi^+$	1^-
	$K_2(1600)^+ \to K^+\rho(770)^0$	1^-
	$K_2(1770)^+ \to K^*(892)^0\pi^+$	1^-
	$K_2(1770)^+ \to K^+\rho(770)^0$	1^-
	$K_2(1770)^+ \to K_2^*(1430)^0\pi^+$	2^+
	$K_2(1770)^+ \to K^+f_2(1270)^0$	2^+
	Non resonant	

at the $K^+\pi^-$ and $\pi^+\pi^-$ mass distributions (Fig. 5.9) in the four $K^+\pi^-\pi^+$ mass intervals introduced in Chapter 3, starting from the model developed by the Belle collaboration for the $B^+ \to J/\psi K^+\pi^-\pi^+$ decay [99] and the information provided by the PDG [89]:

- The mother resonance cannot be scalar or pseudoscalar ($J_1 \neq 0^\pm$), because of helicity conservation in the $B^+ \to K_{\mathrm{res}}^+\gamma$ decay.

- In the $K^+\pi^-$ mass spectrum, an evident peak at the $K^*(892)^0$ mass is observed in each $K^+\pi^-\pi^+$ mass interval, while an additional peak at the $K_2^*(1430)^0$ mass can be observed only in the last interval.

- Analogously in the $\pi^+\pi^-$ mass spectrum, the main component is found to be the $\rho(770)^0$, with an additional peak rising at the $f_2(1270)^0$ mass in the last $K^+\pi^-\pi^+$ mass interval. Following the suggestion of Ref. [99], a $K_1(1270)^+ \to K^+\omega(782)^0$ component is added, expected to have a large interference with the dominant $K_1(1270)^+ \to K^+\rho(770)^0$ decay.

- All fit components are assumed to decay to an S wave state.

121
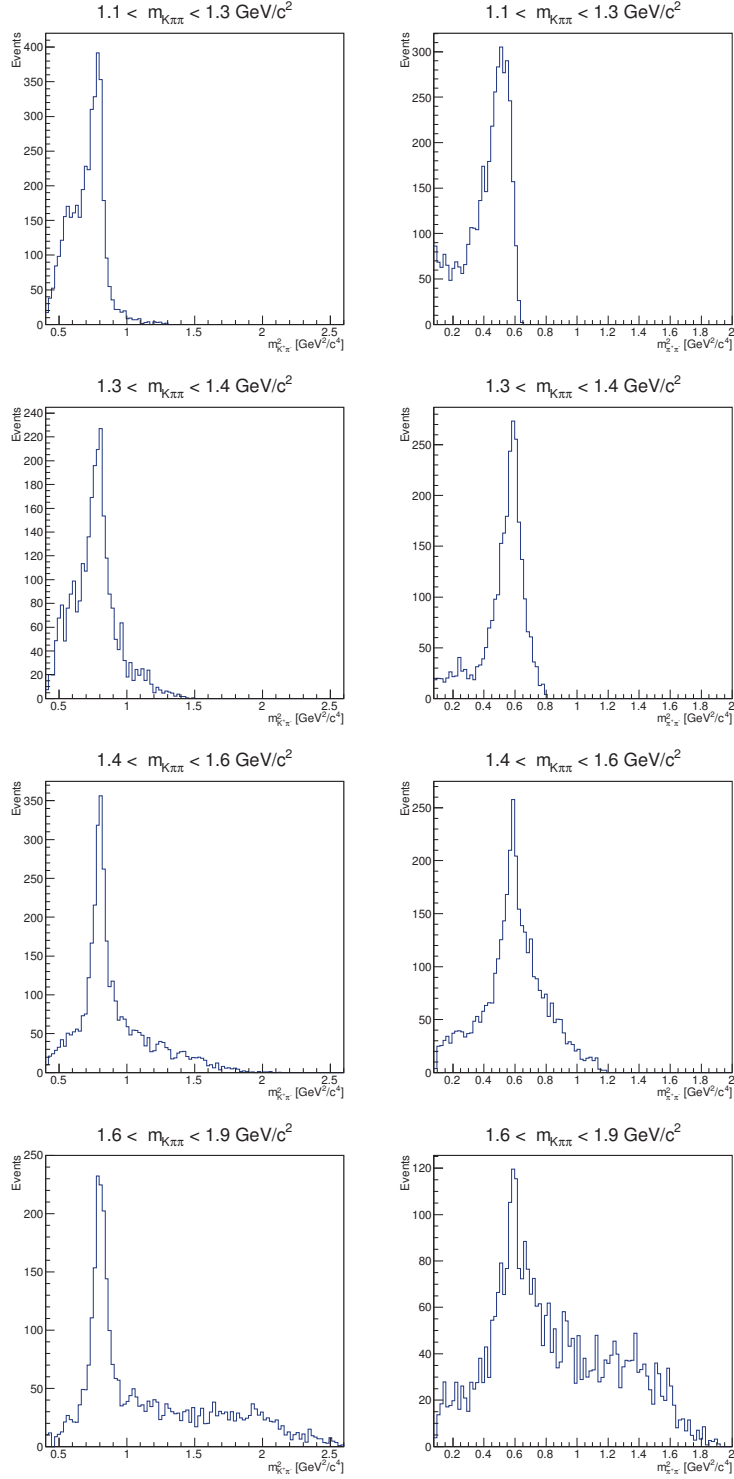
Figure 5.9 Background-subtracted distributions for the $K^+\pi^-$ (left column) and $\pi^+\pi^-$ (right column) invariant masses in the four $K^+\pi^-\pi^+$ mass intervals of interest.

The function built from the 18 amplitudes of the baseline model has 30 free fit parameters, corresponding to the real and imaginary components of the complex decay fractions f_k. The fractions can also be expressed in polar form as $|r_k|\,e^{i\phi_k}$, $|r_k|$ and ϕ_k being the magnitude and phase of the resonance. In each spin-parity term of the PDF, one of the phases is set to zero, so that the remaining ones have to be considered as relative to it. The magnitude for the decay $K_1(1270)^+ \to K^*(892)^0\pi^+$ is set to 1, so that all the other magnitudes are relative to it. The central values and widths of the resonances are fixed in the fit to the corresponding world averages [89]. For the $K_2(1600)^+$, that is not featured in Ref. [89], the central value and width are those of Ref. [92]. In Table 5.4 the masses, widths and spin-parities of the resonances appearing in the model are listed with their respective experimental uncertainties.

Table 5.4   Masses, widths and spin-parities of the resonances appearing in the model. Mother (intermediate) resonances are shown in the upper (lower) panel.

Resonance	mass $[\,\mathrm{GeV}/c^2]$	width $[\,\mathrm{GeV}/c^2]$	J
$K_1(1270)^+$	1.272 ± 0.007	0.090 ± 0.020	1^+
$K_1(1400)^+$	1.403 ± 0.007	0.174 ± 0.013	1^+
$K^*(1410)^+$	1.414 ± 0.020	0.232 ± 0.021	1^-
$K^*(1680)^+$	1.717 ± 0.027	0.320 ± 0.110	1^-
$K_2^*(1430)^+$	1.426 ± 0.002	0.099 ± 0.003	2^+
$K_2(1600)^+$	1.605 ± 0.015	0.115 ± 0.015	2^-
$K_2(1770)^+$	1.773 ± 0.008	0.186 ± 0.014	2^-
$K^*(892)^0$	0.8958 ± 0.0002	0.0474 ± 0.0006	1^-
$\rho(770)^0$	0.7753 ± 0.0003	0.1491 ± 0.0008	1^-
$\omega(782)^0$	0.7827 ± 0.0001	0.00849 ± 0.00008	1^-
$f_2(1270)^0$	1.275 ± 0.001	0.185 ± 0.003	2^+
$K_0^*(1430)^0$	1.425 ± 0.050	0.270 ± 0.080	0^+
$K_2^*(1430)^0$	1.432 ± 0.001	0.109 ± 0.005	2^+

It is important to point out that the fit parameters f_k cannot directly be related to the ratio of branching fractions (and then the abundances of a given decay), since the normalisation of each amplitude and the effect of the phase space must be taken into account. The fit fractions of each decay mode are hence determined integrating over the phase space as

$$FF_k = \frac{|f_k|^2 \int d^3\vec{m}\,\eta(\vec{m})\,\mathcal{A}_k^J(\vec{m})\mathcal{A}_k^{J\,*}(\vec{m})}{\int d^3\vec{m}\ PDF(\vec{m})|_{\xi(\vec{m})=1}}\,, \tag{5.14}$$

where $PDF(\vec{m})|_{\xi(\vec{m})=1}$ is defined as the PDF of Eq. 5.1 with $\xi(\vec{m})=1$. The interferences between different decay modes cause the sum of all fit fractions to deviate from 1. This is fixed introducing fit fractions for the interference terms, defined as

$$FF_{k,l} = \begin{cases} \dfrac{2\mathcal{R}e\big[f_k f_l^*\int d^3\vec{m}\,\eta(\vec{m})\,\mathcal{A}_k^J(\vec{m})\mathcal{A}_l^{J\,*}(\vec{m})\big]}{\int d^3\vec{m}\ PDF(\vec{m})|_{\xi(\vec{m})=1}} & \text{if } k \text{ and } l \text{ interfere } (l>k) \\ 0 & \text{otherwise}\,, \end{cases} \tag{5.15}$$

so that by definition

$$\sum_k \left(FF_k + \sum_{l>k} FF_{k,l} \right) = 1 \,. \qquad (5.16)$$

5.4 Results of the fit to data

The results of the fit to the background-subtracted data distributions in $m^2_{K^+\pi^-\pi^+}$, $m^2_{K^+\pi^-}$ and $m^2_{\pi^+\pi^-}$ using the nominal fit model are shown in Fig. 5.10, with the colour code for the fit components detailed in Table 5.5. The resulting fit parameters and the corresponding fit fractions are listed in Tables 5.6 and 5.7. Simulated distributions generated from the fit results are used to determine the uncertainties on the fit fractions, assigned using 68% confidence level intervals. The results of this simulation are shown in Sec. 5.4.1.

To better understand how the fit components vary with the mass of the $K^+\pi^-\pi^+$ system, the fit results are projected in the four $K^+\pi^-\pi^+$ mass intervals introduced in Chapter 3, meaning that the results obtained from the nominal fit are superimposed to the data distribution in each $m_{K^+\pi^-\pi^+}$ interval. The projections are shown in Fig. 5.11, and the corresponding interval-by-interval fit fractions are listed in Tables 5.8–5.11. The knowledge of the interval-by-interval resonance content is expected to help understanding the differences in the $\cos\hat\theta$ distributions observed in Fig. 4.6.

From Fig. 5.10 it can be seen that the fit to the distribution is not satisfactory for low values of $m^2_{K^+\pi^-\pi^+}$. To account for this effect, the fit on data has been repeated freeing the width of the $K_1(1270)^+$ resonance, obtaining a value of 0.1163 ± 0.0023 GeV/c^2 against a nominal value of 0.090 ± 0.020 GeV/c^2. The change in width reduces the fit fraction of the $K_1(1270)^+ \to K^+\rho(770)^0$ mode from 39.9% to 34.1% (the statistical error being smaller than 1%), while the other fractions adjust to account for this variation. In this configuration, the overall fit to the distribution improves in the low mass region, but it degrades at the $K_1(1270)^+$ peak, indicating that a change in the width alone cannot explain the poor description of the data at low $K^+\pi^-\pi^+$ masses. Including the D wave component of the $K_1(1270)^+ \to K^*(892)\pi^+$ decay and the wide κ resonance, introduced in Sec. 1.3.1, might help increasing the quality of the fit in that region. An additional improvement to the description of the signal function at low $K^+\pi^-\pi^+$ mass might be achieved using a LASS parametrisation [129] for shaping the $K\pi$ scalar (0^+) component.
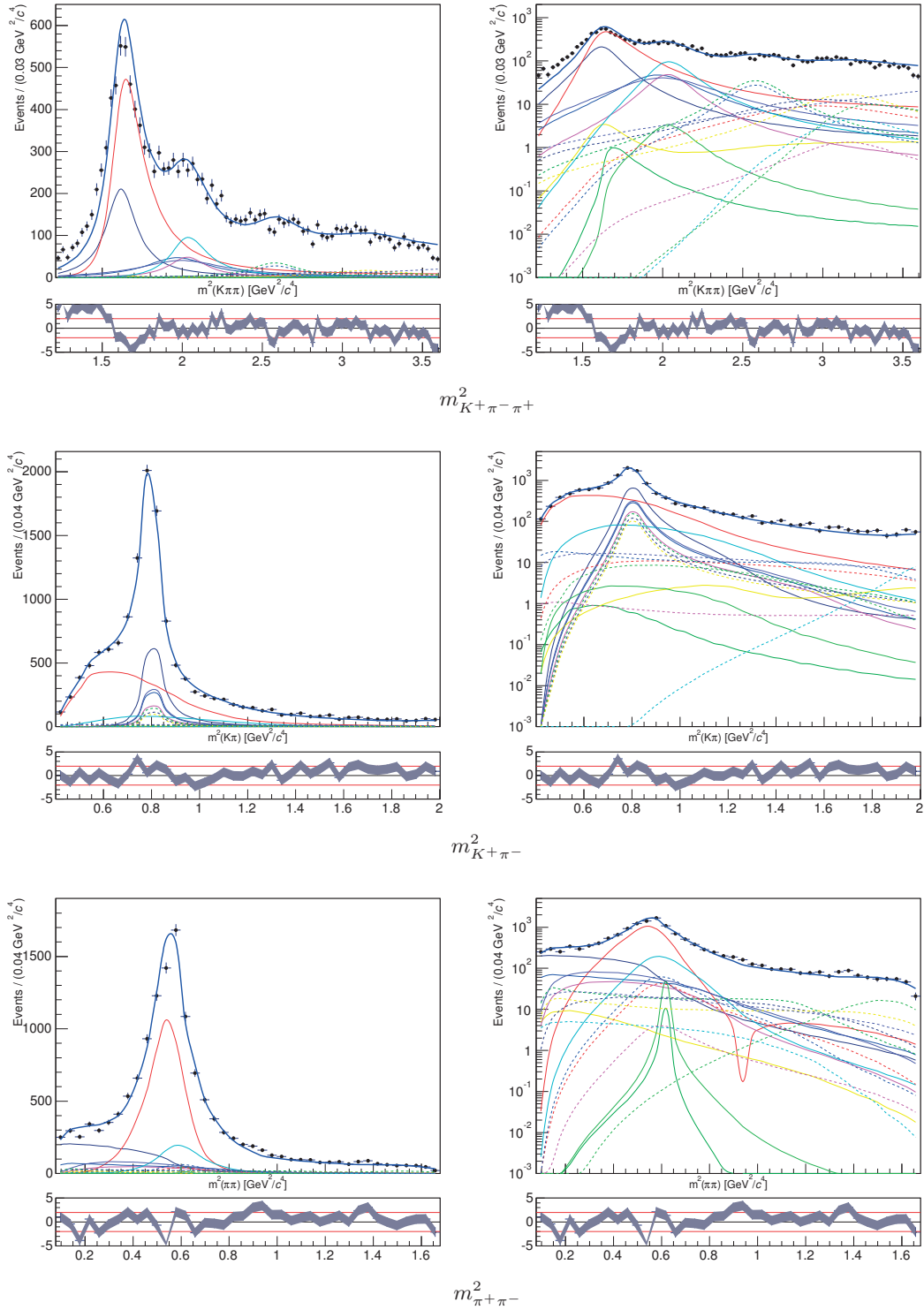
Figure 5.10 Background-subtracted distributions of $m^2_{K^+\pi^-\pi^+}$ (top), $m^2_{K^+\pi^-}$ (middle) and $m^2_{\pi^+\pi^-}$ (bottom) in linear (left) and logarithmic (right) scale. The fit results for the nominal model are superimposed. The colour code for the fit components is given in Table 5.5. The χ^2 residuals are included in the lower part of the plot as an indication of the quality of the fit.

Table 5.5 Colour code for the fit components of the nominal model.

—— Total Fit	—— $K_1(1270) \to K^*(892)\,\pi$
—— $K_1(1270) \to \rho(770)\,K$	—— $K_1(1270) \to \omega(782)\,K$
—— $K_1(1400) \to K^*(892)\,\pi$	—— $K_1(1270) \to K_0^*(1430)\,\pi$
—— $K_2^*(1430) \to K^*(892)\,\pi$	—— $K_2^*(1430) \to \rho(770)\,K$
—— $K_2^*(1430) \to \omega(782)\,K$	—— $K^*(1410) \to K^*(892)\,\pi$
------ $K^*(1680) \to K^*(892)\,\pi$	------ $K^*(1680) \to \rho(770)\,K$
------ $K_2(1600) \to K^*(892)\,\pi$	------ $K_2(1600) \to \rho(770)\,K$
------ $K_2(1770) \to K^*(892)\,\pi$	------ $K_2(1770) \to \rho(770)\,K$
------ $K_2(1770) \to K_2^*(1430)\,\pi$	------ $K_2(1770) \to f_2(1270)\,K$
------ Non resonant	

Table 5.6 Results of the $K^+\pi^-\pi^+$ amplitude analysis using the nominal fit model. The parameters given without error are fixed in the fit. The fit fraction uncertainties are determined from simulation. The table is divided in sections according to the spin-parity of the mother resonances, as in Table 5.3.

Decay channel k	$\mathcal{R}e[f_k]$	$\mathcal{I}m[f_k]$	$FF_k\ (10^{-2})$
$K_1(1270)^+ \to K^*(892)^0\pi^+$	1 (fixed)	0 (fixed)	16.8 ± 0.9
$K_1(1270)^+ \to K^+\rho(770)^0$	1.072 ± 0.050	-1.379 ± 0.047	$39.9\,^{+0.6}_{-0.7}$
$K_1(1270)^+ \to K^+\omega(782)^0$	0.288 ± 0.086	0.090 ± 0.081	$0.068\,^{+0.028}_{-0.180}$
$K_1(1270)^+ \to K^*(1430)^0\pi^+$	-0.025 ± 0.062	-0.381 ± 0.055	$0.69\,^{+0.22}_{-0.20}$
$K_1(1400)^+ \to K^*(892)^0\pi^+$	0.306 ± 0.024	-0.288 ± 0.020	7.8 ± 0.8
$K^*(1410)^+ \to K^*(892)^0\pi^+$	-0.479 ± 0.042	0 (fixed)	$8.4\,^{+2.8}_{-3.3}$
$K^*(1680)^+ \to K^*(892)^0\pi^+$	0.198 ± 0.020	0.094 ± 0.028	$3.5\,^{+1.7}_{-2.1}$
$K^*(1680)^+ \to K^+\rho(770)^0$	0.019 ± 0.025	0.1104 ± 0.0097	2.4 ± 0.4
$K_2^*(1430)^+ \to K^*(892)^0\pi^+$	-0.509 ± 0.034	0 (fixed)	4.8 ± 1.0
$K_2^*(1430)^+ \to K^+\rho(770)^0$	-0.115 ± 0.047	0.497 ± 0.024	9.0 ± 0.8
$K_2^*(1430)^+ \to K^+\omega(782)^0$	-0.234 ± 0.072	-0.236 ± 0.084	$0.30\,^{+0.13}_{-0.26}$
$K_2(1600)^+ \to K^*(892)^0\pi^+$	-0.1666 ± 0.0088	0.044 ± 0.021	$4.4\,^{+0.9}_{-1.0}$
$K_2(1600)^+ \to K^+\rho(770)^0$	-0.073 ± 0.011	0.061 ± 0.013	$3.33\,^{+0.34}_{-0.50}$
$K_2(1770)^+ \to K^*(892)^0\pi^+$	0.1072 ± 0.0078	0 (fixed)	$3.0\,^{+0.6}_{-0.8}$
$K_2(1770)^+ \to K^+\rho(770)^0$	-0.0147 ± 0.0044	0.0103 ± 0.0050	$0.23\,^{+0.08}_{-0.32}$
$K_2(1770)^+ \to K_2^*(1430)^0\pi^+$	-0.041 ± 0.012	-0.0772 ± 0.0077	$0.67\,^{+0.10}_{-0.09}$
$K_2(1770)^+ \to K^+f_2(1270)^0$	0.1673 ± 0.0071	-0.029 ± 0.015	$1.30\,^{+0.15}_{-0.16}$
Non resonant	-0.0511 ± 0.0021	0 (fixed)	4.1 ± 0.5

Table 5.7 Fit fractions, in units of 10^{-2}, obtained for the total fit to the multidimensional data distribution using the nominal fit model. The fit fractions for each decay mode are on the diagonal (in boldface), while the interference fit fractions are out of the diagonal. The table is separated in sections according to the spin-parity of the mother resonances, as in Table 5.3. The errors on the fit fractions are determined from simulation.

1^+

	$K_1(1270)\to K^*\pi$	$K_1(1270)\to K\rho$	$K_1(1270)\to K\omega$	$K_1(1270)\to K^*(1430)\pi$	$K_1(1400)\to K^*\pi$
$K_1(1270)\to K^*\pi$	**16.8 ± 0.9**				
$K_1(1270)\to K\rho$	$-3.4^{+0.5}_{-0.4}$	**39.9$^{+0.6}_{-0.7}$**			
$K_1(1270)\to K\omega$	0.11 ± 0.07	$1.08^{+0.70}_{-0.11}$	**0.068$^{+0.028}_{-0.180}$**		
$K_1(1270)\to K^*(1430)\pi$	-2.5 ± 0.4	1.4 ± 0.7	$-0.032^{+0.024}_{-0.020}$	**0.69$^{+0.22}_{-0.20}$**	
$K_1(1400)\to K^*\pi$	$-2.2^{+1.3}_{-1.5}$	$5.78^{+0.40}_{-0.34}$	$0.028^{+0.027}_{-0.009}$	$-0.75^{+0.28}_{-0.27}$	**7.8 ± 0.8**

1^-

	$K^*(1410)\to K^*\pi$	$K^*(1680)\to K^*\pi$	$K^*(1680)\to K\rho$
$K^*(1410)\to K^*\pi$	**8.4$^{+2.8}_{-3.3}$**		
$K^*(1680)\to K^*\pi$	$-5.9^{+4.4}_{-3.7}$	**3.5$^{+1.7}_{-2.1}$**	
$K^*(1680)\to K\rho$	$-1.5^{+0.8}_{-0.6}$	1.6 ± 0.4	**2.4 ± 0.4**

2^+

	$K_2^*(1430)\to K^*\pi$	$K_2^*(1430)\to K\rho$	$K_2^*(1430)\to K\omega$
$K_2^*(1430)\to K^*\pi$	**4.8 ± 1.0**		
$K_2^*(1430)\to K\rho$	-1.7 ± 0.5	**9.0 ± 0.8**	
$K_2^*(1430)\to K\omega$	0.16 ± 0.04	$-0.7^{+0.7}_{-0.4}$	**0.30$^{+0.13}_{-0.26}$**

2^-

	$K_2(1600)\to K^*\pi$	$K_2(1600)\to K\rho$	$K_2(1770)\to K^*\pi$	$K_2(1770)\to K\rho$	$K_2(1770)\to K^*(1430)\pi$	$K_2(1770)\to K f_2(1270)$
$K_2(1600)\to K^*\pi$	**4.4$^{+0.9}_{-1.0}$**					
$K_2(1600)\to K\rho$	1.0 ± 0.4	**3.33$^{+0.34}_{-0.50}$**				
$K_2(1770)\to K^*\pi$	$-3.6^{+1.3}_{-1.2}$	$-0.95^{+0.11}_{-0.15}$	**3.0$^{+0.6}_{-0.8}$**			
$K_2(1770)\to K\rho$	-0.11 ± 0.08	$0.65^{+0.60}_{-0.05}$	$-0.18^{+0.11}_{-0.12}$	**0.23$^{+0.08}_{-0.32}$**		
$K_2(1770)\to K^*(1430)\pi$	$-0.14^{+0.08}_{-0.07}$	$0.255^{+0.050}_{-0.011}$	-0.31 ± 0.09	$0.047^{+0.028}_{-0.040}$	**0.67$^{+0.10}_{-0.09}$**	
$K_2(1770)\to K f_2(1270)$	$0.57^{+0.07}_{-0.08}$	$0.66^{+0.09}_{-0.06}$	$-0.23^{+0.18}_{-0.17}$	$0.04^{+0.15}_{-0.04}$	$-0.004^{+0.040}_{-0.032}$	**1.30$^{+0.15}_{-0.16}$**

Non resonant

Non resonant	**4.1 ± 0.5**

$m_{K^+\pi^-\pi^+} \in [1.1, 1.3] \text{ GeV}/c^2$

$m_{K^+\pi^-\pi^+} \in [1.3, 1.4] \text{ GeV}/c^2$

$m_{K^+\pi^-\pi^+} \in [1.4, 1.6] \text{ GeV}/c^2$

$m_{K^+\pi^-\pi^+} \in [1.6, 1.9] \text{ GeV}/c^2$

Figure 5.11 Background-subtracted distribution of $m^2_{K^+\pi^-}$ (left) and $m^2_{\pi^+\pi^-}$ (right) in the four $K^+\pi^-\pi^+$ mass intervals (from top to bottom), together with the projections of the nominal fit. The colour code for the fit components is given in Table 5.5.

128

Table 5.8 Fit fractions, in units of 10^{-2}, obtained for the total fit to the multidimensional data distribution using the nominal fit model in the $m_{K^+\pi^-\pi^+}$ mass interval [1.1, 1.3] GeV/c^2. The fit fractions for each decay mode are on the diagonal (in boldface), while the interference fit fractions are out of the diagonal. The table is separated in sections according to the spin-parity of the mother resonances, as in Table 5.3. The errors on the fit fractions are determined from simulation.

1^+

	$K_1(1270)\to K^*\pi$	$K_1(1270)\to K\rho$	$K_1(1270)\to K\omega$	$K_1(1270)\to K^*(1430)\pi$	$K_1(1400)\to K^*\pi$
$K_1(1270)\to K^*\pi$	$\mathbf{34.7^{+1.7}_{-1.5}}$	$-7.0^{+0.9}_{-0.8}$	$0.18^{+0.12}_{-0.13}$	-4.6 ± 0.8	$3.2^{+1.3}_{-1.5}$
$K_1(1270)\to K\rho$		$\mathbf{55.9^{+0.9}_{-1.2}}$	$1.62^{+0.80}_{-0.25}$	2.8 ± 1.0	5.2 ± 0.4
$K_1(1270)\to K\omega$			$\mathbf{0.046^{+0.020}_{-0.120}}$	$-0.030^{+0.040}_{-0.025}$	$0.057^{+0.027}_{-0.010}$
$K_1(1270)\to K^*(1430)\pi$				$\mathbf{0.65^{+0.21}_{-0.20}}$	-0.70 ± 0.25
$K_1(1400)\to K^*\pi$					$\mathbf{3.5\pm0.4}$

1^-

	$K^*(1410)\to K^*\pi$	$K^*(1680)\to K^*\pi$	$K^*(1680)\to K\rho$
$K^*(1410)\to K^*\pi$	$\mathbf{4.3^{+1.4}_{-1.7}}$	-3.0 ± 1.2	$-0.24^{+0.06}_{-0.07}$
$K^*(1680)\to K^*\pi$		$\mathbf{0.55^{+0.27}_{-0.34}}$	$0.085^{+0.014}_{-0.022}$
$K^*(1680)\to K\rho$			$\mathbf{0.073^{+0.013}_{-0.014}}$

2^+

	$K_2^*(1430)\to K^*\pi$	$K_2^*(1430)\to K\rho$	$K_2^*(1430)\to K\omega$
$K_2^*(1430)\to K^*\pi$	$\mathbf{0.97^{+0.20}_{-0.19}}$	-0.23 ± 0.05	0.015 ± 0.006
$K_2^*(1430)\to K\rho$		$\mathbf{0.52\pm0.05}$	$0.009^{+0.014}_{-0.015}$
$K_2^*(1430)\to K\omega$			$\mathbf{0.0081^{+0.0035}_{-0.0070}}$

2^-

	$K_2(1600)\to K^*\pi$	$K_2(1600)\to K\rho$	$K_2(1770)\to K^*\pi$	$K_2(1770)\to K\rho$	$K_2(1770)\to K^*(1430)\pi$	$K_2(1770)\to Kf_2(1270)$
$K_2(1600)\to K^*\pi$	$\mathbf{0.30^{+0.06}_{-0.07}}$	$0.008^{+0.012}_{-0.010}$	$-0.49^{+0.10}_{-0.08}$	$0.003^{+0.006}_{-0.004}$	0.0017 ± 0.0008	-0.0007 ± 0.0007
$K_2(1600)\to K\rho$		$\mathbf{0.044^{+0.004}_{-0.007}}$	$0.006^{+0.014}_{-0.008}$	$0.022^{+0.013}_{-0.006}$	$0.00009^{+0.00020}_{-0.00009}$	$-0.00316^{+0.00033}_{-0.0006}$
$K_2(1770)\to K^*\pi$			$\mathbf{0.21^{+0.04}_{-0.06}}$	$0.0004^{+0.0024}_{-0.0040}$	-0.0008 ± 0.0005	$-0.00001^{+0.00024}_{-0.00032}$
$K_2(1770)\to K\rho$				$\mathbf{0.0028^{+0.0010}_{-0.0040}}$	$(4.3^{+4.5}_{-6.3})\times10^{-5}$	$-0.00077^{+0.00040}_{-0.00028}$
$K_2(1770)\to K^*(1430)\pi$					$\mathbf{(4.5\pm0.7)\times10^{-5}}$	$(-8.9^{+7.4}_{-6.9})\times10^{-6}$
$K_2(1770)\to Kf_2(1270)$						$\mathbf{(7.0^{+0.8}_{-0.9})\times10^{-5}}$

Non resonant	
Non resonant	$\mathbf{0.89\pm0.10}$

129

Table 5.9 Fit fractions, in units of 10^{-2}, obtained for the total fit to the multidimensional data distribution using the nominal fit model in the $m_{K^+\pi^-\pi^+}$ mass interval $[1.3, 1.4]\,\mathrm{GeV}/c^2$. The fit fractions for each decay mode are on the diagonal (in boldface), while the interference fit fractions are out of the diagonal. The table is separated in sections according to the spin-parity of the mother resonances, as in Table 5.3. The errors on the fit fractions are determined from simulation.

1^+	$K_1(1270)$ $\to K^*\pi$	$K_1(1270)$ $\to K\rho$	$K_1(1270)$ $\to K\omega$	$K_1(1270)$ $\to K^*(1430)\pi$	$K_1(1400)$ $\to K^*\pi$
$K_1(1270) \to K^*\pi$	**18.3 ± 1.1**				
$K_1(1270) \to K\rho$	$-3.6^{+0.6}_{-0.5}$	**$62.7^{+1.0}_{-1.3}$**			
$K_1(1270) \to K\omega$	$0.15^{+0.09}_{-0.08}$	$1.79^{+1.20}_{-0.22}$	**$0.15^{+0.05}_{-0.40}$**		
$K_1(1270) \to K^*(1430)\pi$	-2.7 ± 0.5	1.2 ± 1.0	$-0.061^{+0.033}_{-0.034}$	**$0.59^{+0.19}_{-0.17}$**	
$K_1(1400) \to K^*\pi$	$-16.3^{+2.4}_{-2.7}$	9.5 ± 0.6	$-0.022^{+0.040}_{-0.032}$	0.2 ± 0.4	**10.5 ± 1.2**

1^-	$K^*(1410)$ $\to K^*\pi$	$K^*(1680)$ $\to K^*\pi$	$K^*(1680)$ $\to K\rho$
$K^*(1410) \to K^*\pi$	**$9.5^{+3.1}_{-3.6}$**		
$K^*(1680) \to K^*\pi$	$-5.1^{+2.8}_{-2.5}$	**$0.8^{+0.4}_{-0.5}$**	
$K^*(1680) \to K\rho$	$-0.85^{+0.40}_{-0.24}$	0.24 ± 0.06	**0.36 ± 0.07**

2^+	$K^*_2(1430)$ $\to K^*\pi$	$K^*_2(1430)$ $\to K\rho$	$K^*_2(1430)$ $\to K\omega$
$K^*_2(1430) \to K^*\pi$	**$5.0^{+1.1}_{-1.0}$**		
$K^*_2(1430) \to K\rho$	-1.8 ± 0.4	**8.0 ± 0.7**	
$K^*_2(1430) \to K\omega$	0.15 ± 0.04	$-0.6^{+0.6}_{-0.4}$	**$0.30^{+0.13}_{-0.26}$**

2^-	$K_2(1600)$ $\to K^*\pi$	$K_2(1600)$ $\to K\rho$	$K_2(1770)$ $\to K^*\pi$	$K_2(1770)$ $\to K\rho$	$K_2(1770)$ $\to K^*(1430)\pi$	$K_2(1770)$ $\to K f_2(1270)$
$K_2(1600) \to K^*\pi$	**$0.62^{+0.12}_{-0.14}$**					
$K_2(1600) \to K\rho$	0.06 ± 0.04	**$0.296^{+0.029}_{-0.050}$**				
$K_2(1770) \to K^*\pi$	$-0.87^{+0.18}_{-0.14}$	$-0.013^{+0.007}_{-0.035}$	**$0.33^{+0.07}_{-0.08}$**			
$K_2(1770) \to K\rho$	$0.017^{+0.015}_{-0.012}$	$0.131^{+0.070}_{-0.034}$	$-0.005^{+0.007}_{-0.009}$	**$0.015^{+0.006}_{-0.021}$**		
$K_2(1770) \to K^*(1430)\pi$	$0.0030^{+0.0032}_{-0.0029}$	$0.0026^{+0.0013}_{-0.0012}$	$-0.0001^{+0.0010}_{-0.0016}$	$0.000006^{+0.00025}_{-0.00040}$	**$0.00042^{+0.00007}_{-0.00006}$**	
$K_2(1770) \to K f_2(1270)$	$0.0006^{+0.0033}_{-0.0024}$	$-0.013^{+0.005}_{-0.007}$	$-0.0028^{+0.0017}_{-0.0015}$	$-0.0003^{+0.0024}_{-0.0015}$	$(-7.4 \pm 5.9) \times 10^{-5}$	**$0.00068^{+0.00008}_{-0.00009}$**

Non resonant	
Non resonant	$1.12^{+0.12}_{-0.13}$

Table 5.10 Fit fractions, in units of 10^{-2}, obtained for the total fit to the multidimensional data distribution using the nominal fit model in the $m_{K^+\pi^-\pi^+}$ mass interval [1.4, 1.6] GeV/c^2. The fit fractions for each decay mode are on the diagonal (in boldface), while the interference fit fractions are out of the diagonal. The table is separated in sections according to the spin-parity of the mother resonances, as in Table 5.3. The errors on the fit fractions are determined from simulation.

1^+

	$K_1(1270)$ $\to K^*\pi$	$K_1(1270)$ $\to K\rho$	$K_1(1270)$ $\to K\omega$	$K_1(1270)$ $\to K^*(1430)\pi$	$K_1(1400)$ $\to K^*\pi$
$K_1(1270) \to K^*\pi$	$\mathbf{4.69}^{+0.28}_{-0.25}$				
$K_1(1270) \to K\rho$	$-0.95^{+0.18}_{-0.15}$	$\mathbf{20.9}^{+0.4}_{-0.5}$			
$K_1(1270) \to K\omega$	$0.048^{+0.027}_{-0.024}$	$0.44^{+0.40}_{-0.08}$	$\mathbf{0.049}^{+0.020}_{-0.130}$		
$K_1(1270) \to K^*(1430)\pi$	$-0.99^{+0.19}_{-0.21}$	$0.20^{+0.40}_{-0.18}$	-0.026 ± 0.012	$\mathbf{0.48}^{+0.15}_{-0.14}$	
$K_1(1400) \to K^*\pi$	$0.7^{+1.1}_{-1.2}$	$6.6^{+0.5}_{-0.4}$	$0.044^{+0.032}_{-0.011}$	-1.43 ± 0.32	$\mathbf{12.9} \pm 1.4$

1^-

	$K^*(1410)$ $\to K^*\pi$	$K^*(1680)$ $\to K^*\pi$	$K^*(1680)$ $\to K\rho$
$K^*(1410) \to K^*\pi$	$\mathbf{14.1}^{+4.7}_{-5.4}$		
$K^*(1680) \to K^*\pi$	$-6.2^{+6.3}_{-5.4}$	$\mathbf{3.1}^{+1.5}_{-1.9}$	
$K^*(1680) \to K\rho$	$-2.0^{+1.6}_{-1.1}$	$1.32^{+0.33}_{-0.32}$	$\mathbf{2.1} \pm 0.4$

2^+

	$K_2^*(1430)$ $\to K^*\pi$	$K_2^*(1430)$ $\to K\rho$	$K_2^*(1430)$ $\to K\omega$
$K_2^*(1430) \to K^*\pi$	$\mathbf{11.0}^{+2.2}_{-2.3}$		
$K_2^*(1430) \to K\rho$	-4.1 ± 1.2	$\mathbf{23.1}^{+1.9}_{-2.0}$	
$K_2^*(1430) \to K\omega$	0.39 ± 0.10	$-1.8^{+1.7}_{-1.1}$	$\mathbf{0.75}^{+0.33}_{-0.60}$

2^-

	$K_2(1600)$ $\to K^*\pi$	$K_2(1600)$ $\to K\rho$	$K_2(1770)$ $\to K^*\pi$	$K_2(1770)$ $\to K\rho$	$K_2(1770)$ $\to K^*(1430)\pi$	$K_2(1770)$ $\to K f_2(1270)$
$K_2(1600) \to K^*\pi$	$\mathbf{7.4}^{+1.5}_{-1.7}$					
$K_2(1600) \to K\rho$	1.5 ± 0.6	$\mathbf{5.4}^{+0.6}_{-0.9}$				
$K_2(1770) \to K^*\pi$	$-6.0^{+1.6}_{-1.3}$	$-0.76^{+0.23}_{-0.22}$	$\mathbf{1.41}^{+0.29}_{-0.35}$			
$K_2(1770) \to K\rho$	$0.08^{+0.14}_{-0.10}$	$1.28^{+0.80}_{-0.14}$	$-0.06^{+0.04}_{-0.05}$	$\mathbf{0.10}^{+0.04}_{-0.14}$		
$K_2(1770) \to K^*(1430)\pi$	$-0.056^{+0.014}_{-0.060}$	$0.163^{+0.040}_{-0.022}$	$-0.003^{+0.012}_{-0.021}$	$0.016^{+0.005}_{-0.008}$	$\mathbf{0.043}^{+0.007}_{-0.006}$	
$K_2(1770) \to K f_2(1270)$	0.24 ± 0.05	$0.21^{+0.09}_{-0.12}$	$-0.074^{+0.023}_{-0.021}$	$0.00492^{+0.02500}_{-0.00021}$	$-0.0023^{+0.0010}_{-0.0023}$	$\mathbf{0.0312}^{+0.0034}_{-0.0040}$

Non resonant

Non resonant	$\mathbf{3.3} \pm 0.4$

Table 5.11 Fit fractions, in units of 10^{-2}, obtained for the total fit to the multidimensional data distribution using the nominal fit model in the $m_{K^+\pi^-\pi^+}$ mass interval $[1.6, 1.9]$ GeV/c^2. The fit fractions for each decay mode are on the diagonal (in boldface), while the interference fit fractions are out of the diagonal. The table is separated in sections according to the spin-parity of the mother resonances, as in Table 5.3. The errors on the fit fractions are determined from simulation.

1^+

	$K_1(1270)$ $\to K^*\pi$	$K_1(1270)$ $\to K\rho$	$K_1(1270)$ $\to K\omega$	$K_1(1270)$ $\to K^*(1430)\pi$	$K_1(1400)$ $\to K^*\pi$
$K_1(1270) \to K^*\pi$	**2.13** $^{+0.12}_{-0.11}$				
$K_1(1270) \to K\rho$	-0.66 ± 0.04	**10.27** $^{+0.23}_{-0.26}$			
$K_1(1270) \to K\omega$	$0.009^{+0.006}_{-0.007}$	$0.18^{+0.19}_{-0.04}$	**0.021** $^{+0.009}_{-0.060}$		
$K_1(1270) \to K^*(1430)\pi$	$-1.10^{+0.17}_{-0.18}$	1.10 ± 0.21	$-0.007^{+0.009}_{-0.006}$	**1.2** ± 0.4	
$K_1(1400) \to K^*\pi$	$3.25^{+0.27}_{-0.26}$	$0.45^{+0.10}_{-0.09}$	$0.020^{+0.007}_{-0.005}$	$-1.08^{+0.20}_{-0.21}$	**3.6** ± 0.4

1^-

	$K^*(1410)$ $\to K^*\pi$	$K^*(1680)$ $\to K^*\pi$	$K^*(1680)$ $\to K\rho$
$K^*(1410) \to K^*\pi$	**5.5** $^{+1.8}_{-2.1}$		
$K^*(1680) \to K^*\pi$	$-11.6^{+8.9}_{-7.4}$	**13.1** $^{+6.4}_{-8.0}$	
$\to K\rho$	$-3.8^{+1.8}_{-1.3}$	6.2 ± 1.7	**9.6** $^{+1.7}_{-1.8}$

2^+

	$K_2^*(1430)$ $\to K^*\pi$	$K_2^*(1430)$ $\to K\rho$	$K_2^*(1430)$ $\to K\omega$
$K_2^*(1430) \to K^*\pi$	**1.40** $^{+0.28}_{-0.27}$		
$K_2^*(1430) \to K\rho$	$-0.45^{+0.19}_{-0.20}$	**3.55** $^{+0.35}_{-0.33}$	
$\to K\omega$	$0.057^{+0.015}_{-0.013}$	$-0.29^{+0.24}_{-0.15}$	**0.10** $^{+0.04}_{-0.08}$

2^-

	$K_2(1600)$ $\to K^*\pi$	$K_2(1600)$ $\to K\rho$	$K_2(1770)$ $\to K^*\pi$	$K_2(1770)$ $\to K\rho$	$K_2(1770)$ $\to K^*(1430)\pi$	$K_2(1770)$ $\to K f_2(1270)$
$K_2(1600) \to K^*\pi$	**12.2** $^{+2.4}_{-2.9}$					
$K_2(1600) \to K\rho$	3.0 ± 1.1	**9.9** $^{+0.9}_{-1.6}$				
$K_2(1770) \to K^*\pi$	$-9.0^{+4.9}_{-4.6}$	$-4.2^{+0.5}_{-0.8}$	**14.0** $^{+2.9}_{-3.6}$			
$K_2(1770) \to K\rho$	$-0.76^{+0.60}_{-0.32}$	$1.5^{+2.6}_{-0.4}$	$-0.9^{+0.5}_{-0.6}$	**1.1** $^{+0.4}_{-1.6}$		
$K_2(1770) \to K^*(1430)\pi$	$-0.68^{+0.34}_{-0.32}$	$1.18^{+0.22}_{-0.04}$	-1.7 ± 0.5	$0.24^{+0.14}_{-0.20}$	**3.7** ± 0.5	
$K_2(1770) \to K f_2(1270)$	2.8 ± 0.4	$3.41^{+0.50}_{-0.19}$	$-1.2^{+1.0}_{-0.9}$	$0.25^{+0.80}_{-0.20}$	$-0.02^{+0.24}_{-0.17}$	**7.3** $^{+0.8}_{-0.9}$

Non resonant

Non resonant	**14.8** $^{+1.6}_{-1.7}$

5.4.1 Fit validation with simulated experiment

A set of 500 pseudo-experiments is generated from the results of the fit to the data using the baseline model and fitted to the PDF of Eq. 5.1 to evaluate the stability of the fit and validate the fit on data. The resulting fit fractions are expected to distribute around the nominal fit values (Table 5.7), unless their estimation is biased. The distributions obtained are used to determine the error on the fit fractions, assigned using 68% confidence level intervals, centred on the mean of the simulated distribution. The histograms obtained for the two dominant modes $K_1(1270)^+ \to K^*(892)^0\pi^+$ and $K_1(1270)^+ \to K^+\rho(770)^0$ are shown, as an example, in Fig. 5.12.
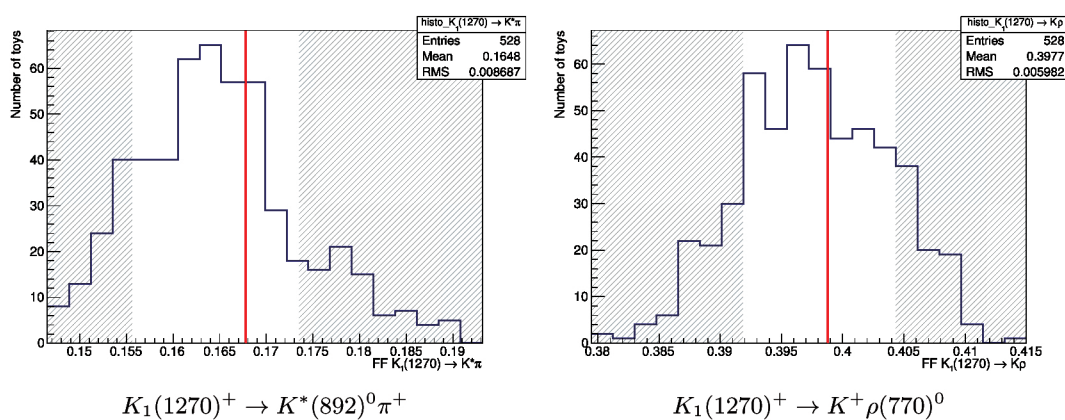
Figure 5.12   Distributions of the fit fractions for the dominant modes $K_1(1270)^+ \to K^*(892)^0\pi^+$ and $K_1(1270)^+ \to K^+\rho(770)^0$ as obtained from 500 pseudo-experiments. The non-shaded area contains 68% of the events. The vertical line is the generated value of the fit fraction.

Table 5.12 reports the ratio between the bias (obtained as the difference between the mean of the distribution and the generated value) and the statistical uncertainty for each fit fraction as an indication on how relevant the fit bias is as a source of systematic error. The fit bias is found to be smaller than the statistical uncertainty for most of the dominant components. It has been noted that the value of the bias depends on the granularity of the numerical integration: a coarser integration step size in $m^2_{\pi^+\pi^-}$, for example, causes the bias to increase for the modes with $\omega(782)^0$ resonances and for those that interfere with them, without affecting the bias for the other decay channels. Therefore, reducing the integration step size would improve the fit, but it is not a viable option for the study presented in this thesis because of the very large amount of CPU time needed.

Table 5.12 Ratio between the bias and the statistical uncertainty for each fit fraction, as obtained from 500 pseudo-experiments generated from the baseline model and fitted to the PDF of Eq. 5.1. The bias is evaluated as the difference between the mean of the fit fraction distribution and the fit fraction value used for generating the dataset.

1^+	$K_1(1270)$ $\to K^*\pi$	$K_1(1270)$ $\to K\rho$	$K_1(1270)$ $\to K\omega$	$K_1(1270)$ $\to K^*(1430)\pi$	$K_1(1400)$ $\to K^*\pi$
$K_1(1270)$ $\to K^*\pi$	**0.4**				
$K_1(1270)$ $\to K\rho$	-0.4	**0.0**			
$K_1(1270)$ $\to K\omega$	-0.6	-1.2	**-1.0**		
$K_1(1270)$ $\to K^*(1430)\pi$	0.3	-0.3	0.7	**-0.4**	
$K_1(1400)$ $\to K^*\pi$	0.3	1.3	0.4	-0.6	**1.3**

1^-	$K^*(1410)$ $\to K^*\pi$	$K^*(1680)$ $\to K^*\pi$	$K^*(1680)$ $\to K\rho$
$K^*(1410)$ $\to K^*\pi$	**-0.4**		
$K^*(1680)$ $\to K^*\pi$	0.3	**-0.3**	
$K^*(1680)$ $\to K\rho$	-0.4	0.6	**0.4**

2^+	$K_2^*(1430)$ $\to K^*\pi$	$K_2^*(1430)$ $\to K\rho$	$K_2^*(1430)$ $\to K\omega$
$K_2^*(1430)$ $\to K^*\pi$	**-0.2**		
$K_2^*(1430)$ $\to K\rho$	-0.2	**-0.2**	
$K_2^*(1430)$ $\to K\omega$	-0.3	1.0	**-0.7**

2^-	$K_2(1600)$ $\to K^*\pi$	$K_2(1600)$ $\to K\rho$	$K_2(1770)$ $\to K^*\pi$	$K_2(1770)$ $\to K\rho$	$K_2(1770)$ $\to K^*(1430)\pi$	$K_2(1770)$ $\to K f_2(1270)$
$K_2(1600)$ $\to K^*\pi$	**-0.2**					
$K_2(1600)$ $\to K\rho$	-0.3	**-0.4**				
$K_2(1770)$ $\to K^*\pi$	0.2	-0.3	**-0.1**			
$K_2(1770)$ $\to K\rho$	0.0	3.9	0.5	**-0.8**		
$K_2(1770)$ $\to K^*(1430)\pi$	-0.3	2.8	0.0	-0.5	**0.3**	
$K_2(1770)$ $\to K f_2(1270)$	0.1	0.5	0.1	-0.7	-0.2	**-0.2**

	Non resonant
Non resonant	**0.6**

5.4.2 Interpretation of the results and comparison with experiment and theory

It is very informative to compare the results obtained from the amplitude analysis of the $K^+\pi^-\pi^+$ system with the previously available experimental results and theory predictions. The fit fractions listed in Table 5.7 show that the $K^+\pi^-\pi^+$ spectrum in the $[1.1, 1.9]\,\text{GeV}/c^2$ mass interval is dominated by the 1^+ resonances, with the $K_1(1270)^+$ being significantly more abundant than the $K_1(1400)^+$, as already observed by the Belle collaboration [81]. It is worth recalling that this result is in disagreement with the theoretical study of Gronau *et al.* [69, 70], whose model for the determination of the photon polarisation in $B^+ \to K^+\pi^-\pi^+\gamma$ decays, being anterior to the publication of Ref. [81], relies on the $K_1(1400)^+$ to be the only 1^+ resonance in the $K^+\pi^-\pi^+$ mass interval of interest, as already pointed out in Ref. [86].

A comparison with the study of the $K^+\pi^-\pi^+$ spectrum in $B^+ \to J/\psi K^+\pi^-\pi^+$ decays performed by the Belle collaboration [92] shows a very good agreement both in the distribution of the data in the $m^2_{K^+\pi^-\pi^+}$, $m^2_{K^+\pi^-}$ and $m^2_{\pi^+\pi^-}$ dimensions, and in the hierarchy of the fitted components, despite the differences in the $K^+\pi^-\pi^+$ mass interval and in the fit model. The improvement in the uncertainties obtained in this study is compatible with the difference in statistics between the two datasets (~ 14000 signal events for the LHCb $B^+ \to K^+\pi^-\pi^+\gamma$ dataset against ~ 8000 signal events for the Belle $B^+ \to J/\psi K^+\pi^-\pi^+$ dataset).

In the $K^+\pi^-\pi^+$ mass interval of interest, the 1^+ resonances play a relevant role, as introduced in Sec. 1.3.1. The $K_1(1270)^+ \to K^+\rho(770)^0$ decay mode has the largest fit fraction ($\sim 40\%$), followed by the $K_1(1270)^+ \to K^*(892)^0\pi^+$ channel ($\sim 17\%$). The phase difference between the two dominant modes is found to be $-52.2° \pm 2.5°$, in reasonable agreement with the value obtained by Belle $-43.8° \pm 4.0° \pm 7.3°$.

The decay mode $K_1(1270)^+ \to K_0^*(1430)^0\pi^+$, accounting for $\sim 1\%$ of the $K_1(1270)^+$ decays, is strongly suppressed with respect to its world average [89], as already observed in the experimental study of Ref. [92] ($\sim 2\%$). A theoretical model predicting a branching fraction for this mode consistent with the latest experimental results is presented in Ref. [91].

Despite the very small contribution from the $K_1(1270)^+ \to K^+\omega(782)^0$ decay measured on data, its interference with the $K_1(1270)^+ \to K^+\rho(770)^0$ channel causes a significant distortion to the $m^2_{\pi^+\pi^-}$ distribution. This effect, studied in detail in Ref. [130] and observed in Ref. [92], is clearly visible in Fig. 5.13 as a sharp drop at the $\omega(782)^0$ mass, correctly described by the signal function. Figure 5.13 highlights also the existence of a singularity in the breakup momentum p_0 of the system in its rest frame, appearing as a dip in the $m^2_{\pi^+\pi^-}$ distribution at $(m_{K_1(1270)} - m_K)^2$ (Eq. 5.6). This effect cannot be reproduced by the signal function used in the fit, because of the non-relativistic Breit-Wigner PDF used to describe the decay of the mother resonance, underlining the need for a more refined signal function for future studies.

The existence of the $K_1(1400)^+$ resonance, for which only an upper limit on the branching
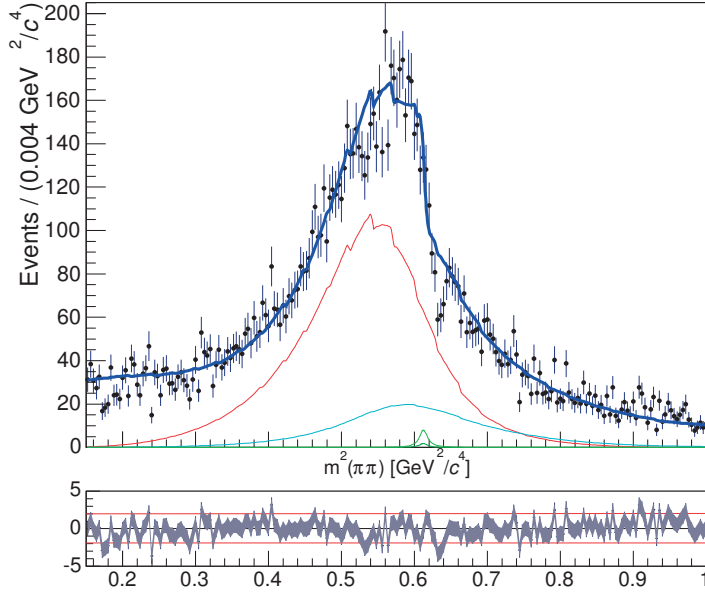
Figure 5.13 Finely binned $m^2_{\pi^+\pi^-}$ distribution showing the distortion effect, a sharp drop at the $\omega(782)^0$ mass, caused by the $\rho(770)^0$–$\omega(782)^0$ interference, and a dip at $(m_{K_1(1270)} - m_K)^2$ due to a singularity in the breakup momentum p_0 of the system in its rest frame. The colour code is given is Table 5.5. For the sake of simplicity, only the projections for the total fit and the $K_1(1270)^+$ and $K_2^*(1430)^+$ resonances decaying each to $K^+\rho(770)^0$ or $K^+\omega(782)^0$ are shown.

fraction exists [81], is confirmed, but with a lower fit fraction than the one found by the Belle collaboration [92]: this is likely due to the difference between the abundance for the $K_2^*(1430)^+$ modes, fixed in the Belle model to values significantly different than the ones obtained in the present study.

5.4.3 Resonance content in the four $K^+\pi^-\pi^+$ mass intervals

Looking at the fit fraction results in the four $K^+\pi^-\pi^+$ mass intervals helps understanding which are the decay modes and the interference patterns that shape the $\cos\hat{\theta}$ distributions obtained in Chapter 4 (Fig. 4.6):

- For $m_{K^+\pi^-\pi^+} \in [1.1, 1.3] \, \text{GeV}/c^2$ the 1^+ resonances are largely dominating; a significant destructive interference pattern between the dominant $K_1(1270)^+$ modes is observed, along with a large interference between the $K_1(1270)^+$ and $K_1(1400)^+$ decay channels.

- Moving along the $K^+\pi^-\pi^+$ mass spectrum ($m_{K^+\pi^-\pi^+} \in [1.3, 1.4] \, \text{GeV}/c^2$) the contributions from 1^- and 2^+ resonances become relevant, still dominated by the 1^+ resonances and their interference patterns.

- Many decay modes, with all the considered spin-parities, have a large fit fraction in the $m_{K^+\pi^-\pi^+} \in [1.4, 1.6]\,\mathrm{GeV}/c^2$ interval. The main contribution corresponds to the 2^+ resonance $K_2^*(1430)^+$ decaying to $K^+\rho(770)^0$.

- In the highest $K^+\pi^-\pi^+$ mass interval ($m_{K^+\pi^-\pi^+} \in [1.6, 1.9]\,\mathrm{GeV}/c^2$) the most relevant fit fraction corresponds to the non resonant contribution, with large fit fractions also for 2^- and 1^- kaon resonances decay modes. The $K_1(1270)^+ \to K^+\rho(770)^0$ channel remains one of the most relevant modes even in the highest $K^+\pi^-\pi^+$ mass interval.

These results will be recalled in Chapter 6, where the simulated shapes of the $\cos\hat{\theta}$ distribution for each spin-parity are shown.

6

Conclusions and outlook

The inclusive $B^+ \to K^+\pi^-\pi^+\gamma$ decay, with a $K^+\pi^-\pi^+$ mass in the $[1,2]$ GeV/c^2 range, has been studied in 3 fb^{-1} of data collected by the LHCb detector in 2011 and 2012 at $\sqrt{s} = 7$ and 8 TeV respectively. After a careful study and characterisation of the backgrounds, a total of $13\,876 \pm 153$ signal events has been observed.

The angular distribution of the photon with respect to the plane defined by the three final-state hadrons has been measured in four intervals of interest in $K^+\pi^-\pi^+$ mass from the distribution of the number of signal events in bins of the angle defined by the direction of the photon. The up-down asymmetry, which is proportional to the photon polarisation parameter λ_γ, has been measured in each mass interval, leading to the first observation of a parity-violating photon polarisation different from zero at the $5.2\,\sigma$ significance level in $b \to s\gamma$ transitions. This study has been published in Ref. [1].

Since none of the available theoretical predictions can describe the full $K^+\pi^-\pi^+$ system, with its multitude of interfering decay modes, the obtained photon angular distributions as well as the up-down asymmetry values cannot be translated into a measurement of the polarisation of the photon. A full Dalitz amplitude analysis of the $B^+ \to K^+\pi^-\pi^+\gamma$ decay is needed, so that the resonances populating the $K^+\pi^-\pi^+$ mass spectrum can be identified and separated. This approach relies on characterising the system using all its degrees of freedom: three invariant masses ($m^2_{K^+\pi^-\pi^+}$, $m^2_{K^+\pi^-}$ and $m^2_{\pi^+\pi^-}$) and two angles (θ and χ) that define the direction of the photon with respect to the decay plane of the final state hadrons.

In this thesis, a first approach to the problem, aimed at understanding the $K^+\pi^-\pi^+$ hadronic structure, has been presented. The amplitude analysis of the $K^+\pi^-\pi^+$ system has been performed integrating over the angular variables defining the direction of the photon, in order to obtain an estimate of the resonance content. This is the first three-dimensional amplitude study of the $K^+\pi^-\pi^+$ system in $B^+ \to K^+\pi^-\pi^+\gamma$ decays, yielding the statistically most precise results. The fit fractions obtained for the main modes are consistent with those observed in previous studies [87]: the $K_1(1270)^+ \to K^+\rho(770)^0$ decay mode is found to be dominant, followed by $K_1(1270)^+ \to K^*(892)^0\pi^+$; the decay

channel $K_1(1270)^+ \to K^*(1430)^0\pi^+$, supposed to be relevant in Ref. [89] is found to be small; the 1^+ resonances and their interference patterns account for more than 90% of the events in the first $K^+\pi^-\pi^+$ mass interval ([1.1, 1.3] GeV/c^2) suggesting a promising mass region for the development of a simplified theory model for the determination of λ_γ.

The current description of the system does not yet allow for a full, high-precision discrimination between the various resonances contributing to the $K^+\pi^-\pi^+$ spectrum, especially in the region around $m_{K^+\pi^-\pi^+} \sim 1.5\,\text{GeV}/c^2$ where most of the resonances are overlapping. For future analyses of the photon polarisation in the $B^+ \to K^+\pi^-\pi^+\gamma$ decay, the fitter needs to be extended to the full five-dimensional scenario, with the angular dimensions expected to provide additional separation power to the fit. For such extension it is recommended to move to a generator-level framework for amplitude analyses, that can be used to generate and fit the full distribution, controlling the angular dimensions together with the invariant masses. The MINT package, first developed for the amplitude analysis of $D^0 \to K^+K^-\pi^+\pi^-$ decays at CLEO [131] and recently extended to be used for the study of B-mesons decays at LHCb (e.g. $B^+ \to K^+\pi^-\pi^+J/\psi$ [132]) is suited to accomplish this goal. As an example, the sources of interference that have not been considered until now, such as the S–D wave interference for the $K_1(1270)^+ \to K^*(892)^0\pi^+$ mode and the interference between mother resonances with different spin-parities, can be introduced within this framework. These interference patterns have never been studied for the $B^+ \to K^+\pi^-\pi^+\gamma$ system and might prove to add a significant contribution to the sensitivity of the fitter to the polarisation of the photon.

To demonstrate how much information is hidden in the photon angular dimensions, the five-dimensional distributions of the kaon resonances $K_1(1400)^+$ (1^+), $K^*(1410)^+$ (1^-), $K_2^*(1430)^+$ (2^+) and $K_2(1770)^+$ (2^-) decaying to a $K^*(892)^0\pi^+$ final state have been generated with the MINT package (Fig. 6.1). The distinctive shape of $\cos\hat\theta$ will be essential to explain the distribution of the photon angle observed in data (Fig. 4.6). Intuitively, these shapes seem coherent with the fit fractions measured for the decay modes in each $K^+\pi^-\pi^+$ mass interval studied (Sec. 5.4.3): the dominant 1^+ resonances are driving the shape of $\cos\hat\theta$ in all bins, with small modifications from the other resonances; the change in shape in the highest $K^+\pi^-\pi^+$ mass interval can be ascribed to the 2^- resonances that are particularly relevant in that $m_{K^+\pi^-\pi^+}$ region.

Following suggestions from theory [133], the possibility of a simultaneous fit of the $B^+ \to K^+\pi^-\pi^+\gamma$ and $B^+ \to K^+\pi^-\pi^+J/\psi$ decay channels should also be considered in future studies. The mode with the J/ψ resonance has much larger statistics because of the high branching fraction ($\sim 8 \times 10^{-4}$) and favourable trigger conditions (the LHCb trigger is very efficient in the $J/\psi \to \mu^+\mu^-$ mode). Therefore, it represents a very good control channel for the evaluation of the strong $K_{\text{res}} \to K^+\pi^-\pi^+$ decay hadronic information, such as the mixing angle between the $K_1(1270)^+$ and $K_1(1400)^+$ resonances, needed as an input to the theoretical models for the determination of the photon polarisation. Moreover, this channel can be used for a precise determination of the width of the $K_1(1270)^+$ resonance that would reduce the systematic uncertainties. However, the presence of the J/ψ resonance introduces complications related to the charmonium and charmonium-like modes as $B^+ \to \psi(2S)(\to J/\psi\pi^+\pi^-)K^+$, $B^+ \to X(3872)(\to J/\psi\pi^+\pi^-)K^+$, $B^+ \to$
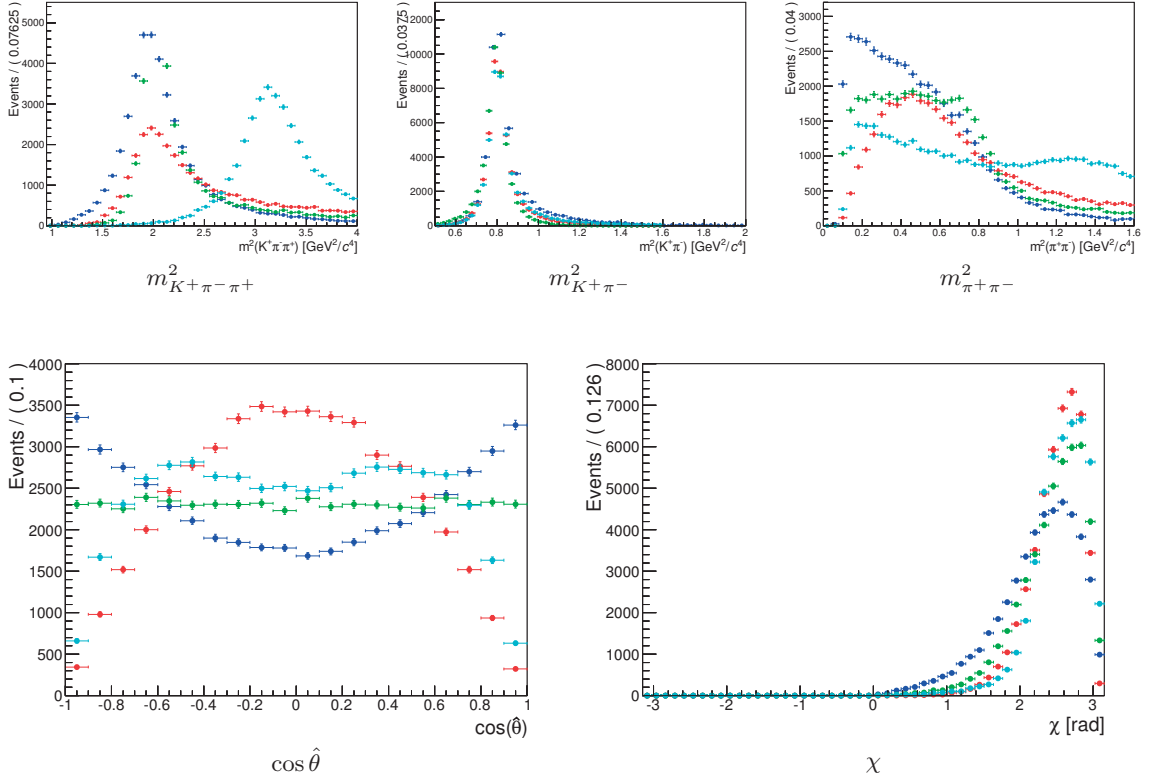
Figure 6.1   Five-dimensional distributions of $K_1(1400)^+$ (1^+ in blue), $K^*(1410)^+$ (1^- in red), $K_2^*(1430)^+$ (2^+ in green) and $K_2(1770)^+$ (2^- in cyan) decaying to a $K^*(892)^0\pi^+$ final state generated with the MINT package. The angular dimensions show distinctive distributions according to the mother resonance spin-parity.

$Y(4260)(\to J/\psi\,\pi^+\pi^-)K^+$ *etc.*, some of which are not well known and that might prove to be very challenging to handle for both theory and experiment.

In the road towards the experimental determination of the polarisation of the photon, the results presented in this thesis represent an essential starting point for the establishment of further theoretical models and a solid foundation for the development of the full amplitude study of the $B^+ \to K^+\pi^-\pi^+\gamma$ decay. With this future study, given the fantastic opportunity to further increase the LHCb statistics in this decay channel offered by the ongoing LHC Run 2, it will finally be possible to achieve the first precise determination of photon polarisation in $b \to s\gamma$ transitions, providing a further test to the SM predictions in a sector still experimentally unexplored.

A

Study of the CP asymmetry in the 2012 data sample

In this Appendix, the study of the *CP* asymmetry performed on the 2012 data sample is presented. The main differences between this study and the one performed on the full LHCb Run I data sample presented in this thesis, the former being chronologically antecedent, will be discussed. This study has lead to the publication of Ref. [134], on which this Appendix is based.

A.1 *CP* asymmetry in *B* meson decays

According to the SM, the mixing between the three generations of quarks described by the CKM matrix is the leading source of *CP* asymmetry. Since the present SM description of *CP* asymmetry fails to explain the difference between matter and antimatter that is observed in the universe, a large effort is being deployed on the search for deviations from CKM predictions. Any disagreement between theory and experiment may point to new sources of asymmetry. Hence, measurements of *CP* violation in B meson decays, providing strong constraints on the flavour parameters of the SM, are extremely important.

The *CP* asymmetry for the radiative decay $B^+ \to K^+\pi^-\pi^+\gamma$ is defined as

$$\mathcal{A}_{CP} = \frac{\Gamma(B^- \to K^-\pi^+\pi^-\gamma) - \Gamma(B^+ \to K^+\pi^-\pi^+\gamma)}{\Gamma(B^- \to K^-\pi^+\pi^-\gamma) + \Gamma(B^+ \to K^+\pi^-\pi^+\gamma)} \,. \tag{A.1}$$

A.2 Event selection

For this study, pp collision data corresponding to an integrated luminosity of 2 fb^{-1}, collected with the LHCb detector at $\sqrt{s} = 8\,\mathrm{TeV}$, have been used.

A cut-based selection is applied, similar to the one introduced in Sec. 3.2.2. Track quality is ensured by requiring a low probability that the track is actually made of pseudorandom

combinations of hits and a good quality track fit. Tracks are required to have a minimum p_T of 500 MeV/c with at least one of them above 1200 MeV/c. Their χ^2_{IP} is required to be larger than 25. DLL criteria are used to identify the tracks as pions or kaons [135].

The χ^2 per degree of freedom of the vertex fit is requested to be below 9. The resonance is also required to be isolated from other charged tracks in the event by comparing the χ^2 of the three-track fit and the χ^2 of all possible vertices that can be obtained by adding an extra track to the original vertex ($\Delta\chi^2 > 4$).

Photons are required to have a transverse energy E_T above 3 GeV.

One kaon and two pions consistent with an intermediate resonance vertex are combined with the photon to build the B candidate. The B mass-constrained invariant mass is requested to be between 1100 and 1900 MeV/c^2. Good reconstruction of the B vertex is ensured by requiring that the cosine of the angle between the reconstructed B momentum and the direction defined by the PV and the B vertex is above 0.9998. The relatively long lifetime of B mesons is exploited to remove background coming from particles produced in the PV by requiring that the flight distance $\chi^2 > 100$.

Peaking backgrounds are vetoed as discussed in Sec. 3.4. The fiducial requirement described in Sec. 3.2.2 is applied to get rid of the effects of the detector geometry on different charge particles.

Additional requirements not described here are the same as in Sec. 3.2, exception made for the multivariate selection.

A.3   *CP* **asymmetry fit**

A simultaneous unbinned extended maximum likelihood fit to two samples split according to the B candidate charge, for the determination of the raw charge asymmetry and signal yield, is performed on the full $K^+\pi^-\pi^+$ spectrum, including the fiducial requirement. The mean and width of the signal mass distributions are free but shared between the two categories, as well as the partially reconstructed background shape parameters. Relative fractions of the backgrounds are left free, allowing for possible charge asymmetries in the background.

Fit results on the B^+ and B^- subsamples are shown in Fig. A.1. The stability of the fit has been confirmed by a large number of pseudoexperiments and by studying the log likelihood profiles of the fitted parameters.

A raw charge asymmetry of -0.022 ± 0.015 is measured. A charge asymmetry of 0.01 ± 0.05 is observed in the combinatorial background, while both the partial and the missing pion backgrounds show asymmetries of 0.04 ± 0.03.
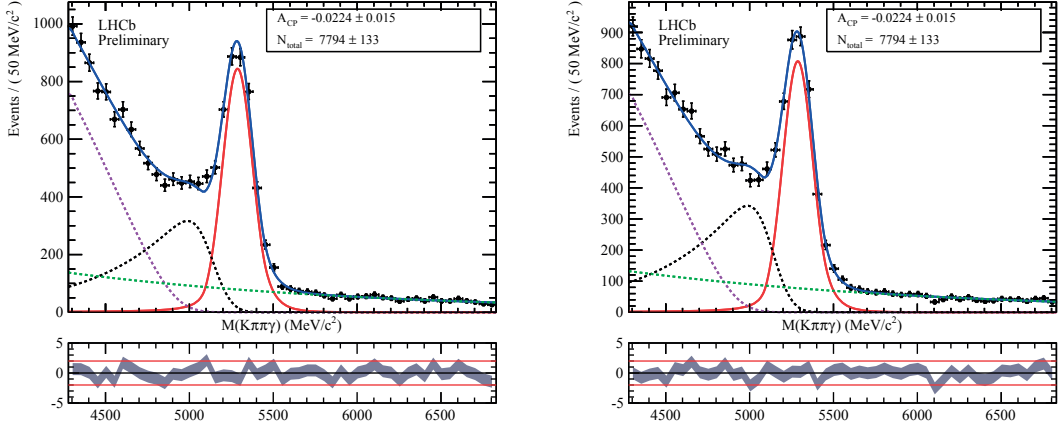
Figure A.1   Invariant $K\pi\pi\gamma$ mass for B^+ (left) and B^- (right) candidates with the result of the simultaneous fit overlaid. Colour code as in Fig. 3.20.

A.4   Determination of *CP* asymmetry

A measure of *CP* violation in the inclusive $B^+ \to K^+\pi^-\pi^+\gamma$ channel is determined from the observed raw charge asymmetry, which is related to the physical *CP*-violating asymmetry $\mathcal{A}_{CP}$ through

$$\mathcal{A}_{CP} = \mathcal{A}_{CP}^{\text{raw}} - \mathcal{A}_{\text{P}} - \mathcal{A}_{\text{D}} + \Delta\mathcal{A}_{CP}^{\text{raw}}, \tag{A.2}$$

where $\mathcal{A}_{\text{P}}$ is the asymmetry in the production of B^+ and B^- in *pp* collisions, $\mathcal{A}_{\text{D}}$ is the asymmetry due to the differences between positive and negative particles that arise in the interaction with matter, detector acceptance, and reconstruction, and $\Delta\mathcal{A}_{CP}^{\text{raw}}$ is the instrumental bias induced by non-uniformities in the detector in the presence of a magnetic field.

The detection and production asymmetries in $B^+ \to K^+\pi^-\pi^+\gamma$ decays are determined from the $B^+ \to J/\psi\,K^+$ control channel, which has a well measured *CP* asymmetry $\mathcal{A}_{CP}(B^+ \to J/\psi\,K^+) = 0.001 \pm 0.007$ [89], and are found to be $\mathcal{A}_{\text{D}} + \mathcal{A}_{\text{P}} = -0.013 \pm 0.008$. Since both signal and control channels involve a charged B meson, the asymmetries arising from B meson from production are equal between them. In addition, both decays have one kaon, so asymmetries from kaon interaction with matter and reconstruction are considered to be the same; the difference in kaon momentum spectra between signal and $B^+ \to J/\psi\,K^+$, which could cause different $\mathcal{A}_{\text{D}}$, is considered as a possible source of systematic uncertainty, but its effect is found to be negligible.

The presence of the magnetic field, which spreads oppositely-charged particles to different regions of the LHCb detector, introduces an additional source of instrumental bias. Non-uniformities in the detector performance can induce a bias in the asymmetry measurement, which is experimentally reduced by regularly flipping the magnet polarity during data taking. To estimate the instrumental bias $\Delta\mathcal{A}_{CP}^{\text{raw}}$, a separate $\mathcal{A}_{CP}$ fit is performed for each of the magnet polarities. Taking into account the imbalance in luminosity between

A.4. Determination of CP asymmetry

Table A.1 Contributions to the value and uncertainty of $\mathcal{A}_{CP}$. The $\mathcal{A}_{CP}^{\mathrm{raw}}$ uncertainty is statistical, while the rest are included in the systematic uncertainty. The total systematic uncertainty is obtained by summing these contributions in quadrature.

Contribution	Value	Uncertainty
$\mathcal{A}_{CP}^{\mathrm{raw}}$	-0.022	0.015
$\mathcal{A}_{\mathrm{D}} + \mathcal{A}_{\mathrm{P}}$	-0.013	0.008
$\Delta\mathcal{A}_{CP}^{\mathrm{raw}}$	0.002	0.001
Simulation parameters	0.000	$^{+0.001}_{-0.000}$
Fit model	0.000	0.002

the two magnet polarities, the correction is found to be $\Delta\mathcal{A}_{CP}^{\mathrm{raw}} = 0.002 \pm 0.001$.

Systematic uncertainties associated with the fit parameters that are fixed from simulation are assessed by means of a large number of pseudoexperiments, which are performed on the same data sample and where the fixed shape parameters are varied randomly within their simulation uncertainties. The systematic uncertainty associated to the fit model is assessed by using different parameterisations of mass shapes, both for the signal and each of the backgrounds, and by varying the B mass window. The contributions from each of the fit components are added in quadrature.

The values obtained for the raw CP asymmetry and for the systematic uncertainties are summarized in Table A.1. Making use of Eq. A.2, the CP asymmetry in the inclusive $B^+ \to K^+\pi^-\pi^+\gamma$ decay is determined for the first time and it is found to be

$$\mathcal{A}_{CP} = -0.007 \pm 0.015 \,(\mathrm{stat}) \pm 0.008 \,(\mathrm{syst})\,. \tag{A.3}$$

$\mathcal{B}$
Up-down asymmetry counting fit

An alternative approach to the determination of the up-down asymmetry consists in splitting the data according to the charge of the $B^{\pm}$ candidate (positive, negative), the direction of the photon (up, down) and the year of data taking (2011, 2012), and perform a simultaneous fit of the resulting data samples. This approach, that is presented in this Appendix as a cross-check of the study performed in Chapter 4, is referred to as *counting* fit, because it is conceptually analogous to determining $\mathcal{A}_{\mathrm{ud}}$ selecting only two bins on $\cos\tilde{\theta}$ and then counting the number of up and down photons in the sample.

The total fit function built from the eight mass PDFs (Eq. 3.15), one for each individual sample, has the following characteristics:

- the eight signal yields are expressed as a combination of the yields from 2012, the total yield, and CP and up-down asymmetries, as described in Sec. B.1;

- the signal mass μ is shared by all the PDFs;

- the signal mass resolution σ is shared by all the PDFs corresponding to the same data-taking year;

- the other signal parameters are fixed from MC;

- the background shape parameters are shared by all the PDFs;

- the eight background yields are independent, allowing for the presence of asymmetries in the background.

The fit is performed separately in each of the four $K^+\pi^-\pi^+$ mass intervals previously introduced, since different up-down asymmetry results are expected according to the resonance contents in the selected window.

B.1 Fit formalism

Introducing the total signal yields for B^+ and B^- as N^+ and N^-, the raw CP asymmetry, *i.e.* the CP asymmetry not corrected for detector effects such as detection and production asymmetries affecting the B^+ and B^- candidates, can be written as

$$\mathcal{A}_{CP}^{\text{raw}} = \frac{N^- - N^+}{N^- + N^+}\,. \tag{B.1}$$

With the total yield $N = N^+ + N^-$, Eq. B.1 implies

$$N^\pm = \frac{1}{2}N(1 \mp \mathcal{A}_{CP}^{\text{raw}})\,. \tag{B.2}$$

Further splitting the data in two bins according to $\cos\tilde{\theta}$, defined in Eq. 1.126, $U^\pm$ $(D^\pm)$ can be introduced as the number of $B^\pm$ decays in the up (down) $\cos\tilde{\theta}$ bin[1], such that $N^\pm = U^\pm + D^\pm$.

The charge-specific up-down asymmetries read

$$\mathcal{A}_{\text{ud}}^\pm = \pm\frac{U^\pm - D^\pm}{U^\pm + D^\pm}\,, \tag{B.3}$$

where the sign change is introduced in order to have the same sign for $\mathcal{A}_{\text{ud}}^+$ and $\mathcal{A}_{\text{ud}}^-$, accounting for the sign flipping of λ_γ between B^+ and B^- (Sec. 1.2). Using these definitions, the up and down yields become

$$U^\pm = \frac{1}{2}N^\pm(1 \pm \mathcal{A}_{\text{ud}}^\pm)\,,$$
$$D^\pm = \frac{1}{2}N^\pm(1 \mp \mathcal{A}_{\text{ud}}^\pm)\,. \tag{B.4}$$

Introducing CP violation in these definitions, the final expression for these four signal yields is obtained

$$U^\pm = \frac{1}{4}N(1 \mp \mathcal{A}_{CP}^{\text{raw}})(1 \pm \mathcal{A}_{\text{ud}}^\pm)\,,$$
$$D^\pm = \frac{1}{4}N(1 \mp \mathcal{A}_{CP}^{\text{raw}})(1 \mp \mathcal{A}_{\text{ud}}^\pm)\,. \tag{B.5}$$

Furthermore, considering the 2011 and 2012 datasets separately

$$U^\pm = U_{2011}^\pm + U_{2012}^\pm\,,$$
$$D^\pm = D_{2011}^\pm + D_{2012}^\pm\,, \tag{B.6}$$

---

[1]The up direction is arbitrarily assigned to the events with $\cos\tilde{\theta}(\cos\theta) > 0$.

one finally obtains

$$U^{\pm}_{2011} = \frac{1}{4}N(1 \mp \mathcal{A}^{\text{raw}}_{CP})(1 \pm \mathcal{A}^{\pm}_{\text{ud}}) - U^{\pm}_{2012} \,,$$

$$D^{\pm}_{2011} = \frac{1}{4}N(1 \mp \mathcal{A}^{\text{raw}}_{CP})(1 \mp \mathcal{A}^{\pm}_{\text{ud}}) - D^{\pm}_{2012} \,,$$

(B.7)

leaving $\mathcal{A}^{+}_{\text{ud}}$, $\mathcal{A}^{-}_{\text{ud}}$, $\mathcal{A}^{\text{raw}}_{CP}$, the total signal yield N and the four 2012 yields as fit parameters for the final simultaneous fit.

In addition, events are weighted with the inverse of the efficiency of the corresponding bin in $\cos\tilde{\theta}$ shown in Fig. 3.10.

B.2 Fit results

Eight samples are used for the simultaneous up-down asymmetry fit as discussed in the previous section. The results of the unbinned extended simultaneous maximum likelihood fit in each of the four intervals of $K^{+}\pi^{-}\pi^{+}$ mass are shown in Figs. B.1–B.4, with the fit parameters summarized in Tables B.1 and B.2. The results obtained using both $\cos\tilde{\theta}$ and $\cos\theta$ (the so-called sign-flip and no-flip scenarios, Sec. 1.2.1) for defining the direction of the photon are reported in the tables. Only the mass plots obtained using $\cos\tilde{\theta}$ are shown.

The obtained signal shapes are compatible with that obtained from the full fit on the $3\,\text{fb}^{-1}$ data sample. The signal resolution shows a dependence on the mass of the $K^{+}\pi^{-}\pi^{+}$ system (addressed in Sec. 5.1). The background composition is found to be very similar for the four intervals of $K^{+}\pi^{-}\pi^{+}$ mass, the partial background contribution being slightly lower in the first two bins. No significant discrepancy is observed between the fit parameters obtained for the 2011 and 2012 data samples.

Table B.1 Fit results for the up-down asymmetry fit on the full 3 fb^{-1} sample obtained using the sign-flip convention ($\cos\tilde{\theta}$). Signal (background) parameters are shown in the upper (lower) section.

Parameter	$m_{K^+\pi^-\pi^+}$ mass interval				Unit
	$[1.1, 1.3]$	$[1.3, 1.4]$	$[1.4, 1.6]$	$[1.6, 1.9]$	GeV/c^2
N_{signal}	3619 ± 80	2557 ± 62	3391 ± 76	3225 ± 76	
$\mathcal{A}_{\text{ud}}^+$	0.096 ± 0.026	0.046 ± 0.030	0.058 ± 0.028	-0.060 ± 0.028	
$\mathcal{A}_{\text{ud}}^-$	0.059 ± 0.026	0.054 ± 0.031	0.051 ± 0.027	-0.017 ± 0.028	
$\mathcal{A}_{CP}^{\text{raw}}$	-0.009 ± 0.019	-0.017 ± 0.022	0.032 ± 0.019	0.003 ± 0.020	
μ	5279.9 ± 2.3	5277.9 ± 2.4	5281.4 ± 2.3	5278.9 ± 2.2	MeV/c^2
σ_{2011}	91.8 ± 3.3	95.9 ± 3.8	95.4 ± 3.7	90.3 ± 3.4	MeV/c^2
σ_{2012}	90.8 ± 2.5	84.0 ± 2.5	87.1 ± 2.5	82.5 ± 2.3	MeV/c^2
$N_{\text{signal, 2012}}^{+,\text{up}}$	706 ± 31	485 ± 24	638 ± 29	533 ± 27	
$N_{\text{signal, 2012}}^{+,\text{down}}$	600 ± 29	446 ± 24	541 ± 27	612 ± 29	
$N_{\text{signal, 2012}}^{-,\text{up}}$	565 ± 28	420 ± 23	567 ± 28	594 ± 29	
$N_{\text{signal, 2012}}^{-,\text{down}}$	673 ± 30	447 ± 24	666 ± 30	524 ± 27	
τ	-0.35 ± 0.14	-0.10 ± 0.19	-0.28 ± 0.15	-0.49 ± 0.13	GeV$^{-1}c^2$
c_{partial}	5 ± 14	-0.8 ± 4.4	-6.4 ± 2.9	-2.1 ± 3.0	
p_{partial}	1.2 ± 0.8	1.7 ± 0.9	2.6 ± 0.6	1.5 ± 0.6	
$N_{\text{bkg, 2011}}^{+,\text{up}}$	509 ± 24	337 ± 20	722 ± 29	565 ± 25	
$N_{\text{bkg, 2012}}^{+,\text{up}}$	1237 ± 38	854 ± 31	1754 ± 44	1440 ± 40	
$N_{\text{bkg, 2011}}^{+,\text{down}}$	469 ± 23	307 ± 19	706 ± 28	574 ± 26	
$N_{\text{bkg, 2012}}^{+,\text{down}}$	1314 ± 39	841 ± 31	1823 ± 45	1536 ± 42	
$N_{\text{bkg, 2011}}^{-,\text{up}}$	515 ± 25	331 ± 19	641 ± 27	568 ± 25	
$N_{\text{bkg, 2012}}^{-,\text{up}}$	1246 ± 38	818 ± 30	1766 ± 44	1436 ± 42	
$N_{\text{bkg, 2011}}^{-,\text{down}}$	473 ± 24	337 ± 20	661 ± 27	577 ± 25	
$N_{\text{bkg, 2012}}^{-,\text{down}}$	1209 ± 38	820 ± 31	1846 ± 45	1470 ± 41	
$f_{\text{miss-}\pi,2011}^{+,\text{up}}$	0.54 ± 0.04	0.51 ± 0.06	0.47 ± 0.04	0.35 ± 0.05	
$f_{\text{miss-}\pi,2012}^{+,\text{up}}$	0.48 ± 0.03	0.48 ± 0.03	0.39 ± 0.02	0.37 ± 0.03	
$f_{\text{miss-}\pi,2011}^{+,\text{down}}$	0.49 ± 0.05	0.52 ± 0.06	0.41 ± 0.04	0.42 ± 0.05	
$f_{\text{miss-}\pi,2012}^{+,\text{down}}$	0.45 ± 0.03	0.42 ± 0.04	0.42 ± 0.02	0.40 ± 0.03	
$f_{\text{miss-}\pi,2011}^{-,\text{up}}$	0.43 ± 0.05	0.50 ± 0.06	0.43 ± 0.04	0.43 ± 0.04	
$f_{\text{miss-}\pi,2012}^{-,\text{up}}$	0.46 ± 0.03	0.50 ± 0.04	0.42 ± 0.02	0.40 ± 0.03	
$f_{\text{miss-}\pi,2011}^{-,\text{down}}$	0.49 ± 0.05	0.67 ± 0.05	0.50 ± 0.04	0.48 ± 0.05	
$f_{\text{miss-}\pi,2012}^{-,\text{down}}$	0.46 ± 0.03	0.59 ± 0.04	0.43 ± 0.02	0.40 ± 0.03	
$f_{\text{partial},2011}^{+,\text{up}}$	0.32 ± 0.04	0.42 ± 0.06	0.42 ± 0.04	0.44 ± 0.05	
$f_{\text{partial},2012}^{+,\text{up}}$	0.36 ± 0.03	0.41 ± 0.03	0.51 ± 0.02	0.43 ± 0.03	
$f_{\text{partial},2011}^{+,\text{down}}$	0.35 ± 0.04	0.37 ± 0.05	0.48 ± 0.04	0.43 ± 0.05	
$f_{\text{partial},2012}^{+,\text{down}}$	0.37 ± 0.03	0.44 ± 0.04	0.46 ± 0.02	0.40 ± 0.03	
$f_{\text{partial},2011}^{-,\text{up}}$	0.37 ± 0.04	0.41 ± 0.06	0.51 ± 0.04	0.46 ± 0.04	
$f_{\text{partial},2012}^{-,\text{up}}$	0.36 ± 0.03	0.38 ± 0.04	0.48 ± 0.04	0.40 ± 0.03	
$f_{\text{partial},2011}^{-,\text{down}}$	0.29 ± 0.04	0.25 ± 0.05	0.42 ± 0.04	0.40 ± 0.04	
$f_{\text{partial},2012}^{-,\text{down}}$	0.35 ± 0.03	0.29 ± 0.03	0.47 ± 0.02	0.42 ± 0.03	

Table B.2   Fit results for the up-down asymmetry fit on the full 3 fb^{-1} sample obtained in the no sign-flip convention ($\cos\theta$). Signal (background) parameters are shown in the upper (lower) section.

| Parameter	$m_{K^+\pi^-\pi^+}$ mass interval				Unit
	$[1.1, 1.3]$	$[1.3, 1.4]$	$[1.4, 1.6]$	$[1.6, 1.9]$	GeV/c^2
N_{signal}	3613 ± 80	2547 ± 62	3391 ± 76	3220 ± 75	
$\mathcal{A}_{\text{ud}}^+$	-0.028 ± 0.026	0.073 ± 0.030	0.048 ± 0.028	-0.038 ± 0.028	
$\mathcal{A}_{\text{ud}}^-$	-0.003 ± 0.026	0.020 ± 0.031	0.069 ± 0.027	-0.070 ± 0.028	
$\mathcal{A}_{CP}^{\text{raw}}$	-0.009 ± 0.019	-0.018 ± 0.022	0.032 ± 0.019	0.004 ± 0.020	
μ	5279.8 ± 2.3	5278.1 ± 2.4	5281.2 ± 2.3	5279.0 ± 2.2	MeV/c^2
σ_{2011}	91.9 ± 3.3	95.6 ± 3.9	95.7 ± 3.6	90.3 ± 3.4	MeV/c^2
σ_{2012}	90.8 ± 2.5	83.8 ± 2.5	87.3 ± 2.5	82.6 ± 2.3	MeV/c^2
$N_{\text{signal, 2012}}^{+,\text{up}}$	638 ± 29	510 ± 25	624 ± 29	541 ± 27	
$N_{\text{signal, 2012}}^{+,\text{down}}$	665 ± 30	418 ± 23	554 ± 28	599 ± 29	
$N_{\text{signal, 2012}}^{-,\text{up}}$	621 ± 29	427 ± 23	584 ± 28	615 ± 29	
$N_{\text{signal, 2012}}^{-,\text{down}}$	612 ± 29	435 ± 24	648 ± 29	502 ± 26	
τ	-0.35 ± 0.14	-0.10 ± 0.19	-0.27 ± 0.15	-0.49 ± 0.13	GeV$^{-1}c^2$
c_{partial}	5 ± 21	-0.6 ± 4.5	-6.3 ± 2.8	-2.0 ± 3.0	
p_{partial}	1.1 ± 0.8	1.7 ± 0.9	2.6 ± 0.5	1.5 ± 0.6	
$N_{\text{bkg, 2011}}^{+,\text{up}}$	482 ± 24	332 ± 20	701 ± 28	550 ± 25	
$N_{\text{bkg, 2012}}^{+,\text{up}}$	1271 ± 39	895 ± 32	1785 ± 44	1472 ± 41	
$N_{\text{bkg, 2011}}^{+,\text{down}}$	496 ± 24	312 ± 19	726 ± 29	589 ± 26	
$N_{\text{bkg, 2012}}^{+,\text{down}}$	1272 ± 39	796 ± 30	1781 ± 45	1492 ± 41	
$N_{\text{bkg, 2011}}^{-,\text{up}}$	491 ± 24	327 ± 19	647 ± 27	542 ± 25	
$N_{\text{bkg, 2012}}^{-,\text{up}}$	1198 ± 38	769 ± 30	1846 ± 45	1448 ± 41	
$N_{\text{bkg, 2011}}^{-,\text{down}}$	497 ± 24	341 ± 20	653 ± 27	603 ± 26	
$N_{\text{bkg, 2012}}^{-,\text{down}}$	1249 ± 38	863 ± 31	1750 ± 44	1448 ± 40	
$f_{\text{miss-}\pi,2011}^{+,\text{up}}$	0.53 ± 0.05	0.59 ± 0.05	0.48 ± 0.04	0.42 ± 0.05	
$f_{\text{miss-}\pi,2012}^{+,\text{up}}$	0.50 ± 0.03	0.46 ± 0.04	0.42 ± 0.02	0.38 ± 0.03	
$f_{\text{miss-}\pi,2011}^{+,\text{down}}$	0.50 ± 0.05	0.45 ± 0.06	0.41 ± 0.04	0.35 ± 0.04	
$f_{\text{miss-}\pi,2012}^{+,\text{down}}$	0.43 ± 0.03	0.45 ± 0.04	0.39 ± 0.02	0.39 ± 0.03	
$f_{\text{miss-}\pi,2011}^{-,\text{up}}$	0.42 ± 0.05	0.58 ± 0.06	0.48 ± 0.04	0.42 ± 0.05	
$f_{\text{miss-}\pi,2012}^{-,\text{up}}$	0.47 ± 0.03	0.55 ± 0.04	0.42 ± 0.02	0.42 ± 0.03	
$f_{\text{miss-}\pi,2011}^{-,\text{down}}$	0.49 ± 0.05	0.61 ± 0.05	0.45 ± 0.04	0.47 ± 0.04	
$f_{\text{miss-}\pi,2012}^{-,\text{down}}$	0.44 ± 0.03	0.55 ± 0.04	0.43 ± 0.02	0.38 ± 0.03	
$f_{\text{partial},2011}^{+,\text{up}}$	0.32 ± 0.04	0.32 ± 0.05	0.41 ± 0.04	0.40 ± 0.05	
$f_{\text{partial},2012}^{+,\text{up}}$	0.35 ± 0.03	0.42 ± 0.04	0.49 ± 0.02	0.42 ± 0.03	
$f_{\text{partial},2011}^{+,\text{down}}$	0.35 ± 0.04	0.47 ± 0.06	0.49 ± 0.04	0.47 ± 0.05	
$f_{\text{partial},2012}^{+,\text{down}}$	0.39 ± 0.03	0.42 ± 0.04	0.49 ± 0.02	0.41 ± 0.03	
$f_{\text{partial},2011}^{-,\text{up}}$	0.36 ± 0.05	0.35 ± 0.06	0.45 ± 0.04	0.46 ± 0.05	
$f_{\text{partial},2012}^{-,\text{up}}$	0.34 ± 0.03	0.34 ± 0.04	0.47 ± 0.02	0.41 ± 0.03	
$f_{\text{partial},2011}^{-,\text{down}}$	0.31 ± 0.04	0.29 ± 0.05	0.49 ± 0.04	0.40 ± 0.04	
$f_{\text{partial},2012}^{-,\text{down}}$	0.38 ± 0.03	0.31 ± 0.03	0.48 ± 0.03	0.40 ± 0.03	
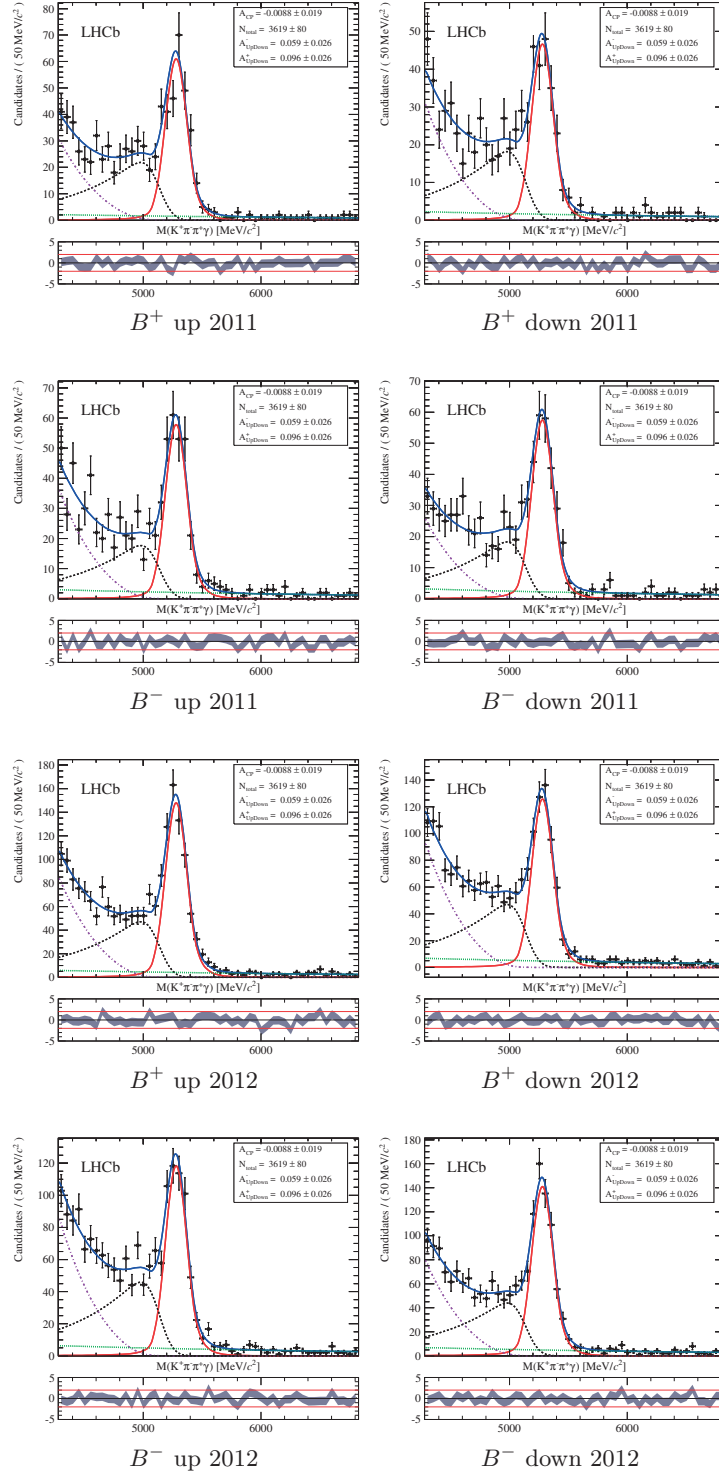
Figure B.1   Simultaneous fit of B^+ and B^- masses with an up and down photon in 2011 and 2012 data in the $1100 < m_{K\pi\pi} < 1300$ MeV/c^2 bin of the full 3 fb^{-1} sample with sign-flip convention (using $\cos\tilde{\theta}$). Colour code is the same as in Fig. 3.20.
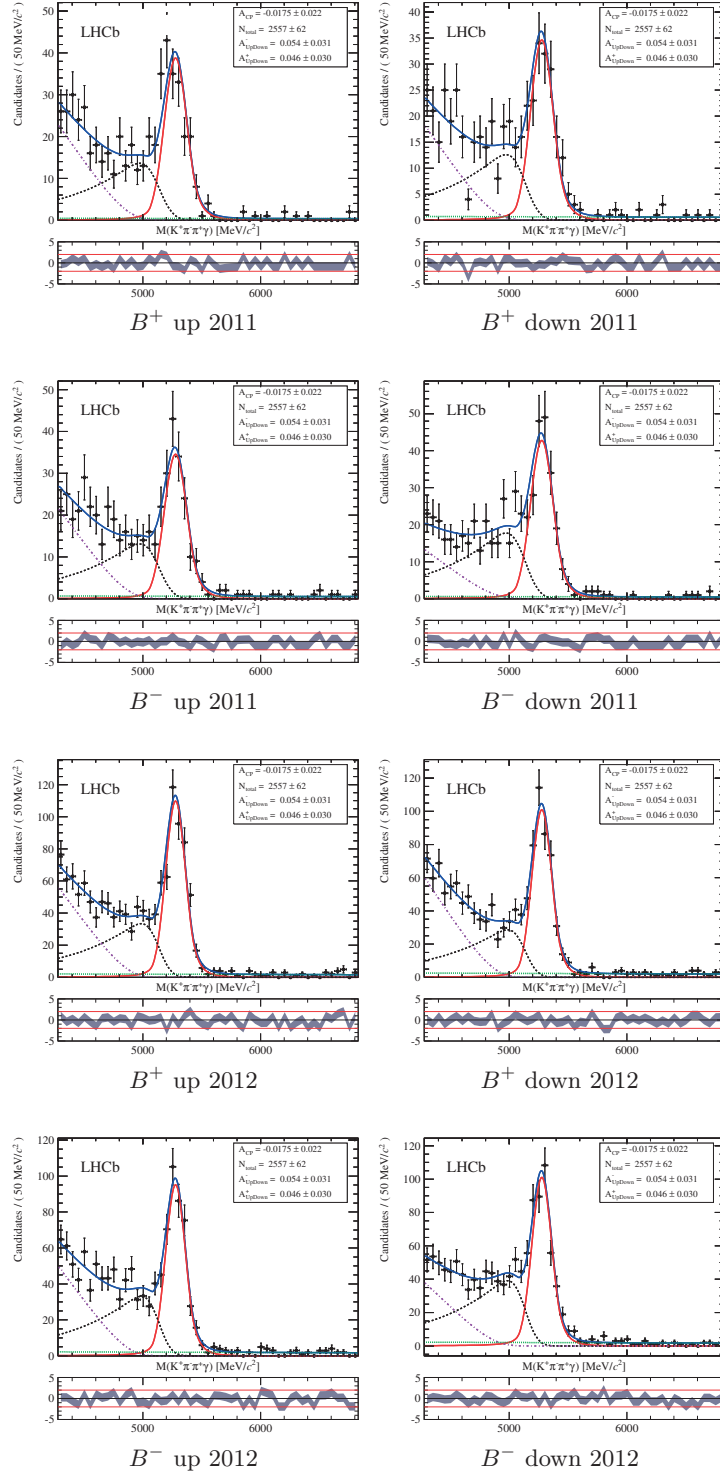
Figure B.2   Simultaneous fit of B^+ and B^- masses with an up and down photon in 2011 and 2012 data in the $1300 < m_{K\pi\pi} < 1400$ MeV/c^2 bin of the full 3 fb^{-1} sample with sign-flip convention (using $\cos\tilde{\theta}$). Colour code is the same as in Fig. 3.20.
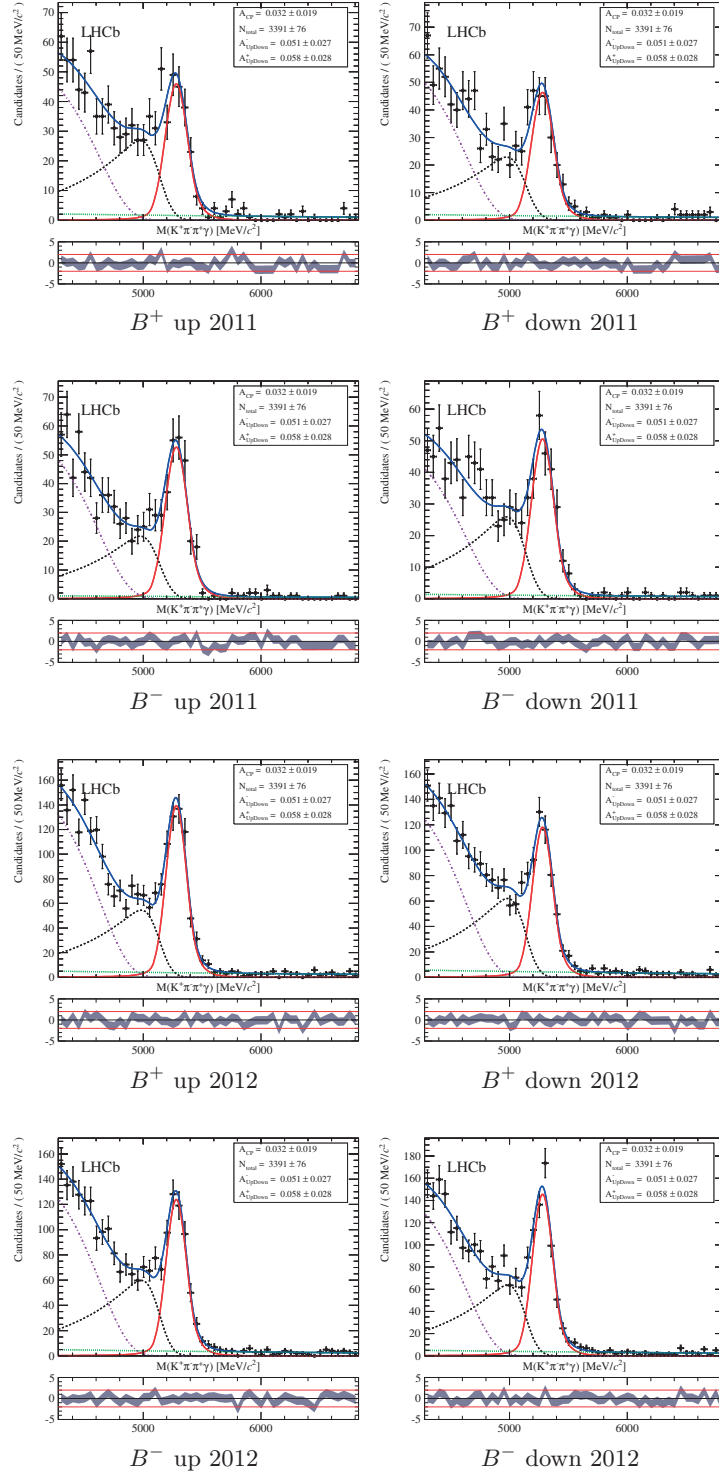
Figure B.3   Simultaneous fit of B^+ and B^- masses with an up and down photon in 2011 and 2012 data in the $1400 < m_{K\pi\pi} < 1600$ MeV/c^2 bin of the full 3 fb^{-1} sample with sign-flip convention (using $\cos\tilde\theta$). Colour code is the same as in Fig. 3.20.
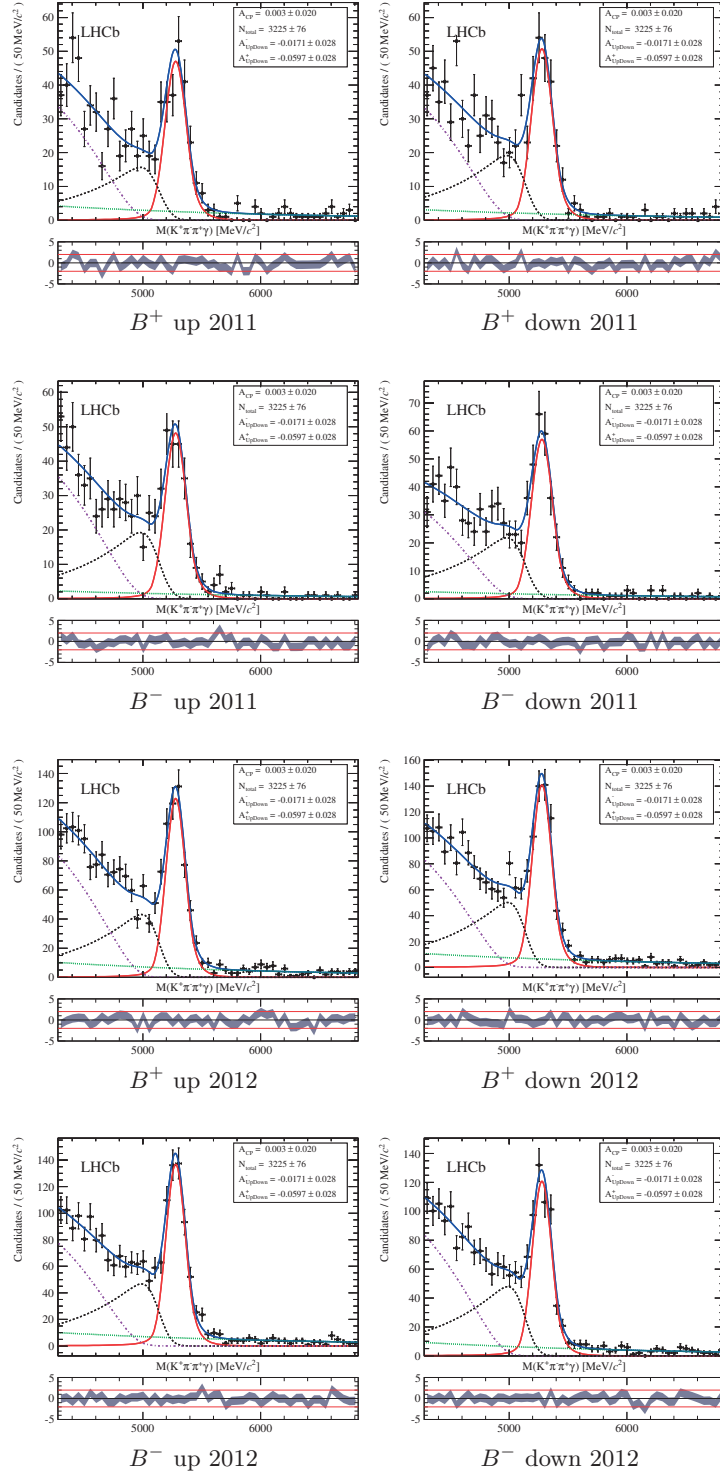
Figure B.4 Simultaneous fit of B^+ and B^- masses with an up and down photon in 2011 and 2012 data in the $1600 < m_{K\pi\pi} < 1900$ MeV/c^2 bin of the full 3 fb^{-1} sample with sign-flip convention (using $\cos\tilde{\theta}$). Colour code is the same as in Fig. 3.20.

B.3   Counting fit systematics

In order to assess the systematic uncertainty associated with the parameters fixed from MC simulations in the fit model, 10 000 fits are performed on the data varying these PDF shape parameters, as described in Sec. 4.1. The distributions obtained for $\mathcal{A}_{\mathrm{ud}}^{+}$ and $\mathcal{A}_{\mathrm{ud}}^{-}$ are shown in Fig. B.5, with the 90 % CL intervals highlighted. The systematic uncertainties on the asymmetries associated with the fit model, evaluated as described in Sec. 4.1, have been fixed to the difference of the original fit values to the fit result under each of the alternative hypotheses. Table B.3 summarizes the systematics uncertainties obtained.

The errors due to the MC-determined acceptance are treated in the same way as the MC-related systematics. Their effect is found to be negligible with respect to the other sources of systematic uncertainty.
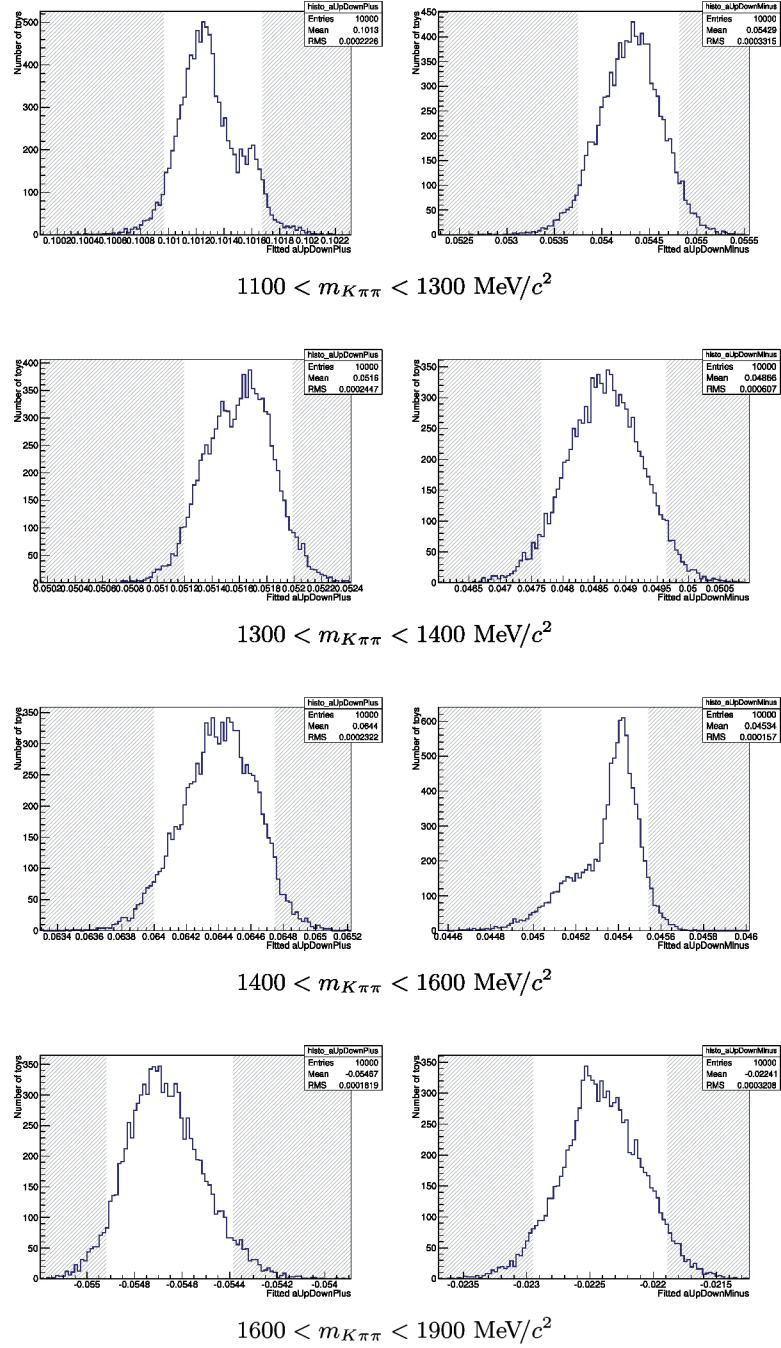
$1100 < m_{K\pi\pi} < 1300$ MeV/c^2

$1300 < m_{K\pi\pi} < 1400$ MeV/c^2

$1400 < m_{K\pi\pi} < 1600$ MeV/c^2

$1600 < m_{K\pi\pi} < 1900$ MeV/c^2

Figure B.5 Distribution of the $\mathcal{A}_{\mathrm{ud}}^{+}$ and $\mathcal{A}_{\mathrm{ud}}^{-}$ parameters obtained (in the sign-flip scenario) when randomly varying the fixed parameters in the full asymmetry fit according to Table 4.1 in the four $K^{+}\pi^{-}\pi^{+}$ mass intervals of interest. The area outside the 90 % CL interval is grayed out.

157

Table B.3   Systematic uncertainties associated with the parameters fixed from MC simulations and with the fit model, obtained for $\mathcal{A}_{\mathrm{ud}}^+$ and $\mathcal{A}_{\mathrm{ud}}^-$ in each interval of $K^+\pi^-\pi^+$ mass. The total systematic error has been evaluated by summing in quadrature the different contributions to the fit model uncertainty, and then adding (still in quadrature) the MC-related uncertainties.

$m_{K^+\pi^-\pi^+}$ interval	sign-flip $(\cos\tilde{\theta})$			no-flip $(\cos\theta)$	
	$\sigma(\mathcal{A}_{\mathrm{ud}}^+)$	$\sigma(\mathcal{A}_{\mathrm{ud}}^-)$		$\sigma(\mathcal{A}_{\mathrm{ud}}^+)$	$\sigma(\mathcal{A}_{\mathrm{ud}}^-)$
	$+0.0004$ -0.0003	$+0.0002$ -0.0008	MC-related	±0.0008	$+0.0006$ -0.0003
	±0.0004	±0.006	Signal shape	±0.0006	±0.0006
	±0.002	±0.002	Resolution	±0.0003	±0.0003
$[1.1, 1.3]$	±0.001	±0.000	Combinatorial bkg	±0.0003	±0.0003
	±0.0003	±0.001	Partial bkg	±0.0004	±0.0003
	±0.002	±0.006	Total	±0.001	$+0.001$ -0.0009
	$+0.0003$ -0.0004	±0.001	MC-related	±0.0002	±0.0007
	±0.003	±0.003	Signal shape	±0.001	±0.007
	±0.004	±0.006	Resolution	±0.002	±0.009
$[1.3, 1.4]$	±0.0008	±0.0002	Combinatorial bkg	±0.0005	±0.002
	±0.0002	±0.0003	Partial bkg	±0.0004	±0.0002
	±0.005	±0.007	Total	±0.002	±0.011
	$+0.0003$ -0.0005	$+0.0002$ -0.0003	MC-related	$+0.0005$ -0.0004	$+0.0003$ -0.0002
	±0.003	±0.002	Signal shape	±0.004	±0.003
	±0.001	±0.0003	Resolution	±0.001	±0.001
$[1.4, 1.6]$	±0.001	±0.0002	Combinatorial bkg	±0.003	±0.0008
	±0.001	±0.0003	Partial bkg	±0.001	±0.00003
	±0.003	±0.002	Total	±0.005	±0.003
	$+0.0001$ -0.0004	$+0.0004$ -0.0006	MC-related	$+0.0003$ -0.0004	$+0.0006$ -0.0004
	±0.0005	±0.007	Signal shape	±0.0008	±0.0003
	±0.0005	±0.0007	Resolution	±0.00007	±0.001
$[1.6, 1.9]$	±0.0002	±0.0002	Combinatorial bkg	±0.0002	±0.001
	±0.0006	±0.0005	Partial bkg	±0.0004	±0.0001
	$+0.0009$ -0.001	±0.007	Total	$+0.0009$ -0.001	±0.001

B.4 Up-down asymmetry results from counting experiment

The up-down asymmetries for B^+ and B^- decays resulting from the counting experiment in the four intervals of $K^+\pi^-\pi^+$ mass are summarized in Fig. B.6.
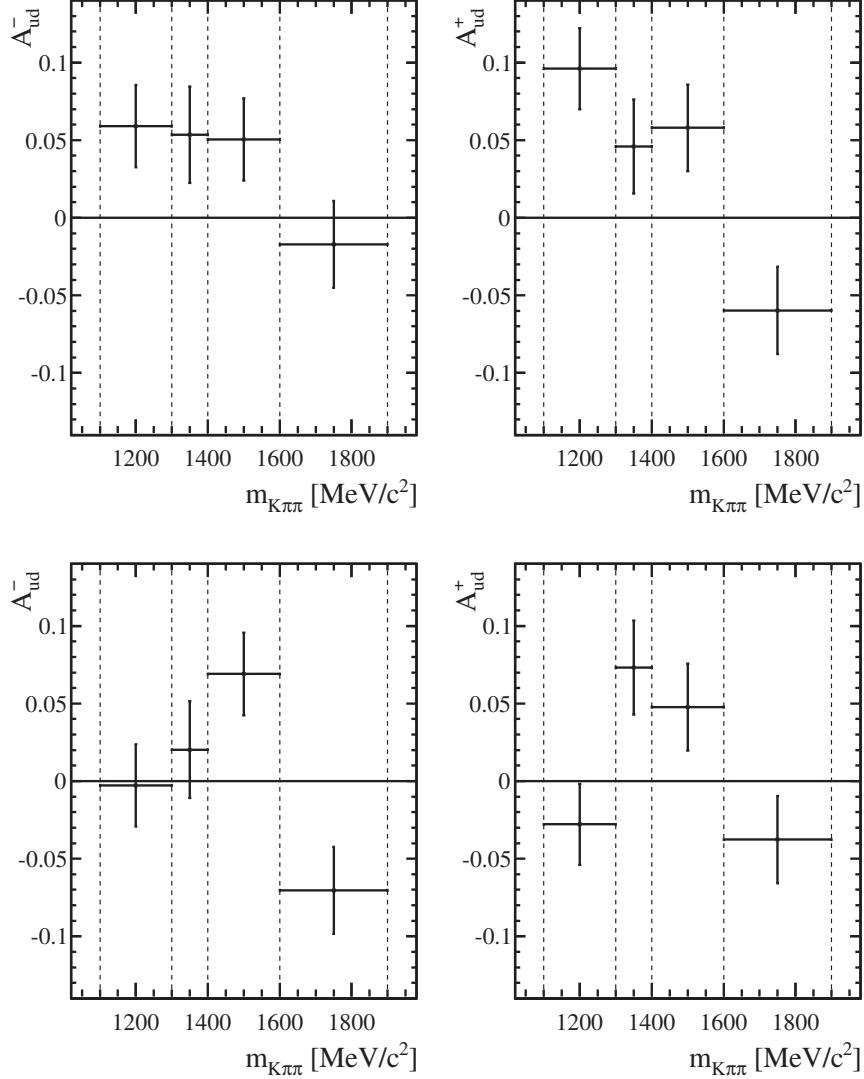

Figure B.6 Up-down asymmetries for B^- (left) and B^+ (right) decays in four intervals of $K^+\pi^-\pi^+$ mass, in the sign-flip (top) and no-flip (bottom) scenarios as obtained in Sec. B.2.

Making use of the profile likelihoods of $\mathcal{A}^{\pm}_{\mathrm{ud}}$, the statistical significance $s^{\pm}_{\mathrm{stat}}$, measured in units of σ, of $\mathcal{A}^{\pm}_{\mathrm{ud}}$ with respect to zero can be calculated as

$$s^{\pm}_{\mathrm{stat}} = \sqrt{2\min(-\ln\mathcal{L}_{\mathcal{A}^{\pm}_{\mathrm{ud}}=0}) - 2\min(-\ln\mathcal{L})}\,, \tag{B.8}$$

where $\min(-\log\mathcal{L})$ is the minimized negative log-likelihood of the fit and $\mathcal{L}_{\mathcal{A}^{\pm}_{\mathrm{ud}}=0}$ cor-

B.4. Up-down asymmetry results from counting experiment

Table B.4 Significances of the $\mathcal{A}_{\mathrm{ud}}^{+}$ and $\mathcal{A}_{\mathrm{ud}}^{-}$ up-down asymmetries with respect to zero, in units of σ, for each bin of $K^{+}\pi^{-}\pi^{+}$ mass in the sign-flip and no-flip scenarios. Both statistical and systematic uncertainties are taken into account.

sign-flip ($\cos\tilde{\theta}$)			no-flip ($\cos\theta$)	
s^{+}	s^{-}	$m_{K\pi\pi}$ [MeV/c^2]	s^{+}	s^{-}
3.7	2.2	[1100, 1300]	1.1	0.11
1.5	1.7	[1300, 1400]	2.3	0.68
2.1	1.9	[1400, 1600]	1.7	2.6
2.1	0.59	[1600, 1900]	1.4	2.5

responds to the likelihood with $\mathcal{A}_{\mathrm{ud}}^{\pm}$ fixed to zero. Given its small size, the systematic uncertainty is not expected to significantly distort the shape of the profile likelihood and thus it can be used directly to obtain the combined significance

$$s^{\pm} = \frac{s_{\mathrm{stat}}^{\pm}}{\sqrt{1 + \left(\frac{\sigma_{\mathrm{syst}}}{\sigma_{\mathrm{stat}}}\right)^2}} \,. \tag{B.9}$$

The significances of the up-down asymmetries are summarized in Table B.4, separately for $\mathcal{A}_{\mathrm{ud}}^{+}$ and $\mathcal{A}_{\mathrm{ud}}^{-}$.

Under the assumption that the sign-weighted photon polarisation is the same for B^{+} and B^{-} mesons, $\mathcal{A}_{\mathrm{ud}}^{+}$ and $\mathcal{A}_{\mathrm{ud}}^{-}$ are independent measurements of the same quantity. Hence, the composition of their likelihoods provides a combined measurement, of the up-down asymmetry $\mathcal{A}_{\mathrm{ud}}$. The combined likelihoods are shown in Fig. B.7 and the resulting values for $\mathcal{A}_{\mathrm{ud}}$ are summarized in Table B.5 , where the systematic uncertainty is propagated from the $\mathcal{A}_{\mathrm{ud}}^{\pm}$ systematic uncertainties as half of their sum in quadrature, that is, assuming no correlation between them. The results are in good agreement with those obtained from the angular fit of Chapter 4 (Table 4.6).

Repeating this process in each of the $K^{+}\pi^{-}\pi^{+}$ mass intervals, four independent values for the up-down asymmetry significance with respect to zero are obtained (Table B.6), corresponding to a p-value of 5.9×10^{-7} and to a $5.0\,\sigma$ significance for the up-down asymmetry to be different from zero in the sign-flip scenario. A $3.6\,\sigma$ effect is found using

Table B.5 Values obtained for $\mathcal{A}_{\mathrm{ud}}$ in each bin of $K^{+}\pi^{-}\pi^{+}$ mass. The first error is statistical and the second in systematic.

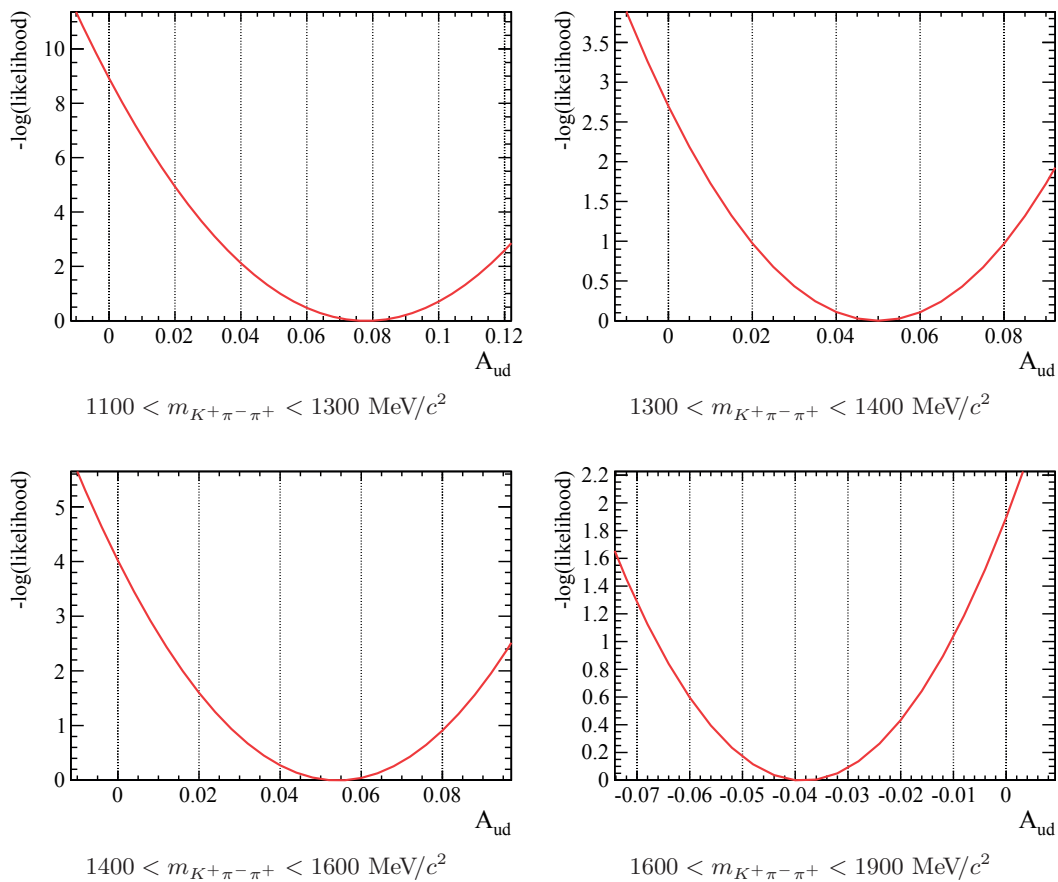| $m_{K^{+}\pi^{-}\pi^{+}}$ [MeV/c^2]	sign-flip ($\cos\tilde{\theta}$)	no-flip ($\cos\theta$)
[1100, 1300]	$+0.078 \pm 0.018 \pm 0.003$	$-0.015 \pm 0.019 \pm 0.001$
[1300, 1400]	$+0.050 \pm 0.022 \pm 0.004$	$+0.047 \pm 0.022 \pm 0.006$
[1400, 1600]	$+0.055 \pm 0.019 \pm 0.002$	$+0.059 \pm 0.019 \pm 0.003$
[1600, 1900]	$-0.039 \pm 0.020 \pm 0.004$	$-0.054 \pm 0.020 \pm 0.001$

Figure B.7   Negative log-likelihood curves for $\mathcal{A}_{\mathrm{ud}}$ in the sign-flip scenario, obtained in each $K^+\pi^-\pi^+$ mass interval combining the corresponding curves obtained for $\mathcal{A}_{\mathrm{ud}}^+$ and $\mathcal{A}_{\mathrm{ud}}^-$.

$\cos\theta$ for describing the direction of the photon (no-flip scenario).

As in the case of the angular fit, observation of photon polarisation in the studied decay can be claimed.

Table B.6 Significance of $\mathcal{A}_{\mathrm{ud}}$ with respect to zero, in units of σ, for each interval of $K^+\pi^-\pi^+$ mass for the sign-flip and no-flip scenarios, as obtained from combining the likelihoods for $\mathcal{A}_{\mathrm{ud}}^+$ and $\mathcal{A}_{\mathrm{ud}}^-$.

$m_{K^+\pi^-\pi^+}$ [MeV/c^2]	sign-flip $(\cos\tilde{\theta})$	no-flip $(\cos\theta)$
$[1100, 1300]$	4.2	0.79
$[1300, 1400]$	2.2	2.1
$[1400, 1600]$	2.9	3.0
$[1600, 1900]$	1.9	2.7

B.4.1 Significance consistency check

A simulation study has been realized to check whether the differences in significance obtained in the sign-flip scenario from the angular fit (Sec. 4.2) and the counting experiment (Sec. B.4) are consistent. The $\cos\hat{\theta}$ shapes obtained from the fit on data are used to generate simulated angular distributions, one for each $K^+\pi^-\pi^+$ mass interval. In each interval, the up-down asymmetry is determined using both approaches and a value for the significance in computed. The combined significances are determined as described in Sec. 4.2 and B.4, and the difference in significance is determined.

The histogram (Fig. B.8) built from the difference in the significance of the two methods shows that the angular fit is on average more sensitive to the up-down asymmetry than the counting experiment for a given distribution of data. The mean difference in significances is in agreement with what observed in data ($\sim 0.15\,\sigma$).
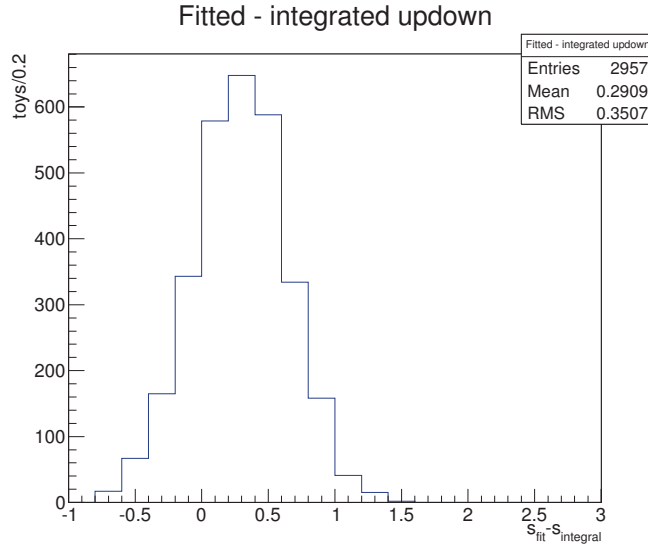

Figure B.8 Histogram built from the difference in significance in the sign-flip scenario between the angular fit and the counting experiment. The angular fit is expected to be more sensitive to the up-down asymmetry, as observed in data.

Bibliography

[1] LHCb collaboration, R. Aaij *et al.*, *Observation of photon polarization in the $b \rightarrow s\gamma$ transition*, Phys. Rev. Lett. **112** (2014) 161801, `arXiv:1402.6852`.

[2] J. J. Thomson, *Cathode rays*, Phil. Mag. **44** (1897) 293.

[3] W. Roentgen, *On a new kind of rays*, Nature **53** (1895) 274.

[4] E. Rutherford and T. Royds, *Spectrum of the radium emanation*, Phil. Mag. **16** (1908) 313.

[5] N. Bohr, *On the constitution of atoms and molecules*, Phil. Mag. **26** (1913) 1.

[6] J. Chadwick, *Possible existence of a neutron*, Nature **129** (1932) 312.

[7] F. Reines and C. L. Cowan, *Detection of the free neutrino*, Phys. Rev. **92** (1953) 830.

[8] E. Fermi, *Tentativo di una teoria dei raggi β*, Il Nuovo Cimento (1924-1942) **11** (1934) 1.

[9] H. Yukawa, *On the interaction of elementary particles I*, Proc. Phys. Math. Soc. Jap. **17** (1935) 48.

[10] S. Tomonaga, *On a relativistically invariant formulation of the quantum theory of wave fields*, Prog. Theor. Phys. **1** (1946) 27.

[11] J. Schwinger, *On quantum-electrodynamics and the magnetic moment of the electron*, Phys. Rev. **73** (1948) 416.

[12] J. Schwinger, *Quantum electrodynamics. A covariant formulation*, Phys. Rev. **74** (1948) 1439.

[13] R. P. Feynman, *The theory of positrons*, Phys. Rev. **76** (1949) 749.

Bibliography

[14] R. P. Feynman, *Space-time approach to quantum electrodynamics*, Phys. Rev. **76** (1949) 769.

[15] R. P. Feynman, *Mathematical formulation of the quantum theory of electromagnetic interaction*, Phys. Rev. **80** (1950) 440.

[16] G. P. S. Occhialini and C. F. Powell, *Nuclear disintegration produced by slow charged particles of small mass*, Nature **159** (1987) 186.

[17] C. M. G. Lattes, G. P. S. Occhialini, and C. F. Powell, *Observations on the tracks of slow mesons in photographic emulsions*, Nature **160** (1947) 453.

[18] C. D. Anderson, *The positive electron*, Phys. Rev. **43** (1933) 491.

[19] O. Chamberlain, E. Segrè, C. Wiegand, and T. Ypsilantis, *Observation of antiprotons*, Phys. Rev. **100** (1955) 947.

[20] C. D. Anderson and S. H. Neddermeyer, *Cloud chamber observations of cosmic rays at 4300 meters elevation and near sea-level*, Phys. Rev. **50** (1936) 263.

[21] M. Gell-Mann, *The eightfold way: a theory of strong interaction symmetry*, CTSL-20, TID-12608, 1961.

[22] G. Zweig, *An SU(3) model for strong interaction symmetry and its breaking*, CERN-TH-401, 1964.

[23] M. Y. Han and Y. Nambu, *Three-triplet model with double $SU(3)$ symmetry*, Phys. Rev. **139** (1965) B1006.

[24] S. L. Glashow, *Partial symmetries of weak interactions*, Nucl. Phys. **22** (1961) 579.

[25] A. Salam, *Weak and electromagnetic interactions*, in *Svartholm: Elementary particle theory,* procs. Nobel Symposium, Lerum, Sweden, pp. 367–377, 1968.

[26] S. Weinberg, *A model of leptons*, Phys. Rev. Lett. **19** (1967) 1264.

[27] Gargamelle Neutrino collaboration, F. J. Hasert *et al.*, *Observation of neutrino-like interactions without muon or electron in the Gargamelle Neutrino experiment*, Phys. Lett. **B46** (1973) 138.

[28] UA1 collaboration, G. Arnison *et al.*, *Experimental observation of isolated large transverse energy electrons with associated missing energy at $\sqrt{s} = 540$ GeV*, Phys. Lett. **B122** (1983) 103.

[29] UA1 collaboration, G. Arnison *et al.*, *Experimental observation of lepton pairs of invariant mass around 95 GeV/c^2 at the CERN SPS collider*, Phys. Lett. **B126** (1983) 398.

[30] L. Maiani and O. Benhar, *Meccanica quantistica relativistica*, Editori Riuniti, Roma, 2012.

[31] L. Maiani, *Interazioni elettrodeboli*, Editori Riuniti, Roma, 2013.

[32] F. Englert and R. Brout, *Broken symmetry and the mass of gauge vector mesons*, Phys. Rev. Lett. **13** (1964) 321.

[33] P. W. Higgs, *Broken symmetries, massless particles and gauge fields*, Phys. Lett. **12** (1964) 132.

[34] P. W. Higgs, *Spontaneous symmetry breakdown without massless bosons*, Phys. Rev. **145** (1966) 1156.

[35] CMS collaboration, S. Chatrchyan *et al.*, *Observation of a new boson at a mass of 125 GeV with the CMS experiment at the LHC*, Phys. Lett. **B716** (2013) 30, `arXiv:1207.7235`.

[36] ATLAS collaboration, G. Aad *et al.*, *Observation of a new particle in the search for the Standard Model Higgs boson with the ATLAS detector at the LHC*, Phys. Lett. **B716** (2013) 1, `arXiv:1207.7214`.

[37] Planck, R. Adam *et al.*, *Planck 2015 results. I. Overview of products and scientific results*, `arXiv:1502.0158`.

[38] Super-Kamiokande collaboration, Y. Ashie *et al.*, *Evidence for an oscillatory signature in atmospheric neutrino oscillation*, Phys. Rev. Lett. **93** (2004) 101801, `arXiv:hep-ex/0404034`.

[39] SNO collaboration, B. Aharmim *et al.*, *Electron energy spectra, fluxes, and day-night asymmetries of ^8B solar neutrinos from measurements with NaCl dissolved in the heavy-water detector at the Sudbury Neutrino Observatory*, Phys. Rev. **C72** (2005) 055502.

[40] E. Noether, *Invariante Variationsprobleme*, Nachr. d. König. Gesellsch. d. Wiss. zu Göttingen, Math-phys. Klasse (1918) 235, translation by M. A. Tavel in *Transport Theory and Statistical Physics*, **1** (1971) 183.

[41] C. S. Wu *et al.*, *Experimental test of parity conservation in β decay*, Phys. Rev. **105** (1957) 1413.

[42] R. L. Garwin, L. M. Lederman, and M. Weinrich, *Observations of the failure of conservation of parity and charge conjugation in meson decays: the magnetic moment of the free muon*, Phys. Rev. **105** (1957) 1415.

[43] J. Christenson, J. Cronin, V. Fitch, and R. Turlay, *Evidence for the 2π decay of the K_2^0 meson*, Phys. Rev. Lett. **13** (1964) 138.

[44] G. Lüders, *Proof of the TCP theorem*, Ann. Phys. **2** (1957) 1 .

[45] C.-N. Yang and R. L. Mills, *Conservation of isotopic spin and isotopic gauge invariance*, Phys. Rev. **96** (1954) 191.

[46] J. Goldstone, *Field theories with superconductor solutions*, Nuovo Cim. **19** (1961) 154.

[47] M. Kobayashi and T. Maskawa, *CP violation in the renormalizable theory of weak interaction*, Prog. Theor. Phys. **49** (1973) 652.

[48] N. Cabibbo, *Unitary symmetry and leptonic decays*, Phys. Rev. Lett. **10** (1963) 531.

[49] L. Wolfenstein, *Parametrization of the Kobayashi-Maskawa Matrix*, Phys. Rev. Lett. **51** (1983) 1945.

[50] J. Charles *et al.*, *CP violation and the CKM matrix: assessing the impact of the asymmetric B factories*, Eur. Phys. J. **C41** (2005) 1, updated results and plots available at http://ckmfitter.in2p3.fr.

[51] S. L. Glashow, J. Iliopoulos, and L. Maiani, *Weak interactions with lepton-hadron symmetry*, Phys. Rev. **D2** (1970) 1285.

[52] D. J. Gross and F. Wilczek, *Ultraviolet behavior of non-abelian gauge theories*, Phys. Rev. Lett. **30** (1973) 1343.

[53] H. D. Politzer, *Reliable perturbative results for strong interactions?*, Phys. Rev. Lett. **30** (1973) 1346.

[54] S. Weinberg, *The quantum theory of fields. Vol. 2: Modern applications*, Cambridge University Press, 1996.

[55] J. R. Ellis, K. A. Olive, Y. Santoso, and V. C. Spanos, *Phenomenological constraints on patterns of supersymmetry breaking*, Phys. Lett. **B573** (2003) 162, arXiv:hep-ph/0305212.

[56] D. Atwood, M. Gronau, and A. Soni, *Mixing induced CP asymmetries in radiative B decays in and beyond the Standard Model*, Phys. Rev. Lett. **79** (1997) 185, arXiv:hep-ph/9704272.

[57] L. L. Everett *et al.*, *Alternative approach to $b \rightarrow s\gamma$ in the uMSSM*, JHEP **01** (2002) 022, arXiv:hep-ph/0112126.

[58] J. C. Pati and A. Salam, *Lepton number as the fourth color*, Phys. Rev. **D10** (1974) 275, erratum ibid. **D11** (1975) 703.

[59] R. Mohapatra and J. C. Pati, *A natural left-right symmetry*, Phys. Rev. **D11** (1975) 2558.

[60] R. N. Mohapatra and J. C. Pati, *Left-right gauge symmetry and an isoconjugate model of CP violation*, Phys. Rev. **D11** (1975) 566.

[61] G. Senjanovic and R. N. Mohapatra, *Exact left-right symmetry and spontaneous violation of parity*, Phys. Rev. **D12** (1975) 1502.

[62] G. Senjanovic, *Spontaneous breakdown of parity in a class of gauge theories*, Nucl. Phys. **B153** (1979) 334.

[63] R. N. Mohapatra and G. Senjanovic, *Neutrino masses and mixings in gauge models with spontaneous parity violation*, Phys. Rev. **D23** (1981) 165.

[64] C. Lim and T. Inami, *Lepton flavor nonconservation and the mass generation mechanism for neutrinos*, Prog. Theor. Phys. **67** (1982) 1569.

[65] D. Bečirević, E. Kou, A. Le Yaouanc, and A. Tayduganov, *Future prospects for the determination of the Wilson coefficient $C'_{7\gamma}$*, JHEP **08** (2012) 090, arXiv:1206.1502.

[66] J. Matias, *Exploring New Physics in radiative B decays and a bit more*, presented at 2nd Radiative Workshop, Barcelona, Spain, 2015.

[67] LHCb collaboration, R. Aaij *et al.*, *Differential branching fraction and angular analysis of the decay $B^0 \to K^{*0}\mu^+\mu^-$*, JHEP **1308** (2013) 131, arXiv:1304.6325.

[68] LHCb collaboration, *Angular analysis of the $B^0 \to K^{*0}\mu^+\mu^-$ decay*, LHCb-CONF-2015-002.

[69] M. Gronau, Y. Grossman, D. Pirjol, and A. Ryd, *Measuring the photon helicity in radiative B decays*, Phys. Rev. Lett. **88** (2002) 051802, arXiv:hep-ph/0107254.

[70] M. Gronau and D. Pirjol, *Photon polarization in radiative B decays*, Phys. Rev. **D66** (2002) 054008, arXiv:hep-ph/0205065.

[71] F. Muheim, Y. Xie, and R. Zwicky, *Exploiting the width difference in $B_s^0 \to \phi\gamma$*, Phys. Lett. **B664** (2008) 174 .

[72] D. Atwood, M. Gronau, and A. Soni, *Mixing-induced CP asymmetries in radiative B decays in and beyond the standard model*, Phys. Rev. Lett. **79** (1997) 185.

[73] W. Altmannshofer *et al.*, *Symmetries and asymmetries of $B \to K^*\mu^+\mu^-$ decays in the Standard Model and beyond*, JHEP **01** (2009) 019, arXiv:0811.1214.

[74] F. Kruger and J. Matias, *Probing new physics via the transverse amplitudes of $B^0 \to K^{*0}(\to K^-\pi^+)l^+l^-$ at large recoil*, Phys. Rev. **D71** (2005) 094009, arXiv:hep-ph/0502060.

[75] D. Becirevic and E. Schneider, *On transverse asymmetries in $B \to K^*l^+l^-$*, Nucl. Phys. **B854** (2012) 321, arXiv:1106.3283.

[76] G. Hiller, M. Knecht, F. Legger, and T. Schietinger, *Photon polarization from helicity suppression in radiative decays of polarized Λ_b to spin-3/2 baryons*, Phys. Lett. **B649** (2007) 152, arXiv:hep-ph/0702191.

[77] T. Mannel and S. Recksiegel, *Flavor changing neutral current decays of heavy baryons: The case $\Lambda_b^0 \to \Lambda\gamma$*, J. Phys. **G24** (1998) 979, arXiv:hep-ph/9701399.

[78] F. Legger and T. Schietinger, *Photon helicity in $\Lambda_b^0 \to pK\gamma$ decays*, Phys. Lett. **B645** (2007) 204, `arXiv:hep-ph/0605245`.

[79] LHCb collaboration, R. Aaij *et al.*, *Measurements of the $\Lambda_b^0 \to J/\psi\Lambda$ decay amplitudes and the Λ_b^0 polarisation in pp collisions at $\sqrt{s} = 7$ TeV*, Phys. Lett. **B724** (2013) 27, `arXiv:1302.5578`.

[80] M. Knecht and T. Schietinger, *Probing photon helicity in radiative b decays via charmonium resonance interference*, Phys. Lett. **B634** (2006) 403.

[81] Belle collaboration, H. Yang *et al.*, *Observation of $B^+ \to K_1(1270)^+\gamma$*, Phys. Rev. Lett. **94** (2005) 111802, `arXiv:hep-ex/0412039`.

[82] Belle collaboration, J. Li and *et al.*, *Measurement of the time-dependent CP asymmetries in $B^0 \to K_S^0\rho^0\gamma$ decays*, Phys. Rev. Lett. **101** (2008) 251601.

[83] S. Akar, *Study of $B^+ \to K^+\pi^-\pi^+\gamma$ dacays with the BaBar experiment: the photon helicity and the resonant structure of the $K^+\pi^-\pi^+$ system*, PhD thesis, Université Pierre et Marie Curie - Paris VI, 2013.

[84] E. Ben Haim, *Last results on radiative penguin decays at BaBar*, presented at Rencontres de Moriond, Electroweak Interactions and Unified Theories, La Thuile, Italy, 2014.

[85] S. Nishida, *New results on $B \to V\gamma$ decays*, presented at CKM Workshop on the Unitarity Triangle, Rome, Italy, 2008.

[86] E. Kou, A. Le Yaouanc, and A. Tayduganov, *Determining the photon polarization of the $b \to s\gamma$ using the $B \to K_1(1270)\gamma \to (K\pi\pi)\gamma$ decay*, Phys. Rev. **D83** (2011) 094007, `arXiv:1011.6593`.

[87] M. Suzuki, *Strange axial-vector mesons*, Phys. Rev. **D47** (1993) 1252.

[88] CLEO collaboration, D. M. Asner *et al.*, *Resonance structure of $\tau^- \to K^-\pi^+\pi^-\nu_\tau$ decays*, Phys. Rev. **D62** (2000) 072006.

[89] Particle Data Group, K. Olive *et al.*, *Review of particle physics*, Chin. Phys. **C38** (2014) 090001.

[90] C. Daum *et al.*, *Diffractive production of strange mesons at 63 GeV*, Nucl. Phys. **B187** (1981) 1.

[91] A. Tayduganov, E. Kou, and A. Le Yaouanc, *The strong decays of K_1 resonances*, Phys. Rev. **D85** (2012) 074011, `arXiv:1111.6307`.

[92] Belle collaboration, H. Guler *et al.*, *Study of the $K^+\pi^-\pi^+$ final state in $B^+ \to J/\psi K^+\pi^+\pi^-$ and $B^+ \to \psi'K^+\pi^+\pi^-$*, Phys. Rev. **D83** (2011) 032005.

[93] S. Descotes-Genon and B. Moussallam, *The $K^*(800)^0$ scalar resonance from Roy–Steiner representations of πK scattering*, Eur. Phys. J. **C48** (2006) 553.

[94] R. Dalitz, *On the analysis of τ-meson data and the nature of the τ-meson*, The London, Edinburgh, and Dublin Philosophical Magazine and Journal of Science **44** (1953) 1068.

[95] R. H. Dalitz, *Decay of τ mesons of known charge*, Phys. Rev. **94** (1954) 1046.

[96] Belle and BaBar collaborations, A. J. Bevan *et al.*, *The physics of the B factories*, Eur. Phys. J. **C74** (2014) 3026, `arXiv:1406.6311`.

[97] R. M. Sternheimer and S. J. Lindenbaum, *Extension of the isobaric nucleon model for pion production in pion-nucleon, nucleon-nucleon, and antinucleon-nucleon interactions*, Phys. Rev. **123** (1961) 333.

[98] D. J. Herndon, P. Söding, and R. J. Cashmore, *Generalized isobar model formalism*, Phys. Rev. **D11** (1975) 3165.

[99] H. Guler, *An analysis of the $K^+\pi^+\pi^-$ final state in $B^+ \to J/\psi\,K^+\pi^+\pi^-$ and $B^+ \to \psi'K^+\pi^+\pi^-$*, PhD thesis, University of Hawaii, 2008.

[100] LHCb collaboration, A. A. Alves Jr. *et al.*, *The LHCb detector at the LHC*, JINST **3** (2008) S08005.

[101] LHCb collaboration, R. Aaij *et al.*, *LHCb detector performance*, Int. J. Mod. Phys. **A30** (2015) 1530022.

[102] R. Aaij *et al.*, *The LHCb trigger and its performance in 2011*, JINST **8** (2013) P04022, `arXiv:1211.3055`.

[103] A. Puig, *The LHCb trigger in 2011 and 2012*, LHCb-PUB-2014-046, 2014.

[104] LHCb collaboration, *LHCb computing: Technical Design Report*, CERN-LHCC-2005-019, LHCb-TDR-011, 2005.

[105] LHCb collaboration, *LHCb VELO upgrade Technical Design Report*, CERN-LHCC-2013-021, LHCb-TDR-013, 2013.

[106] LHCb collaboration, *LHCb tracker upgrade Technical Design Report*, CERN-LHCC-2014-001, LHCb-TDR-015, 2014.

[107] LHCb collaboration, *LHCb PID upgrade Technical Design Report*, CERN-LHCC-2013-022, LHCb-TDR-014, 2013.

[108] LHCb collaboration, *LHCb trigger and online Technical Design Report*, CERN-LHCC-2014-016, LHCb-TDR-016, 2014.

[109] Belle collaboration, S. Nishida *et al.*, *Radiative B meson decays into $K\pi\gamma$ and $K\pi\pi\gamma$ final states*, Phys. Rev. Lett. **89** (2002) 231801, `arXiv:hep-ex/0205025`.

[110] BaBar collaboration, B. Aubert *et al.*, *Measurement of branching fractions and mass spectra of $B \to K\pi\pi\gamma$*, Phys. Rev. Lett. **98** (2007) 211804, `arXiv:hep-ex/0507031`.

Bibliography

[111] T. Sjöstrand, S. Mrenna, and P. Skands, *PYTHIA 6.4 physics and manual*, JHEP **05** (2006) 026, `arXiv:hep-ph/0603175`; T. Sjöstrand, S. Mrenna, and P. Skands, *A brief introduction to PYTHIA 8.1*, Comput. Phys. Commun. **178** (2008) 852, `arXiv:0710.3820`.

[112] A. Puig, *The HLT2 radiative topological lines*, LHCb-PUB-2012-002, 2012.

[113] V. Gligorov, C. Thomas, and M. Williams, *The HLT inclusive B triggers*, LHCb-PUB-2011-016, 2011.

[114] O. Deschamps *et al.*, *Photon and Neutral Pion reconstruction*, LHCb-2003-091, 2003.

[115] A. Carbone, V. Vagnoni, M. Charles, and G. Wilkinson, *Search for time-integrated CP violation in $D^0 \to K^- K^+, \pi^- \pi^+$ in the 2011 data*, LHCb-ANA-2011-010, 2012.

[116] I. Leboucq, *Observation of the decay $B^+ \to K^+ \pi^- \pi^+ \gamma$ at LHCb*, Master's thesis, EPFL, 2013.

[117] L. Breiman, J. H. Friedman, R. A. Olshen, and C. J. Stone, *Classification and regression trees*, Wadsworth international group, Belmont, California, USA, 1984.

[118] R. E. Schapire and Y. Freund, *A decision-theoretic generalization of on-line learning and an application to boosting*, J. Comp. and Syst. Sc. **55** (1997) 119.

[119] A. Powell, P. Hunt *et al.*, *PIDCalib package*, link to webpage.

[120] Heavy Flavor Averaging Group (HFAG), Y. Amhis *et al.*, *Averages of b-hadron, c-hadron, and τ-lepton properties as of summer 2014*, `arXiv:1412.7515`.

[121] O. Deschamps and A. Puig, *Measurement of the ratio of branching fractions $B(B^0 \to K^{*0}\gamma)/B(B_s^0 \to \phi\gamma)$ and direct CP violation in $B^0 \to K^{*0}\gamma$*, LHCb-ANA-2012-014, 2012.

[122] M. Pivk and F. R. Le Diberder, *sPlot: A statistical tool to unfold data distributions*, Nucl. Instrum. Meth. **A555** (2005) 356, `arXiv:physics/0402083`.

[123] V. Bellée, *Search for $B_s^0 \to \phi\phi\gamma$ at LHCb*, Master's thesis, EPFL, 2015.

[124] V. Filippini, A. Fontana, and A. Rotondi, *Covariant spin tensors in meson spectroscopy*, Phys. Rev. **D51** (1995) 2247.

[125] D. J. Lange, *The EvtGen particle decay simulation package*, Nucl. Instrum. Meth. **A462** (2001) 152.

[126] J. G. Ticó, cFit *package*, https://github.com/cfit.

[127] F. James and M. Roos, *Minuit: A system for function minimization and analysis of the parameter errors and correlations*, Comput. Phys. Commun. **10** (1975) 343.

[128] LHCb collaboration, R. Aaij *et al.*, *Precision measurement of CP violation in $B_s^0 \to J/\psi K^+ K^-$ decays*, Phys. Rev. Lett. **114** (2015) 041801, `arXiv:1411.3104`.

[129] D. Aston *et al.*, *A study of $K^-\pi^+$ scattering in the reaction $K^- p \to K^-\pi^+ n$ at 11 GeV/c*, Nucl. Phys. **B296** (1988) 493.

[130] CMD-2 collaboration, R. R. Akhmetshin *et al.*, *High-statistics measurement of the pion form factor in the rho-meson energy range with the CMD-2 detector*, Phys. Lett. **B648** (2007) 28, `arXiv:hep-ex/0610021`.

[131] CLEO collaboration, M. Artuso *et al.*, *Amplitude analysis of $D^0 \to K^+ K^- \pi^+ \pi^-$*, Phys. Rev. **D85** (2012) 122002, `arXiv:1201.5716`.

[132] P. d'Argent, *Amplitude analysis of $B^+ \to J/\psi K^+ \pi^- \pi^+$ decays at the LHCb experiment*, Master's thesis, Physikalisches Institut Heidelberg, 2014.

[133] E. Kou, *Photon polarisation measurement by $B \to K\pi\pi\gamma$*, presented at workshop *Novel aspects of $b \to s$ transitions: investigating new channels*, Université Aix-Marseille, Marseille, France, 2015.

[134] LHCb collaboration, *CP and up-down asymmetries in $B^\pm \to K^\pm \pi^\mp \pi^\pm \gamma$ decays*, LHCb-CONF-2013-009, 2013.

[135] A. Powell *et al.*, *Particle identification at LHCb*, PoS **ICHEP2010** (2010) 020.

Observation of Photon Polarization in the $b \to s\gamma$ Transition

R. Aaij *et al.**
(LHCb Collaboration)

This Letter presents a study of the flavor-changing neutral current radiative $B^{\pm} \to K^{\pm}\pi^{\mp}\pi^{\pm}\gamma$ decays performed using data collected in proton-proton collisions with the LHCb detector at 7 and 8 TeV center-of-mass energies. In this sample, corresponding to an integrated luminosity of 3 fb^{-1}, nearly 14 000 signal events are reconstructed and selected, containing all possible intermediate resonances with a $K^{\pm}\pi^{\mp}\pi^{\pm}$ final state in the [1.1, 1.9] GeV/c^2 mass range. The distribution of the angle of the photon direction with respect to the plane defined by the final-state hadrons in their rest frame is studied in intervals of $K^{\pm}\pi^{\mp}\pi^{\pm}$ mass and the asymmetry between the number of signal events found on each side of the plane is obtained. The first direct observation of the photon polarization in the $b \to s\gamma$ transition is reported with a significance of 5.2σ.

The standard model (SM) predicts that the photon emitted from the electroweak penguin loop in $b \to s\gamma$ transitions is predominantly left-handed, since the recoiling s quark that couples to a W boson is left-handed. This implies maximal parity violation up to small corrections of the order m_s/m_b. While the measured inclusive $b \to s\gamma$ rate [1] agrees with the SM calculations, no direct evidence exists for a nonzero photon polarization in this type of decay. Several extensions of the SM [2], compatible with all current measurements, predict that the photon acquires a significant right-handed component, in particular, due to the exchange of a heavy fermion in the penguin loop [3].

This Letter presents a study of the radiative decay $B^+ \to K^+\pi^-\pi^+\gamma$, previously observed at the B factories with a measured branching fraction of $(27.6 \pm 2.2) \times 10^{-6}$ [1,4,5]. The inclusion of charge-conjugate processes is implied throughout. Information about the photon polarization is obtained from the angular distribution of the photon direction with respect to the normal to the plane defined by the momenta of the three final-state hadrons in their center-of-mass frame. The shape of this distribution, including the *up-down asymmetry* between the number of events with the photon on either side of the plane, is determined. This investigation is conceptually similar to the historical experiment that discovered parity violation by measuring the up-down asymmetry of the direction of a particle emitted in a weak decay with respect to an axial vector [6]. In $B^+ \to K^+\pi^-\pi^+\gamma$ decays, the up-down asymmetry is proportional to the photon polarization λ_γ [7,8] and therefore measuring a value different from zero corresponds to demonstrating that the photon is polarized. The

currently limited knowledge of the structure of the $K^+\pi^-\pi^+$ mass spectrum, which includes interfering kaon resonances, prevents the translation of a measured asymmetry into an actual value for λ_γ.

The differential $B^+ \to K^+\pi^-\pi^+\gamma$ decay rate can be described in terms of θ, defined in the rest frame of the final state hadrons as the angle between the direction opposite to the photon momentum $\vec{p}_\gamma$ and the normal $\vec{p}_{\pi,\text{slow}} \times \vec{p}_{\pi,\text{fast}}$ to the $K^+\pi^-\pi^+$ plane, where $\vec{p}_{\pi,\text{slow}}$ and $\vec{p}_{\pi,\text{fast}}$ correspond to the momenta of the lower and higher momentum pions, respectively. Following the notation and developments of Ref. [7], the differential decay rate of $B^+ \to K^+\pi^-\pi^+\gamma$ can be written as a fourth-order polynomial in $\cos\theta$

$$
\frac{d\Gamma}{ds\,ds_{13}\,ds_{23}\,d\cos\theta} \propto \sum_{i=0,2,4} a_i(s, s_{13}, s_{23})\cos^i\theta
$$
$$
+ \lambda_\gamma \sum_{j=1,3} a_j(s, s_{13}, s_{23})\cos^j\theta, \quad (1)
$$

where $s_{ij} = (p_i + p_j)^2$ and $s = (p_1 + p_2 + p_3)^2$, and p_1, p_2, and p_3 are the four-momenta of the π^-, π^+, and K^+ mesons, respectively. The functions a_k depend on the resonances present in the $K^+\pi^-\pi^+$ mass range of interest and their interferences. The up-down asymmetry is defined as

$$
\mathcal{A}_{\text{ud}} \equiv \frac{\int_0^1 d\cos\theta \frac{d\Gamma}{d\cos\theta} - \int_{-1}^0 d\cos\theta \frac{d\Gamma}{d\cos\theta}}{\int_{-1}^1 d\cos\theta \frac{d\Gamma}{d\cos\theta}}, \quad (2)
$$

which is proportional to λ_γ.

The LHCb detector [9] is a single-arm forward spectrometer covering the pseudorapidity range $2 < \eta < 5$, designed for the study of particles containing b or c quarks. The detector includes a high-precision tracking system consisting of a silicon-strip vertex detector surrounding the

---

*Full author list given at the end of the article.

pp interaction region, a large-area silicon-strip detector located upstream of a dipole magnet with a bending power of about 4 Tm, and three stations of silicon-strip detectors and straw drift tubes placed downstream. The combined tracking system provides a momentum measurement with relative uncertainty that varies from 0.4% at 5 GeV/c to 0.6% at 100 GeV/c, and impact parameter resolution of 20 μm for tracks with a few GeV/c of transverse momentum (p_T). Different types of charged hadrons are distinguished by information from two ring-imaging Cherenkov detectors. Photon, electron, and hadron candidates are identified by a calorimeter system consisting of scintillating-pad and preshower detectors, an electromagnetic calorimeter, and a hadronic calorimeter. The trigger consists of a hardware stage, based on information from the calorimeter and muon systems, followed by a software stage, which applies a full event reconstruction.

Samples of simulated events are used to understand signal and backgrounds. In the simulation, pp collisions are generated using Pythia [10] with a specific LHCb configuration [11]. Decays of hadronic particles are described by EvtGen [12], in which final state radiation is generated using Photos [13]. The interaction of the generated particles with the detector and its response are implemented using the Geant4 toolkit [14] as described in Ref. [15].

This analysis is based on the LHCb data sample collected from pp collisions at 7 and 8 TeV center-of-mass energies in 2011 and 2012, respectively, corresponding to 3 fb^{-1} of integrated luminosity. The $B^+ \to K^+\pi^-\pi^+\gamma$ candidates are built from a photon candidate and a hadronic system reconstructed from a kaon and two oppositely charged pions satisfying particle identification requirements. Each of the hadrons is required to have a minimum p_T of 0.5 GeV/c and at least one of them needs to have a p_T larger than 1.2 GeV/c. The isolation of the $K^+\pi^-\pi^+$ vertex from other tracks in the event is ensured by requiring that the χ^2 of the three-track vertex fit and the χ^2 of all possible vertices that can be obtained by adding an extra track differ by more than 2. The $K^+\pi^-\pi^+$ mass is required to be in the [1.1, 1.9] GeV/c^2 range. High transverse energy (> 3.0 GeV) photon candidates are constructed from energy depositions in the electromagnetic calorimeter. The absence of tracks pointing to the calorimeter is used to distinguish neutral from charged electromagnetic particles. A multivariate algorithm based on the energy cluster shape parameters is used to reject approximately 65% of the $\pi^0 \to \gamma\gamma$ background in which the two photons are reconstructed as a single cluster, while keeping about 95% of the signal photons. The B^+ candidate mass is required to be in the [4.3, 6.9] GeV/c^2 range. Backgrounds that are expected to peak in this mass range are suppressed by removing all candidates consistent with a $D^0 \to K^+\pi^-\pi^0$ or $\rho^+ \to \pi^+\pi^0$ decay when the photon candidate is assumed to be a π^0.

A boosted decision tree [16,17] is used to further improve the separation between signal and background. Its training is based on the following variables: the impact parameter χ^2 of the B^+ meson and of each of the final state hadrons, defined as the difference between the χ^2 of a primary vertex (PV) reconstructed with and without the considered particle; the cosine of the angle between the reconstructed B^+ momentum and the vector pointing from the PV to the B^+ decay vertex; the flight distance of the B^+ meson, and the $K^+\pi^-\pi^+$ vertex χ^2.

The mass distribution of the selected $B^+ \to K^+\pi^-\pi^+\gamma$ signal is modeled with a double-tailed Crystal Ball [18] probability density function (PDF), with power-law tails above and below the B mass. The four tail parameters are fixed from simulation; the width of the signal peak is fit separately for the 2011 and 2012 data to account for differences in calorimeter calibration. Combinatorial and partially reconstructed backgrounds are considered in the fit, the former modeled with an exponential PDF, the latter described using an ARGUS PDF [19] convolved with a Gaussian function with the same width as the signal to account for the photon energy resolution. The contribution to the partially reconstructed background from events with only one missing pion is considered separately.

The fit of the mass distribution of the selected $B^+ \to K^+\pi^-\pi^+\gamma$ candidates (Fig. 1) returns a total signal yield of 13876 ± 153 events, the largest sample recorded for this channel to date. Figure 2 shows the background-subtracted $K^+\pi^-\pi^+$ mass spectrum determined using the technique of Ref. [20], after constraining the B mass to its nominal value. No peak other than that of the $K_1(1270)^+$ resonance can be clearly identified. Many kaon resonances, with various masses, spins, and angular momenta, are expected to contribute and interfere in the considered mass range [1].

The contributions from single resonances cannot be isolated because of the complicated structure of the
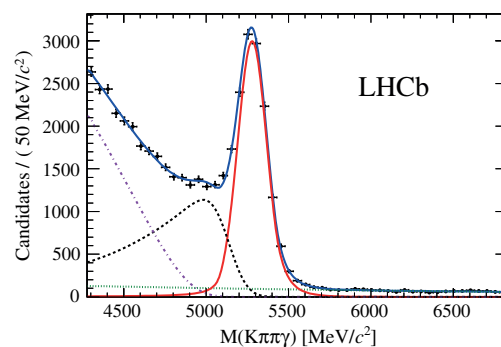

FIG. 1 (color online).   Mass distribution of the selected $B^+ \to K^+\pi^-\pi^+\gamma$ candidates. The blue solid curve shows the fit results as the sum of the following components: signal (red solid), combinatorial background (green dotted), missing pion background (black dashed), and other partially reconstructed backgrounds (purple dash-dotted).
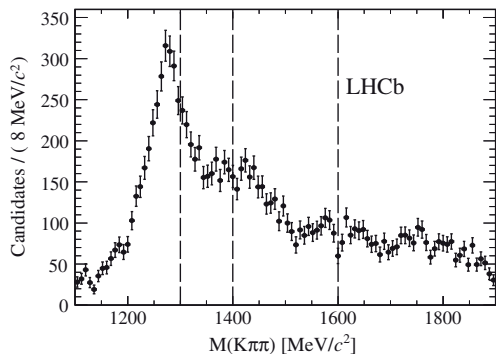
FIG. 2. Background-subtracted $K^+\pi^-\pi^+$ mass distribution of the $B^+ \to K^+\pi^-\pi^+\gamma$ signal. The four intervals of interest, separated by dashed lines, are shown.

$K^+\pi^-\pi^+$ mass spectrum. The up-down asymmetry is thus studied inclusively in four intervals of $K^+\pi^-\pi^+$ mass. The $[1.4, 1.6]$ GeV/c^2 interval, studied in Ref. [7], includes the $K_1(1400)^+$, $K_2^*(1430)^+$ and $K^*(1410)^+$ resonances with small contributions from the upper tail of the $K_1(1270)^+$. At the time of the writing of Ref. [7], the $K_1(1400)^+$ was believed to be the dominant 1^+ resonance, so the $K_1(1270)^+$ was not considered. However, subsequent experimental results [21] demonstrated that the $K_1(1270)^+$ is more prominent than the $K_1(1400)^+$; hence, the $[1.1, 1.3]$ GeV/c^2 interval is also studied here. The $[1.3, 1.4]$ GeV/c^2 mass interval, which contains the overlap region between the two K_1 resonances, and the $[1.6, 1.9]$ GeV/c^2 high mass interval, which includes spin-2 and spin-3 resonances, are also considered.

In each of the four $K^+\pi^-\pi^+$ mass intervals, a simultaneous fit to the B-candidate mass spectra in bins of the photon angle is performed in order to determine the background-subtracted angular distribution; the previously described PDF is used to model the mass spectrum in each bin, with all of the fit parameters being shared except for the yields. Since the sign of the photon polarization depends on the sign of the electric charge of the B candidate, the angular variable $\cos\hat{\theta} \equiv \mathrm{charge}(B)\cos\theta$ is used. The resulting background-subtracted $\cos\hat{\theta}$ distribution, corrected for the selection acceptance and normalized to the inverse of the bin width, is fit with a fourth-order polynomial function normalized to unit area,

$$f(\cos\hat{\theta}; c_0 = 0.5, c_1, c_2, c_3, c_4) = \sum_{i=0}^{4} c_i L_i(\cos\hat{\theta}), \quad (3)$$

where $L_i(x)$ is the Legendre polynomial of order i and c_i is the corresponding coefficient. Using Eqs. (1) and (3) the up-down asymmetry defined in Eq. (2) can be expressed as

$$\mathcal{A}_{\mathrm{ud}} = c_1 - \frac{c_3}{4}. \quad (4)$$

As a cross-check, the up-down asymmetry in each mass interval is also determined with a counting method, rather than an angular fit, as well as considering separately the B^+ and B^- candidates. All these checks yield compatible results.

The results obtained from a χ^2 fit of the normalized binned angular distribution, performed taking into account the full covariance matrix of the bin contents and all of the systematic uncertainties, are summarized in Table I. These systematic uncertainties account for the effect of choosing a different fit model, the impact of the limited size of the simulated samples on the fixed parameters, and the possibility of some events migrating from a bin to its neighbor because of the detector resolution, which gives the dominant contribution. The systematic uncertainty associated with the fit model is determined by performing the mass fit using several alternative PDFs, while the other two are estimated with simulated pseudoexperiments. Such uncertainties, despite being of the same size as the statistical uncertainty, do not substantially affect the fit results since they are strongly correlated across all angular bins.

The fitted distributions in the four $K^+\pi^-\pi^+$ mass intervals of interest are shown in Fig. 3. In order to illustrate the effect of the up-down asymmetry, the results of another fit imposing $c_1 = c_3 = 0$, hence forbidding the terms that carry the λ_γ dependence, are overlaid for comparison.

The combined significance of the observed up-down asymmetries is determined from a χ^2 test where the null hypothesis is defined as $\lambda_\gamma = 0$, implying that the up-down asymmetry is expected to be zero in each mass interval. The corresponding χ^2 distribution has 4 degrees of freedom, and the observed value corresponds to a p value of 1.7×10^{-7}. This translates into a 5.2σ significance for nonzero up-down asymmetry. Up-down asymmetries can be computed also for an alternative definition of the photon

TABLE I. Legendre coefficients obtained from fits to the normalized background-subtracted $\cos\hat{\theta}$ distribution in the four $K^+\pi^-\pi^+$ mass intervals of interest. The up-down asymmetries are obtained from Eq. (4). The quoted uncertainties contain statistical and systematic contributions. The $K^+\pi^-\pi^+$ mass ranges are indicated in GeV/c^2 and all the parameters are expressed in units of 10^{-2}. The covariance matrices are given in Ref. [22].

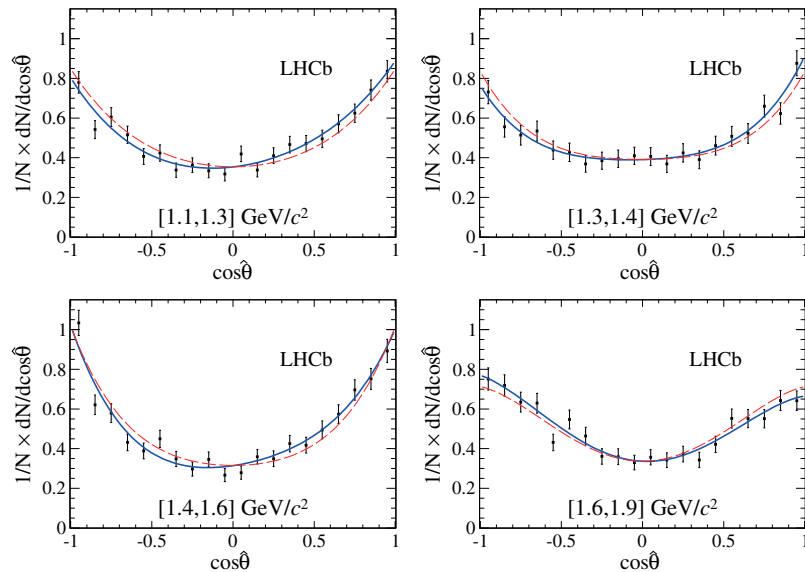|	[1.1,1.3]	[1.3,1.4]	[1.4,1.6]	[1.6,1.9]
c_1	6.3 ± 1.7	5.4 ± 2.0	4.3 ± 1.9	-4.6 ± 1.8
c_2	31.6 ± 2.2	27.0 ± 2.6	43.1 ± 2.3	28.0 ± 2.3
c_3	-2.1 ± 2.6	2.0 ± 3.1	-5.2 ± 2.8	-0.6 ± 2.7
c_4	3.0 ± 3.0	6.8 ± 3.6	8.1 ± 3.1	-6.2 ± 3.2
$\mathcal{A}_{\mathrm{ud}}$	6.9 ± 1.7	4.9 ± 2.0	5.6 ± 1.8	-4.5 ± 1.9

FIG. 3 (color online).   Distributions of $\cos\hat{\theta}$ for $B^+ \to K^+\pi^-\pi^+\gamma$ signal in four intervals of $K^+\pi^-\pi^+$ mass. The solid blue (dashed red) curves are the result of fits allowing all (only even) Legendre components up to the fourth power.

angle, obtained using the normal $\vec{p}_{\pi^-} \times \vec{p}_{\pi^+}$, instead of $\vec{p}_{\pi,\text{slow}} \times \vec{p}_{\pi,\text{fast}}$. The obtained values, along with the relative fit coefficients, are listed in Table II.

To summarize, a study of the inclusive flavor-changing neutral current radiative $B^+ \to K^+\pi^-\pi^+\gamma$ decay, with the $K^+\pi^-\pi^+$ mass in the $[1.1, 1.9]$ GeV/c^2 range, is performed on a data sample corresponding to an integrated luminosity of 3 fb^{-1} collected in pp collisions at 7 and 8 TeV center-of-mass energies by the LHCb detector. A total of 13876 ± 153 signal events is observed. The shape of the angular distribution of the photon with respect to the plane defined by the three final-state hadrons in their rest frame is determined in four intervals of interest in the $K^+\pi^-\pi^+$ mass spectrum. The up-down asymmetry, which is proportional to the photon polarization, is measured for the first

TABLE II.   Legendre coefficients obtained from fits to the normalized background-subtracted $\cos\hat{\theta}$ distribution, using the alternative normal $\vec{p}_{\pi^-} \times \vec{p}_{\pi^+}$ for defining the direction of the photon, in the four $K^+\pi^-\pi^+$ mass intervals of interest. The up-down asymmetries are obtained from Eq. (4). The quoted uncertainties contain statistical and systematic contributions. The $K^+\pi^-\pi^+$ mass ranges are indicated in GeV/c^2 and all the parameters are expressed in units of 10^{-2}. The covariance matrices are given in Ref. [22].

	[1.1,1.3]	[1.3,1.4]	[1.4,1.6]	[1.6,1.9]
c_1'	-0.9 ± 1.7	7.4 ± 2.0	5.3 ± 1.9	-3.4 ± 1.8
c_2'	31.6 ± 2.2	27.4 ± 2.6	43.6 ± 2.3	27.8 ± 2.3
c_3'	0.8 ± 2.6	0.8 ± 3.1	-4.4 ± 2.8	2.3 ± 2.7
c_4'	3.4 ± 3.0	7.0 ± 3.6	8.0 ± 3.1	-6.6 ± 3.2
$\mathcal{A}_{\text{ud}}'$	-1.1 ± 1.7	7.2 ± 2.0	6.4 ± 1.8	-3.9 ± 1.9

time for each of these $K^+\pi^-\pi^+$ mass intervals. The first observation of a parity-violating photon polarization different from zero at the 5.2σ significance level in $b \to s\gamma$ transitions is reported. The shape of the photon angular distribution in each bin, as well as the values for the up-down asymmetry, may be used, if theoretical predictions become available, to determine for the first time a value for the photon polarization, and thus constrain the effects of physics beyond the SM in the $b \to s\gamma$ sector.

[1] J. Beringer *et al.* (Particle Data Group), Phys. Rev. D **86**, 010001 (2012), and 2013 partial update for the 2014 edition.

[2] J. C. Pati and A. Salam, Phys. Rev. D **10**, 275 (1974); **11** 703 (1975); R. Mohapatra and J. C. Pati, Phys. Rev. D **11**, 2558 (1975); R. N. Mohapatra and J. C. Pati, Phys. Rev. D **11**, 566 (1975); G. Senjanovic and R. N. Mohapatra, Phys. Rev. D **12**, 1502 (1975); G. Senjanovic, Nucl. Phys. **B153**, 334 (1979); R. N. Mohapatra and G. Senjanovic, Phys. Rev. D **23**, 165 (1981); C. Lim and T. Inami, Prog. Theor. Phys. **67**, 1569 (1982); L. Everett, S. Rigolin, G. L. Kane, L.-T. Wang, and T. T. Wang, J. High Energy Phys. 01 (2002) 022.

[3] D. Atwood, M. Gronau, and A. Soni, Phys. Rev. Lett. **79**, 185 (1997).

[4] S. Nishida *et al.* (Belle Collaboration), Phys. Rev. Lett. **89**, 231801 (2002).

[5] B. Aubert *et al.* (BaBar Collaboration), Phys. Rev. Lett. **98**, 211804 (2007).

[6] C. S. Wu, E. Ambler, R. W. Hayward, D. D. Hoppes, and R. P. Hudson, Phys. Rev. **105**, 1413 (1957).

[7] M. Gronau and D. Pirjol, Phys. Rev. D **66**, 054008 (2002).

[8] E. Kou, A. Le Yaouanc, and A. Tayduganov, Phys. Rev. D **83**, 094007 (2011).

[9] A. A. Alves, Jr. *et al.* (LHCb Collaboration), JINST **3**, S08005 (2008).

[10] T. Sjöstrand, S. Mrenna, and P. Skands, J. High Energy Phys. 05 (2006) 026; Comput. Phys. Commun. **178**, 852 (2008).

[11] I. Belyaev *et al.*, *Nuclear Science Symposium Conference Record (NSS/MIC)*, (IEEE, Bellingham, WA, 2010), p. 1155.

[12] D. J. Lange, Nucl. Instrum. Methods Phys. Res., Sect. A **462**, 152 (2001).

[13] P. Golonka and Z. Was, Eur. Phys. J. C **45**, 97 (2006).

[14] J. Allison *et al.* (Geant4 Collaboration), IEEE Trans. Nucl. Sci. **53**, 270 (2006); S. Agostinelli *et al.*, (Geant4 Collaboration), Nucl. Instrum. Methods Phys. Res., Sect. A **506**, 250 (2003).

[15] M. Clemencic, G. Corti, S. Easo, C. R. Jones, S. Miglioranzi, M. Pappagallo, and P. Robbe, J. Phys. Conf. Ser. **331**, 032023 (2011).

[16] L. Breiman, J. H. Friedman, R. A. Olshen, and C. J. Stone, *Classification and Regression Trees* (Wadsworth International Group, Belmont, CA, 1984).

[17] R. E. Schapire and Y. Freund, J. Comput. Syst. Sci. **55**, 119 (1997).

[18] T. Skwarnicki, Ph.D thesis, Institute of Nuclear Physics, 1986 [DESY F31-86-02, Appendix E].

[19] H. Albrecht *et al.* (ARGUS Collaboration), Phys. Lett. B **241**, 278 (1990).

[20] M. Pivk and F. R. Le Diberder, Nucl. Instrum. Methods Phys. Res., Sect. A **555**, 356 (2005).

[21] H. Yang *et al.* (Belle Collaboration), Phys. Rev. Lett. **94**, 111802 (2005).

[22] See Supplemental Material at http://link.aps.org/supplemental/10.1103/PhysRevLett.112.161801 for details.

R. Aaij,[41] B. Adeva,[37] M. Adinolfi,[46] A. Affolder,[52] Z. Ajaltouni,[5] J. Albrecht,[9] F. Alessio,[38] M. Alexander,[51] S. Ali,[41] G. Alkhazov,[30] P. Alvarez Cartelle,[37] A. A. Alves Jr.,[25] S. Amato,[2] S. Amerio,[22] Y. Amhis,[7] L. Anderlini,[17,a] J. Anderson,[40] R. Andreassen,[57] M. Andreotti,[16,b] J. E. Andrews,[58] R. B. Appleby,[54] O. Aquines Gutierrez,[10] F. Archilli,[38] A. Artamonov,[35] M. Artuso,[59] E. Aslanides,[6] G. Auriemma,[25,c] M. Baalouch,[5] S. Bachmann,[11] J. J. Back,[48] A. Badalov,[36] V. Balagura,[31] W. Baldini,[16] R. J. Barlow,[54] C. Barschel,[39] S. Barsuk,[7] W. Barter,[47] V. Batozskaya,[28] T. Bauer,[41] A. Bay,[39] J. Beddow,[51] F. Bedeschi,[23] I. Bediaga,[1] S. Belogurov,[31] K. Belous,[35] I. Belyaev,[31] E. Ben-Haim,[8] G. Bencivenni,[18] S. Benson,[50] J. Benton,[46] A. Berezhnoy,[32] R. Bernet,[40] M.-O. Bettler,[47] M. van Beuzekom,[41] A. Bien,[11] S. Bifani,[45] T. Bird,[54] A. Bizzeti,[17,d] P. M. Bjørnstad,[54] T. Blake,[48] F. Blanc,[39] J. Blouw,[10] S. Blusk,[59] V. Bocci,[25] A. Bondar,[34] N. Bondar,[30] W. Bonivento,[15,38] S. Borghi,[54] A. Borgia,[59] M. Borsato,[7] T. J. V. Bowcock,[52] E. Bowen,[40] C. Bozzi,[16] T. Brambach,[9] J. van den Brand,[42] J. Bressieux,[39] D. Brett,[54] M. Britsch,[10] T. Britton,[59] N. H. Brook,[46] H. Brown,[52] A. Bursche,[40] G. Busetto,[22,e] J. Buytaert,[38] S. Cadeddu,[15] R. Calabrese,[16,b] O. Callot,[7] M. Calvi,[20,f] M. Calvo Gomez,[36,g] A. Camboni,[36] P. Campana,[18,38] D. Campora Perez,[38] F. Caponio,[21] A. Carbone,[14,h] G. Carboni,[24,i] R. Cardinale,[19,j] A. Cardini,[15] H. Carranza-Mejia,[50] L. Carson,[50] K. Carvalho Akiba,[2] G. Casse,[52] L. Cassina,[20] L. Castillo Garcia,[38] M. Cattaneo,[38] C. Cauet,[9] R. Cenci,[58] M. Charles,[8] P. Charpentier,[38] S.-F. Cheung,[55] N. Chiapolini,[40] M. Chrzaszcz,[40,26] K. Ciba,[38] X. Cid Vidal,[38] G. Ciezarek,[53] P. E. L. Clarke,[50] M. Clemencic,[38] H. V. Cliff,[47] J. Closier,[38] C. Coca,[29] V. Coco,[38] J. Cogan,[6] E. Cogneras,[5] P. Collins,[38] A. Comerma-Montells,[36] A. Contu,[15,38] A. Cook,[46] M. Coombes,[46] S. Coquereau,[8] G. Corti,[38] I. Counts,[56] B. Couturier,[38] G. A. Cowan,[50] D. C. Craik,[48] M. Cruz Torres,[60] S. Cunliffe,[53] R. Currie,[50] C. D'Ambrosio,[38] J. Dalseno,[46] P. David,[8] P. N. Y. David,[41] A. Davis,[57] I. De Bonis,[4] K. De Bruyn,[41] S. De Capua,[54] M. De Cian,[11] J. M. De Miranda,[1] L. De Paula,[2] W. De Silva,[57] P. De Simone,[18] D. Decamp,[4] M. Deckenhoff,[9] L. Del Buono,[8] N. Déléage,[4] D. Derkach,[55] O. Deschamps,[5] F. Dettori,[42] A. Di Canto,[11] H. Dijkstra,[38] S. Donleavy,[52] F. Dordei,[11] M. Dorigo,[39] P. Dorosz,[26,k] A. Dosil Suárez,[37] D. Dossett,[48] A. Dovbnya,[43] F. Dupertuis,[39] P. Durante,[38] R. Dzhelyadin,[35] A. Dziurda,[26] A. Dzyuba,[30] S. Easo,[49] U. Egede,[53] V. Egorychev,[31] S. Eidelman,[34] S. Eisenhardt,[50] U. Eitschberger,[9] R. Ekelhof,[9] L. Eklund,[51,38] I. El Rifai,[5] C. Elsasser,[40] S. Esen,[11] A. Falabella,[16,b] C. Färber,[11] C. Farinelli,[41] S. Farry,[52] D. Ferguson,[50] V. Fernandez Albor,[37] F. Ferreira Rodrigues,[1] M. Ferro-Luzzi,[38] S. Filippov,[33] M. Fiore,[16,b] M. Fiorini,[16,b] C. Fitzpatrick,[38] M. Fontana,[10]

F. Fontanelli,[19,j] R. Forty,[38] O. Francisco,[2] M. Frank,[38] C. Frei,[38] M. Frosini,[17,38,a] J. Fu,[21] E. Furfaro,[24,i] A. Gallas Torreira,[37] D. Galli,[14,h] S. Gambetta,[19,j] M. Gandelman,[2] P. Gandini,[59] Y. Gao,[3] J. Garofoli,[59] J. Garra Tico,[47] L. Garrido,[36] C. Gaspar,[38] R. Gauld,[55] L. Gavardi,[9] E. Gersabeck,[11] M. Gersabeck,[54] T. Gershon,[48] P. Ghez,[4] A. Gianelle,[22] S. Giani',[39] V. Gibson,[47] L. Giubega,[29] V. V. Gligorov,[38] C. Göbel,[60] D. Golubkov,[31] A. Golutvin,[53,31,38] A. Gomes,[1,l] H. Gordon,[38] M. Grabalosa Gándara,[5] R. Graciani Diaz,[36] L. A. Granado Cardoso,[38] E. Graugés,[36] G. Graziani,[17] A. Grecu,[29] E. Greening,[55] S. Gregson,[47] P. Griffith,[45] L. Grillo,[11] O. Grünberg,[61] B. Gui,[59] E. Gushchin,[33] Y. Guz,[35,38] T. Gys,[38] C. Hadjivasiliou,[59] G. Haefeli,[39] C. Haen,[38] T. W. Hafkenscheid,[64] S. C. Haines,[47] S. Hall,[53] B. Hamilton,[58] T. Hampson,[46] S. Hansmann-Menzemer,[11] N. Harnew,[55] S. T. Harnew,[46] J. Harrison,[54] T. Hartmann,[61] J. He,[38] T. Head,[38] V. Heijne,[41] K. Hennessy,[52] P. Henrard,[5] L. Henry,[8] J. A. Hernando Morata,[37] E. van Herwijnen,[38] M. Heß,[61] A. Hicheur,[1] D. Hill,[55] M. Hoballah,[5] C. Hombach,[54] W. Hulsbergen,[41] P. Hunt,[55] N. Hussain,[55] D. Hutchcroft,[52] D. Hynds,[51] M. Idzik,[27] P. Ilten,[56] R. Jacobsson,[38] A. Jaeger,[11] E. Jans,[41] P. Jaton,[39] A. Jawahery,[58] F. Jing,[3] M. John,[55] D. Johnson,[55] C. R. Jones,[47] C. Joram,[38] B. Jost,[38] N. Jurik,[59] M. Kaballo,[9] S. Kandybei,[43] W. Kanso,[6] M. Karacson,[38] T. M. Karbach,[38] M. Kelsey,[59] I. R. Kenyon,[45] T. Ketel,[42] B. Khanji,[20] C. Khurewathanakul,[39] S. Klaver,[54] O. Kochebina,[7] I. Komarov,[39] R. F. Koopman,[42] P. Koppenburg,[41] M. Korolev,[32] A. Kozlinskiy,[41] L. Kravchuk,[33] K. Kreplin,[11] M. Kreps,[48] G. Krocker,[11] P. Krokovny,[34] F. Kruse,[9] M. Kucharczyk,[20,26,38,f] V. Kudryavtsev,[34] K. Kurek,[28] T. Kvaratskheliya,[31,38] V. N. La Thi,[39] D. Lacarrere,[38] G. Lafferty,[54] A. Lai,[15] D. Lambert,[50] R. W. Lambert,[42] E. Lanciotti,[38] G. Lanfranchi,[18] C. Langenbruch,[38] B. Langhans,[38] T. Latham,[48] C. Lazzeroni,[45] R. Le Gac,[6] J. van Leerdam,[41] J.-P. Lees,[4] R. Lefèvre,[5] A. Leflat,[32] J. Lefrançois,[7] S. Leo,[23] O. Leroy,[6] T. Lesiak,[26] B. Leverington,[11] Y. Li,[3] M. Liles,[52] R. Lindner,[38] C. Linn,[38] F. Lionetto,[40] B. Liu,[15] G. Liu,[38] S. Lohn,[38] I. Longstaff,[51] J. H. Lopes,[2] N. Lopez-March,[39] P. Lowdon,[40] H. Lu,[3] D. Lucchesi,[22,e] H. Luo,[50] E. Luppi,[16,b] O. Lupton,[55] F. Machefert,[7] I. V. Machikhiliyan,[31] F. Maciuc,[29] O. Maev,[30,38] S. Malde,[55] G. Manca,[15,m] G. Mancinelli,[6] M. Manzali,[16,b] J. Maratas,[5] U. Marconi,[14] C. Marin Benito,[36] P. Marino,[23,n] R. Märki,[39] J. Marks,[11] G. Martellotti,[25] A. Martens,[8] A. Martín Sánchez,[7] M. Martinelli,[41] D. Martinez Santos,[42] F. Martinez Vidal,[63] D. Martins Tostes,[2] A. Massafferri,[1] R. Matev,[38] Z. Mathe,[38] C. Matteuzzi,[20] A. Mazurov,[16,38,b] M. McCann,[53] J. McCarthy,[45] A. McNab,[54] R. McNulty,[12] B. McSkelly,[52] B. Meadows,[57,55] F. Meier,[9] M. Meissner,[11] M. Merk,[41] D. A. Milanes,[8] M.-N. Minard,[4] J. Molina Rodriguez,[60] S. Monteil,[5] D. Moran,[54] M. Morandin,[22] P. Morawski,[26] A. Mordà,[6] M. J. Morello,[23,n] R. Mountain,[59] F. Muheim,[50] K. Müller,[40] R. Muresan,[29] B. Muryn,[27] B. Muster,[39] P. Naik,[46] T. Nakada,[39] R. Nandakumar,[49] I. Nasteva,[1] M. Needham,[50] N. Neri,[21] S. Neubert,[38] N. Neufeld,[38] A. D. Nguyen,[39] T. D. Nguyen,[39] C. Nguyen-Mau,[39,o] M. Nicol,[7] V. Niess,[5] R. Niet,[9] N. Nikitin,[32] T. Nikodem,[11] A. Novoselov,[35] A. Oblakowska-Mucha,[27] V. Obraztsov,[35] S. Oggero,[41] S. Ogilvy,[51] O. Okhrimenko,[44] R. Oldeman,[15,m] G. Onderwater,[64] M. Orlandea,[29] J. M. Otalora Goicochea,[2] P. Owen,[53] A. Oyanguren,[36] B. K. Pal,[59] A. Palano,[13,p] F. Palombo,[21,q] M. Palutan,[18] J. Panman,[38] A. Papanestis,[49,38] M. Pappagallo,[51] L. Pappalardo,[16] C. Parkes,[54] C. J. Parkinson,[9] G. Passaleva,[17] G. D. Patel,[52] M. Patel,[53] C. Patrignani,[19,j] C. Pavel-Nicorescu,[29] A. Pazos Alvarez,[37] A. Pearce,[54] A. Pellegrino,[41] M. Pepe Altarelli,[38] S. Perazzini,[14,h] E. Perez Trigo,[37] P. Perret,[5] M. Perrin-Terrin,[6] L. Pescatore,[45] E. Pesen,[65] G. Pessina,[20] K. Petridis,[53] A. Petrolini,[19,j] E. Picatoste Olloqui,[36] B. Pietrzyk,[4] T. Pilař,[48] D. Pinci,[25] A. Pistone,[19] S. Playfer,[50] M. Plo Casasus,[37] F. Polci,[8] A. Poluektov,[48,34] E. Polycarpo,[2] A. Popov,[35] D. Popov,[10] B. Popovici,[29] C. Potterat,[36] A. Powell,[55] J. Prisciandaro,[39] A. Pritchard,[52] C. Prouve,[46] V. Pugatch,[44] A. Puig Navarro,[39] G. Punzi,[23,r] W. Qian,[4] B. Rachwal,[26] J. H. Rademacker,[46] B. Rakotomiaramanana,[39] M. Rama,[18] M. S. Rangel,[2] I. Raniuk,[43] N. Rauschmayr,[38] G. Raven,[42] S. Reichert,[54] M. M. Reid,[48] A. C. dos Reis,[1] S. Ricciardi,[49] A. Richards,[53] K. Rinnert,[52] V. Rives Molina,[36] D. A. Roa Romero,[5] P. Robbe,[7] D. A. Roberts,[58] A. B. Rodrigues,[1] E. Rodrigues,[54] P. Rodriguez Perez,[37] S. Roiser,[38] V. Romanovsky,[35] A. Romero Vidal,[37] M. Rotondo,[22] J. Rouvinet,[39] T. Ruf,[38] F. Ruffini,[23] H. Ruiz,[36] P. Ruiz Valls,[36] G. Sabatino,[25,i] J. J. Saborido Silva,[37] N. Sagidova,[30] P. Sail,[51] B. Saitta,[15,m] V. Salustino Guimaraes,[2] B. Sanmartin Sedes,[37] R. Santacesaria,[25] C. Santamarina Rios,[37] E. Santovetti,[24,i] M. Sapunov,[6] A. Sarti,[18] C. Satriano,[25,c] A. Satta,[24] M. Savrie,[16,b] D. Savrina,[31,32] M. Schiller,[42] H. Schindler,[38] M. Schlupp,[9] M. Schmelling,[10] B. Schmidt,[38] O. Schneider,[39] A. Schopper,[38] M.-H. Schune,[7] R. Schwemmer,[38] B. Sciascia,[18] A. Sciubba,[25] M. Seco,[37] A. Semennikov,[31] K. Senderowska,[27] I. Sepp,[53] N. Serra,[40] J. Serrano,[6] P. Seyfert,[11] M. Shapkin,[35] I. Shapoval,[16,43,b] Y. Shcheglov,[30] T. Shears,[52] L. Shekhtman,[34] O. Shevchenko,[43] V. Shevchenko,[62] A. Shires,[9] R. Silva Coutinho,[48] G. Simi,[22] M. Sirendi,[47] N. Skidmore,[46] T. Skwarnicki,[59] N. A. Smith,[52] E. Smith,[55,49] E. Smith,[53] J. Smith,[47] M. Smith,[54] H. Snoek,[41] M. D. Sokoloff,[57] F. J. P. Soler,[51] F. Soomro,[39] D. Souza,[46] B. Souza De Paula,[2] B. Spaan,[9] A. Sparkes,[50] F. Spinella,[23] P. Spradlin,[51] F. Stagni,[38] S. Stahl,[11] O. Steinkamp,[40] S. Stevenson,[55] S. Stoica,[29] S. Stone,[59] B. Storaci,[40] S. Stracka,[23,38] M. Straticiuc,[29]

U. Straumann,[40] R. Stroili,[22] V. K. Subbiah,[38] L. Sun,[57] W. Sutcliffe,[53] S. Swientek,[9] V. Syropoulos,[42] M. Szczekowski,[28] P. Szczypka,[39,38] D. Szilard,[2] T. Szumlak,[27] S. T'Jampens,[4] M. Teklishyn,[7] G. Tellarini,[16,b] E. Teodorescu,[29] F. Teubert,[38] C. Thomas,[55] E. Thomas,[38] J. van Tilburg,[11] V. Tisserand,[4] M. Tobin,[39] S. Tolk,[42] L. Tomassetti,[16,b] D. Tonelli,[38] S. Topp-Joergensen,[55] N. Torr,[55] E. Tournefier,[4,53] S. Tourneur,[39] M. T. Tran,[39] M. Tresch,[40] A. Tsaregorodtsev,[6] P. Tsopelas,[41] N. Tuning,[41] M. Ubeda Garcia,[38] A. Ukleja,[28] A. Ustyuzhanin,[62] U. Uwer,[11] V. Vagnoni,[14] G. Valenti,[14] A. Vallier,[7] R. Vazquez Gomez,[18] P. Vazquez Regueiro,[37] C. Vázquez Sierra,[37] S. Vecchi,[16] J. J. Velthuis,[46] M. Veltri,[17,s] G. Veneziano,[39,†] M. Vesterinen,[11] B. Viaud,[7] D. Vieira,[2] X. Vilasis-Cardona,[36,g] A. Vollhardt,[40] D. Volyanskyy,[10] D. Voong,[46] A. Vorobyev,[30] V. Vorobyev,[34] C. Voß,[61] H. Voss,[10] J. A. de Vries,[41] R. Waldi,[61] C. Wallace,[48] R. Wallace,[12] S. Wandernoth,[11] J. Wang,[59] D. R. Ward,[47] N. K. Watson,[45] A. D. Webber,[54] D. Websdale,[53] M. Whitehead,[48] J. Wicht,[38] J. Wiechczynski,[26] D. Wiedner,[11] G. Wilkinson,[55] M. P. Williams,[48,49] M. Williams,[56] F. F. Wilson,[49] J. Wimberley,[58] J. Wishahi,[9] W. Wislicki,[28] M. Witek,[26] G. Wormser,[7] S. A. Wotton,[47] S. Wright,[47] S. Wu,[3] K. Wyllie,[38] Y. Xie,[50,38] Z. Xing,[59] Z. Yang,[3] X. Yuan,[3] O. Yushchenko,[35] M. Zangoli,[14] M. Zavertyaev,[10,t] F. Zhang,[3] L. Zhang,[59] W. C. Zhang,[12] Y. Zhang,[3] A. Zhelezov,[11] A. Zhokhov,[31] L. Zhong[3] and A. Zvyagin[38]

(LHCb Collaboration)

[1]*Centro Brasileiro de Pesquisas Físicas (CBPF), Rio de Janeiro, Brazil*
[2]*Universidade Federal do Rio de Janeiro (UFRJ), Rio de Janeiro, Brazil*
[3]*Center for High Energy Physics, Tsinghua University, Beijing, China*
[4]*LAPP, Université de Savoie, CNRS/IN2P3, Annecy-Le-Vieux, France*
[5]*Clermont Université, Université Blaise Pascal, CNRS/IN2P3, LPC, Clermont-Ferrand, France*
[6]*CPPM, Aix-Marseille Université, CNRS/IN2P3, Marseille, France*
[7]*LAL, Université Paris-Sud, CNRS/IN2P3, Orsay, France*
[8]*LPNHE, Université Pierre et Marie Curie, Université Paris Diderot, CNRS/IN2P3 Paris, France*
[9]*Fakultät Physik, Technische Universität Dortmund, Dortmund, Germany*
[10]*Max-Planck-Institut für Kernphysik (MPIK), Heidelberg, Germany*
[11]*Physikalisches Institut, Ruprecht-Karls-Universität Heidelberg, Heidelberg, Germany*
[12]*School of Physics, University College Dublin, Dublin, Ireland*
[13]*Sezione INFN di Bari, Bari, Italy*
[14]*Sezione INFN di Bologna, Bologna, Italy*
[15]*Sezione INFN di Cagliari, Cagliari, Italy*
[16]*Sezione INFN di Ferrara, Ferrara, Italy*
[17]*Sezione INFN di Firenze, Firenze, Italy*
[18]*Laboratori Nazionali dell'INFN di Frascati, Frascati, Italy*
[19]*Sezione INFN di Genova, Genova, Italy*
[20]*Sezione INFN di Milano Bicocca, Milano, Italy*
[21]*Sezione INFN di Milano, Milano, Italy*
[22]*Sezione INFN di Padova, Padova, Italy*
[23]*Sezione INFN di Pisa, Pisa, Italy*
[24]*Sezione INFN di Roma Tor Vergata, Roma, Italy*
[25]*Sezione INFN di Roma La Sapienza, Roma, Italy*
[26]*Henryk Niewodniczanski Institute of Nuclear Physics Polish Academy of Sciences, Kraków, Poland*
[27]*Faculty of Physics and Applied Computer Science, AGH—University of Science and Technology, Kraków, Poland*
[28]*National Center for Nuclear Research (NCBJ), Warsaw, Poland*
[29]*Horia Hulubei National Institute of Physics and Nuclear Engineering, Bucharest-Magurele, Romania*
[30]*Petersburg Nuclear Physics Institute (PNPI), Gatchina, Russia*
[31]*Institute of Theoretical and Experimental Physics (ITEP), Moscow, Russia*
[32]*Institute of Nuclear Physics, Moscow State University (SINP MSU), Moscow, Russia*
[33]*Institute for Nuclear Research of the Russian Academy of Sciences (INR RAN), Moscow, Russia*
[34]*Budker Institute of Nuclear Physics (SB RAS) and Novosibirsk State University, Novosibirsk, Russia*
[35]*Institute for High Energy Physics (IHEP), Protvino, Russia*
[36]*Universitat de Barcelona, Barcelona, Spain*
[37]*Universidad de Santiago de Compostela, Santiago de Compostela, Spain*
[38]*European Organization for Nuclear Research (CERN), Geneva, Switzerland*
[39]*Ecole Polytechnique Fédérale de Lausanne (EPFL), Lausanne, Switzerland*
[40]*Physik-Institut, Universität Zürich, Zürich, Switzerland*
[41]*Nikhef National Institute for Subatomic Physics, Amsterdam, The Netherlands*

[42]Nikhef National Institute for Subatomic Physics and VU University Amsterdam, Amsterdam, The Netherlands

[43]NSC Kharkiv Institute of Physics and Technology (NSC KIPT), Kharkiv, Ukraine

[44]Institute for Nuclear Research of the National Academy of Sciences (KINR), Kyiv, Ukraine

[45]University of Birmingham, Birmingham, United Kingdom

[46]H.H. Wills Physics Laboratory, University of Bristol, Bristol, United Kingdom

[47]Cavendish Laboratory, University of Cambridge, Cambridge, United Kingdom

[48]Department of Physics, University of Warwick, Coventry, United Kingdom

[49]STFC Rutherford Appleton Laboratory, Didcot, United Kingdom

[50]School of Physics and Astronomy, University of Edinburgh, Edinburgh, United Kingdom

[51]School of Physics and Astronomy, University of Glasgow, Glasgow, United Kingdom

[52]Oliver Lodge Laboratory, University of Liverpool, Liverpool, United Kingdom

[53]Imperial College London, London, United Kingdom

[54]School of Physics and Astronomy, University of Manchester, Manchester, United Kingdom

[55]Department of Physics, University of Oxford, Oxford, United Kingdom

[56]Massachusetts Institute of Technology, Cambridge, Massachusetts, USA

[57]University of Cincinnati, Cincinnati, Ohio, USA

[58]University of Maryland, College Park, Maryland, USA

[59]Syracuse University, Syracuse, New York, USA

[60]Pontifícia Universidade Católica do Rio de Janeiro (PUC-Rio), Rio de Janeiro, Brazil
(associated with Universidade Federal do Rio de Janeiro (UFRJ), Rio de Janeiro, Brazil)

[61]Institut für Physik, Universität Rostock, Rostock, Germany
(associated with Physikalisches Institut, Ruprecht-Karls-Universität Heidelberg, Heidelberg, Germany)

[62]National Research Centre Kurchatov Institute, Moscow, Russia
(associated with Institute of Theoretical and Experimental Physics (ITEP), Moscow, Russia)

[63]Instituto de Fisica Corpuscular (IFIC), Universitat de Valencia-CSIC, Valencia, Spain
(associated with Universitat de Barcelona, Barcelona, Spain)

[64]KVI—University of Groningen, Groningen, The Netherlands
(associated with Nikhef National Institute for Subatomic Physics, Amsterdam, The Netherlands)

[65]Celal Bayar University, Manisa, Turkey
(associated with European Organization for Nuclear Research (CERN), Geneva, Switzerland)

[a]Also at Università di Firenze, Firenze, Italy.

[b]Also at Università di Ferrara, Ferrara, Italy.

[c]Also at Università della Basilicata, Potenza, Italy.

[d]Also at Università di Modena e Reggio Emilia, Modena, Italy.

[e]Also at Università di Padova, Padova, Italy.

[f]Also at Università di Milano Bicocca, Milano, Italy.

[g]Also at LIFAELS, La Salle, Universitat Ramon Llull, Barcelona, Spain.

[h]Also at Università di Bologna, Bologna, Italy.

[i]Also at Università di Roma Tor Vergata, Roma, Italy.

[j]Also at Università di Genova, Genova, Italy.

[k]Also at AGH - University of Science and Technology, Faculty of Computer Science, Electronics and Telecommunications, Kraków, Poland.

[l]Also at Universidade Federal do Triângulo Mineiro (UFTM), Uberaba-MG, Brazil.

[m]Also at Università di Cagliari, Cagliari, Italy.

[n]Also at Scuola Normale Superiore, Pisa, Italy.

[o]Also at Hanoi University of Science, Hanoi, Vietnam.

[p]Also at Università di Bari, Bari, Italy.

[q]Also at Università degli Studi di Milano, Milano, Italy.

[r]Also at Università di Pisa, Pisa, Italy.

[s]Also at Università di Urbino, Urbino, Italy.

[t]Also at P.N. Lebedev Physical Institute, Russian Academy of Science (LPI RAS), Moscow, Russia.

[†]Corresponding author.giovanni.veneziano@cern.ch

CURRICULUM VITAE – GIOVANNI VENEZIANO

PERSONAL INFORMATION

Giovanni Veneziano
Chemin des Cottages 12
1007 Lausanne, Switzerland
tel: +41 (0)76 7816154
office: +41 (0)21 6930493
gio.veneziano@gmail.com
giovanni.veneziano@epfl.ch

I was born on November 13th 1985 in Formia (Italy), where I spent my childhood before moving to Rome. There, I started my studies in theoretical physics at the University of Rome Sapienza, having the pleasure to attend Profs Nicola Cabibbo and Luciano Maiani's lectures. I graduated in December 2010, after spending a semester in London (UK) as an exchange student, in order to improve my English and broaden my cultural and scientific horizon.

After getting my master's degree, I moved to Switzerland to work as *assistant doctorant* (Ph.D. student) at the École Polytechnique Fédérale de Lausanne (EPFL). As a member of the LHCb collaboration, my work has been mainly focused on the experimental study of radiative *B*-mesons decays, with particular attention to the study of photon polarization. I have also been involved in hardware studies for the scintillating fibre technology for the LHCb tracker upgrade. As part of my doctoral studies, I had the opportunity to be teaching assistant for statistics, particle physics and laboratory work classes.

I spend most of my free time reading, trying to have my own opinion about everything. When I am not facing a laptop, I enjoy travelling and photography.

EDUCATION

Ph.D. in Physics at the École Polytechnique Fédérale de Lausanne (EPFL), under the lead of Prof. Olivier Schneider and Dr Fred Blanc, as a member of the LHCb collaboration at CERN.
Thesis title: *Towards the measurement of photon polarisation in the decay $B^+ \rightarrow K^+ \pi^- \pi^+ \gamma$*.
Thesis exam passed on the 26/11/2015. Public defence scheduled for the 15/01/2016.

Master's degree (MS) in Physics from the University of Rome Sapienza, 110 cum laude/110, obtained on the 21/12/2010.
Thesis advisor: Dr Omar Benhar Noccioli (INFN).
Thesis title: *Studio della diffusione neutrino-nucleo in regime quasi elastico*. Study of neutrino-nuclei diffusion in the quasi-elastic regime.

Bachelor degree (BS) in Physics and Astrophysics from the University of Rome Sapienza, 110/110, obtained on the 18/07/2008.
Thesis advisor: Dr Marco De Petris.
Thesis title: *L'effetto Sunyaev-Zel'dovich*. Study of the Sunyaev-Zel'dovich effect on the cosmic microwave background radiation.

ERASMUS exchange program Study abroad semester at Queen Mary University of London (QMUL) and University College London (UCL) in 2010.

PUBLICATIONS   All the LHCb collaboration publications since June 2012 on (221 papers). A complete list can be found at https://cds.cern.ch/collection/LHCb%20Papers.

Amongst such publications, I am contact author of

- LHCb collaboration, *Observation of photon polarization in the $b \to s\gamma$ transition*, Phys. Rev. Lett. 112, 161801 (2014) http://journals.aps.org/prl/abstract/10.1103/PhysRevLett.112.161801
- LHCb collaboration, *CP and up-down asymmetries in $B^{\pm} \to K^{\pm}\pi^{\mp}\pi^{\pm}\gamma$ decays*, CERN-LHCb-CONF-2013-009. http://cds.cern.ch/record/1556018

O. Benhar, G. Veneziano, *Nuclear effects in neutral current quasi-elastic neutrino interactions*, Phys. Lett. B **702** 433 (2011). http://dx.doi.org/10.1016/j.physletb.2011.07.032

CONFERENCE TALKS AND POSTER PRESENTATIONS

LHCb Rare decays, LHCP 2015, Saint Petersburg, Russia (September 2015).

Observation of photon polarization in the $b \to s\gamma$ transition, 2014 CHIPP Annual Plenary Meeting PhD/Postdoc days, University of Fribourg, Switzerland(July 2014).

LHCC poster session 2014, CERN, Switzerland (March 2014).

Testing the Standard Model with rare decays at LHCb, Lake Louise Winter Institute 2014 - Lake Louise, Alberta, Canada (February 2014). https://cds.cern.ch/record/1662514

SLAC Summer Institute 2013 Poster Session, Menlo Park, California, USA(July 2013).

INTERNAL NOTES

Veneziano G., Puig A., Schneider O., *Up-down asymmetry and angular study of $B \to K\pi\pi\gamma$ decays*, CERN-LHCb-ANA-2013-094.

Puig A., Veneziano G., Schneider O., *CP and up-down asymmetries in $B \to K\pi\pi\gamma$ decays*, CERN-LHCb-ANA-2013-044.

Bay A. *et al.*, *Viability assessment of a scintillating fibre tracker for the LHCb upgrade*, LHCb-INT-2013-004.

SELECTION OF SCHOOLS AND COURSES ATTENDED

SLAC Summer Institute 2013, Menlo Park, California, USA (July 2013).

CHIPP Ph.D. Winter School 2013, Grindelwald, Switzerland (January 2013).

Statistics for Physicists, Prof F. James, CUSO course (autumn 2013).

Angular Momentum in Particle Physics, Prof S.U. Chung, CUSO course (spring 2015).

TEACHING DUTIES   *Particules Elementaires*, Prof A. Bay, from autumn 2013 to autumn 2015.

Chapitres Choisis de Physique des Particules, Prof A.Bay, F. Blanc and T.M. Tam, spring 2013.

Statistics for Physicists, Prof F. James, autumn 2012.

Travaux Pratique 3, spring and autumn 2012.

COMPUTER SKILLS **Programming and scripting languages** Python, C++ and Bash (daily).
Markup languages LaTeX (daily) and HTML (seldomly).

LANGUAGE SKILLS **Italian**: Native tongue. **English**: Fluent. **French**: Beginner. **Portuguese**: Beginner.